Secondary Organic Aerosol Formation from α-dicarbonyls in Aerosol Water: Salt interactions and multi-phase chemistry

by

E. M. Waxman

B.S., California Institute of Technology, 2008

A thesis submitted to the

Faculty of the Graduate School of the

University of Colorado in partial fulfillment

of the requirements for the degree of

Doctor of Philosophy

Department of Chemistry and Biochemistry

2015

This thesis entitled:
Secondary Organic Aerosol Formation from α-dicarbonyls in Aerosol Water: Salt interactions and multi-phase chemistry
written by E. M. Waxman
has been approved for the Department of Chemistry and Biochemistry

_____

Prof. Rainer Volkamer

_____

Prof. Paul Ziemann

Date _____

The final copy of this thesis has been examined by the signatories, and we find that both the content and the form meet acceptable presentation standards of scholarly work in the above mentioned discipline.

Waxman, E. M. (Ph.D., Chemistry)

Secondary Organic Aerosol Formation from α-dicarbonyls in Aerosol Water: Salt interactions and multi-phase chemistry

Thesis directed by Prof. Rainer Volkamer

This thesis advances our understanding of secondary organic aerosol (SOA) formation from small, water soluble molecules like glyoxal and methyl glyoxal that partition to the aerosol aqueous phase according to Henry's law. Their partitioning behavior can be altered by the presence of inorganic salts, which are abundant in aerosols. If the molecules become more soluble this is called "salting in" and the reverse is "salting out". We present the first measurements of salting constants of glyoxal and methyl glyoxal in the aerosol-relevant salts ammonium sulfate, ammonium nitrate, sodium chloride, and sodium nitrate, as well as additional salts for theory-measurement comparison purposes: tetramethylammonium bromide, tetrabutylammonium bromide, and sodium oxalate. We find that glyoxal "salts in" to all salts tested, while methyl glyoxal "salts out". Explanations for their salting behavior are presented using quantum-mechanical calculations to quantify molecule-ion attractions and proposed literature mechanisms to predict repulsive forces (solution volume decrease upon salt addition, dielectric decrement). We calculate a ΔG of interaction (the enthalpy for replacing a water molecule in the hydration shell of an ion with an organic molecule) for isoprene epoxydiol (IEPOX) and its ring-opening product methyl tetrol with sulfate, and given the structural similarities of IEPOX and methyl tetrol with methyl glyoxal, we find that the values are similar to the value for methyl glyoxal. Therefore we predict that trans-β-IEPOX and its methyl tetrol likely salt out with a salting constant similar to methyl glyoxal.

Partitioning also influences reactivity. In a series of simulation chamber experiments we have studied the effect of NH_3 on the rate of gly-SOA formation and find that in the presence of added NH_3 we observe a significant enhancement in total SOA mass formed from glyoxal, especially in the formation of nitrogen-containing products (imidazoles) and the overall aerosol N/C. We present

the results of simulation chamber experiments that focus on the chemical composition of gly-SOA. We are able to identify a number of imidazoles resulting from the reaction of glyoxal + NH_4^+. We also use time-resolved data to propose a mechanism for their formation. By comparing imidazole formation under a variety of different chamber conditions we are able to determine under what conditions they will contribute most strongly to brown carbon formation.

We have further used a box model to simulate SOA formation in Mexico City during the MCMA-2003 campaign using an explicit aqueous-phase mechanism for glyoxal processing (gly-SOA). This gly-SOA was compared to SOA from semi/intermediate volatility gases (S/I VOC) using a near explicit gas-phase oxidation mechanism, and two different volatility basis sets to characterize their partitioning. We also have applied our measured salting constants to predict SOA formation over the continental United States using the Community Multi-scale Air Quality Model (CMAQ). Significant SOA forms from the further reactions of these precursors in the aerosol, but the effect of salt is most important. The small Henry's law constant for methyl glyoxal combined with the fact that it salts out means that even though methyl glyoxal is far more abundant in the gas phase than glyoxal, methyl glyoxal forms significantly less SOA than glyoxal. Our results suggest that salts also play an important role in modulating the SOA formation from isoprene.

Dedication

To my husband Kevin.

Acknowledgements

I would first like to thank my advisor Professor Rainer Volkamer for taking me on as a graduate student and providing such an interesting project to work on. I would also like to thank the Volkamer group members (past, present, and unofficial) for making this such a great place to work: Sunil Baidar, Randall Chiu, Sean Coburn, Doug Day, Barbara Dix, Laura Gonzalez, Natasha Goss, Phil Handley, Christopher Kampf, Natalie Kille, Ted Koenig, Michael Lechner, Hilke Oetjen, Ivan Ortega, Roman Sinreich, Ryan Thalman, Siyuan Wang, and Kyle Zarzana.

I would also like to thank the many collaborators who contributed to this work. Katja Dzepina, Barbara Ervens, and Julia Lee-Taylor contributed modeling work to Chapter 2 and Jose Jimenez, Bernard Aumont, and Sasha Madronich provided thoughtful input to this work. Natasha Goss measured the ^{13}C glyoxal cross section used in Chapter 3, Sean Coburn provided coding assistance, and Ted Koenig collected the glyoxal spectra. Annmarie Carlton and Neha Sareen did the CMAQ modeling and Paul Ziemann provided valuable input for the design of the salting constant measurements in Chapter 4. Jonas Elm and Theo Kurtén did the quantum calculations for Chapter 5. Urs Baltensperger, Josef Dommen, Jay Slowik, André Prévôt, Nivedita Kumar, Felix Klein, and Manuel Krapf operated the chamber and AMS for the work in Chapter 6 and Barbara Nozière, Aurelia Maxut, Thorsten Hoffmann, Christopher Kampf, and Ronit Jakob, provided additional imidazole measurements. Alex Laskin, Julia Laskin, and Peng Lin hosted analysis at PNNL.

Funding was provided by Eurochamp Proposal E2-2013-04-10-0088, NSF CAREER Award ATM-0847793, US DOE Office of Science Award DE-SC0006080, a National Science Foundation Graduate Research Fellowship and a CIRES Graduate Research Fellowship.

Contents

Chapter

Tables

Table

Figures

Figure

Chapter 1

Introduction

Aerosols are small liquid or solid particles suspended in the air (Seinfeld and Pandis, 2006). Submicron aerosols are important because they affect the climate and impact public health. Their size, location, and chemical composition determines how much of an impact it will have.

There are three primary ways of classifying aerosols: by size, by chemical composition, and by generation. Particles above 1 μm in diameter are considered coarse particles. These are typically formed from physical processes such as wind lofting of dust particles or sea spray. Particles smaller than 1 μm in diameter are considered fine particles and are further divided in to nucleation-mode particles (less than 10 nm in diameter), Aitken-mode particles (between 10 and 100 nm in diameter) and accumulation-mode particles (those between 100 and 1000 nm in diameter). Fine particles are formed chemically and often start as nucleation-mode particles (Kulmala, 2003; Kulmala and Kerminen, 2008; Kulmala et al., 2013). The nucleation process starts because molecules continually form and break small clusters (<1.3 nm) due to evaporation and chemical reactions. Once a cluster reaches a size of between about 1.3 nm and 1.9 nm, it has reached a critical size and grows due to condensation by sulfuric acid and other molecules. These clusters are then stabilized by the condensation of ammonia, amines, and organic molecules. Once clusters get above 1.9 nm, they begin to grow much more rapidly, likely due to the condensation of oxidized organic vapors (Kulmala et al., 2013). These nucleation-mode particles can then coagulate to form Aitken-mode particles, which coagulate further to form accumulation-mode particles (Seinfeld and Pandis, 2006). Unless otherwise stated, the work in this thesis refers to accumulation-mode fine particles.

Aerosols can also be classified by their chemical composition and source. Primary organic aerosols (POA) are emitted directly as aerosols, while secondary organic aerosols (SOA) are formed when gas-phase molecules partition to the aerosol in some manner. Aerosols typically contain inorganic species including salts, such as sodium chloride (NaCl) from sea salt, or ammonium nitrate or ammonium sulfate (NH_4NO_3 and $(NH_4)_2SO_4$, respectively) from anthropogenic emissions. Aerosols in the northern hemisphere almost always also contain organic carbon in addition to inorganic species and are thus considered organic aerosol (Zhang et al., 2007). Particles that contain only elemental carbon or soot are called elemental carbon (EC) or black carbon (BC) aerosols. SOA is sometimes further classified by its source. Aerosols produced from forest fires and other biomass burning are called biomass-burning organic aerosols (BB-OA). Aerosols produced from cooking, especially of meat, are called cooking-influenced organic aerosols (CI-OA). Aerosols formed from aqueous-phase reactions are called aqueous organic aerosol (aq-OA).

The third method of classifying aerosols is based on their generation. Aerosols that are emitted directly as aerosols are called primary aerosols. Sea spray is a form of primary aerosol as are particles emitted directly from car tailpipes. Organic aerosols that are emitted as particles are primary organic aerosols (POA). These can be formed from combustion (of fossil fuels and biomass burning), meat cooking, and even leaf wax (Seinfeld and Pandis, 2006). Aerosols that gain mass after emission are called secondary aerosols, especially secondary organic aerosols (SOA). These are considered secondary because much of the aerosol mass was emitted as gases rather than as particulate matter. Formation of SOA is discussed further in Sections 1.2.2 and 1.2.2.2.

1.1 Aerosol Climate Impacts

Aerosols change the amount and spectral content of light that reaches the Earth. Aerosols can impact the climate in several ways: by scattering or absorbing incoming light (aerosol direct effect), or by changing cloud formation and indirectly modifying the incoming light through clouds (aerosol indirect effect) (Stocker et al., 2013). The amount of scattering, absorption, and cloud interactions depends strongly on the chemical composition of the aerosol.

Scattering and absorption are quantified by the complex refractive index of the aerosol, $m = n + ki$, where m is the complex refractive index, n is the scattering component, and k is the absorption component. n and k are both greater than or equal to zero. n is typically between 0 and 1.5, with greater values indicating greater scattering. k is typically between 0 and 0.5, with larger values indicating higher absorption (Zarzana et al., 2012; Moise et al., 2015).

1.1.1 Aerosol Direct Effects

Aerosols can directly change the climate by scattering or absorbing incoming light. On one end of the spectrum, white inorganic aerosols (e.g. NaCl or ammonium sulfate) only scatter light. The refractive index of ammonium sulfate has been measured to be $1.535 + 0i$ at 589 nm (Garland et al., 2007). This means that it only scatters light (it has a non-zero real (scattering) index of refraction and no imaginary (absorbing) index of refraction). Scattering light decreases the amount of solar radiation that reaches the Earth, which results in a net cooling. This has been observed in ambient measurements: for example, during the 1991 eruption of Mt. Pinatubo, H_2SO_4/H_2O aerosol was formed from the volcanic SO_2 emissions. This increase in the scattering from aerosols decreased the Earth's albedo by 4.3 W/m^2 between 40° N and 40° S (McCormick et al., 1995) and contributed to a net cooling of the Earth.

On the other extreme, black carbon aerosol, which has an index of refraction of $1.95 + 0.79i$, absorbs light very strongly at all visible wavelengths. The absorption of light heats the atmosphere around the black carbon and also reduces the amount of light that is scattered back to the atmosphere. Since the sources of black carbon are anthropogenic, and thus BC aerosols are most prevalent at the surface of the Earth, it results in a net heating. BC aerosol is estimated to be the second most important climate warming agent after CO_2 with an estimated effect of 1.1 W/m^2 (Bond et al., 2013).

While white inorganic aerosol and black soot aerosol are two extremes, much aerosol, especially in urban areas where aerosols have undergone significant chemical processing, is brown carbon (BrC) aerosol. Formation of BrC is discussed further in Section 1.2.2.3. BrC is defined as

aerosol whose absorption increases from the visible to UV wavelengths (Laskin et al., 2015). The radiative effects of organic carbon are not yet well understood, but are likely highly dependent on BrC chemical composition. For example, brown carbon formed from aqueous phase processing has been reported to have an index of refraction of (1.55-1.65) + (0.035-0.114)i, making it weakly to moderately absorbing (Zarzana et al., 2012; Moise et al., 2015). Humic-like substances (HULIS, large molecular weight polyfunctional molecules) are typically more weakly absorbing with reported refractive indices of (1.561-1.685) + (0.0016 - 0.049)i (Hoffer et al., 2006; Dinar et al., 2008). This huge range in absorption of BrC measurements results in a large uncertainty for the radiative forcing due to brown carbon. In Chapter 6 we discuss one possible brown carbon formation pathway.

1.1.2 Aerosol Indirect Effects

Aerosols also modify incoming solar radiation by acting as cloud condensation nuclei (CCN) or ice nucli (IN) and inducing liquid-water cloud or ice cloud formation. Clouds, in turn, have a complicated effect on the Earth's radiative balance. At short wavelengths (UV, visible, and near-IR), they result in a decrease in radiative forcing by scattering light back to the atmosphere. However, at long wavelengths (mid-IR and beyond) they result in a net increase through the greenhouse effect where heat emitted from the Earth is trapped between the Earth and the cloud (Stocker et al., 2013). The net effect is an interplay between these processes and depends on a number of factors including cloud altitude and thickness.

Aerosols act as CCN by absorbing water and inducing cloud droplet formation in an air mass that is supersaturated. Efficient CCN are activated at low supersaturation values while less effient CCN require higher supersaturation to absorb water. How efficiently an aerosol acts as a CCN depends on its chemical composition. The CCN behavior of pure inorganic aerosols is fairly well understood, but the CCN behavior of mixed organic/inorganic particles is more complex. In order to attempt to quantify the the aerosol CCN efficiency, the hygroscopicity parameter κ was developed from κ-Köhler theory (Petters and Kreidenweis, 2007). More hygroscopic species have higher κ values (Petters and Kreidenweis, 2007). This parameter can be measured experimentally

by fitting CCN activity or hygrosopic growth factor data. Inorganic species tend to have large κ values close to one indicating strong CCN behavior, while organic species are quite varied. For example, chamber aerosol formed from biogenic precursors (α-pinene, β-caryophyllene, limonene, linalool, and myrcene) have quite a range of hygroscopicity, ranging from 0 to 0.15 (Alfarra et al., 2013) and the hygroscopic growth depends significantly on amount of time exposed to oxidants and initial precursor concentration. Thus CCN behavior is quite composition-dependent and difficult to predict and a better understanding of aerosol chemical composition is necessary.

1.1.3 Aerosol Health Effects

There are a number of studies that show a strong correlation between $PM_{2.5}$ (aerosols 2.5 μm in diameter and smaller) concentration and increased mortality (Dockery et al., 1993; Pope et al., 1995, 2002, 2004; Jerrett et al., 2005; Pope and Dockery, 2006; Laden et al., 2006). The original study on the health effects of aerosols was the Harvard Six Cities Study (Dockery et al., 1993), where a correlation was found between mortality and PM_{10}, $PM_{2.5}$, and sulfate, but the strongest correlation was found with $PM_{2.5}$. In this study, short-term increases in $PM_{2.5}$ over the background resulting in a 1% increase in mortality were detected, as were correlations with longer-term increases in $PM_{2.5}$.

The mechanisms of mortality based on PM inhalation are complex. When aerosols reach the lungs, they can cause inflammation and reduced lung function and can worsen chronic diseases such as COPD. The particles can then move into the bloodstream, where they can change the viscosity, reduce the oxygen saturation level, and cause blood clots. The changes in blood chemistry and decrease in lung function can induce inflammation responses in the body, including changes in heart function, atherosclerosis, and vasoconstriction. Ultimately, this can result in restriction of blood flow to the heart and brain (Pope and Dockery, 2006).

1.2 Aerosol Formation

Accumulation-mode aerosols are formed by a variety of processes which depend on the aerosol composition and environmental factors. All of the formation processes include uptake and/or further reactions of gas-phase or aqueous-phase molecules.

1.2.1 Non-Organic Aerosol Formation

Inorganic aerosols are formed from the gas-phase processing of anthropogenic species NO_2 and SO_2 to form nitric or sulfuric acid followed by reaction with gas-phase NH_3 to form NH_4NO_3 or $(NH_4)_2SO_4$. NO_2 is primarily produced from fossil fuel combustion, with smaller contributions from biomass burning, direct soil emissions, and lightning (Seinfeld and Pandis, 2006). NO_2 is then oxidized by $OH^{\cdot}$ to form nitric acid:

(R1.1) $OH^{\cdot} + NO_2 + M \rightarrow HNO_3 + M$

SO_2 is also primarily produced from fossil fuel combustion (e.g. coal-fired power plants), with small contributions from volcanoes and biomass burning (Seinfeld and Pandis, 2006). SO_2 also reacts with $OH^{\cdot}$ to form sulfuric acid via the following reactions:

(R1.2) $SO_2 + OH^{\cdot} + M \rightarrow HOSO_2^{\cdot} + M$

(R1.3) $HOSO_2^{\cdot} + O_2 \rightarrow HO_2^{\cdot} + SO_3$

(R1.4) $SO_3 + H_2O + M \rightarrow H_2SO_4 + M$

The next step in aerosol formation is reaction with NH_3, which is emitted from sources that include agriculture (e.g. fertilizers and livestock), soils, and biomass burning. Reactions with ammonia neutralizes the acids to form ammonium salts. These salts have low vapor pressures and thus condense to form aerosols. These salts can strongly influence the uptake of aerosol precursors, which is discussed in Chapters 4 and 5.

1.2.2 Secondary Organic Aerosol Formation

Secondary organic aerosols are formed via a number of different mechanisms.

1.2.2.1 Vapor Pressure Partitioning

Volatile organic compounds (VOCs) that have sufficiently low vapor pressures can condense directly on to pre-existing aerosols. There is an equilibrium between the particle phase and the gas phase for these molecules, so the vapor pressure necessary for condensation depends on the aerosol concentration. At higher aerosol concentrations (e.g. in polluted urban areas), molecules with higher vapor pressures (more volatile compounds) can condense to the aerosols. At lower aerosol concentrations (e.g. clean marine background air), molecules with lower vapor pressures (less volatile compounds) will partition to aerosols. This is a dynamic process, so VOCs that have partitioned to the aerosol can evaporate out of the aerosol if e.g. the aerosol is transported to a more clean region with a lower aerosol concentration. The fraction of a particular gas that is found in the aerosol phase can be calculated by:

$$\xi_i = (1 + C_i^*/C_{OA})^{-1} \tag{1.1}$$

where ξ_i is the fraction found in the condensed phase, C_i^* is the saturation mass concentration, the organic mass concentration at which 50% of the species mass will be found in the condensed phase, and C_{OA} is the atmospheric aerosol mass loading (Donahue et al.).

Additionally, VOCs that are too volatile to partition to aerosols can undergo gas-phase oxidation by OH, O_3, or NO_3. Particularly for early-generation oxidation, this results in functionalization where functional groups such as alcohol, carbonyl, carboxylic acid, or nitrate moities. These decrease the vapor pressure of the VOC and allow them to partition further to the particle phase. There is a competition between functionalization and fragmentation, as these reactions lead to radical formation and this can lead to bond breaking. However, in the first several generations of oxidation, functionalization is favored over fragmentation and the net result is additional SOA formation.

1.2.2.2 Organic Aerosol Formation by Aqueous Phase Processing

A third mechanism for SOA formation is aqueous phase processing. Small molecules that are highly water-soluble and too volatile to form SOA through vapor pressure partitioning can partition to the water in an aerosol e.g. (Hastings et al., 2005; Kroll et al., 2005; De Haan et al., 2009b; Shapiro et al., 2009; Ervens and Volkamer, 2010; Lim et al., 2010; Yasmeen et al., 2010; De Haan et al., 2010; Ervens et al., 2011; Zarzana et al., 2012; Lee et al., 2012; Liu et al., 2012; Ortiz-Montalvo et al., 2012; Waxman et al., 2013; Kampf et al., 2013; Aregahegn et al., 2013; Carlton and Turpin, 2013; Epstein et al., 2013; Hamilton et al., 2013; He et al., 2013; Lee et al., 2013; Lim et al., 13; Nguyen et al., 2013; Zhao et al., 2013; Yli-Juuti et al., 2013; Renard et al., 2013; Powelson et al., 2013; Cerully et al., 2014; Galloway et al., 2014; Hawkins et al., 2014; Ortiz-Montalvo et al., 2014; Yu et al., 2014; Xu et al., 2014; Schöne et al., 2014; Romonosky et al., 2014; Renard et al., 2015). This processing is applicable to molecules like formaldehyde, glyoxal, methyl glyoxal, acetaldehyde, and hydroxyacetone.

These species' partitioning between the gas phase and the aqueous phase governed by Henry's law (K_H) which is an equilibrium constant that describes the ratio between the aqueous and gas phase (typically reported in M/atm) (e.g. (Ip et al., 2009; Sander, 2015), (R5)). Molecules containing aldehyde groups can have an effective Henry's law constant ($K_{H,eff}$) because they can hydrate (R6). The effective Henry's law constant is the ratio of the gas-phase species to the sum of the aqueous phase species, hydrated and unhydrated. This results in Henry's law values up to several orders of magnitude larger than Henry's law values for the unhydrated species:

(R1.5) $A_{(g)} \rightleftharpoons A_{(aq)}$, $K_H = \frac{A_{(aq)}}{A_{(g)}}$ in M/atm

(R1.6) 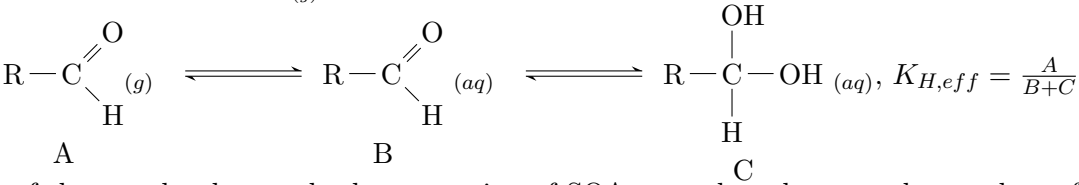

$K_{H,eff} = \frac{A}{B+C}$

Uptake of these molecules can lead to accretion of SOA mass, but they can then undergo further reactions. These molecules can undergo oligomerization reactions to form dimers, and in the case of glyoxal, trimers and even higher order oligomers (Whipple, 1970; Hastings et al., 2005; Loeffler

et al., 2006; Noziere et al., 2009; De Haan et al., 2009b; Avzianova and Brooks, 2013):

(R1.7) 2 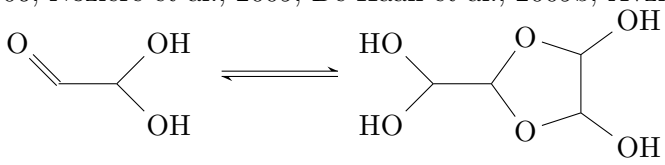

(R1.8) 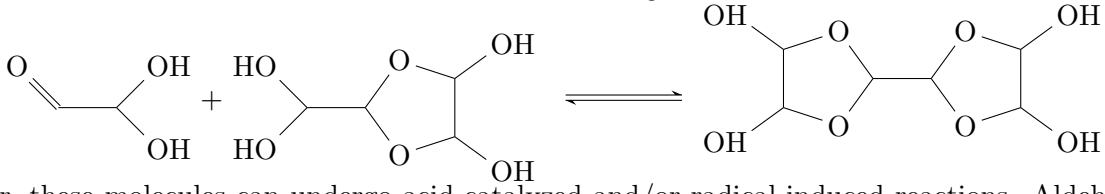

Further, these molecules can undergo acid-catalyzed and/or radical-induced reactions. Aldehydes can react with ammonium, amines, and amino acids for form aromatic nitrogen-containing compounds (Liggio et al., 2005a; Noziere et al., 2009; Galloway et al., 2009; Kua et al., 2011; De Haan et al., 2010; Ortiz-Montalvo et al., 2012; Kampf et al., 2012b; Hamilton et al., 2013; Lee et al., 2013; Powelson et al., 2013; Hawkins et al., 2014; Galloway et al., 2014). All species can react with aqueous-phase OH or other radicals to form further oxidized compounds such as organic acids, or organosulfates. All further reactions lower the vapor pressure of the molecule in comparison with the original species, resulting in favored partitioning towards the aqueous phase. This results in net mass accretion and SOA formation.

1.2.2.3 Brown Carbon Formation

Brown carbon is organic carbon that absorbs visible light (and thus appears brown). Molecules that are expected to contribute to brown carbon formation are often conjugated and contain nitrogen. Brown carbon can form in a number of ways. It has been shown to form between small aldehydes (glyoxal or methyl glyoxal) and ammonium, amines, and amino acids. Combining these species and evaporating the water results in significant brown carbon formation likely due to the formation of nitrogen-containing rings (Noziere et al., 2009; De Haan et al., 2010; Kampf et al., 2012b; Laskin et al., 2014; Lin et al., 2014).

1.2.3 Changes in Aerosols Since Pre-Industrial Times

Aerosols have changed significantly since pre-industrial times. The concentrations of anthropogenic inorganic species (SO_2, NO_2, and NH_3) which are processed in to the common inorganic ions (sulfate, SO_4^{2-}; nitrate, NO_3^-; ammonium, NH_4^+) have increased substantially since pre-industrial times. This increase is well-documented in ice-core data where the inorganic ions are deposited on the ice through aerosol deposition (Schwikowski et al., 1999; Bigler et al., 2002). In fact, the only distinct increase in SO_4^{2-} in a Greenland ice core is observable since the industrial era started (Bigler et al., 2002). Primarily natural emissions such as Na^+ and Cl^- from sea salt have not significantly increased over the time periods when anthropogenic species have increased as based on an ice core from the Alps (Schwikowski et al., 1999). This increase in anthropogenic inorganic aerosols means that salting for small, water-soluble molecules that can partition to the aerosol aqueous phase is significantly more important than it was prior to the industrial age.

Additionally, POA emissions are estimated to be about a factor of three lower in pre-industrial times and anthropogenic VOCs that are SOA precursors are expected to be a factor of twenty lower. Pre-industrial POA emissions result from biomass burning. This results in an overall modeled decrease of 59% in the total organic aerosol burden in pre-industrial times (Hoyle et al., 2009). Biogenic VOC emissions have likely decreased since 1850 due to land cover change. However, SOA formation from biogenic VOCs is complicated because the quantity of aerosol precursor formed is dependent on the NO_x concentration, which has increased substatntially. The total amount of aerosol formed is also dependent on the total amount of aerosol available for partitioning, which has also increased (Unger, 2014). Thus not only was the total aerosol burden very different in pre-industrial times, the chemical composition would also have been quite different as it would have been primarily natural inorganic aerosol and biomass burning aerosol.

The changes in aerosols since preindustrial times significantly impacts the inorganic component. This is important because the inorganic component can change partitioning to the aqueous phase of the aerosol through salting (Setschenow, 1889). In some cases, higher concentrations of

salts increase the solubility of organic molecules (salting in) and in other cases it decreases the solubility of the the organic molecules (salting out). This results in further changes in the organic composition of the aerosol (see Knote et al. (2014), especially Figure 15.)

1.3 Modeling Aerosol Formation

Models that predict aerosol formation are typically one of two forms: semi-explicit, or volatility basis set (VBS). Because the molecules that form aerosol are so varied (and some are likely not yet known), it is computationally very expensive to model aerosol formation from every single molecule that is a precursor. Models that do some grouping to save computational expense (e.g. treating all C_5H_{12} compounds as *n*-pentane) but predict gas-phase chemistry and the change in partitioning for the product molecules are considered semi-explicit. Models that group all species with similar vapor pressures together in to bins and then treat the entire bin as one species whose volatility can change based on OH concentration and total reaction time are considered VBS models.

VBS models were developed to deal with the discovery that some gases are semi-volatile, that is, they can partition between the gas and particle phases based on the aerosol mass loading (Donahue et al., 2006; Robinson et al., 2007). A basis set using C^* bins of e.g. 0.01, 0.1, 1, 10, 100, 1000, 10 000, 100 000 $\mu g/m^3$ and the mass of atmospheric compounds with a given C^* value is added to each bin. Changes in the mass of each bin are based on additional emissions (which will increase the overall C_{OA}), mixing air masses and dilution, which will change the distribution based on changes in total C_{OA}, temperature changes (which can change the C_i^* values for a given molecule), and chemical reactions which moves mass between bins. If the mass becomes less volatile (e.g. due to functionalization), this results in a net increase in C_{OA}. If the overall mass becomes more volatile (e.g. due to fragmentation), this results in a net decrease of C_{OA}. A number of volatility distributions and bin changes due to reactions have been proposed, based on different emissions scenarios, e.g. Robinson et al. (2007); Grieshop et al. (2009).

Semi-explict models have also been developed to predict aerosol formation. One semi-explicit model is the Generator of Explict Chemistry and Kinetics of Organics in the Atmosphere (GECKO-

A) (Aumont et al., 2005; Lee-Taylor et al., 2011; Aumont et al., 2012). This model takes emitted species and prescribes reactions with $OH^{\cdot}$, O_3, and NO_3 based on functional group as well as photolysis and thermal decomposition. Peroxy alkyl ($ROO^{\cdot}$), peroxy acyl ($RC(O)OO^{\cdot}$) and alkoxy ($RO^{\cdot}$) chemistry is considered as well. The vapor pressure of each precursor and product molecule is prescribed and aerosol formation can be calculated. This treats species individually, unlike VBS systems, and theoretically should be a more accurate representation of how aerosols are formed.

1.3.1 Aerosol Mass in Models

One important criterion on whether the models are correctly predicting aerosol formation is whether they are able to obtain mass closure. Each model has been compared against laboratory or field studies. The volatility basis set from Robinson et al. (2007) was designed to match their chamber studies of OA formation from diesel fuel oxidation. The VBS from Grieshop et al. (2009) was designed to match their chamber experiments from wood stove combustion. However, when aerosol predictions from the VBS models were compared against ambient organic aerosol measurements from the MILAGRO campaign in Mexico City in 2006, the aerosol mass predictions for the Grieshop VBS were found to significantly over-estimate the actual mass (Dzepina et al., 2011). GECKO-A was able to reasonably reproduce the diurnal cycle of the aerosol mass during the same campaign (Lee-Taylor et al., 2011). Thus these models are sometimes but not always able to always correctly predict aerosol mass.

1.3.2 Aerosol Chemical Properties

Aerosol chemical properties are a second metric to evaluate how accurately models are predicting aerosol formation. If the models are getting aerosol chemical composition incorrect, then it means they are not predicting formation from the correct pathways. Aerosol atomic O/C ratio is one metric for evaluating aerosol chemical composition. This is one way of quantifying how oxidized an aerosol is: a higher O/C ratio means that there are more oxidized compounds in the aerosol. This has also been compared with the MILAGRO campaign for the three models described above.

In contrast to the mass, the Grieshop VBS gets the O/C close to correct, whereas the Robinson model (which got the mass correct) predicts the O/C to be too low by a factor of 2 (Dzepina et al., 2011). The GECKO-A model is able to reproduce the O/C and H/C ratios for the first two days of the model simulation. After that, the H/C ratio remains accurate, but the O/C ratio increases too slowly (Lee-Taylor et al., 2011). Thus models can sometimes reproduce the aerosol chemical properties, but not always which means that if they are getting the aerosol mass correct, it is not necessarily for the right reason.

1.4 Glyoxal

Glyoxal is the smallest α-dicarbonyl. It is an important SOA precursor and forms aerosol through aqueous-phase processing. It has a very high O/C ratio (1 in the unhydrated molecule, 2 in the hydrate) which could make it an important species for closing the aerosol chemical composition gap. Additionally, it can undergo aqueous-phase reactions with ammonium and amines to form brown carbon products. This means its contributions to SOA can help correct both the O/C gap and be important for organic aerosol absorption. Additionally, it can form brown carbon by reacting with ammonia and other nitrogen-containing species. Thus it is a potentially important contributor to aerosols because it can help solve some of the issues with aerosol modeling as well as contributing to our understanding of organic aerosol absorption.

1.4.1 Sources of Glyoxal

Glyoxal is formed from oxidation of several anthropogenic precursors. Glyoxal has a 65% yield from acetylene (Hatakeyama et al., 1986) as well as a 35% yield from benzene and 38% yields from toluene and *p*-xylene (Volkamer et al., 2001).

Glyoxal is also formed from biogenic species, most notably isoprene. In fact, 47% of the 45 Tg/year of glyoxal are predicted to be formed from isoprene (Fu et al., 2008). The exact yield from isoprene as well as the mechanism is a matter of ongoing research. Dibble (2004) propose that glyoxal is formed from secondary isoprene alkoxy radicals, but do not give a yield. However, Paulot

et al. (2009) find an overall yield of glyoxal of 6.2%, with a 2.9% first-generation yield and a 3.3% second generation yield under high-NO_x conditions. A second high-NO_x study found a 3% primary yield of glyoxal from isoprene and a 4-5% secondary yield (Volkamer et al., 2006a). Regardless of the mechanism that produces glyoxal from isoprene, this is a significant contributor to glyoxal production because isoprene is emitted in such high yields. Glyoxal is also formed from β-pinene in a 4-5% yield (Volkamer et al., 2006a) and additional monoterpenes as well as biomass burning (Fu et al., 2008).

Glyoxal was recently detected in the marine boundary layer over the remote tropical Pacific Ocean (Sinreich et al., 2010; Coburn et al., 2014). Because glyoxal has a lifetime of only a few hours, this means that the glyoxal must be produced in the vicinity of the measurements rather than being transported from land. A mechanism for the formation of glyoxal from poly unsaturated fatty acids was recently proposed (Zhou et al., 2014). These are species present in the sea surface microlayer and are reactive with both ozone and OH and are a potential source for glyoxal.

Other small aldehydes have been detected when ocean water was irradiated with UV light and the same species were detected when humic acid was added to sea water samples (Kieber et al., 1990). Humic acids are large, high molecular weight polyfunctional species that form through the photodegradation of organic macromolecules. The chromophores in these molecules could potentially act as photosensitizers, initiating the formation of radicals that can lead to VOC production. This has been observed with other chromophores, especially imidazoles, though not in the context of glyoxal production (Aregahegn et al., 2013; Rossignol et al., 2014). Additionally, small amounts of isoprene and α-pinene are emitted from the ocean (Luo and Yu, 2010), so some glyoxal is likely produced from these species but not enough to explain the amount observed (Sinreich et al., 2010).

1.4.2 Aqueous-phase processing of glyoxal and SOA formation

Glyoxal is a very soluble molecule, so it can partition to the aerosol aqueous phase. Because it is a dialdehyde, it can hydrate forming both a monohydrate and a dihydrate and thus it has an

effective Henry's law constant which is defined as:

$$K_{H,eff} = \frac{C_{gly} + C_{mono} + C_{di}}{P_{gly}} \tag{1.2}$$

where $K_{H,eff}$ is the effective Henry's law constant (M/atm), C_{gly} is the aqueous phase concentration of unhydrated glyoxal (M), C_{mono} is the aqueous phase concentration of the monohydrate (M), C_{di} is the aqueous phase concentration of the dihydrate, and P_{gly} is the gas-phase pressure of glyoxal (atm) (Ervens and Volkamer, 2010). The aqueous-phase species are shown below:

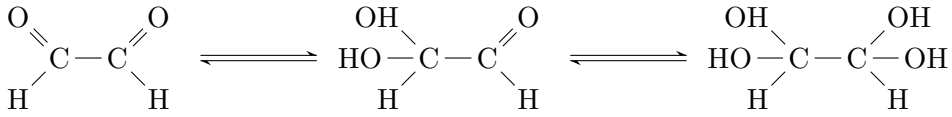

Glyoxal Glyoxal monohydrate Glyoxal dihydrate

Glyoxal can also oligomerize, as described in Section 1.2.2.2 (Ervens and Volkamer, 2010; Avzianova and Brooks, 2013). Glyoxal can also be oxidized by OH radicals to form glyoxylic acid and then to oxalic acid (Ervens et al., 2003). This can change the pH due to acid formation, which can further affect chemistry.

Glyoxal is also able to react with ammonia, amines, and amino acids to form nitrogen-containing species. This can lead to brown carbon formation as discussed in Section 1.2.2.3. Rate constants for these reactions have been published for ammonia (Noziere et al., 2009), and glycine, serine, and arginine (De Haan et al., 2009a). It is also possible that glyoxal can react with SO_4^{2-} to form organosulfates (Liggio et al., 2005a; Galloway et al., 2009).

1.5 Outlook

In this work, we focus on secondary organic aerosol formation from small, water-soluble molecules, especially glyoxal and methyl glyoxal. We model SOA formation from glyoxal and compare this with SOA formed from two VBS systems and a semi-explicit model to determine if with the addition of glyoxal we can more accurately reproduce the chemical properties of the aerosol, specifically the atomic O/C ratio. We further measure salting constants for glyoxal and

methyl glyoxal in aerosol relevant salts. We apply this to a regional model (CMAQ) to study the effect of salting on aerosol formation. We also compare the measured salting constants against two salting theories in the literature and quantum calculations to understand salting behavior. We apply our increased understanding of salting constants to isoprene epoxide to predict its salting constant in ammonium sulfate. Finally we performed a series of chamber experiments that focus on the chemical composition of SOA formed from glyoxal. We find that the addition of gas-phase NH_3 greatly increases the formation of molecules that contribute to aerosol absorption.

Chapter 2

SOA Formation From Glyoxal and S/I-VOCs in Mexico City During MCMA-2003

This chapter was published as: Waxman, E. M., Dzepina, K., Ervens, B., Lee-Taylor, J., Aumont, B., Jimenez, J.-L., Madronich, S., and Volkamer, R., Secondary organic aerosol formation from semi- and intermediate-volatility organic compounds and glyoxal: Relevance of O/C as a tracer for aqueous multiphase chemistry, Geophys. Res. Lett., 40, 978-982, doi:10.1002/GRL.50203, 2013.

The role of aqueous multiphase chemistry in the formation of secondary organic aerosol (SOA) remains difficult to quantify. We investigate it here by testing the rapid formation of moderate oxygen-to-carbon (O/C) SOA during a case study in Mexico City. A novel laboratory-based glyoxal-SOA (GLY-SOA) mechanism is applied to the field data and explains why less gas-phase glyoxal mass is observed than predicted. Further, we compare an explicit gas-phase chemical mechanism for SOA formation from semi- and intermediate-volatility organic compounds (S/IVOCs) with empirical parameterizations of S/IVOC aging. The mechanism representing our current understanding of chemical kinetics of S/IVOC oxidation combined with traditional SOA sources and mixing of background SOA underestimates the observed O/C by a factor of two at noon. Inclusion of GLY-SOA with O/C of 1.5 brings O/C predictions within measurement uncertainty, suggesting that field observations can be reconciled on reasonable time scales using laboratory-based empirical relationships for aqueous chemistry.

2.1 Introduction

Initially, models predicted Secondary Organic Aerosol (SOA) formation from the gas-phase oxidation of specific precursor volatile organic compounds (VOCs) whose product saturation vapor pressures are low enough to partition to the aerosol phase (Seinfeld and Pankow, 2003). This framework for SOA formation has been expanded to include semivolatile and intermediate volatility organic compounds (S/IVOCs) (Robinson et al., 2007; Grieshop et al., 2009). Inclusion of S/IVOCs significantly improved predictions of SOA mass in polluted areas (Dzepina et al., 2009; Hodzic et al., 2010; Dzepina et al., 2011; Lee-Taylor et al., 2011), but reveals shortcomings in predicting chemical properties such as the atomic oxygen to carbon ratio (O/C ratio) on short aging time scales (Dzepina et al., 2009).

During the Mexico City Metropolitan Area (MCMA-2003) case study on 9 April 2003, rapid SOA formation produced significantly more aerosol mass than expected (Volkamer et al., 2006b), which was mostly attributed to the rapid aging of S/IVOCs (Dzepina et al., 2009). Simultaneously, less gas-phase glyoxal was observed than predicted by a gas-phase mechanism that did not consider particle-phase partitioning or processing (Volkamer et al., 2007). It was hypothesized that this imbalance could be due to SOA formation from glyoxal since it is highly soluble and quite reactive in the aqueous phase. Glyoxal is likely to add to SOA through multiphase reactions where it can contribute a small amount of mass with a very high O/C ratio due to its ability to form low-volatility, high molecular weight products in the aerosol aqueous phase [e.g. (Volkamer et al., 2009; Hennigan et al., 2009; Lim et al., 2010; Ervens et al., 2011)].

O/C ratios are primarily used as a metric for relating organic aerosol (OA) chemical composition to aerosol age, hygroscopicity, and volatility (Ng et al., 2007; Jimenez et al., 2009). However, they can also provide a means to test our process level understanding of SOA formation mechanisms. During this case study the observed O/C from oxygenated organic aerosol (OOA) was significantly higher than predicted by models incorporating S/IVOCs but not aqueous-phase processing (Dzepina et al., 2009). This imbalance is currently not understood, and no previous

attempts have been made to understand O/C based on a molecular modeling perspective of SOA. Here we compare the O/C time evolution as measured by Aerosol Mass Spectrometry (AMS) to results from a molecular modeling perspective to test our mechanistic understanding of SOA formation, including - for the first time - treatment of both S/I VOC gas-phase and aerosol multiphase chemical reactions.

2.2 Description of model approaches

2.2.1 Chemical mechanism of glyoxal reactions in aerosol water

To predict the amount of SOA formed from glyoxal (GLY-SOA), we apply an observationally-constrained box model that simulates processing of glyoxal in aerosol water based on a laboratory-derived glyoxal-SOA mechanism (Ervens and Volkamer, 2010). We constrain the model with ambient measurements from 9 April 2003 in Mexico City to determine if glyoxal uptake and aqueous-phase processing can explain the glyoxal imbalance from MCMA-2003.

SOA formation is represented in the model as a surface-limited uptake process, bulk-phase reactions, or a combination of the two (see Figure 1 of Ervens and Volkamer (2010)). Briefly, the mechanism includes partitioning of glyoxal into aerosol water based on its Henry's law constant and explicit hydration reactions to form the monohydrate and dihydrate using the kinetic and equilibrium constants derived by Ervens and Volkamer (2010). This results in a very high effective Henry's law value of 4.2×10^5 M/atm (Ip et al., 2009). These species then become part of an organic aqueous phase where they undergo further processing, including oligomerization and reactions with OH and ammonium. Sensitivity studies were carried out that varied the mass accommodation coefficient α (physical uptake parameter), reactive uptake coefficient γ (includes aqueous phase reactivity), OH-radical concentration, Henry's law constant for unhydrated glyoxal (H), and SOA hygroscopicity κ. The model parameters, ambient observations used as model constraints, and predicted GLY-SOA mass from individual simulations are shown in Table 2.1.

Table 2.1: Comparison of predicted GLY-SOA masses from box model simulations using the mechanism by Ervens and Volkamer (2010). All masses are given in ng/m^3. Product distribution values are given in %. Surface: assuming a surface-limited process that occurs in addition to the other reactions. The surface-limited process products are not well-constrained, but likely include oligomers not formed directly from glyoxal, such as radical-catalyzed oligomerization. Bulk: assuming GLY-SOA formation in the bulk of the aerosol phase. Accom: Used γ before 10 am ($\gamma = 0$ after 10 am), and decreasing mass accommodation coefficient, α, after 10 am ($\alpha = 0.01$ before 10 am). The product distribution is shown for the time-dependent mass accommodation simulation.

Model						7 am	11 am	2 pm	Run
Observed Glyoxal Imbalance (μg/m^3)						547	1918	2915	
Type	Size Dist.	κ	γ	α	H (M/atm)				
Surface	4 bins	0.17	γ = 0.0033	1	5	280	1218	3359	1
Accom.	4 bins	0.17	γ = 0.005	var.	750	427	1127	2548	2
Bulk	4 bins	0.17	----	1	5	0.05	2	27	3
Bulk	4 bins	0.17	----	1	750	7	210	2903	4
Bulk	Aitken	0.17	----	1	5992	73	2164	25,472	5
Bulk	Coarse	0.17	----	1	5992	53	1177	20,319	6
Surface	4 bins	0	γ = 0.016	1	5	1251	5536	15,209	7
Surface	4 bins	0.17	γ = 0.008	1	5	672	2922	8031	8
Surface	Aitken	0.17	γ = 0.008	1	5	3991	18,320	67,970	9
Surface	Coarse	0.17	γ = 0.008	1	5	39	172	643	10
Product Distribution (%)						7 am	11 am	2 pm	4
$Gly_{(aq)}$						1e-6	3e-5	5e-5	
$CHOCH(OH)_2$						1.5e-3	3e-3	7e-3	
$(CH(OH)_2)_2$						0.3	0.6	1.5	
Glyoxal oligomers						4e-5	2e-4	1e-3	
Gly + NH_4^+						1	8	93	
Gly + OH						4e-3	2	5	
Unaccounted mass (grey circles – orange line in Fig. 2.1)						99	89	0.004	

2.2.1.1 Model Inputs

The mechanism for the box model is based on the one in Ervens and Volkamer (2010). The input data to the box model containing this mechanism are from the date of the case study, 9 April 2003, which was selected because it is a well-characterized day with minimal mixing (de Foy et al., 2005; Johnson et al., 2006; Volkamer et al., 2006b). Immediately preceding this case study, recent rain has removed coarse mode particles and low wind speeds and high soil moisture during the case study prevent their emission. The absence of dust and biomass burning influences during the April 9 case study is demonstrated by the absence of K and very low concentrations of Si, Ca, and Mg in the PIXE data reported by Johnson et al. (2006).

The model uses ambient temperature (K), pressure (millibar) and relative humidity (%). Gas-phase glyoxal data were taken from Differential Optical Absorption Spectroscopy measurements (Volkamer et al., 2005a) and gas-phase OH data from Laser Induced Fluorescence measurements (Shirley et al., 2006) which were increased by thirty percent to compensate for a previously unrecognized calibration error in the original data (Dzepina et al., 2009; Sheehy et al., 2010). Size-resolved aerosol chemical composition data (ammonium, nitrate, sulfate, chloride, and total organics) were taken from AMS data (and additional size data outside of the AMS measurement range from LASIR Optical Particle Counter data), with only a small fraction (<10%) of the mass in particles larger than 1000 nm (Salcedo et al., 2006). Inorganic mass distribution is shown as a function of time in Figure 2.1a and the particle size distribution at 2 pm is shown in Figure 2.1b. Overall, the inorganic mass is dominated by nitrate. For further information on aerosol chemical composition, see Salcedo et al. (2006). Aerosol size data was combined from 273 measurement mode size bins to 4 model mode size bins (an Aitken mode, two accumulation modes, and a coarse mode) to save computational power while keeping total mass constant and surface area constant to within 13%. The box model assumes equilibrium particle sizes and ideal conditions and uses chemical composition to calculate aerosol liquid water content (ALWC) based on the thermodynamic equilibrium model ISORROPIA (Fountoukis and Nenes, 2007). The model accounts for air

mass dilution due to vertical mixing from the rising boundary layer over the course of the day (see Figure 1 of Volkamer et al. (2006b)).

Using the AMS and ALWC data, the model calculates the mass fractions of each GLY-SOA species in the aerosol. The OOA fraction of the aerosol is set to hygroscopic or non-hygroscopic by assuming κ values of approximately 0.17 and 0, respectively. These same κ values were used in Ervens and Volkamer (2010) and used to derive the two sets of γ values. The HOA fraction is treated as non-hygroscopic.

2.2.1.2 Model simulations

All data and results are given in CDT (Central Daylight Time, GMT-5). The SOA mass from each of the explicit reactions described in Ervens and Volkamer (2010) is updated in the box model every second for the entire 24 hours; reactions of amines and amino acids with glyoxal are not considered due to lack of field data. Concentrations of all products were scaled to account for dilution due to rising boundary layer height during the course of the day (Volkamer et al., 2006b).

Additional sensitivity studies were performed to examine the effect of size distribution on the GLY-SOA mass. The total mass was kept constant, but was either divided over the four bins to reflect the actual mass distribution, or was placed entirely in the smallest or largest mode. Little size dependence was observed for the bulk case, but the surface process parameterization showed a high sensitivity to size distribution due to changes in the surface to volume ratio, where simulations using only the Aitken mode formed significantly more aerosol mass than simulations using only the coarse mode. The initial conditions and model output are compared for different model runs in Table 2.1.

While good agreement using a surface process suggests that glyoxal is lost by reactions at aerosol surfaces, we do not rule out the possibility that GLY-SOA is formed through reactions in the bulk phase as well. The rate limiting step is diffusion of glyoxal or its reactants into the bulk, e.g. a mass accommodation limitation. We obtain similarly good agreement if we set γ to 0.0033 until 10 am and increase the Henry's law constant of glyoxal (H) from 5 M/atm (dilute

Figure 2.1: A) Inorganic bulk mass of Mexico City aerosol, as a sum over all particle sizes. Inorganic particle mass is dominated by nitrate, and ammonium also forms a significant fraction. B) Size-resolved species at 2:00 pm CDT.

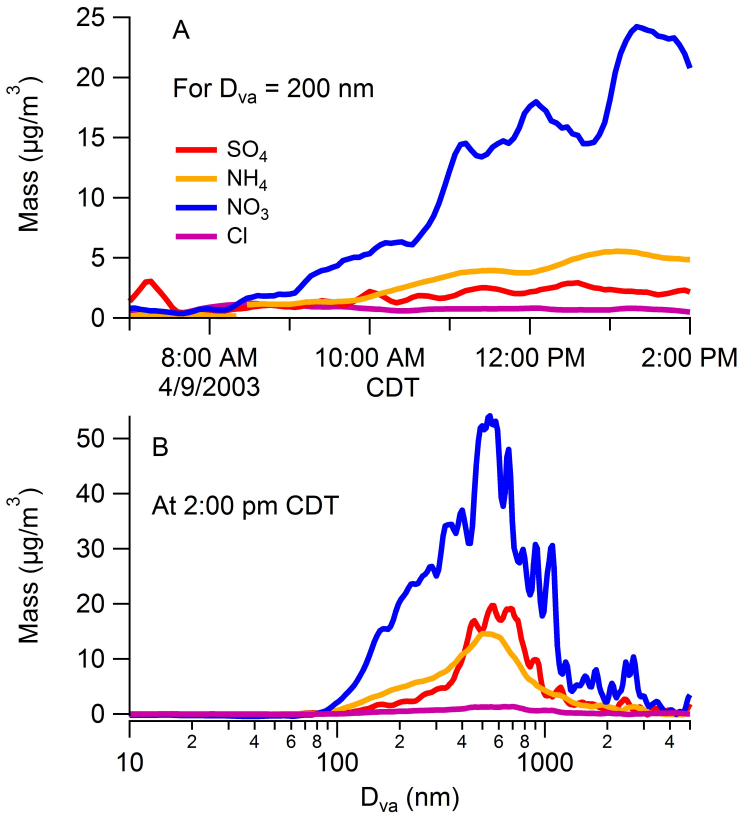

aqueous phase) to 750 M/atm (aerosol water, equivalent to $H_{eff} = 5{\times}10^7$ M/atm) as observed on mixed ammonium sulfate/organic seed particles (Volkamer et al., 2009); possibly due to hydrogen bonding of glyoxal hydrates with sulfate (Ip et al., 2009; Yu et al., 2011); this Henry's law value is further consistent with the salting constants determined from chamber experiments (Kampf et al., 2013). This represents a salting in effect due to the interaction of glyoxal and sulfate. In the same simulation, we decrease α after 10 am to represent (1) condensing semi-volatile molecules that modify the surface composition of organics and trap glyoxal in the particle phase where it converts to SOA over the course of the day, and (2) increases in particle viscosity (Shiraiwa et al., 2011) at decreasing RH (Figure 2.5c) that affect reaction rates in the bulk.

2.2.2 Chemical mechanisms of S/IVOC aging

The representation of gas-phase S/IVOC aging to date is largely based on empirical parameterizations, except for the few mechanisms that utilize explicit chemistry such as GECKO-A (Generator of Explicit Chemistry and Kinetics of Organics in the Atmosphere (Aumont et al., 2005; Camredon et al., 2007)) or the near-explicit Leeds Master Chemical Mechanism (MCM, Bloss et al. (2005)). Empirical representations such as the volatility basis set (VBS) prescribe oxygen addition and volatility decreases for each gas phase oxidation step. Two prominent VBS approaches to S/IVOC ageing, Robinson et al. (2007) (ROB), and Grieshop et al. (2009) (GRI), are treated as described in their respective references and used here as done in Dzepina et al. (2009). The major differences between these two approaches are that ROB uses an OH rate constant of 4.0×10^{-11} cm^3 molec^{-1} sec^{-1}, an oxygen addition of 1.075 per generation, and the volatility of a compound is shifted by one bin, while GRI uses an OH rate constant of 2.0×10^{-11} cm^3 molec^{-1} sec^{-1}, an oxygen addition of 1.4 per generation, and compounds are shifted by two volatility bins (Robinson et al., 2007; Grieshop et al., 2009).

We compare these parameterizations with a third mechanism, GECKO-A, which uses a near-explicit molecular-based approach to S/IVOC oxidation and gas-particle partitioning. GECKO-A self-generates chemical mechanisms via structure-activity relationships based on our current

understanding of gas-phase chemistry and kinetics. S/IVOCs are oxidized by OH, O_3, and NO_3; peroxy radical intermediates react with NO, NO_2, NO_3, HO_2, or RO_2, and alkoxy radicals react with O_2 and undergo isomerization and decomposition reactions (Aumont et al., 2005; Camredon et al., 2007). As in Lee-Taylor et al. (2011), the mechanism presented here uses *n*-alkanes to represent all S/IVOC precursors.

2.2.2.1 GECKO-A model details

The GECKO-A model was run very similarly to the study done by Lee-Taylor et al. (2011). We assimilated measured J_{NO_2} and J_{O_3} to scale photolysis rate constants with the overall effect of slightly decreasing SOA formation relative to clear-sky conditions. Emissions were as described in Lee-Taylor et al. (2011). GECKO-A predictions for NO, NO_2, NO_x, CO, OH, and O_3 were compared with measurements of those species from the campaign and with the exception of O_3, show good agreement. Modeled and measured time series are shown in Figure 2.2, and correlation plots for the six species are shown in Figure 2.3. For C_{16} oxidation by OH and NO, at 11 am (2 pm, 6 pm) GECKO-A predicts a branching ratio of 27.9% (27.7%, 18.7%) alkyl nitrates, 20% (19.7%, 10.8%) hydroxyl nitrates, and 45.6% (45.0%, 27.7%) hydroxyl carbonyls, with the remainder made up primarily of polyfunctional molecules and negligible amounts of RO_2 reaction products.

As seen in Figure 2.2, the GECKO-A model slightly over-estimates OH, particularly after noon. This overestimation of the OH concentration could result in the over-prediction of SOA by the GECKO-A model due to excess oxidation of SOA precursors by OH. To account for the OH over-estimation, the ratio of measured to modeled integral OH concentrations was used to scale the SOA predictions for GECKO-A. This scaling factor was 0.93 at 11 am and 0.84 at 2 pm, where a scaling factor of 1 represents no scaling. This scaled value represents an upper limit on the SOA formation, since it ignores feedback from reduced partitioning of SOA into lower OA mass. NO_2 and O_3 are not scaled as reactions of VOCs with either compound are not expected to contribute significant SOA mass and the over-estimation of NO eliminates the possibility of NO_3 chemistry. PAN formation may be overestimated but these speices are not major SOA mass contributors

(Lee-Taylor et al., 2011). The chemical composition of the organic aerosol fraction based on the GECKO-A model is shown in Figure 2.4.

2.2.3 Calculation of the O/C ratio of the organic aerosol fraction

All O/C ratios discussed herein are atomic, and all simulations begin at midnight Central Daylight Time (CDT, local time). We use four components to calculate the total SOA O/C ratios: (1) background SOA (BG-SOA), OOA measured before sunrise which is either present at night or results from mixing in from the residual layer aloft in the morning (Dzepina et al., 2009); (2) VOC SOA (V-SOA), predicted from gas-phase precursor measurements of e.g. single-ring aromatics, as described by Dzepina et al. (2009); (3) S/IVOC-SOA (SI-SOA) predicted from VBS parameterizations of emissions of $C_{\leq 11}$ according to the oxidation parameterizations of ROB or GRI, or the GECKO-A oxidation mechanism; and (4) glyoxal SOA (GLY-SOA), as described in Section 2.2.1. The O/C ratios for V-SOA and the ROB and GRI S/I-SOA are taken from the literature and previous model results (Robinson et al., 2007; Grieshop et al., 2009; Dzepina et al., 2009). The O/C ratios for GECKO-A SI-SOA and GLY-SOA are calculated in situ, and the O/C for BG-SOA was measured in Mexico City (see sections 2.2.3.1 and 2.2.3.2). We perform a second O/C comparison for total organic aerosol (OA) that also includes hydrocarbon-like organic aerosol (HOA) measured by the AMS, or primary organic aerosol (POA) calculated from GECKO-A. This second analysis thus avoids the possibility of bias from comparing the SOA surrogate OOA to SOA predictions by models.

2.2.3.1 O/C calculation in the box model to predict glyoxal SOA

The O/C for glyoxal$_{(aq)}$ is 1, 1.5 for the monohydrate, 2 for the dihydrate, 1.2 for glyoxal oligomers in solutions that are considered as proxies for aerosol water (Lim et al., 2010), 1.1 for products of glyoxal + ammonium based on product data in Noziere et al. (Noziere et al., 2009), and 1.5 for products of glyoxal + OH based on products described in Tan et al. (2009). Sensitivity studies were performed on the total O/C ratio by assigning the products from bulk or surface-limited

Figure 2.2: Comparison between measurements (Shirley et al., 2006; Volkamer et al., 2005a) (dots) and GECKO-A box model simulations (lines) for NO_2 (A), NO (B), NO_x (C), CO (D), O_3 (E), and OH (F). Generally good agreement is observed between Mexico City measurements and modeled values, except for ozone which the model significantly over-predicts. All model simulations include dilution from vertical mixing due to boundary layer height increases over the course of the day.

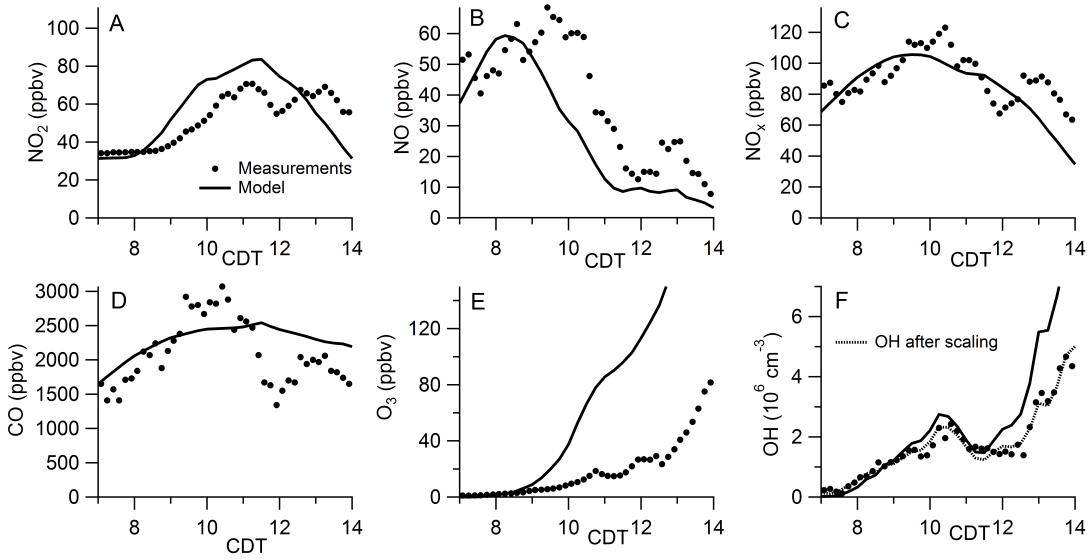

Figure 2.3: Statisitical analysis of GECKO-A model versus MCMA-2003 measurements for A: NO_2, B: NO, C: NO_x, D: CO, E: O_3, F: OH. Generally good agreement is shown between the model predictions and measurements except for O_3 which the model over-predicts. This overprediction in O_3 is partly due the overprediction in OH radicals (slope = 1.7 before correction, and 1.0 after correction).

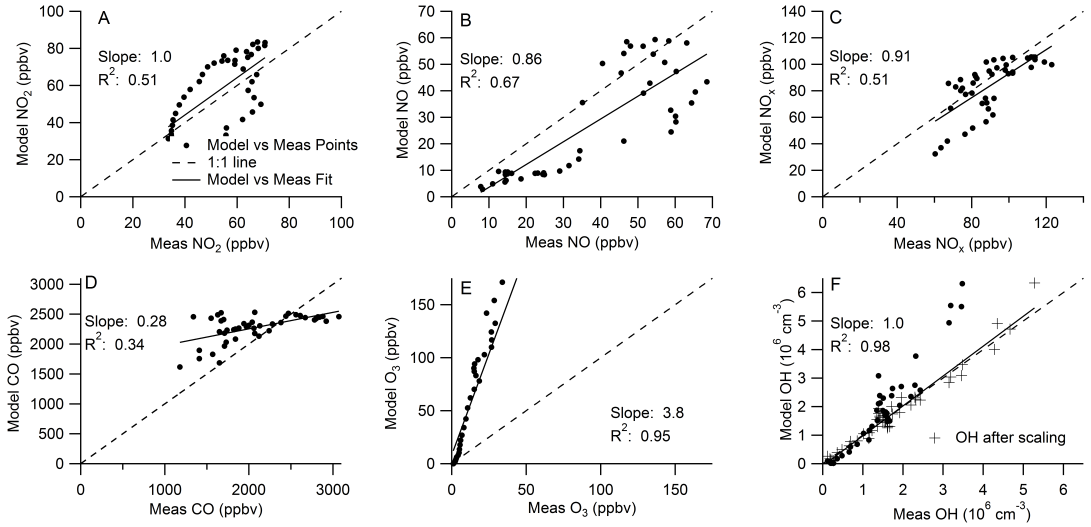

Figure 2.4: GECKO-A predicted SOA and POA mass (A) and mass fractions (B) based on carbon number (C_3 - C_{25+}). Grey is from POA, colors from SOA. $C_{\leq 11}$ compounds are considered SI-SOA in this work, and represent an increasing fraction of OA mass. POA absolute mass remains relatively constant, but due to the growth of SOA, results in a diminishing POA mass fraction.

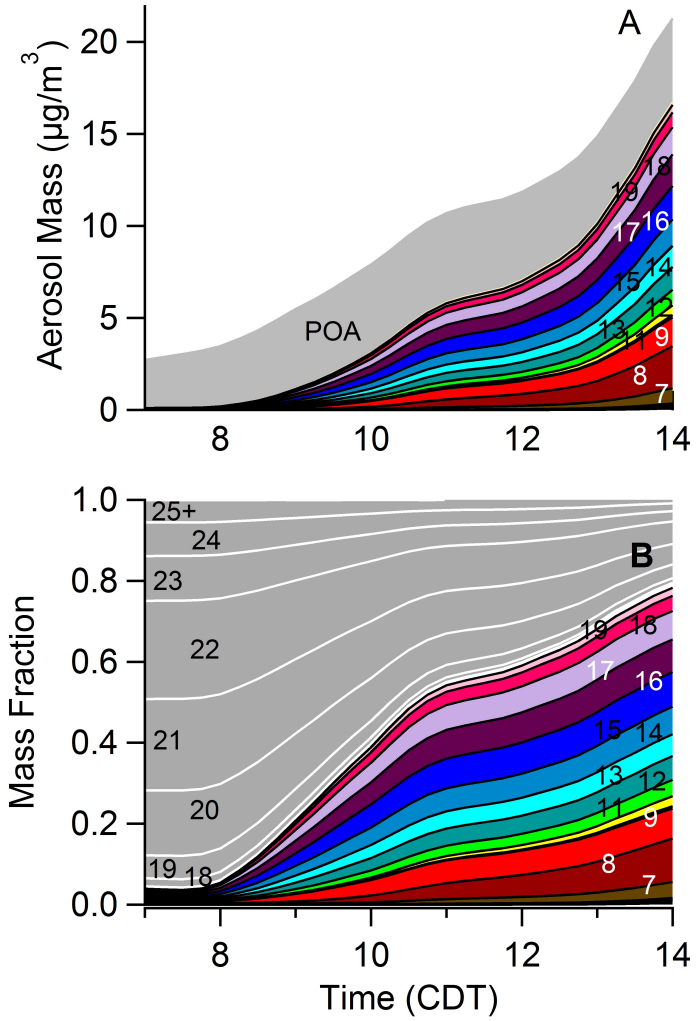

processes an O/C ratio between 1 and 1.5, well within the reasonable range for glyoxal product O/C ratio values in aerosol water. Since GLY-SOA has such a high O/C, measured between 1 and 1.8 in the laboratory (Lim et al., 2010; Chhabra et al., 2010; Lee et al., 2011), it is expected to be internally mixed in the aerosol aqueous phase, and not just the aerosol organic phase (Bertram et al., 2011).

2.2.3.2 O/C for GECKO-A

Atomic O/C is calculated in the GECKO-A model directly from the species that produce SOA. The O/C ratio from the GECKO-A model may be calculated for specific subsets of species. Here, it was broken down in to C_{10} and smaller compounds, and C_{11} and larger compounds. We used results from the latter subset as an explicit S/IVOC proxy.

2.2.3.3 Total aerosol O/C

Total aerosol O/C was calculated as done in Dzepina et al. (2009, 2011) by summing the total number of C and O atoms in each OA contributor as follows:

$$M_i = 16n_{O,i} + 12n_{C,i} \tag{2.1}$$

$$\frac{n_{O,i}}{n_{C,i}} = O/C_i \tag{2.2}$$

where M_i is the mass of OA fraction i, $n_{O,i}$ is the number of moles of oxygen atoms in that fraction, and $n_{C,i}$ is the number of moles of carbon atoms in that fraction, and O/C_i is the O/C ratio of OA fraction i. From Equations 2.1 and 2.2, we derive

$$n_{C,i} = \frac{M_i}{16 \times O/C_i + 12} \tag{2.3}$$

$$n_{O,i} = O/C_i \times n_{C,i} = O/C_i \times \frac{M_i}{16 \times O/C_i + 12} \tag{2.4}$$

And the total aerosol O/C ratio can be written as

$$O/C_{tot} = \frac{\sum_i n_{O,i}}{\sum_i n_{C,i}} \tag{2.5}$$

Mass of H and N were ignored in the O/C calculations because H mass is negligible in comparison to heavier atoms, and during MILAGRO the N/C was on average 0.02, a factor of 20 less than the O/C (Aiken et al., 2008), so N is expected to contribute a negligible amount to the aerosol mass. The exclusions of H and N from the calculations are expected to result in a less than 5% overestimation error of the true O/C ratio.

Better agreement between Case 1 and Case 3 and the AMS data (see Section 2.3.2) can be found by increasing the BG O/C from 0.41 to 0.75. This higher value is in agreement with other highly oxidized aerosol O/C measurements from MILAGRO (DeCarlo et al., 2008); however, due to the very low background SOA levels on 9 April 2003, we use the measured BG O/C of 0.41 in the analysis.

2.3 Model results and discussion

2.3.1 Modeled GLY-SOA formation in Mexico City

The difference between the gas-phase glyoxal predicted to be formed in Mexico City and the amount actually measured is termed the glyoxal imbalance, which was hypothesized to be due to particle uptake (Volkamer et al., 2007). The amount of GLY-SOA predicted by our laboratory-based mechanism can explain our previous estimate of the imbalance on similar time scales to those measured in Mexico City (Figure 2.5). The temporal evolution of the predicted GLY-SOA shows a very different time trace depending on whether a bulk process or a surface process is represented in the box model. Calculations using a surface-limited process match the shape of the imbalance better than calculations using bulk phase reactions, with best agreement for $\gamma = 0.0033$. The rate of glyoxal uptake to aerosols is generally compatible with laboratory-measured γ values. The optimum γ of 0.0033 is slightly lower than the γ of 0.0037 derived in Volkamer et al. (2007) to account for the previously neglected water uptake by the organic fraction of the aerosols. Similar γ values have been observed in chamber experiments (Liggio et al., 2005b; Trainic et al., 2011) show comparable aerosol mass growth rates. The kinetics of glyoxal mass transfer can vary by

several orders of magnitude between laboratory experiments (Kroll et al., 2005; Galloway et al., 2011; Nakao et al., 2012); the reasons for this variability are as of yet unclear. In our case study, about 1 in every 300 collisions of glyoxal with surfaces of the metastable particles on average results in uptake.

The product distribution from glyoxal reactions in the bulk aerosol changes as a function of time of day (see Table 2.1). Reactions with ammonium increase in relative importance over OH radical reactions in the later morning, due to increasing NH_4^+ aerosol mass (see Figure 2.1). The product distribution is most sensitive to the H value for glyoxal and particle pH, and it only weakly depends on gas-phase OH radical concentrations. The SOA mass formed from OH radical reactions with glyoxal in the aqueous phase is added as a dashed orange line in Figure 2.5 and accounts at maximum for 5.5% of the GLY-SOA. Gas-phase OH is the only OH source considered in particles during these model runs (Figure 2.6). Additional radical sources are not considered, but may result from organic photochemistry in aerosol water (Volkamer et al., 2009; Monge et al., 2012). With increasing H and pH, the ammonium reaction gains in relative importance because the NH_4^+ availability is not mass transfer limited; at lower H the OH-radical reaction is relatively more important. The rate constant of glyoxal with NH_4^+ is a strong function of pH (Noziere et al., 2009), which is constant (pH of approximately 4) during this case study based on thermodynamic modeling using ISORROPIA (Volkamer et al., 2007). For aerosol chemical composition April 9 is not an anomalous day (Salcedo et al., 2006). Reaction channels other than NH_4^+ gain in relative importance at lower pH, where the overall rate of GLY-SOA formation is lower than at high pH. Our results apply to the conditions in Mexico City, and a similar analysis in other urban environments will need to characterize parameters including H, pH, LWC, and aerosol phase state, which all influence the rate of GLY-SOA formation.

In this model, OH enters the aerosol via the resistance model, which includes gas-phase diffusion, partitioning via Henry's law, and a surface uptake coefficient. The model does not include additional aqueous phase OH radical sources, e.g., H_2O_2, or nitrate photolysis, or other sources for oxidants (e.g., Monge et al. (2012)). On the other hand, the product distribution in Table 2.1 is

Figure 2.5: Comparison of temporal evolution of GLY-SOA as predicted by the model with that calculated from the measured glyoxal imbalance. A) GLY-SOA mass shown for five cases: bulk processes using H for dilute aqueous phase (red) and aerosol water (orange), surface processes using Mexico City-derived uptake coefficients (γ) (blue), results from a bulk process using time-resolved α and γ (black), and results from including a surface process with no bulk reactions and a bulk reaction with no surface process (green). Grey circles denote the glyoxal imbalance from Volkamer et al. (Volkamer et al., 2007). B) Difference (%) between Aerosol Liquid Water Content (ALWC, black), wet aerosol surface area (red), and wet aerosol volume (green) between the hygroscopic and non-hygroscopic SOA cases. C) Input data for temperature, pressure, and RH.

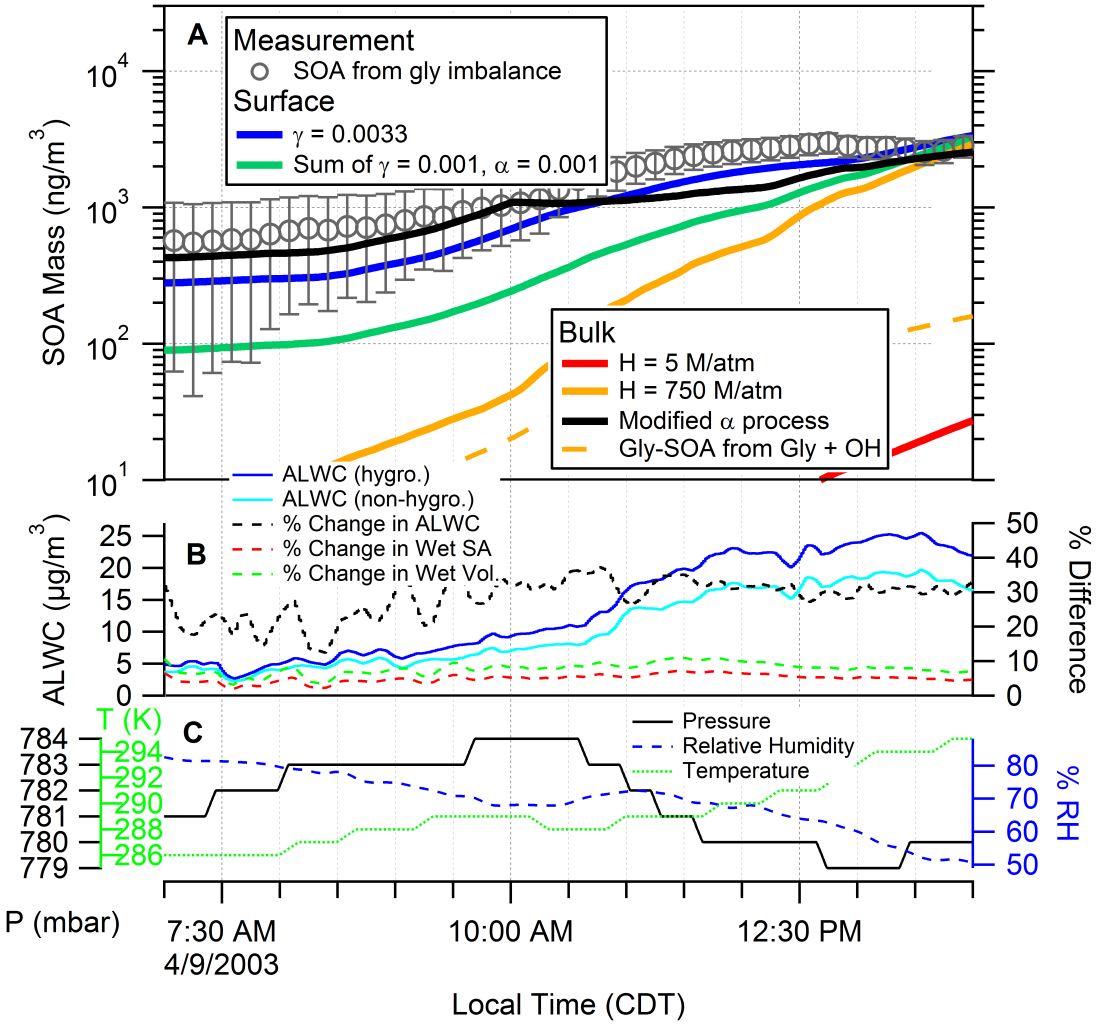

Figure 2.6: Sensitivity study of model-predicted aqueous-phase OH. Solid lines: using an H_{gly} of 5 M/atm. Dashed lines: using an H_{gly} of 750 M/atm. Red: in the absence of any $OH_{(aq)}$ reactions. Blue: with only OH + (glyoxal + monohydrate + dihydrate) to products. Green: all GLY-SOA + OH to products. Turquoise: OH + dissolved OOA to products.

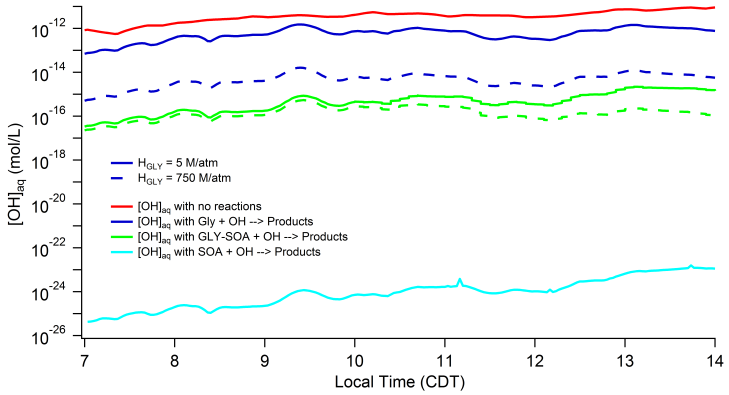

calculated assuming OH reacts only with glyoxal momomers, and with neither oligomers nor with other SOA components.

Results from a sensitivity study of aqueous-phase OH concentrations to different OH-radical sink reactions are shown in Figure 2.6. Solid lines indicate a Henry's law constant of 5 M/atm for glyoxal; dashed lines are for a Henry's law constant of 750 M/atm. The red trace is $[OH_{(aq)}]$ (M) in the absence of any reactions or sinks. This is consistent with the values predicted using solely Henrys law and the values shown in Figure 3 of Ervens and Volkamer (Ervens and Volkamer, 2010) where the lower OH concentrations shown are based on the resistance model and additional aqueous-phase losses. The blue traces show $[OH_{(aq)}]$ when the glyoxal + OH reaction is turned on with a k_{OH} of 1.0×10^9 $M^{-1}s^{-1}$. This case is representative for the product distribution shown in Table 2.1. Other model runs include an additional OH sink. The results shown by green lines include an additional OH sink of all GLY-SOA + OH with a rate constant of 1.0×10^9 $M^{-1}s^{-1}$. The results shown in turquoise include an additional OH sink of aerosol OOA + OH with a rate constant of 1.0×10^8 $M^{-1}s^{-1}$ to include the possibility that OH could react with SOA already present in the aerosol. This figure shows that OH is efficiently suppressed by adding additional OH radical sink reactions, and in none of the cases treated reaches thermodynamic equilibrium despite the lack of

a mass accommodation limitation into the bulk due to diffusion, due to rapid sink reactions inside the aerosol. Since SOA with O/C larger than 0.7 is believed to form a single phase with water attracted by the inorganic aerosol components (Bertram et al., 2011), we believe that such SOA has the potential to strongly suppress the aqueous phase OH radical concentration (see Figure 2.6). The model predicted aqueous phase OH radical concentration, while uncertain, is thus more likely overestimated due to this strong sensitivity to OH-radical sinks. If additional sources of oxidants were present, the irreversible rate of GLY-SOA formation could be higher, which could help reduce the amount of unaccounted GLY-SOA in the early morning.

2.3.2 Comparison of model SOA O/C and mass with measurements

The SOA formed from S/IVOC oxidation is predicted to dominate overall SOA mass. Comparable SI-SOA amounts are predicted from ROB and GECKO-A simulations (Figure 2.7). GRI results in the highest S/I-SOA mass and O/C predictions, consistent with previous work (Dzepina et al., 2011). The sum of HOA measured by AMS (or POA predicted by the GECKO-A model), BG-SOA, V-SOA, GLY-SOA, and either ROB or GECKO-A is very close to the OA mass measured by the AMS, while using GRI as the SI-SOA component significantly over-estimates OA mass (Figure 2.7b).

Figure 2.7a compares the O/C ratio of the individual OA components. For an integral OH exposure over the time period of 7 am to 2 pm (up to 4.5×10^6 molecules/cm^3 as shown in Figure 2.2) and defined as $\int[OH]\,\mathrm{d}t$, of 1.8×10^{10} molec cm^{-3} s (4.7×10^{10} molec cm^{-3} s) at 11am (2pm), the O/C ratios are 0.5 (0.6), 0.11 (0.16) and 0.12 (0.13) for the GRI, ROB and GECKO-A SOA components, respectively. GECKO-A shows the slowest rate of O/C increase among these three aging mechanisms: at 9 am, the O/C is 0.12 and O/C has increased by 10% at 2 pm. In contrast, the O/C predicted from ROB doubles from 0.082 at 7am to 0.16 by 2pm, and the GRI O/C is 0.43 at 7am, and increases by 40% by 2pm. The slow rate of O/C increase from GECKO-A SI-SOA extends to longer ageing time scales as well ($\mathrm{O/C}_{SOA,C16} < 0.25$ at $\int[OH]\,\mathrm{d}t = 1.7\times10^{11}$ molec cm^{-3} s) (Aumont et al., 2012), generally consistent with laboratory observations (Lambe et al.,

Figure 2.7: Comparison of measured and predicted O/C for different mechanisms. A) Time-dependent O/C ratios for each OA component. B) Temporal evolution of predicted OA mass for each component. The sum of HOA + BG-SOA + V-SOA + GLY-SOA + ROB SI-SOA or GECKO-A SOA matches the value of the measured OA mass, but GRI SI-SOA overestimates. C) Comparison between O/C ratio measured in Mexico City and predicted by the mechanisms as described in Section 2.3. Green lines: includes GRI SI-SOA; blue lines: includes ROB SI-SOA; turquoise lines: includes GECKO-A SOA from $C_{\leq 11}$ species. Solid lines: BG-SOA + V-SOA + SI-SOA but no GLY-SOA. Dashed lines: include GLY-SOA with an O/C of 1.5.

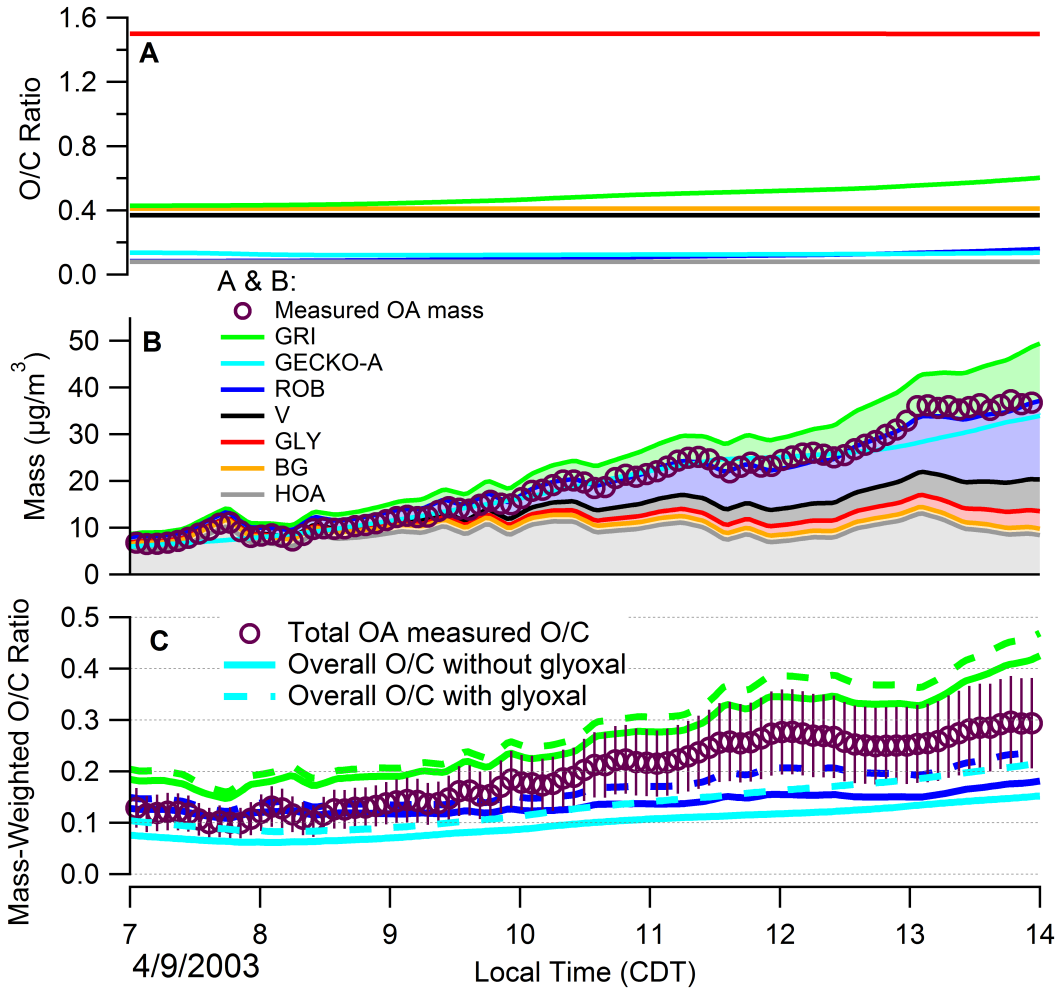

2011).

Predicted OA O/C is compared to observations in Figure 2.7c. For the solid lines, four components (BG-SOA, V-SOA, S/I-SOA, and POA) are used to calculate O/C for three cases that differ only in the SI-SOA parameterization: Case 1 (ROB), Case 2 (GRI) and Case 3 (GECKO-A). In the absence of GLY-SOA, Case 2 over-estimates both SOA mass and O/C, and this VBS parameterization is therefore deemed unrealistic. Case 1 and Case 3 underestimate AMS-measured O/C ratio. The dashed lines in Figure 2.7c show the predicted O/C when the contribution of GLY-SOA (Section 2.1) is included, using a GLY-SOA O/C of 1.5 which was selected as close to the middle of the range of O/C values of 1 to 1.8 observed in laboratory studies (Lim et al., 2010; Chhabra et al., 2010; Lee et al., 2011). With the addition of GLY-SOA better agreement is observed between Cases 1 and 3 and the AMS data. Sensitivity studies indicate that the total SOA O/C is rather insensitive to BG-SOA in the afternoon. BG-SOA transport thus cannot explain the O/C mismatch, discussed previously.

A similar analysis was done comparing total SOA only, and shows similar results (see Figure 2.8). Overall, these SOA calculations confirm the OA case shown above illustrating that HOA serves as a good proxy for POA during this case study. In the absence of GLY-SOA, GRI over-estimates both mass and O/C while GECKO-A and ROB get the mass approximately correct but underestimates the O/C ratio. With the addition of GLY-SOA, Case 1 and Case 3 predict OA mass very close to that measured, while Case 2 over-estimates mass. In the absence of GLY-SOA, Case 2 over-estimates total SOA O/C, while Case 1 and Case 3 significantly under-estimate the O/C. Case 1 and Case 3 still under-estimate total SOA O/C in the presence of GLY-SOA, but are closer to the measured values. We conclude that the addition of GLY-SOA helps explain between 30-50% of the O/C gap to observations on similar time scales to the oxidation in Mexico City, but it appears insufficient to fully close the O/C gap.

In order to test whether mixing of high O/C BG-SOA could provide alternative means to obtain O/C closure, we carried out a sensitivity study that assumes that BG-SOA mass increases over time, instead of introducing aqueous-phase processing to form GLY-SOA. While BG-SOA

Figure 2.8: Comparison of measured and predicted O/C for different mechanisms. A) Time-dependent O/C ratios for each SOA component. B) Temporal evolution of predicted SOA mass for each component. The sum of BG-SOA + V-SOA + GLY-SOA + ROB SOA or GECKOA-SOA matches the value of the measured SOA mass, but GRI SI-SOA overestimates. C) Comparison between O/C ratio measured in Mexico City and predicted by the mechanisms as described in Section 2.3. Green lines: includes GRI SI-SOA; blue lines: includes ROB SI-SOA; turquoise lines: includes GECKO-A SOA from $C_{\leq 11}$ species. Solid lines: BG-SOA + V-SOA + SI-SOA but no GLY-SOA. Dashed lines: include GLY-SOA with an O/C of 1.5.

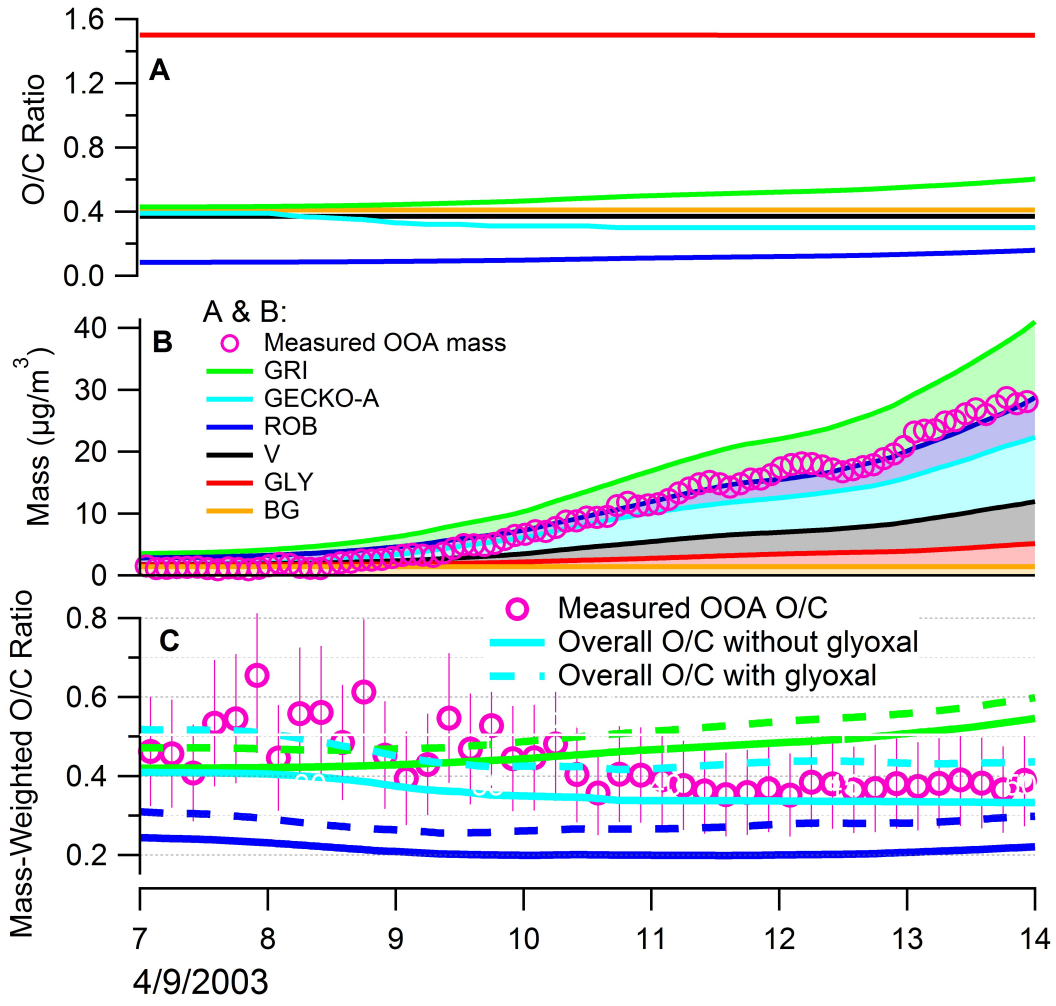

transport is inefficient during the calm conditions and shallow boundary layer on 9 April 2003, there has not been a previous assessment of the efficiency of this SOA component based on O/C modeling. Assuming BG-SOA has a very high constant O/C of 0.75 at 2 pm we calculate that 14 $\mu g/m^3$ (or ~50% of the observed OOA mass) of BG-SOA would be necessary to close the O/C gap using Case 1 (ROB). A significantly larger BG-SOA mass would be needed if a lower O/C of 0.41 is assumed. Case 3 (GECKO-A) would require a total of 22 $\mu g/m^3$ of BG-SOA (or ~80% of the observed OOA mass). Case 2 (GRI) over-estimates O/C even in the absence of GLY-SOA, and requires a reduction of the aerosol oxidation state in the afternoon to obtain closure, which is a non-physical result. In either Case 1 or Case 3, the BG-SOA needed to close the O/C gap would result in mass over-estimation. For these reasons we conclude that an O/C modeling perspective provides further corroborating evidence that transport of BG-SOA is not contributing to the SOA growth during the 9th April 2003 case study of SOA formation in Mexico City. This result can likely be generalized to SOA formation in Mexico City on other dates for reasons discussed in the literature (Volkamer et al., 2006b, 2007; Dzepina et al., 2009; Hodzic et al., 2010; DeCarlo et al., 2010; Dzepina et al., 2011; Lee-Taylor et al., 2011; Hodzic and Jimenez, 2011).

Accurate predictions of aerosol O/C are important for estimating the magnitude of climate change. O/C shows a strong linear correlation with aerosol hygroscopicity (Jimenez et al., 2009; Chang et al., 2010). As O/C increases, the aerosol becomes more hygroscopic, and thus larger due to water absorption. This results in a lower critical supersaturation at which the aerosol can behave as a cloud condensation nuclei (Petters and Kreidenweis, 2007). There is additional evidence that the aerosol O/C is correlated with aerosol scattering cross sections (Cappa et al., 2011). Thus accurately modeling aerosol O/C is important not only to test our understanding of SOA formation mechanisms, but also for predictions of the aerosol direct effect (scattering incident radiation) and the aerosol indirect effect (cloud formation).

2.4 Conclusions and outlook

For the first time, the glyoxal imbalance from Volkamer et al. (2007) was evaluated using a laboratory-based model. A surface-limited process is found to best reproduce the time evolution of the glyoxal imbalance with an uptake coefficient, $\gamma = 0.0033$, consistent with laboratory data (Liggio et al., 2005b; Trainic et al., 2011). For the bulk reaction case, the GLY-SOA product distribution depends strongly on the Henrys law constant of glyoxal, and particle pH, and less on the gas-phase OH radical concentration. When the only source for aqueous phase OH radicals is transfer from the gas-phase, the SOA mass formed from aqueous phase OH radical reactions is very small ($\leq$5% of GLY-SOA); additional radical sources from organic photochemistry are likely (Volkamer et al., 2009; Monge et al., 2012). The dominant GLY-SOA formation route in the model is from the catalytic reaction with NH_4^+ at the elevated particle pH in Mexico City (Table 2.1).

While S/IVOCs are predicted to contribute most (50-70%) of the SOA mass, the comparison of different S/IVOC aging schemes gives little confidence in predicting the observed O/C ratio over aging times equivalent to 4.7×10^{10} molec cm^{-3} s OH exposure (about 4.3 hours at [OH] = 3×10^6 molec cm^{-3}). The GECKO-A model was found to produce S/I-SOA with substantial mass yields, but mostly in a reduced state (O/C < 0.13) that does not match the highly oxygenated OA component typically found in situ. The sum of SI-SOA, V-SOA, and BG-SOA can account for only about half the observed O/C during the afternoon. These results suggest a gap in our understanding of the gas phase oxidation and/or efficient chemistry occurring in the condensed phase. We conclude that aqueous phase processing helps to explain the observed time evolution of aerosol O/C on rapid time scales similar to those observed in Mexico City. While GLY-SOA alone can only explain 30-50% of the O/C gap, glyoxal serves as an indicator for other soluble molecules that may undergo multiphase chemistry (e.g., methyl glyoxal, glycolaldehyde). More laboratory work is needed to identify reaction products from glyoxal and other soluble molecules that undergo aqueous multiphase chemistry, in particular to constrain their gas/aqueous phase partitioning, pH-, ALWC-, and aerosol phase state dependence of the rate of SOA formation.

Chapter 3

Application of a ^{13}C Glyoxal Cross Section to DOAS Measurements and Laboratory Studies

Parts of this chapter were published as: Goss, N. R., Waxman, E. M., Coburn, S. C., Koenig, T. K., Thalman, R. M., Dommen, J., Hannigan, J. W., Tyndall, G. S., and Volkamer, R. M., Measurements of the absorption cross section of ^{13}CHO^{13}CHO at visible wavelengths and application to DOAS retrievals, J. Phys. Chem. A, doi:10.1021/jp511357s, 2015

Glyoxal (CHOCHO) is a trace gas that forms from the atmospheric oxidation of hydrocarbons and is a precursor to secondary organic aerosol (SOA). An isotopically labeled ^{13}C glyoxal (^{13}CHO^{13}CHO) cross section was recently measured for the strong absorption bands between 430-470 nm. This isotopic cross section shows a significant shift of 0.29 nm at the 455 nm peak, and no shift ($<$ 0.01 nm, the cross section resolution) at 440 nm, as shown in Figure 3.2. This significant shift means that is possible to distinguish the two isotopes of glyoxal (^{12}CHO^{12}CHO and ^{13}CHO^{13}CHO) with a DOAS or other broad-band retrieval in this region. The isotopic form then has the potential to be used as a tracer in laboratory experiments whereby knowing that the gas-phase (or precursor) is isotopically labeled, we can link potential products from glyoxal to either source glyoxal or background contamination by studying the isotopic composition of the products. We performed two such experiments using isotopically-labeled glyoxal at the Paul Scherrer Institut atmospheric simulation chambers. Here, we present results on the DOAS analysis of two chamber experiments, one using ^{12}C glyoxal and one using ^{13}C glyoxal. We particularly focus on the effect of orthogonalizing the two cross sections using the Gram-Schmidt method and the implications for simultaneous retrieval of both ^{12}C and ^{13}C glyoxal.

3.1 Introduction

Secondary organic aerosol (SOA) formation from small water-soluble molecules is a topic of growing interest (Liggio et al., 2005b,a; Volkamer et al., 2009; Galloway et al., 2009, 2011; Kampf et al., 2013). One such water soluble molecule is glyoxal (CHOCHO), the smallest α-dicarbonyl. Glyoxal forms SOA by partitioning to the aerosol aqueous phase where it can undergo oligomerization reactions to form dimers, trimers, and higher oligomers. It can also react with inorganics and radicals to form imidazoles (nitrogen-containing ring species) and additional high molecular weight species ((Ervens and Volkamer, 2010) and references therein).

SOA formation from glyoxal has been studied in a number of chamber experiments. Volkamer et al. (2009) studied the effect of light on the formation of SOA from glyoxal and found that UV light significantly increased the rate of SOA formation compared to dark reactions. Kampf et al. (2013) found that the salt concentration in the aerosol has a significant impact on the amount of glyoxal that can be taken up. Additionally, many studies have focused on product formation from glyoxal. Dimers and trimers of glyoxal have been reported (Liggio et al., 2005a; Galloway et al., 2009; Noziere et al., 2009), as have a number of imidazole compounds (Galloway et al., 2009), and organosulfates (Liggio et al., 2005a; Galloway et al., 2009).

However, there exists conflicting data on the formation of organosulfates from glyoxal. Chamber, studies including ones by Liggio et al. (2005a) and Galloway et al. (2009), report the detection of glyoxal sulfate, an organosulfate formed from glyoxal. Liggio et al. (2005a) used a low-resolution quadrupole aerosol mass spectrometer that had approximately unit mass resolution preventing the determination of the exact chemical composition of the fragments. Galloway et al. (2009) did a series of experiments using a high resolution time of flight aerosol mass spectrometer (ToF-AMS) and used the higher resolution to assign the organosulfate peaks from Liggio et al. (2005a) as $C_5H_5O_5^+$ and $C_6H_7O_6^+$. Galloway et al. (2009) also reported organosulfates that they assigned as glycolic acid sulfate. However, glyoxal uptake experiments are highly sensitive to background contamination and it is possible that some products detected in laboratory experiments could result from the

chamber background. Galloway et al. (2011) determined in a later set of experiments that their glyoxal uptake was significantly decreased due to chamber background organics condensing on seed aerosols, forming a barrier to uptake. Similar effects may have impacted earlier experiments as well.

Complicating the identification of glyoxal sulfate versus glycolic acid sulfate is the fact that the proposed structures for these species are isomers of each other: they both have the formula $C_2H_3O_6SR^-$ (Galloway et al., 2009). Species of this mass have been detected in ambient aerosols, but using mass spectrometry it is not possible to identify which product is formed (Hatch et al., 2011). Therefore, the use of a tracer for glyoxal reaction products would allow one to unambiguously identify products formed from glyoxal versus products resulting from the chamber background. ^{13}C glyoxal is an ideal tracer because of its relatively low natural abundance compared to ^{12}C glyoxal. In laboratory experiments using only ^{13}C glyoxal as a reactant, a ^{13}C signature in products would provide definitive proof of production from glyoxal whereas a ^{12}C only signature would indicate that the product is the result of background contamination. Thus the measurement of this ^{13}C cross section can eventually be used in clean ^{13}C experiments where products from the source glyoxal can be unambiguously identified.

3.2 Experimental

3.2.1 Chamber Experiments

All glyoxal uptake experiments were performed at the Laboratory for Atmospheric Chemistry simulation chamber at the Paul Scherrer Institut in Villigen, Switzerland (Paulsen et al., 2005). For experimental details, please see Chapter 6. Briefly, glyoxal was formed in situ from acetylene via the reactions below (Hatakeyama et al., 1986):

R1: $HONO + h\nu \rightarrow OH^{\cdot} + NO$

R2: $C_2H_2 + OH^{\cdot} + O_2 \rightarrow CHOCHO + OH^{\cdot}$, 65% yield

R3: $C_2H_2 + OH^{\cdot} + O_2 \rightarrow CO + HCOOH$, 35% yield

A total of eighteen experiments were performed. The first sixteen used unlabeled glyoxal with a normal isotopic abundance (^{12}C glyoxal) and the last two used isotopically labeled glyoxal from isotopically labeled acetylene. Results from two experiments (Exp. 15 and Exp. 17) are presented in this section. Experiment 15 was the last ^{12}C glyoxal experiment, so prior to and during this experiment the chamber has seen only ^{12}C glyoxal. Experiment 17 is the second of the two ^{13}C glyoxal experiments, so immediately prior to and during this experiment, the chamber was exposed to only ^{13}C glyoxal. The spectra used for wavelength stability regions were taken after 18 hours of cleaning with OH and ozone prior to glyoxal production in the chamber. Data with low but non-zero NO_2 and background glyoxal is used and the time series data (see Section 3.3.3) is taken from the first glyoxal production period.

3.2.2 The CU-LED-CE-DOAS Instrument

Gas-phase measurements of glyoxal during the chamber experiments were made with the CU LED-CE-DOAS instrument. Details of this instrument can be found in Thalman and Volkamer (Thalman and Volkamer, 2010). Briefly, light from a blue LED (centered at 455 nm, LED Engin, San Jose, CA) is coupled into a pair of highly reflective mirrors (R = 99.996%, Advanced Thin Films, Boulder, CO). Light exiting the cavity is coupled into an optical fiber that directs the light in to an Ocean Optics QE-65000 spectrometer. Individual spectra were acquired for 1 minute. Under these conditions, the cavity had part per trillion by volume (pptv) sensitivity. Analysis was performed with the DOAS software WinDOAS 2.1 (Fayt and van Roozendael, 2001). For further details, see Section 3.2.3 and Figure 3.1.

Immediately downstream of the connection to the chamber, there was a 0.2 μm filter to prevent aerosol particles from reaching the cavity which would reduce the intensity of the collected light due to Mie scattering. Additionally, a dilution flow was introduced into the sample prior to reaching the cavity in order to reduce the concentration of gases from the chamber (balancing

sample concentration with extinction losses inside the cavity) and lower the relative humidity of the sample (minimize glyoxal losses in sample tubing).

3.2.3 WinDOAS Analysis

As previously mentioned, spectra were analyzed with WinDOAS 2.1 software (Fayt and van Roozendael, 2001). Cross sections were fit in two windows: a glyoxal window at 438-465 nm and an O_4 window at 457-487 nm. Cross sections for O_4 (Thalman and Volkamer, 2013), NO_2 (high and low concentrations, using path lengths assuming 20 ppbv and 0 ppbv NO_2 respectively (Vandaele et al., 2002), see Section 3.2.3.2, ^{12}C glyoxal (Volkamer et al., 2005b), ^{13}C glyoxal (Goss et al., 2015), H_2O (Rot), and O_3 (Bogumil et al., 2003) were fit along with a polynomial (3^{rd} order in the O_4 window and 4^{th} order in the glyoxal window) to remove broadband absorption due to Rayleigh and Mie scattering. All molecular cross sections were convoluted with the instrument line function, which was measured using a standard Hg calibration light source and determined to be approximately Gaussian with a 0.55 nm full width half max (FWHM). All cross sections were scaled as described in (Thalman and Volkamer, 2010). A ten minute spectrum of pure nitrogen was used as the reference. All cross sections except for the two glyoxal cross sections had a coupled shift (no stretch was allowed). The two glyoxal cross sections were given their own coupled shift.

3.2.3.1 Isotopic glyoxal cross section

The measurement of the ^{13}C glyoxal cross section and background subtraction are described in (Goss et al., 2015). The high resolution ^{12}C and ^{13}C glyoxal cross sections are shown in Figure 3.2. There is a very apparent shift at 455 nm (the position of the strong absorption band, inset B) and no shift at 440 nm (the position of the weak band, inset A). These spectra have been convolved with the instrument line shape (0.55 nm FWHM) in Figure 3.3. The shift at 455 nm is still quite prominent even at the lower resolution. This suggests that the two isotopes of glyoxal should be able to be differentiated.

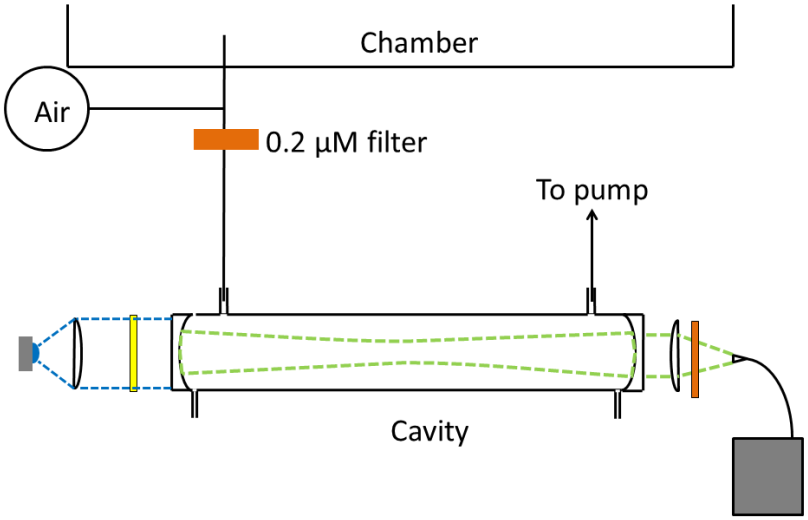

Figure 3.1: Schematic of cavity hook up to chamber during the PSI campaigns. Air was pulled from the chamber through the cavity via a pump. Immediately after leaving the chamber, the air was diluted to minimize loss to the Teflon tubing and filter due to the high relative humidity and to decrease the concentration of NO_2. Immediately following this, the air was filtered to remove aerosols and minimize extinction loss due to Mie scattering.

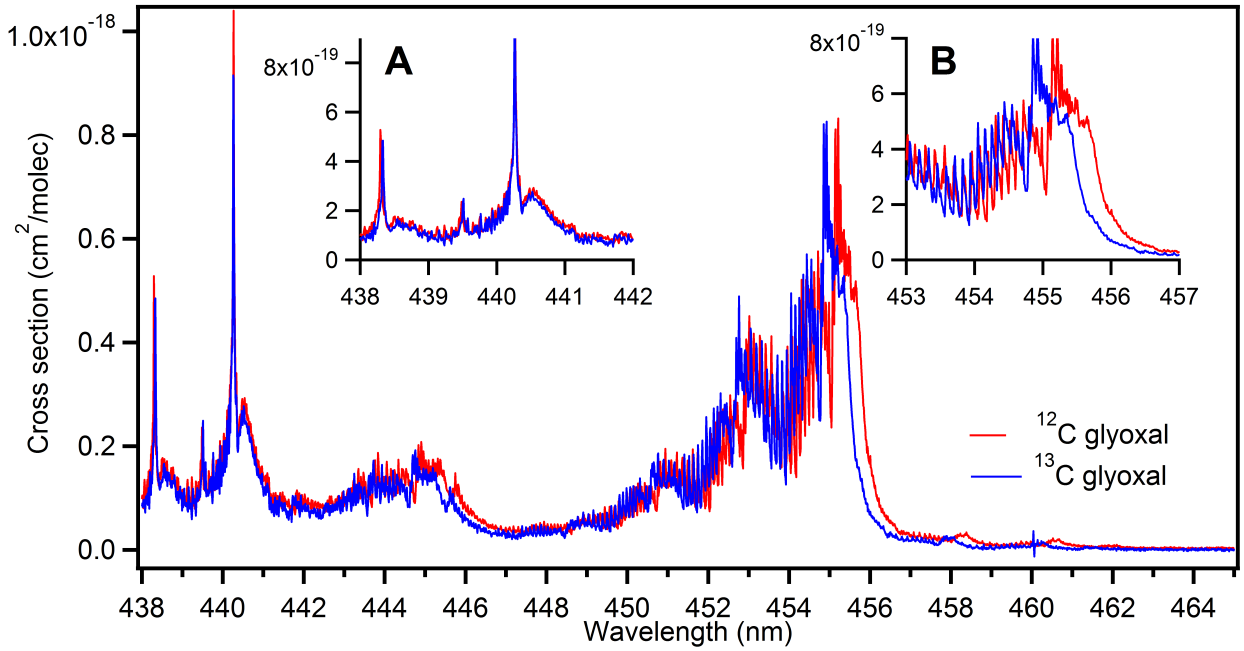

Figure 3.2: High-resolution ^{12}C glyoxal (red) and ^{13}C glyoxal (blue) as measured in Goss et al. (Goss et al., 2015). The shift is very apparent at 455 nm but absent at 440 nm. This can be seen more clearly in the insets, where it is more apparent that the peaks at 440.2 nm and the shoulder at 440.5 lie exactly on top of each other (inset A) and that there is a shift of about 0.3 nm at 455 nm (inset B).

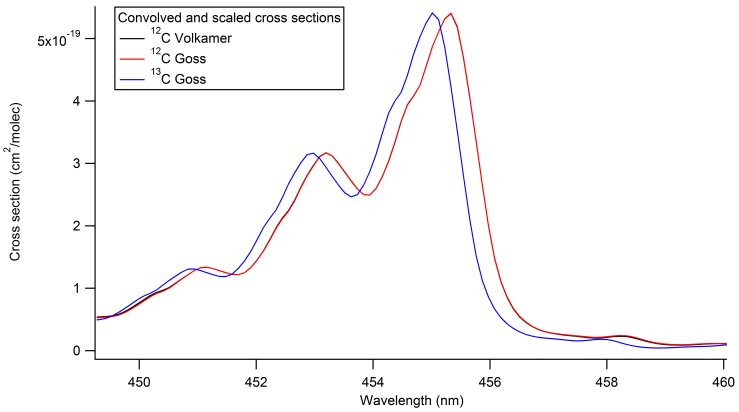

Figure 3.3: ^{12}C (red) and ^{13}C (blue) cross sections convolved with the spectrometer line function (Gaussian, 0.55 nm FWHM). At this lower resolution, the shift at the 455 nm peak is still very visible and the lack of shift at 440 nm is apparent.

3.2.3.2 Generation of the high-concentration NO_2 cross section

Two NO_2 cross sections were used in the WinDOAS fit to improve the quality of the fitting procedure at high NO2 concentrations. Above a few ppb, the NO_2 is no longer a weak absorber and it decreases the photon path length. This affects the shape of the absorber as seen by the detector and requires a second cross section with a slightly different shape to account for the NO_2 absorption.

The low concentration cross section is the standard (Vandaele et al., 2002) cross section scaled as described in (Thalman and Volkamer, 2010). In the absence of absorbers, the cavity path length is calculated as:

$$L_{eff}(\lambda) = \frac{d_0}{1 - R(\lambda) + \epsilon Ray(\lambda) d_0} \tag{3.1}$$

where $L_{eff}(\lambda)$ is the effective path length in the cavity as a function of wavelength, d_0 is the full length of the cavity (the mirror-to-mirror distance), $R(\lambda)$ is the mirror reflectivity as a function of wavelength, and $\epsilon Ray(\lambda)$ is the Rayleigh scattering cross section as a function of wavelength. Thus the effective path length is dependent especially on the mirror reflectivity (the higher the reflectivity, the longer the path length because the light makes more passes within the cavity) and Rayleigh scattering by molecules. This has a λ^{-4} dependence, so it is much more important at longer wavelengths. Mie scattering by molecules is not applicable in this context because of the 0.2 μm filter that removed aerosols prior to the sample flow entering the cavity. Because photons travel a different number of passes at different wavelengths, the absorption shape observed by the detector is slightly different than the unscaled absorption cross section. The detector sees higher absorbance at longer path lengths because the photons have traversed through the cavity more times. To account for this, the cross section is scaled as done in Thalman and Volkamer (2010):

$$F(\lambda) = \frac{L_{eff}(\lambda)}{L_{eff}(peak\lambda of absorption)} \tag{3.2}$$

where $L_{eff}(peak\lambda of absorption)$ is the path length at the peak absorption wavelength, determined independently for both the glyoxal and O_4 windows.

The high concentration cross section used a different scaling factor to account for light attenuation due to NO_2 absorption. In the limit that NO_2 is no longer a weak absorber, the cavity path length is calculated as:

$$L_{eff}(\lambda) = \frac{d_0}{1 - R(\lambda) + \epsilon Ray(\lambda) d_0 + \sigma NO_2(\lambda) d_s c_{NO_2}} \tag{3.3}$$

where $\sigma NO_2(\lambda)$ is the NO_2 molecular cross section, d_s is the sample gas path length (the distance from the sample inlet to the sample outlet), and c_{NO_2} is the NO_2 concentration in molecules/cm^3, typically chosen to be 20 ppbv. This accounts for the decrease in path length due to NO_2 absorption. The NO_2 cross section is then scaled to the shortened path length from Eq. 3.3 using equation 3.2. Adding in this cross section results in a lower, more statistical residual compared to a fit using just one low NO_2 cross section.

3.2.3.3 Slant column density and conversion to concentration

The primary output of WinDOAS is slant column density, or $SCD = l \times c$ where l is the path length in centimeters and c is the concentration in molecules cm^{-3}. This can be converted to unitless optical density by multiplying by the molecular cross section σ in cm^2 molecule^{-1}, or can be converted to concentration by dividing by the path length.

In order to obtain concentration measurements from the CE-DOAS data, we use O_4 which is a collision-induced absorption signal from oxygen. O_4 has a known cross section (Thalman and Volkamer, 2013) and its concentration depends solely on the oxygen mixing ratio and the ambient pressure. Therefore, since O_2 has a known mixing ratio in air of exactly 20.946 % and pressure inside the cavity is measured, we can calculate the O_4 concentration and from the slant column density we can obtain the path length for the O_4 window.

Because the light path is wavelength-dependent (see Equation 3.1), the path lengths in the glyoxal fit window and the O_4 fit window are different. The measured NO_2 signal from these

experiments is used to scale the path length determined from the O_4 window to the glyoxal window. This is possible due to the large wavelength range covered by the NO_2 absorption cross section, which spans both fitting windows. Since we know the NO_2 slant column density in the O_4 window, we can calculate the NO_2 concentration with the path length for the O_4 window. Since the NO_2 concentration is not a function of wavelength, the concentration in the O_4 window must be the same as the concentration in the glyoxal window. Thus we know the concentration of NO_2 in the glyoxal window, and from the NO_2 slant column density, we can calculate the path length in the glyoxal window. Then we can calculate the glyoxal concentration using the path length in the glyoxal window.

3.2.3.4 Wavelength stability tests

The standard glyoxal analysis window in WinDOAS is 438-465 nm. This region encompasses the strong band with a peak at nominally 455 nm and the weaker band at nominally 440 nm, thus including the region where there is a shift between the two glyoxal isotopes. In this full window, we expect to be able to differentiate between the two isotopes due to this shift. In order to identify narrower wavelength regions that can still differentiate between ^{13}C and ^{12}C glyoxal, a series of sensitivity tests were performed by changing the starting and ending wavelength of the glyoxal window.

The lower wavelength varied from 438 to 462.5 nm and the upper wavelength varied from 440.5 to 465 nm. Thus the width of the window varied from 2.5 nm to 27 nm. Two spectra were analyzed to identify regions where the glyoxal fit is stable for simultaneous detection of both ^{12}C and ^{13}C glyoxal. The two spectra were taken during Exp 15 and Exp 17 (one from each experiment)and selected as described above in Section 3.2.1. This analysis was done for both cross sections which had been convoluted with the instrument lineshape, and for cross sections which had been convoluted with the instrument lineshape and then orthogonalized (see Section 3.2.4).

3.2.4 Cross Section Orthogonalization

Orthogonalization is a mathematical process that identifies which parts of the vector basis set are identical and which parts are unique to each vector. It then creates a new, orthogonal basis set that contains the original initial vector and then only those components of additional vectors that are unique to those vectors. In the case of orthogonalizing two cross sections, the vectors are considered to be the two original cross sections and orthogonolization identifies those peaks that are unique to the second cross section.

Orthogonalization of the convolved cross sections was done internally in WinDOAS which uses Gram-Schmidt orthogonalization (Fayt and van Roozendael, 2001). This is a method of creating orthogonal vectors by subtracting the contribution of the first vector from subsequent vectors and then subtracting the contribution of the second vector from subsequent vectors, etc (Wong, 1935). The initial basis set is made up of vectors A_1 through A_n, where

$A_i = (a_{i1}, , a_{in})$

The normalized basis set is made up of vectors B_1 through B_n where

$B_i = (b_{i1}, , b_{in})$

The normalized basis set is created in the following manner (Wong, 1935):

$$B_1 = A_1 \tag{3.4}$$

$$B_2 = A_2 - \frac{A_2, B_1}{n(B_1)} B_1 \tag{3.5}$$

In this case, the initial basis set is the 12C and 13C cross sections. B_1 is the cross section for the isotope of glyoxal that is expected to be observed in the experiment, i.e. for Experiment 15, B_1 is the ^{12}C glyoxal cross section and for Experiment 17, B_1 is the ^{13}C glyoxal cross section. The other cross section, B_2, is where the two cross sections differ and contains the most information in the 455 nm region.

3.3 Results and Discussion

3.3.1 Proof of glyoxal detection

Spectral proof of detection in two spectra, one from Exp. 15 and one from Exp. 17, are shown in Figure 3.4, in panels A and B respectively. The top row shows the residual RMS for the fit, which is a measure of the quality of the DOAS fitting procedure. For both spectra is quite statistical, contains no obvious structure, and the values of 2.5×10^{-4} are very good for this instrument and spectrometer combination. This means that the absorbers fitted in these windows can explain the entire absorbance in the spectrum.

The second row shows the amount of ^{12}C glyoxal detected in each spectrum. The amount of ^{12}C glyoxal in the chamber background prior to Exp 15 is significantly higher than in Exp 17, as expected, since prior to Exp 15 only ^{12}C glyoxal had been used in the chamber while ^{13}C glyoxal had been used in the experiment immediately prior to Exp 17. There is a small amount of glyoxal detected in the spectrum from Exp 17. This is likely real and due to the large amount of ^{12}C glyoxal that had partitioned to the chamber walls during Exp 0 – Exp 15.

The third row shows the amount of ^{13}C glyoxal detected in each spectrum. As expected, only the spectrum from Exp 17 contains ^{13}C glyoxal. The fit for Exp 15 is slightly negative, but is not significant within the 3σ limit determined in (Goss et al., 2015). The fourth row shows the NO_2 fit as the sum of the low and high concentration fits. There is clearly background NO_2 in both spectra and it does not interfere with the glyoxal fit.

3.3.2 Results of orthogonalization and wavelength stability sensitivity studies

In order to better identify regions where the cross sections differ, the high resolution cross sections were orthogonalized in Igor using the math described above. The ^{13}C cross section was orthogonalized to the ^{12}C cross section using the following equations:

$A_i = (^{12}C, ^{13}C)$

and

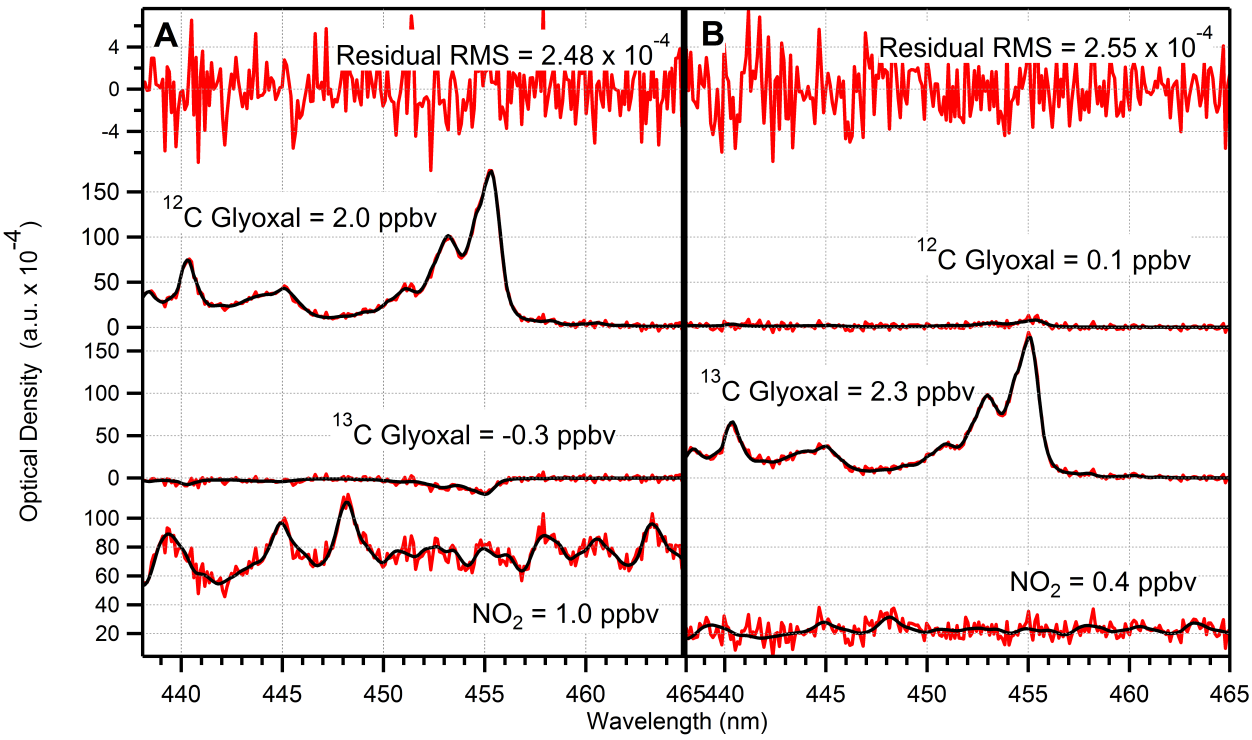

Figure 3.4: Spectral proof of ^{12}C and ^{13}C glyoxal detection. Spectrum from Exp. 15 (^{12}C experiment) is shown in panel A and spectrum from Exp. 17 (^{13}C experiment) is shown in panel B. Fits for dominant trace absorbers, glyoxal and NO_2, are shown along with the residual.

B_i = normalized cross sections and using equations 3.4 and 3.5 from Section 3.2.4,

$$B_1 = {}^{12}C \tag{3.6}$$

$$B_2 = {}^{13}C - \frac{{}^{13}C,{}^{12}C}{{}^{12}C,{}^{12}C}({}^{12}C) \tag{3.7}$$

This cross section is shown in Figure 3.5 in red. The cross section is largest at 455 nm, indicating that the most information in orthogonalization is found there. This is consistent with the two cross sections because they are the most shifted at 455 nm. Below about 440 nm, where the cross sections show essentially no shift, the orthogonal cross section is essentially noise. A similar calculation was done to orthogonalize the ^{12}C cross section to the ^{13}C cross section. This is shown in Figure 3.5 in blue. These two are inverses because with a two vector basis set, the ^{13}C orthogonalized to ^{12}C is essentially the ^{12}C cross section subtracted from the ^{13}C cross section and vice versa for ^{12}C orthogonalized to ^{13}C. Thus the two cross sections are opposites, as reflected in Figure 3.5.

The effect of instrument resolution on the shape of the orthogonalized cross section is shown in Figure 3.6 and described in Table 3.1. As the resolution decreases, spectral features are lost and the main peaks at 455 and 455.5 nm broaden and flatten. This is shown in Figure 3.6, where the high resolution orthogonal cross section is convolved to several different Gaussian line functions. The difference between the maximum cross section value and minimum cross section value are given in Table 3.1, along with the wavelength difference between the maximum and minimum cross section values. Despite the broadening and flattening, there is still structure in the orthogonal cross section even at 2.0 nm FWHM resolution. This suggests that even at this quite low resolution, ^{12}C and ^{13}C glyoxal may still be able to be measured simultaneously.

Fits to the same two spectra using orthogonalization instead of two different cross sections are shown in Figure 3.7. The fits shown in Figure 3.7 have very low slant column densities for the orthogonal cross sections. This indicates that very little of the absorbance in the spectrum from glyoxal is different from the expected form of glyoxal. The slant column densities of the orthogonal

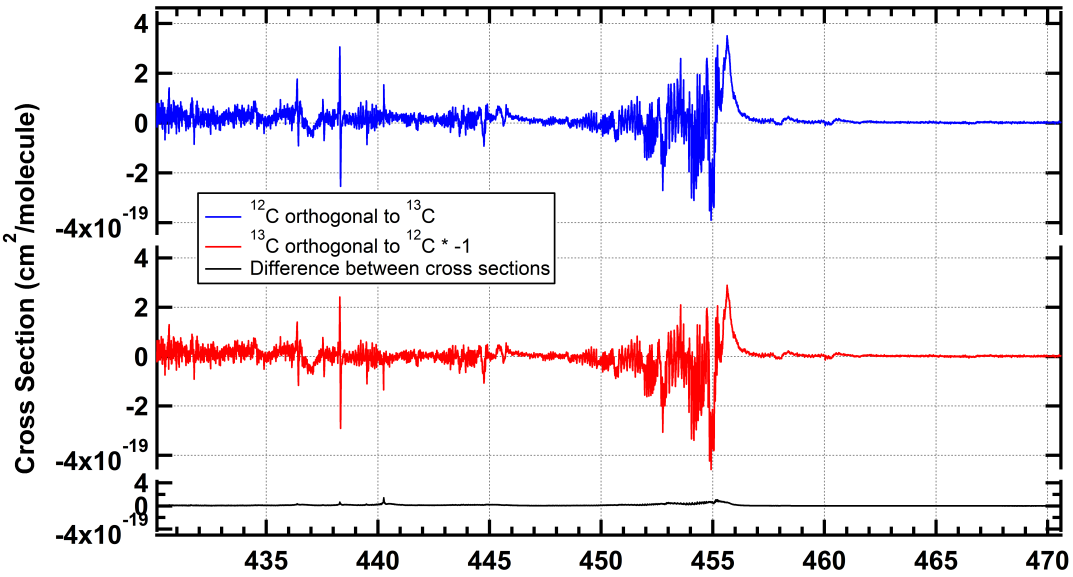

Figure 3.5: Isotopic cross sections orthogonalized to each other using Gram-Schmidt orthogonalization. ^{12}C orthogonalized to ^{13}C shown in blue; ^{13}C orthogonalized to ^{12}C shown in red (multiplied by -1 to better compare the shape of the two cross sections); difference between the blue and red lines shown in black.

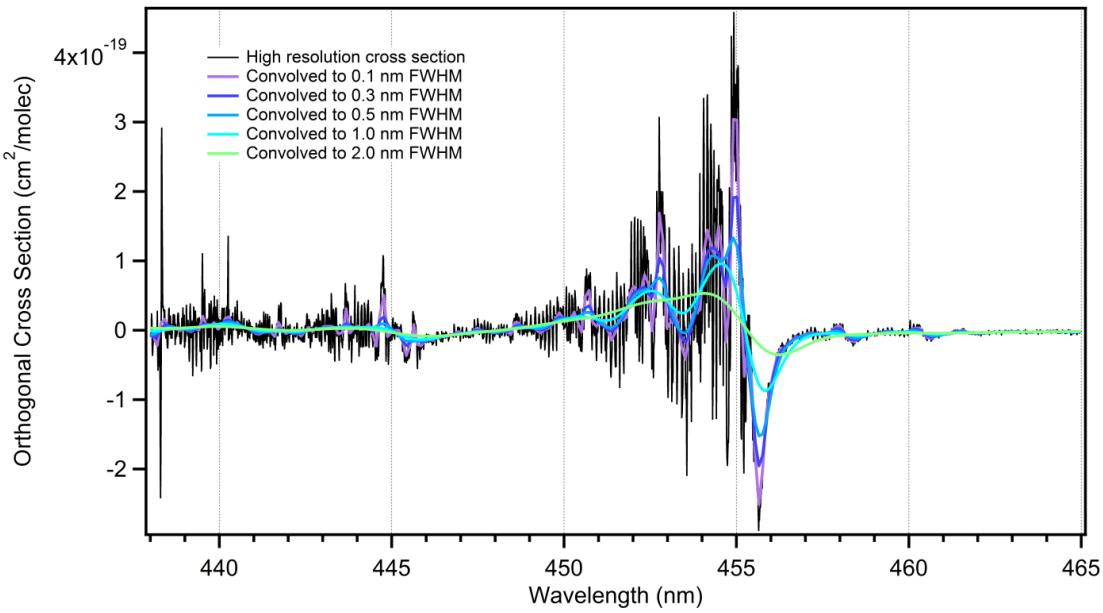

Figure 3.6: Effect of instrument resolution on shape of orthogonal cross section. As the simulated instrument resolution decreases, the peaks in the orthogonal cross section broaden and flatten. Black: unconvolved high resolution cross section. Purple: convolved to 0.1 nm FWHM. Dark blue: convolved to 0.3 nm FWHM. Medium blue: convolved to 0.5 nm FWHM. Turquoise: convolved to 1.0 nm FWHM. Green: convolved to 2.0 nm FWHM.

Resolution	Δ xs (cm^2/molecule	$\Delta\lambda$ (nm)
High Resolution	7.46×10^{-19}	0.719
0.1 nm FWHM	5.55×10^{-19}	0.747
0.3 nm FWHM	3.87×10^{-19}	0.640
0.5 nm FWHM	2.85×10^{-19}	0.747
1.0 nm FWHM	1.83×10^{-19}	1.282
2.0 nm FWHM	8.83×10^{-20}	2.242

Table 3.1: Effect of decreasing instrument resolution on orthogonal cross section. As the resolution decreases, the magnitude of the differential cross section (max value minus minimum value) decreases and the width (wavelength difference between maximum and minimum cross section value) increases.

cross sections are not different from zero using the 3σ criterion. This is consistent with the results from fitting both ^{12}C and ^{13}C glyoxal, which also indicates that the only statistically significant form of glyoxal present in each spectrum is the expected form. The slightly negative fit of the orthogonal cross section in Exp 15 is expected based on the Gram-Schmidt method. Thus we can selectively detect glyoxal isotopes and the presence of NO_2 does not impact that detection.

In order to identify regions where we can selectively detect glyoxal isotopes, we performed a series of sensitivity studies by changing the width of the analysis window (see Section 3.2.3.4). The results of these tests are shown in Figure 3.8. The top row of Figure 3.8 shows the percent difference between the slant column density output and the slant column density output in the standard glyoxal window (438-465 nm). Since the true glyoxal slant column is not known, the fit in the standard window is taken to be the "true" value since the width of this window and other parameters were determined after significant testing (Thalman and Volkamer, 2010). Panel A is for ^{12}C glyoxal and panel B is for ^{13}C glyoxal orthogonalized to ^{12}C glyoxal. Because there is significant glyoxal, the 12C fit is stable over a wide range of window widths. The most stable region for the orthogonalized ^{13}C is around 455 nm, where the cross section contains the most information. Outside of this region, the fit varies widely. A similar trend is seen for Experiment 17. Panel D is the ^{13}C cross section and panel C is the ^{12}C cross section orthogonalized to the ^{13}C cross section. Here the ^{13}C cross section is stable over a number of different wavelength windows and the orthogonalized cross section is again stable only in windows that contain the 455 nm band

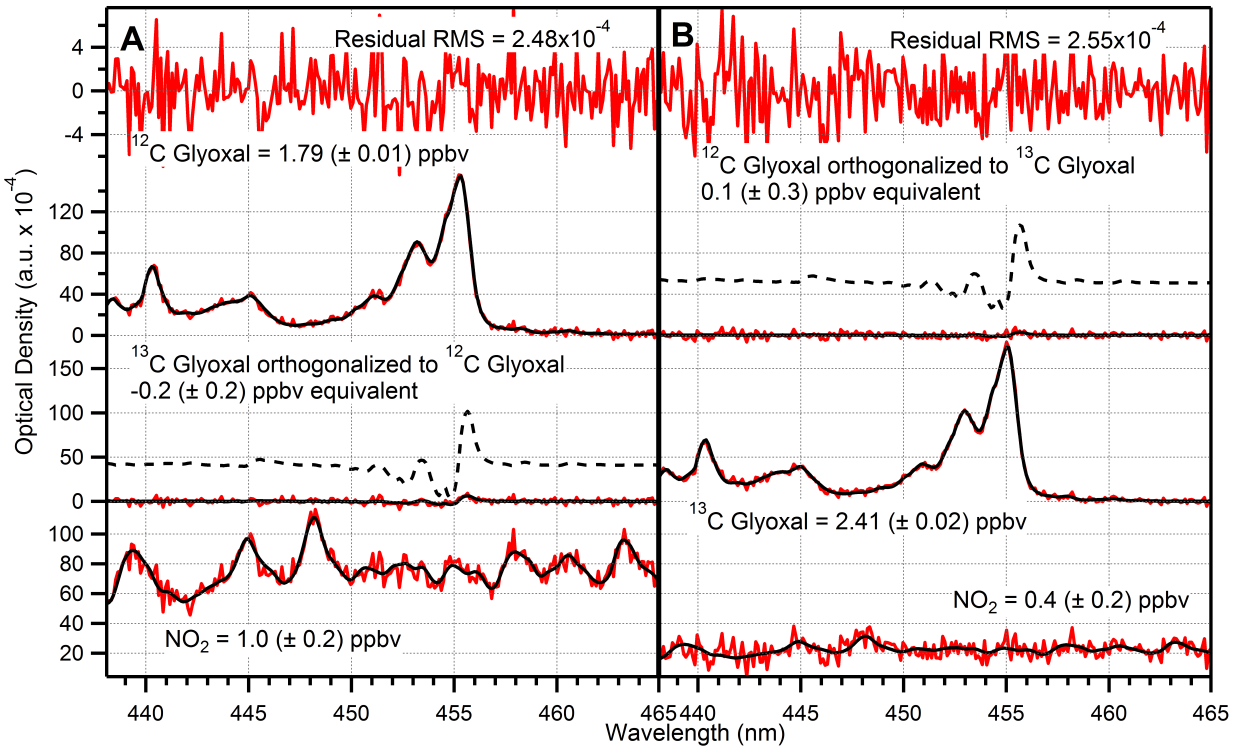

Figure 3.7: Spectral proof of ^{12}C and ^{13}C glyoxal detection using orthogonalized cross sections. As in Fig. 3.4, panel A is for Exp. 15 and panel B is for Exp. 17. The top row shows the RMS from the fit. The second row shows the ^{12}C fit (Exp. 15) and ^{12}C orthognalized to ^{13}C (Exp. 17). The third row shows the ^{13}C cross section orthogonalized to ^{12}C (Exp. 15) or the ^{13}C cross section (Exp. 17). The bottom row is NO_2. Dashed lines are the orthogonal cross section expanded and offset to show detail.

and is widely variable outside of this region.

3.3.3 Time series including orthogonalization

Two analyses were run for each of Exp. 15 and Exp. 17 that varied the orthogonal cross section. One analysis orthogonalized ^{13}C to ^{12}C glyoxal, and the other orthogonalized ^{12}C to ^{13}C glyoxal. Results are shown in Figure 3.9. For each analysis, the most meaningful fit is found for the isotope expected to be present in the experiment. For Exp. 15, when ^{13}C is orthogonalized to ^{12}C, the orthogonal result (turquoise) has a slant column of approximately zero, while the ^{12}C fit (blue) has a meaningful value that is representative of the amount of glyoxal in the chamber. When ^{12}C is orthogonalized to ^{13}C, the orthogonal cross section (dark green, now representing ^{12}C) shows a meaningful time trace. However, the ^{13}C cross section (bright green) shows a time series nearly identical to the dark blue line. This output is meaningless because there is no ^{13}C glyoxal in the chamber. The reverse is true for Exp 17: the most meaningful information is found in the ^{13}C fit, and the ^{12}C fit when ^{13}C is orthogonalized to ^{12}C is meaningless. Therefore, the most meaningful analysis occurs when the less prevalent isotope is orthogonalized to the more prevalent isotope.

3.4 Conclusions and Outlook

For the first time, we have applied isotopic measurements of glyoxal to CE-DOAS data from laboratory measurements. We find that the shift between the two cross sections is sufficiently resolved even at instrument line functions of 0.55 nm FWHM that we are able to quantify both species from a DOAS retrieval without detecting a false positive signal from the other isotope. We have additionally created an orthogonal cross section that contains only the information where the two cross sections differ and we are successfully able to fit this to the experimental data. Through a series of sensitivity studies we have determined that the simultaneous fit of both an orthogonalized and non-orthogonalized cross section is most stable when the fit region contains the strong peak at 455 nm where the shift is strongest. The simultaneous retrieval of both isotopes opens up the ability to use ^{13}C-labeled glyoxal as a tracer for mechanistic studies.

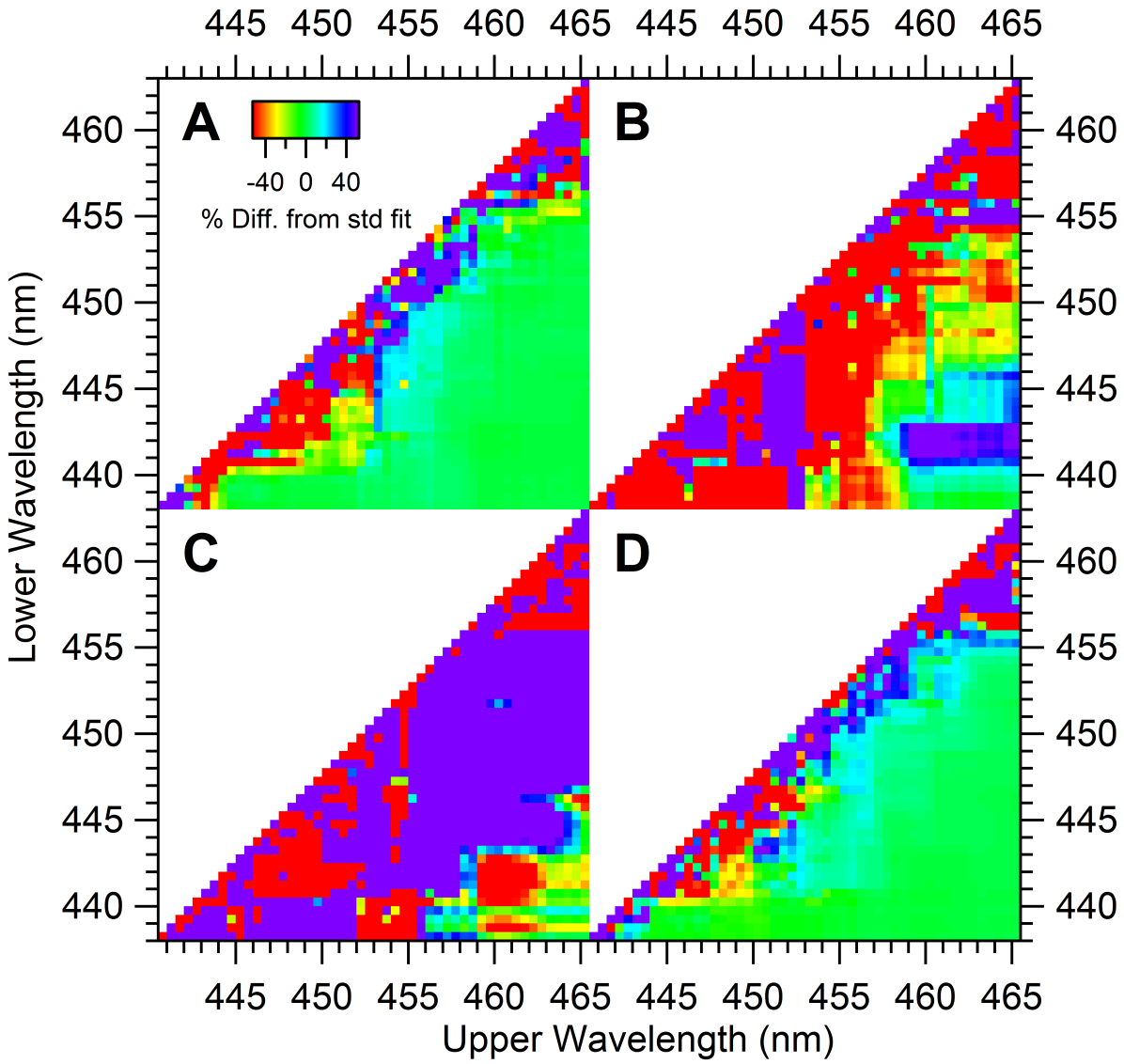

Figure 3.8: Stability of glyoxal retrieval in fit windows of varying sizes. Top row: Exp. 15 (^{12}C experiment). Bottom row: Exp. 17 (^{13}C experiment). Panel A: ^{12}C fit. Panel B: ^{13}C orthogonalized to ^{12}C. Panel D: ^{13}C fit. Panel C: ^{12}C orthogonalized to ^{13}C. Color code: Percent difference from standard fit in glyoxal window over wavelength range 438-465 nm.

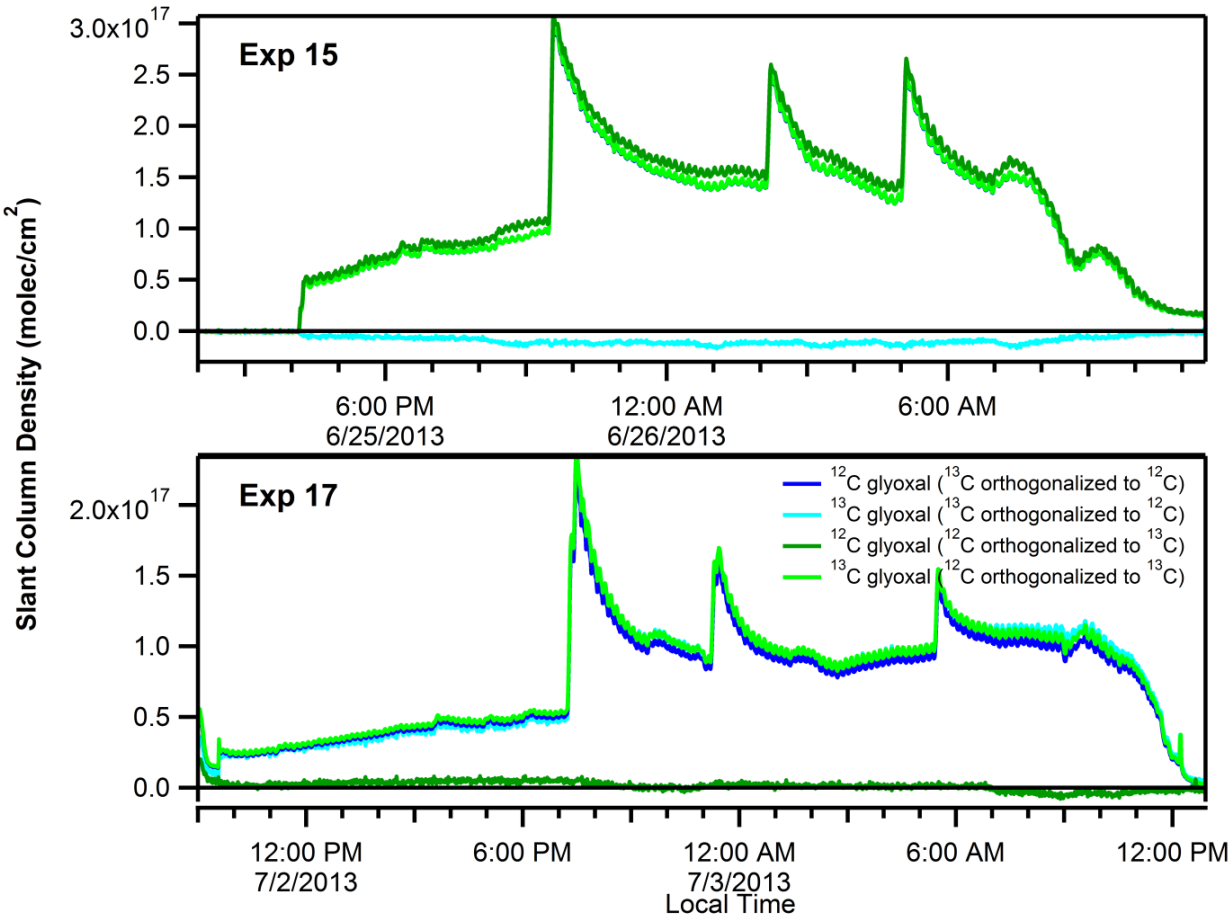

Figure 3.9: Time series for Exp. 15 (top) and Exp. 17 (bottom) varying orthogonalization criteria.

Chapter 4

Setschenow Salting Constants of Glyoxal and Methyl Glyoxal in Sulfate, Nitrate and Chloride Salts: Implications for Secondary Organic Aerosol Formation in the Southeastern United States

Setschenow salting-constants, K_S, describe the exponential dependence of the gas- / aqueous phase partitioning (Henry's Law constant) on the salt concentration. Knowledge about K_S is of particular importance to predict secondary organic aerosol (SOA) formation from soluble species in aerosol water, where the salt concentrations are typically very high. We have measured K_S of glyoxal and methyl glyoxal using (1) Solid Phase Micro Extraction / Gas Chromatography (SPME/GC), and (2) Atmospheric Pressure Inlet / Ion Trap Mass Spectrometry (API-ITMS), and find that glyoxal 'salts in' (negative K_S), while methyl glyoxal 'salts out' in a range of atmospherically relevant salts. K_S values are found to be -0.16, -0.06, -0.065, -0.1 for glyoxal and +0.16, +0.075, +0.02, +0.06 for methyl glyoxal in $(NH_4)_2SO_4$, NH_4NO_3, $NaNO_3$ and NaCl, respectively. Additionally, we find that a mixture of $(NH_4)_2SO_4$ and NH_4NO_3 is additive. The incorporation of salting constants into Community Multi-scale Air Quality Model (CMAQ) predicts a strong effect from sulfate and nitrate over the continental US. While methyl glyoxal is about 3 times more abundant than glyoxal in the gas phase at the SOAS site located in Centreville, AL, the glyoxal concentration in aerosol water is consistently higher, i.e., 2 times higher if K_S for both species is set to zero, or 16 times higher if the measured K_S values of sulfate and nitrate are incorporated in the model. Atmospheric implications for the partitioning of other relevant SOA precursor molecules (e.g., isoprene epoxide) are discussed.

4.1 Introduction

Secondary organic aerosol (SOA) formation from small, water-soluble molecules has become a topic of recent interest (Hastings et al., 2005; Volkamer et al., 2009; De Haan et al., 2009b,a; Shapiro et al., 2009; De Haan et al., 2010; Ervens and Volkamer, 2010; Sareen et al., 2010; Kampf et al., 2013; Waxman et al., 2013; Hawkins et al., 2014). Current studies have focused on the aqueous-phase processing of these species or modeling the uptake and further SOA formation from aqueous and multi-phase reactions. However, aside from some studies on product formation from the reaction between aldehydes and ammonium, little work has been done on studying the interaction of organics with inorganic species in the aerosol. The presence of inorganic species in aerosols can modify the partitioning of organic species between the aqueous and gas phases. This interaction is characterized by the Setschenow constant (Setschenow, 1889), which quantifies the change in partitioning as a function of salt concentration. If the partitioning shifts away from the aqueous phase (towards the gas phase), the molecule has a positive Setschenow constant and it salts out of the aerosol. Conversely, if it favors the aqueous phase, it has a negative Setschenow constant and it salts in. Setschenow constants are defined as (Setschenow, 1889; Wang et al., 2014a):

$$log\left(\frac{S_0}{S}\right) = K_S C \tag{4.1}$$

where S_0 is the solubility of the organic species in pure water, S is the solubility of the organic species in a salt solution of concentration C, and K_S is the Setschenow or salting constant.

Henry's law is

$$K_H = \frac{C_{org}}{p_{org}} \tag{4.2}$$

where C_{org} is the aqueous-phase concentration of the organic species and p_{org} is the vapor pressure of the organic species. The Setschenow equation can then be rewritten as:

$$log\left(\frac{K_{H,w}}{K_{H,salt}}\right) = K_S C \tag{4.3}$$

where $K_{H,w}$ is the Henry's law constant of the organic species in pure water and $K_{H,salt}$ is the Henry's law constant of the organic species in salt concentration C. Expanding the Setschenow

equation to include the explicit definition of Henry's law, this can be written as:

$$log\left(\frac{\frac{C_w}{p_w}}{\frac{C_{salt}}{p_{salt}}}\right) = K_S C \tag{4.4}$$

where C_w is the concentration of the organic species in pure water, p_w is the vapor pressure of the organic species over that solution, C_{salt} is the concentration of the organic species in the salt solution with concentration C and p_{salt} is the vapor pressure of the organic species over that salt solution.

Setschenow constants can thus be used to describe the change in Henry's law as a function of salt concentration. This is important not only for understanding the partitioning of aqueous SOA building blocks to the aerosol, but also for understanding the reaction rate constants. Bulk reaction rate constants include the Henry's law constant (Finlayson-Pitts and Pitts, 1999):

$$k_{bulk} = \frac{4K_H RT}{u_{av}}\sqrt{D_l k} \tag{4.5}$$

where k_{bulk} is the bulk-phase reaction rate constant, K_H is the Henry's law constant, R is the gas constant, T is the temperature, u_{av} is the average molecular speed in the gas phase, D_l is the liquid-phase diffusion constant and k is the first order reaction rate constant. Thus knowing the Setschenow constant allows one to accurately calculate the bulk reaction rate constant for building block species.

Very few measurements of Setschenow constants have been made for aqueous aerosol precursor species. One measurement has been made for glyoxal: Kampf et al. (2013) found that in a series of chamber studies, glyoxal salted in to ammonium sulfate and ammonium sulfate/fulvic acid aerosols. Calculations showed that this is due to the strong interactions between glyoxal monohydrate and glyoxal dihydrate with sulfate (Kurtén et al., 2015). However, most work on salting constants focuses on molecules that are not likely aqueous SOA precursors (such as benzene, toluene, and xylenes) (Gordon and Thorne, 1967a,b; Endo et al., 2012; Kurtén et al., 2015; Wang et al., 2014a; Sander, 2015).

Isoprene is the most important biogenic emission species and is a precursor for a number of small, water-soluble molecules including glyoxal, methyl glyoxal, and IEPOX (Fu et al., 2008;

Paulot et al., 2009). These species can form SOA through aqueous-phase reactions and thus salting is very important for their partitioning. Here, we use the Community Multi-scale Air Quality (CMAQ) model to predict gas-phase glyoxal, methyl glyoxal, and isoprene epoxides (IEPOX) as well as salt concentrations in the aerosols. The partitioning of these species to the aerosol phase and the impact of salting on SOA formation from these species is then discussed.

4.2 Experimental

4.2.1 Salting Constant Measurements

Salting constant measurements for glyoxal and methyl glyoxal were performed using two different sets of instrumentation: a novel inlet coupled with a quadrupole ion trap mass spectrometer (ITMS measurements), and gas chromatography (GC-FID measurements). Since salting constant values for these species are previously unreported, the intercomparison between the two methods serves as method validation.

For both sets of measurements, 10.00 mL solutions of 0.1 M methyl glyoxal (40% w/w solution, Sigma Aldrich) or 0.2 M glyoxal (40% w/w solution, Sigma Aldrich) were prepared in 18 M water (Millipore). Solution concentrations were chosen to minimize oligomerization but give sufficient gas-phase signal. In addition to glyoxal or methyl glyoxal, the solutions also contained 0, 0.5, 1.0, 1.5, 2.0., or 3.0 molar salt (ammonium sulfate, ammonium nitrate, sodium nitrate, or sodium chloride, all Sigma Aldrich) or 0.075 molar and 0.15 molar (sodium oxalate; limited by solubility). Sodium oxalate solutions were monitored for pH to ensure that the oxalate was in the $C_2O_4^{2-}$ form rather than $HC_2O_4^-$. We additionally did one set of glyoxal measurements at 1.5 M ammonium sulfate plus 1.5 M ammonium nitrate to determine the effect of mixing salts. All measurements were performed at room temperature (22 $\pm$ 2°C). A list of experimental conditions and number of repeats are listed in Table 4.1.

Table 4.1: Experimental conditions for salting constant measurements of glyoxal and methyl glyoxal.

Salt	Conc. (M)	Conc. (M)	n^a	$C_{(org)}$ (M)^b	P_{org} (atm)^c	$K_{H,eff}$ (M/atm)	T (°C)
Glyoxal (GC-FID)							
$(NH_4)_2SO_4$	0	0	6	0.2	4.8×10^{-7}	4.2×10^{5}	22 ± 2
	1.5	1.64	6	0.2	3.1×10^{-7}	6.4×10^{5}	22 ± 2
	3	3.83	6	0.2	1.2×10^{-7}	17×10^{5}	22 ± 2
NH_4NO_3	0	0	6	0.2	4.8×10^{-7}	4.2×10^{5}	22 ± 2
	1.5	1.66	6	0.2	4.5×10^{-7}	4.4×10^{5}	22 ± 2
	3	3.45	6	0.2	3.0×10^{-7}	6.6×10^{5}	22 ± 2
$NaNO_3$	0	0	5	0.2	4.8×10^{-7}	4.2×10^{5}	22 ± 2
	1.5	1.65	5	0.2	3.9×10^{-7}	5.1×10^{5}	22 ± 2
	3	3.34	5	0.2	2.9×10^{-7}	6.9×10^{5}	22 ± 2
$NaCl$	0	0	6	0.2	4.8×10^{-7}	4.2×10^{5}	22 ± 2
	1.5	1.55	6	0.2	2.9×10^{-7}	6.9×10^{5}	22 ± 2
	3	3.18	6	0.2	2.4×10^{-7}	8.5×10^{5}	22 ± 2
Methyl Glyoxal (GC-FID)							
$(NH_4)_2SO_4$	0	0	3	0.1	3.1×10^{-6}	3.2×10^{4}	22 ± 2
	0.5	0.52	3	0.1	5.1×10^{-6}	2.0×10^{4}	22 ± 2
	1	1.07	3	0.1	5.2×10^{-6}	1.9×10^{4}	22 ± 2
	1.5	1.67	3	0.1	7.3×10^{-6}	1.4×10^{4}	22 ± 2
	2	2.31	3	0.1	7.9×10^{-6}	1.3×10^{4}	22 ± 2
NH_4NO_3	0	0	3	0.1	3.1×10^{-6}	3.2×10^{4}	22 ± 2
	0.5	0.51	3	0.1	3.7×10^{-6}	2.7×10^{4}	22 ± 2
	1	1.06	3	0.1	4.2×10^{-6}	2.4×10^{4}	22 ± 2
	1.5	1.66	3	0.1	5.9×10^{-6}	1.7×10^{4}	22 ± 2
	2	2.21	3	0.1	5.0×10^{-6}	2.0×10^{4}	22 ± 2
$NaNO_3$	0	0	3	0.1	3.1×10^{-6}	3.2×10^{4}	22 ± 2
	0.5	0.52	3	0.1	3.3×10^{-6}	3.0×10^{4}	22 ± 2
	1	1.03	3	0.1	3.7×10^{-6}	2.7×10^{4}	22 ± 2
	1.5	1.65	3	0.1	3.3×10^{-6}	3.0×10^{4}	22 ± 2
	2	2.19	3	0.1	3.5×10^{-6}	2.9×10^{4}	22 ± 2
$NaCl$	0	0	3	0.1	3.1×10^{-6}	3.2×10^{4}	22 ± 2
	0.5	0.5	3	0.1	3.4×10^{-6}	2.9×10^{4}	22 ± 2
	1	1	3	0.1	3.1×10^{-6}	3.3×10^{4}	22 ± 2
	1.5	1.53	3	0.1	3.7×10^{-6}	2.7×10^{4}	22 ± 2
	2	2.08	3	0.1	4.0×10^{-6}	2.5×10^{4}	22 ± 2
Methyl Glyoxal (ITMS)							
$(NH_4)_2SO_4$	0	0	3	0.1	3.1×10^{-6}	3.2×10^{4}	22 ± 2
	0.5	0.52	3	0.1	3.8×10^{-6}	2.7×10^{4}	22 ± 2
	1	1.07	3	0.1	4.5×10^{-6}	2.2×10^{4}	22 ± 2
	1.5	1.67	3	0.1	6.1×10^{-6}	1.6×10^{4}	22 ± 2
	2	2.31	3	0.1	6.6×10^{-6}	1.5×10^{4}	22 ± 2
NH_4NO_3	0	0	3	0.1	3.1×10^{-6}	3.2×10^{4}	22 ± 2
	0.5	0.51	3	0.1	3.5×10^{-6}	2.9×10^{4}	22 ± 2
	1	1.06	3	0.1	3.6×10^{-6}	2.8×10^{4}	22 ± 2
	1.5	1.66	3	0.1	3.2×10^{-6}	3.1×10^{4}	22 ± 2
	2	2.21	3	0.1	4.1×10^{-6}	2.4×10^{4}	22 ± 2
$NaNO_3$	0	0	3	0.1	3.1×10^{-6}	3.2×10^{4}	22 ± 2
	0.5	0.52	3	0.1	2.8×10^{-6}	3.6×10^{4}	22 ± 2
	1	1.03	3	0.1	3.0×10^{-6}	3.3×10^{4}	22 ± 2
	1.5	1.65	3	0.1	3.1×10^{-6}	3.2×10^{4}	22 ± 2
	2	2.19	3	0.1	3.4×10^{-6}	3.0×10^{4}	22 ± 2
$NaCl$	0	0	3	0.1	3.1×10^{-6}	3.2×10^{4}	22 ± 2
	0.5	0.5	3	0.1	3.3×10^{-6}	3.1×10^{4}	22 ± 2
	1	1	3	0.1	3.7×10^{-6}	2.7×10^{4}	22 ± 2
	1.5	1.53	3	0.1	4.2×10^{-6}	2.4×10^{4}	22 ± 2
	2	2.08	3	0.1	4.2×10^{-6}	2.4×10^{4}	22 ± 2

[a] number of repeat measurements performed
[b] calculated assuming 40% w/w solution
[c] calculated assuming $K_H = 4.2\times10^5$ M/atm for glyoxal and 3.2×10^4 M/atm for methyl glyoxal

4.2.1.1 Quadrupole Ion Trap Measurements

A novel atmospheric pressure inlet was developed for these measurements. A diagram of this inlet is shown in Figure 4.1, panel A. Solutions were added to a 10 mL graduated cylinder outfitted to connect to a 0.5 inch UltraTorr. The system in front of the ion trap was then pumped down to house vacuum pressures (nominally 45 Torr) to remove excess O_2 and N_2. The air in equilibrium with the solution leaked through the pinhole (0.0007 inches, O'Keefe Controls). This ensured that the system was in an effusion regime. The valve to the quadrupole ion trap mass spectrometer (Thermo-Finnigan LCQ) was then opened, letting the sample in via the gas chromatography port. Data was collected for thirty minute at which point signal in the mass spectrometer had stabilized (Figure 4.2). No change in solution volume was observed so there was no change in solution temperature due to evaporation.

A blank (18 MΩ water, Millipore) was run between each methyl glyoxal solution to determine the extent of background methyl glyoxal signal remaining in the ion trap. Signal was normalized to m/z 19 (H_3O^+, the strongest ion in the spectrum and not a methyl glyoxal fragment) to account for any variability in ion trap signal. The water spectrum immediately preceding a methyl glyoxal spectrum was then subtracted from the methyl glyoxal spectrum to remove any residual background methyl glyoxal, N_2, O_2, and instrument contaminants. A typical spectrum is shown in Figure 4.1, panel B. The standard NIST Electron Impact (EI) spectrum is shown in black on the top and the blank-corrected methyl glyoxal EI spectrum measured in this experiment is shown on the bottom in red. There is excellent agreement between the two spectra. The signal at m/z 32 and around m/z 16 and 18 are due to incomplete water and air subtraction, and the extra signal at m/z 58 is due to background contamination from the ion trap but overall this method does an excellent job of correcting for background signal. In this experiment, C_w and C_{salt} are the same (0.1 M methyl glyoxal or 0.2 M glyoxal), so this reduces to:

$$log\left(\frac{p_{salt}}{p_{water}}\right) = K_S C \tag{4.6}$$

Figure 4.1: A) Salting constant inlet for mass spectrometer. Solutions of known organic and salt concentration are added to graduated cylinder. System is pumped down to remove oxygen and nitrogen. Water and organics leak through the pinhole to create an effusion regime and then enter the mass spectrometer. B) Mass spectrometric proof of methyl glyoxal detection in EI mode. The standard NIST EI spectrum of methyl glyoxal is shown on the top in black and the spectrum recorded in the lab is shown on the bottom in red with air and water subtracted out. The very good agreement between the spectra is proof of methyl glyoxal detection. C) Schematic of SPME and GC-FID measurements. SPME fiber samples the headspace above the solution of organic and salt, and results in a two-peak chromatogram.

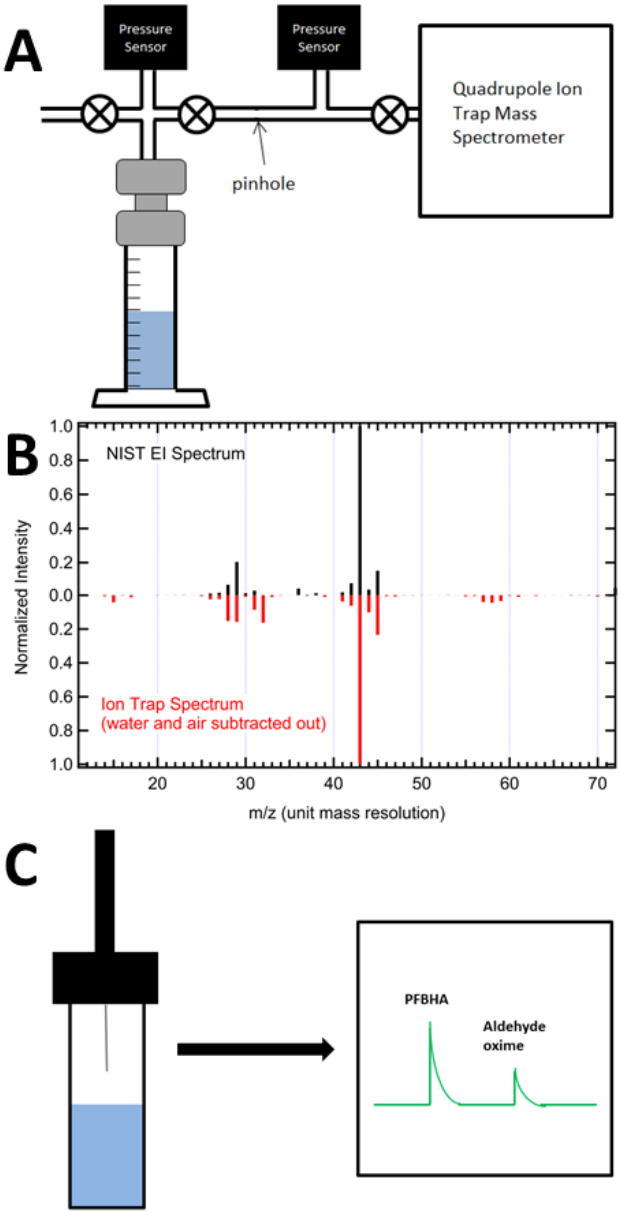

Figure 4.2: Ion trap signal from the methyl glyoxal fragment m/z 43 during typical runs. Black: 0.1 M methyl glyoxal in pure water; grey: 0.1 M methyl glyoxal in 2.0 M ammonium sulfate. Signal used to calculate constants was used from the last five minutes of data collection (to the right of the vertical black line).

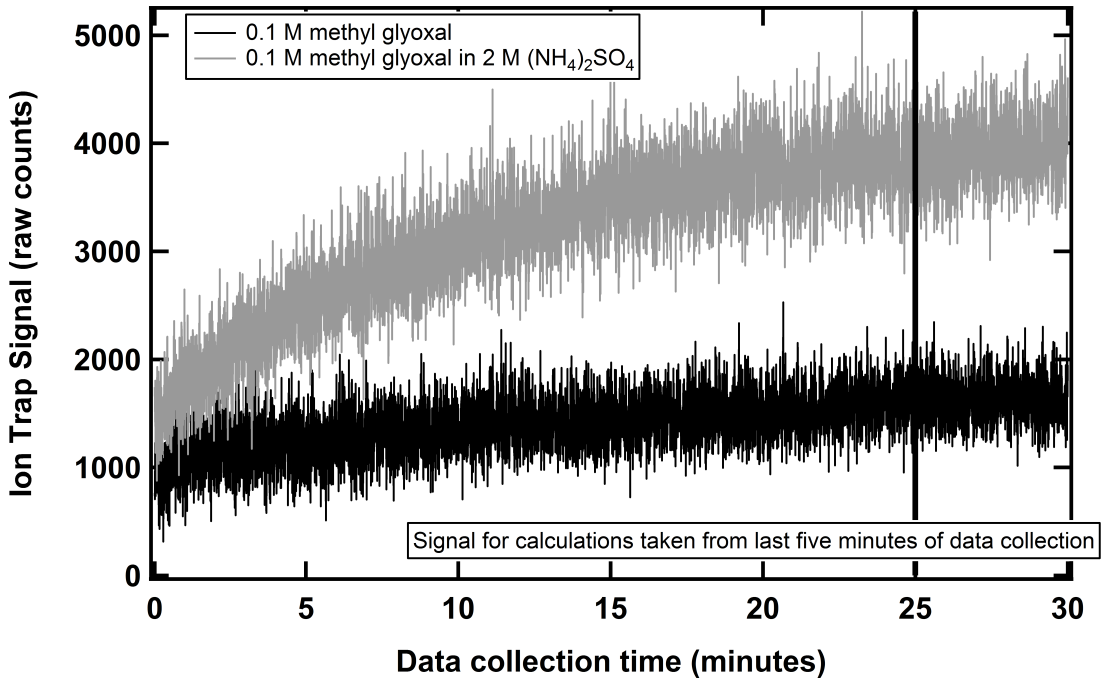

The signal from the ion trap is taken to be a proxy for the vapor pressure because only relative measurements (rather than absolute pressure measurements) are necessary. Thus the salting constants can be calculated solely from the ion trap signal. Typical ion trap signals are shown in Figure 4.2.

4.2.1.2 Gas Chromatography Measurements

Methyl glyoxal and glyoxal salting constant measurements were also made using gas chromatography with flame ionization detection. GC-FID instruments are most sensitive to reduced carbon and signal is proportional to the number of reduced carbons that volatilize from the column at a given time. Methyl glyoxal has one reduced carbon; glyoxal has none. Therefore, to increase the number of reduced carbons and thus the sensitivity of the GC, as well as lowering the vapor pressure of the molecules, both glyoxal and methyl glyoxal were derivatized with *O*-(2,3,4,5,6-Pentafluorobenzyl)hydroxylamine hydrochloride (PFBHA, Sigma Aldrich). This molecule reacts with carbonyl groups to form an oxime and adds seven reduced carbon atoms per carbonyl group.

Solutions were added to 22 mL Supelco vials with Mininert valves with septa. A schematic of this is shown in Figure 4.1, Panel C. Solutions were allowed to equilibrate for 45 minutes (at longer time scales, imidazoles were formed in ammonium sulfate/glyoxal solutions and the aqueous phase concentration of glyoxal could no longer be assumed to be the same as the initial concentration of glyoxal). A solid phase micro extraction (SPME) fiber (65 μm poly(dimethylsiloxane)/divinylbenzene, (PDMS/DVB) Supelco) was first exposed to the headspace above a continuously stirred 17 mg/mL solution of PFBHA for two minutes. The fiber was then exposed to the salting solution for one minute (methyl glyoxal) or fifteen minutes (glyoxal). The fiber was then injected in to the GC and measured immediately. The GC program was as follows: 40°C for 2 minutes, 10°C/min to 110°C, 5°C/min to 155°C, 10°C/min to 280°C, 280°C for 5 minutes. The inlet was held at 250°C. PFBHA was always measured in significant excess to the oxime products, indicating that the amount of oxime formed was limited by the amount of gas-phase glyoxal or methyl glyoxal, rather than the amount of PFBHA. Tests showed that after a run, all PFBHA and oxime products had been

volatilized off of the SPME fiber so no blanks were run between measurements. For analysis, peak areas were used as the proxy for p_w and p_{salt}.

4.2.2 CMAQ and Henry's law implementation

Regional-scale modeling was performed with the Community Multi-scale Air Quality Model (CMAQ, v5.0.1) (Foley et al., 2010). CMAQ accounts for advection, diffusion, gas-phase chemistry, aerosol-phase chemistry, and deposition. It was run over the continental United States for the dates of June 6-15, 2013 during the Southern Oxidant and Aerosol Study (SOAS). It was run using conditions similar to Pye et al. (2013), including with updated isoprene chemistry. This includes gas-phase formation of isoprene epoxide (IEPOX). ISORROPIA-II is used for calculating ion concentrations and aerosol water. To get particle-phase concentrations of glyoxal, methyl glyoxal, and IEPOX, the gas-phase concentrations were extracted from the model output and calculated based on Henry's law. CMAQ prescribes Henry's law constants of 3.6×10^5 M/atm for glyoxal, 3.2×10^4 M/atm for methyl glyoxal, and 2.7×10^6 M/atm for IEPOX (Pye et al., 2013). The value for IEPOX was calculated using the bond contribution method of HenryWin 3.1 (Meylan and Howard, 1991; Pye et al., 2013). This Henry's law value is consistent with the field observations reported by Pye et al. (2013). Salting is not treated in the standard CMAQ model, so this was incorporated using:

$$K_{H,salt} = K_H e^{K_S \times C_{salt}} \tag{4.7}$$

This was only done for salt concentrations less than 12 molal (Kampf et al., 2013). IEPOX was treated as salting out with the same salting constants as methyl glyoxal. For runs with mixed ammonium sulfate and ammonium nitrate, Henry's law values were calculated as:

$$K_{H,salt} = K_H e^{K_{S,AS} \times C_{AS} + K_{S,AN} \times C_{AN}} \tag{4.8}$$

Additionally, time-series data was extracted for gas-phase and particle-phase concentrations of all three species (both with and without salting) for two locations: Centreville, Alabama and downtown Los Angeles. All particle-phase results are based solely on gas-particle partitioning;

further aqueous-phase processing is not included.

CMAQ modeling results are for part of SOAS, which was a six-week field campaign that took place in Talladega National Forest between June 1 and July 15, 2013. The vegetation in this region predominantly emit isoprene and other terpenes. Therefore, high gas-phase concentrations of glyoxal, methyl glyoxal, and IEPOX are expected as these are all isoprene oxidation products (Paulot et al., 2009).

4.3 Results and Discussion

4.3.1 Salting Constant Measurements of Inorganic Ions

The results of the salting constant measurements are shown in Figure 4.3. Salting constants for ammonium sulfate ($(NH_4)_2SO_4$)are shown in panel A, ammonium nitrate (NH_4NO_3)in panel B, sodium nitrate ($NaNO_3$)in panel C, and sodium chloride (NaCl)in panel D. Methyl glyoxal ITMS measurements are shown with open circles in brighter colors. Fits to the ITMS data are designated with solid lines. Methyl glyoxal GC-FID measurements are shown in darker colors with open squares. Fits to the methyl glyoxal GC-FID measurements are given with dotted lines. Glyoxal GC-FID measurements are shown in darker colors with solid diamonds. Fits to the glyoxal data are given with dashed lines. The grey lines are the average of the slopes of the GC-FID and ITMS measurements for methyl glyoxal.

All salting constant values are presented in Table 4.2 in both molarity and molality. A subset is presented in Table 4.3, where the values of the methyl glyoxal ITMS and GC-FID values have been averaged along with the smallest, most water-soluble species measured in Wang et al. (2014a) and Endo et al. (2012) (converted to molality). Excellent agreement is observed between the ITMS measurements and the GC-FID measurements for all the salts, except for ammonium nitrate, where measurements only agree marginally within error. Generally the good agreement for other salts confirms that both methods gave consistent results.

Additionally, good agreement is observed between the glyoxal-ammonium sulfate salting con-

Figure 4.3: Salting constants for glyoxal (solid diamonds, dashed fit) and methyl glyoxal calculated from both ITMS data (open circles, solid fit) and GC-FID data (open squares, dotted fit). Solid grey lines: average of KS from ITMS and GC-FID data for methyl glyoxal. Excellent agreement is observed between both methyl glyoxal measurements except for NH_4NO_3. The positive slopes for methyl glyoxal indicate that it salts out. The negative slopes for glyoxal indicate that it salts in.

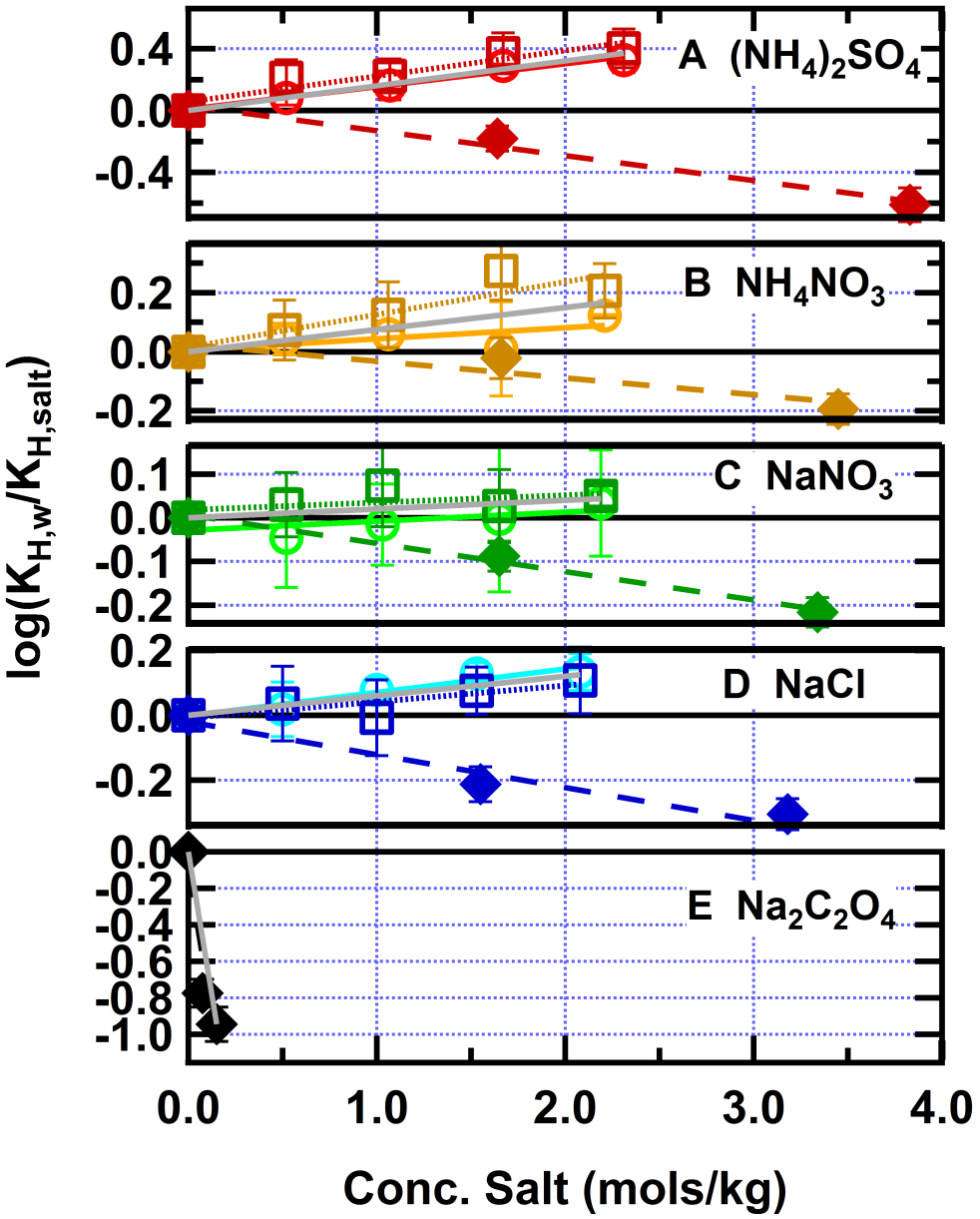

Table 4.2: All salting constants measured for glyoxal and methyl glyoxal, reported in both M^{-1} (molarity) and M^{-1} (molality).

	$(NH_4)_2SO_4$	NH_4NO_3	$NaNO_3$	NaCl	$Na_2C_2O_4$
Glyoxal	-0.20 ± 0.05 M^{-1}	-0.07 ± 0.03 M^{-1}	-0.072 ± 0.008 M^{-1}	-0.10 ± 0.02 M^{-1}	-6.3 M^{-1}
(GC-FID)	-0.16 ± 0.02 M^{-1}	-0.06 ± 0.02 M^{-1}	-0.065 ± 0.006 M^{-1}	-0.10 ± 0.02 M^{-1}	-6.3 M^{-1}
Methyl glyoxal	0.19 ± 0.03 M^{-1}	0.12 ± 0.03 M^{-1}	0.02 ± 0.02 M^{-1}	0.05 ± 0.02 M^{-1}	–
(GC-FID)	0.16 ± 0.03 M^{-1}	0.11 ± 0.03 M^{-1}	0.017 ± 0.015 M^{-1}	0.05 ± 0.02 M^{-1}	–
Methyl glyoxal	0.17 ± 0.01 M^{-1}	0.05 ± 0.03 M^{-1}	0.02 ± 0.02 M^{-1}	0.07 ± 0.02 M^{-1}	–
(IT-MS)	0.15 ± 0.01 M^{-1}	0.04 ± 0.02 M^{-1}	0.02 ± 0.02 M^{-1}	0.07 ± 0.01 M^{-1}	–

Table 4.3: Compilation of K_S values for small oxygenated species in ammonium sulfate and ammonium nitrate. Good agreement is observed between the literature value and the value measured in this work for glyoxal in ammonium sulfate despite the different salt regimes and different methods used for measuring the gas and aqueous phase concentrations. All species except for glyoxal are determined to salt out of solution. [a] Kampf et al. (2013) ES&T. [b] This work. [c] Wang et al. (2014) ES&T.

Molecule	**K_S $(NH_4)_2SO_4$**	**K_S NH_4NO_3**	**K_S $NaNO_3$**	**K_S NaCl**	**Reference**
Glyoxal	-0.24±0.02 M^{-1}	–	–	–	Kampf (2013)[a]
	-0.16±0.02 M^{-1}	-0.06±0.02 M^{-1}	-0.065±0.006 M^{-1}	-0.10±0.02 M^{-1}	this work
Methyl glyoxal	0.16±0.03 M^{-1}	0.075±0.03 M^{-1}	0.02±0.02 M^{-1}	0.06±0.02 M^{-1}	this work
2-hexanone	0.38±0.01 M^{-1}	–	–	0.18±0.02 M^{-1}	Wang (2014)[b]
	–	–	–	0.198±0.004 M^{-1}	Endo (2012)[c]
Heptanal	0.35±0.03 M^{-1}	–	–	–	Wang (2014)[b]
	–	–	–	0.24±0.01 M^{-1}	Endo (2012)[c]
1-hexanol	0.364±0.006 M^{-1}	–	–	0.21±0.01 M^{-1}	Wang (2014)[b]
	–	–	–	0.221±0.004 M^{-1}	Endo (2012)[c]
2-butoxyethanol	0.31±0.02 M^{-1}	–	–	–	Wang (2014)[b]
	–	–	–	0.211±0.09 M^{-1}	Endo (2012)[c]

stant as measured in Kampf et al. (2013) and in this work, given the very different salt concentration regimes (this work: 0 to 3.8 M ammonium sulfate in bulk solutions; Kampf et al. (2013): 4-15 M ammonium sulfate in metastable aerosols) and different methods of measuring both the gas and aqueous phase concentrations. The discrepancy in the Kampf et al. (2013) measurements is likely due to the method used for particle-phase glyoxal measurements. The work in Kampf et al. (2013) calculated Henry's law constants from gas-phase glyoxal measurements from the CE-DOAS (Thalman and Volkamer, 2010) and particle-phase measurements from HPLC-ESI-MS (Kampf et al., 2012a). However, the particle-phase measurements likely quantify both free glyoxal (unhydrated glyoxal monomers, monohydrate monomers, and dihydrate monomers) as well as any oligomers that decompose during the measurement process. This results in an over-estimation of the particle-phase free glyoxal concentration, which will result in over-estimating the strength of salting in.

Glyoxal very clearly salts in to aqueous salts, whereas methyl glyoxal salts out. This indicates that molecular structure is critical for determining the salting behavior of a species, as glyoxal and methyl glyoxal are fairly similar. They are both small α-dicarbonyl species, have very high Henry's law constants, have the ability to form hydrates in water, and have very high O/C ratios. However, the addition one methyl group and the conversion of an aldehyde group to a ketone switches the species from salting in to salting out. Additionally, even the smallest, most water-soluble species (2-butoxyethanol) tested in Wang et al. (2014a) also salts out more strongly than methyl glyoxal. The finding that glyoxal coupled with atmospherically relevant salts exhibits sating in behavior is surprising given the number of species measured in previous studies (Endo et al. (2012); Wang et al. (2014a)) as well as methylglyoxal in this study that salt out. Additionally, there is a large difference in the magnitude of the salting constants for methyl glyoxal and for the species from Wang et al. (2014a), where the larger species in Wang et al. (2014a) were found to salt out of ammonium sulfate solutions much more strongly than methyl glyoxal. Interestingly, there seems to be an inverse correlation with expected number of OH groups and magnitude of the salting out constant measured in Wang et al. 1-hexanol (1 OH group) salts out less than 2-hexanone (0 OH groups as hydration is not expected) with values of 0.364 M^{-1} and 0.38 M^{-1} respectively.

Heptanal (2 OH groups expected due to hydration; hexanal was not measured) salts out even less than 1-hexanol with values of 0.35 M^{-1} and 0.364 M^{-1} respectively. This is significant because there is a clear trend with increasing salting out constants with carbon number as Wang et al. (2014a) measured a series of 2-ketones from 2-hexanone to 2-decanone. Therefore, hexanal would be expected to salt out even less than heptanal. This is consistent with work by Kurtén et al. (2015) who found that the salting in from glyoxal is due to the interaction of the OH groups in glyoxal monohydrate and glyoxal dihydrate with the sulfate anion. This means that significant care should be taken when selecting a proxy species if the salting constants for a molecule are not known.

Additionally, the salting behavior of a given molecule is different for ammonium sulfate and ammonium nitrate salts. In both cases, ammonium sulfate had a stronger effect on the salting behavior than ammonium nitrate; glyoxal salts in to ammonium sulfate more than for ammonium nitrate and methyl glyoxal salts out of ammonium sulfate more strongly than for ammonium nitrate. Because glyoxal salts in, it will make more aerosol in the presence of pure ammonium sulfate than pure ammonium nitrate. However, since aerosols tend to contain multiple inorganic species and indeed aerosols at SOAS are predicted to contain both (see Figure 4.5), the presence of nitrate in the aerosol enhances the sulfate salting resulting in further glyoxal uptake. Based on this data and other data in the literature which indicates a similar trend that ammonium sulfate has a stronger effect on salting than nitrate salts (Gordon and Thorne, 1967a,b) the salting constants should be chosen for the salt(s) most applicable, rather than using ammonium sulfate to represent all salts.

We also find a decrease in vapor pressure upon going from 1.5 M ammonium sulfate to 1.5 M ammonium nitrate. The decrease is consistent with that observed upon going from 0 M ammonium nitrate to 1.5 M ammonium nitrate. This suggests that salting constants are additive and the concentration of glyoxal that partitions to the aerosol will be dependent on the concentration of all salts. The expected vapor pressure decrease of glyoxal above a mixed ammonium sulfate/ammonium nitrate system is shown in Figure 4.4 calculated using

$$log\left(\frac{K_{H,w}}{K_{H,salt}}\right) = -0.24 \times C_{AS} + -0.07 \times C_{AN} \tag{4.9}$$

The x-axis shows ammonium sulfate concentration in molality (0-12 molal), the y-axis shows the ammonium nitrate concentration in molality (0-12 molal), and the z-axis (and color shading) represent the relative vapor pressure of glyoxal relative to that above pure water. The edge along the x-axis shows the vapor pressure decrease in the absence of ammonium nitrate as one moves from pure water (relative vapor pressure = 1, dark blue) to 12 molal ammonium sulfate (orange, relative vapor pressure = 0.06; 6% of the vapor pressure above pure water). The edge along the y-axis shows the vapor pressure decrease in the absence of ammonium sulfate as one moves from pure water (dark blue) to 12 molal ammonium nitrate (green, relative vapor pressure = 0.48). The surface represents the decrease in vapor pressure for mixed solutions. For example, at 6 molal ammonium sulfate and 6 molal ammonium nitrate, the relative vapor pressure is 0.17 (light orange), which is lower than that of 6 molal ammonium sulfate and 0 molal ammonium nitrate (0.24, yellow) or 0 molal ammonium sulfate and 6 molal ammonium nitrate (0.70, turquoise).

Measurements are shown by the three spheres on the surface. These are the vapor pressures relative to that above pure water at 1.6 molal ammonium sulfate and 0 molal ammonium nitrate, 0 molal ammonium sulfate and 1.6 molal ammonium nitrate, and 1.6 molal ammonium sulfate and 1.6 molal ammonium nitrate. The colors of the spheres are representative of the relative vapor pressure, on the same scale as the surface. This shows good agreement with the values calculated for the surface.

Very few measurements have been made that systematically investigate mixtures of salts. Several studies have focused on sea water (e.g. Zhou and Mopper (1990); Xie et al. (1997)). These studies sometimes compare Henry's law constants in natural sea water versus synthetic sea water or pure sodium chloride solutions, but sea water is dominated by sodium chloride which minimizes the effects of the additional ion species. Gordon and Thorne (1967b) performed a systematic series

Figure 4.4: Calculated vapor pressure of glyoxal over mixed ammonium sulfate/ammonium nitrate systems relative to that in pure water. The x-axis is ammonium sulfate concentration (molality), the y-axis is ammonium nitrate concentration (molality), and the z-axis and color shading on the surface are vapor pressure of glyoxal over solutions of the composition prescribed by the x and y coordinates, relative to the vapor pressure over pure water. Pure water is shown in the upper left corner, which has a relative ratio of 1. Measurements for relative vapor pressures of 1.6 molal ammonium sulfate, 1.6 molal ammonium nitrate, and mixed 1.6 molal ammonium sulfate plus 1.6 molal ammonium nitrate are indicated by spheres on the plot using the same color shading as the surface. Good agreement is observed between the calculated surface values assuming additive salting constants and measurements.

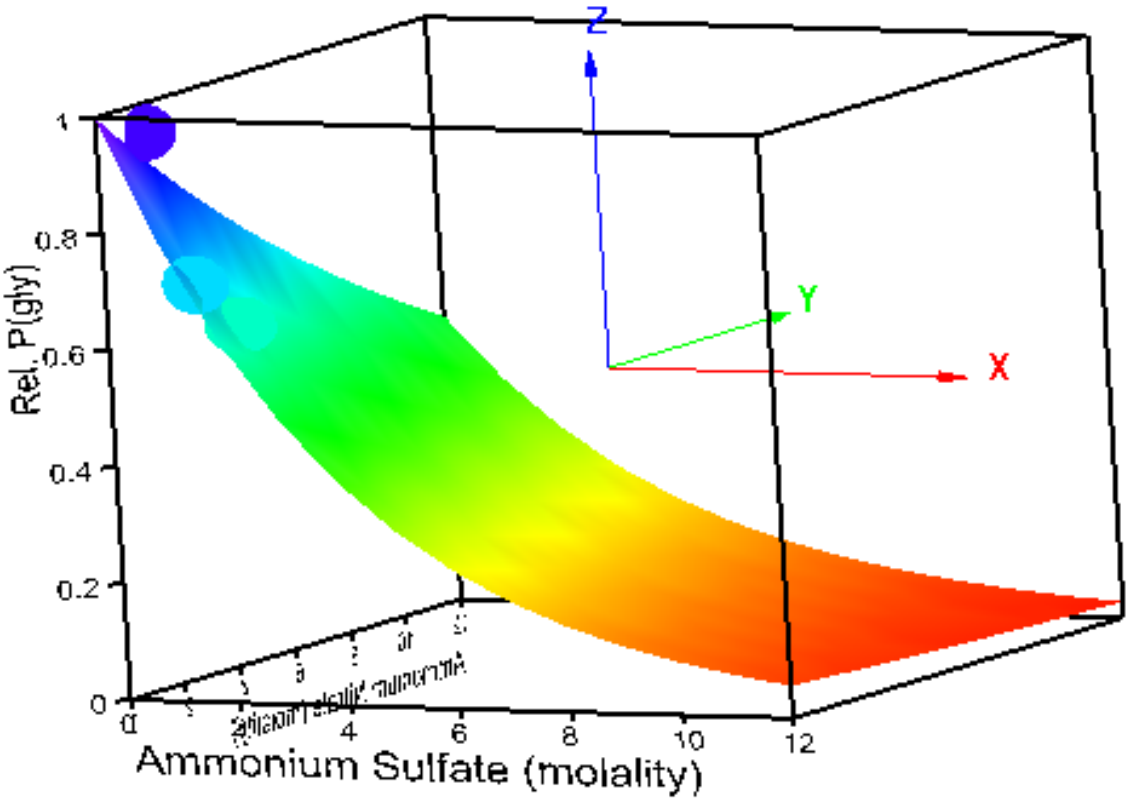

of salting constant measurements on naphthalene in mixed salt solutions. They also found that the effects of salts are additive for mixtures of sodium chloride with magnesium chloride, sodium sulfate, cesium bromide, calcium bromide, and potassium bromide. Our results are thus in good agreement with this study since we also find that mixtures of salts are additive.

4.3.2 Salting Constant Measurements of Organics

Results of the glyoxal in sodium oxalate measurements are shown in panel E of Figure 4.3. Glyoxal salts in to sodium oxalate much more strongly than any of the other salts. What is unique about oxalate in comparison with the other salts is that it is an anion derived from the organic molecule oxalic acid rather than an inorganic ion. It is possible that the increased salting behavior is due to the fact that oxalate is organic ion.

In a series of chamber experiments that probed glyoxal uptake on seed aerosols in the presence and absence of UV light, Volkamer et al. (2009) found a factor of four enhancement in the effective Henry's law constant of glyoxal for uptake on pure organic fulvic acid seeds (with no inorganic salts) compared to the uptake on pure inorganic seeds. Additionally, this uptake to pure organic seed was a factor of 1500 larger than the value for pure water reported by Ip et al. (2009). The enhanced uptake to inorganic seeds compared to pure water is now understood, but what is surprising about this set of measurements is that they saw further enhancements in the effective Henry's law constant by a factor of almost four for seeds containing pure fulvic acid or a mixture of fulvic acid plus ammonium sulfate. This is possibly a manifestation of the same effect observed with the oxalate – that organics can cause "salting in" as well or better than inorganic ions.

The concept that organic solutes can potentially pull in additional molecules and essentially contribute to salting in could have significant impacts for SOA formation. Studies have found humic-like substances in aerosols (Hoffer et al., 2006; Dinar et al., 2008)and oxalate has been detected at concentrations of 0.3 μg/m^3 (Bian et al., 2014). This effect warrants further study.

4.3.3 CMAQ results

The modeled aerosol water concentrations and aerosol sulfate and aerosol nitrate concentrations are shown in Figure 4.5. The highest water concentrations (panel A) are over the industrial northeast, where it is both humid and high concentrations of anthropogenic pollutants result in inorganic aerosol species that can take up water. In contrast, the highest concentrations of aqueous-phase aerosol sulfate (panel B) and nitrate (panel C) are in regions that have low aerosol water content, as this concentrates the aerosol-phase species. Thus based on salt concentration, salting is expected to have the greatest effect over the dry southwestern United States. A kinetic limitation to glyoxal uptake was observed in Kampf et al. (2013) at concentrations greater than 12 molal sulfate (see Figure 1 of Kampf et al. (2013)). At concentrations beyond 12 molal sulfate, a further enhancement in the glyoxal uptake was not observed and remained flat at the 12 molal value. This is hypothesized to be due to a change in the phase state of the aerosol from a liquid to a semi-solid or glassy aerosol where the particle-phase diffusion rate is significantly decreased. Thus we expect no further enhancement of salting beyond the 12 molal concentrations for sulfate or nitrate aerosol. This kinetic limitation was first implemented by Knote et al. (2014) for the CalNex time period in a model that included aqueous-phase glyoxal chemistry, such as the formation of oligomers and imidazoles. They found that the net result of this limitation is that mass transfer from the gas phase limited the overall SOA formation rate from glyoxal. This resulted in the formation of one-third as much SOA from glyoxal when the mass transfer limitation was accounted for than when it was omitted.

Predicted aerosol-phase concentrations of glyoxal, methyl glyoxal, and IEPOX with no salting (pure Henrys law partitioning), ammonium sulfate salting, and ammonium nitrate salting are shown in Figure 4.6. The top row (A, B, C) shows simulated glyoxal concentrations, the middle row (D, E, F) shows methyl glyoxal concentrations, and the bottom row (G, H, I) shows IEPOX concentrations (assuming salting out with the same constants methyl glyoxal). The left-most column shows predictions in the absence of salting, the middle column includes ammonium sulfate

Figure 4.5: CMAQ results for water content (A), ammonium sulfate concentration (molality, B), and ammonium nitrate concentration (molality, C) over the continental United States during SOAS. Regions with high water content have the lowest predicted aerosol salt concentration.

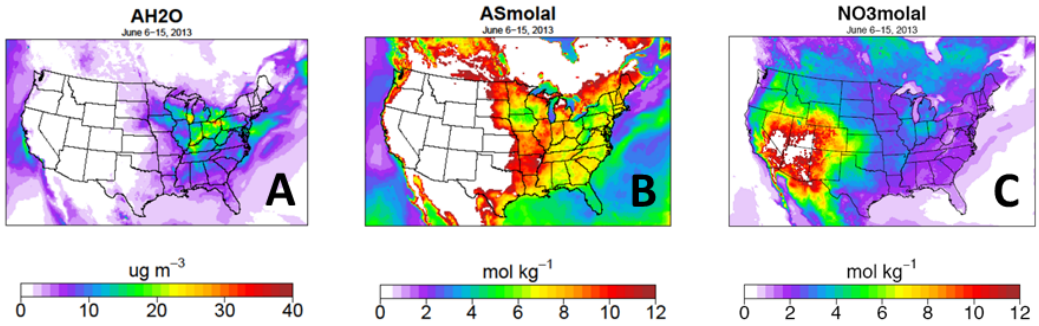

salting, and the right column includes ammonium nitrate salting. Assuming pure Henry's law partitioning ($K_{H,w} = 3.6\times10^5$ M/atm for glyoxal, 3.2×10^4 M/atm for methyl glyoxal, and 2.7×10^6 M/atm for IEPOX), IEPOX is expected to have the highest aqueous phase concentrations due to its extremely high effective Henry's law constant. Methyl glyoxal has the lowest predicted aqueous-phase concentration, and glyoxal is in the middle. If salting due to ammonium sulfate is included, glyoxal and IEPOX are expected to produce similar concentrations of SOA while methyl glyoxal is expected to make very little SOA. Ammonium nitrate has a much weaker salting effect than ammonium sulfate and is present in much lower concentrations than ammonium sulfate, so it is not expected to change SOA formation significantly from the case in which salting is neglected. This indicates that choosing a salting constant appropriate for the aerosol is important as it can drastically effect the predicted SOA formation.

Gas-phase concentrations of three aqueous SOA precursor species are shown in the top row of Figure 4.7. These species are all formed from the gas-phase oxidation of isoprene by OH. The highest concentrations of these species over the continental United States is over the southeast, where there are very high isoprene emissions. Methyl glyoxal (panel B) is predicted to have the highest gas-phase concentration, followed by IEPOX (panel C) and glyoxal (panel A) is predicted to have the lowest gas-phase concentrations.

Particle-phase concentrations of these species are shown in the bottom row of Figure 4.7 for salting that includes both ammonium sulfate and ammonium nitrate. The salts were treated as additive so that the calculated partitioning is due to the salting resulting from ammonium sulfate plus the salting resulting from ammonium nitrate. Because it salts out of ammonium sulfate and ammonium nitrate and has a comparatively low K_H, methyl glyoxal (panel E) has the lowest particle-phase concentration of the three species. Because glyoxal (panel D) salts in to both ammonium sulfate and ammonium nitrate, it has a much higher particle-phase concentration than methyl glyoxal despite the lower gas-phase concentration. IEPOX (panel E) has a slightly lower gas-phase concentration than methyl glyoxal but a very high K_H. However, because it likely salts out of ammonium sulfate and ammonium nitrate, this compensates for the high uptake due

Figure 4.6: CMAQ aqueous-phase concentrations of glyoxal (top row; panels A, B, and C), methyl glyoxal (middle row; panels D, E and F) and IEPOX (bottom row; panels G, H and I) during SOAS. The left-most column (panels A, D, and G) show partitioning based solely on Henry's law constants. The middle column (panels B, E, and H) show partitioning including the effect of sulfate (assuming the methyl glyoxal salting out constant for IEPOX, panel H). The right-most column (panels C, F, and I) show partitioning including the effect of nitrate (assuming the methyl glyoxal salting out constant for IEPOX, panel I).

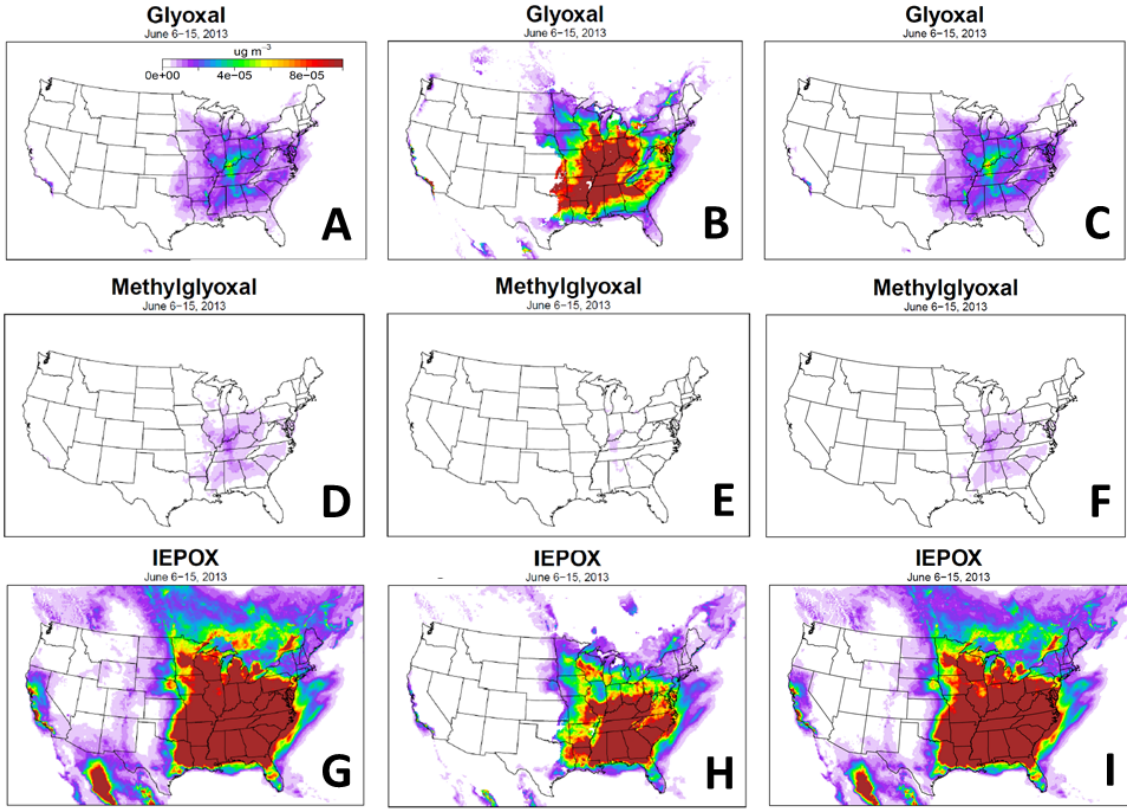

Figure 4.7: Gas-phase concentrations of glyoxal (panel A), methyl glyoxal (panel B), IEPOX (panel C). Aerosol-phase concentrations including salting from both ammonium sulfate and ammonium nitrate for glyoxal (panel D), methyl glyoxal (panel E), and IEPOX (panel F). Methyl glyoxal has the highest gas-phase concentration and glyoxal the lowest, but the particle-phase distributions are very different due to the different salting behavior of the molecules.

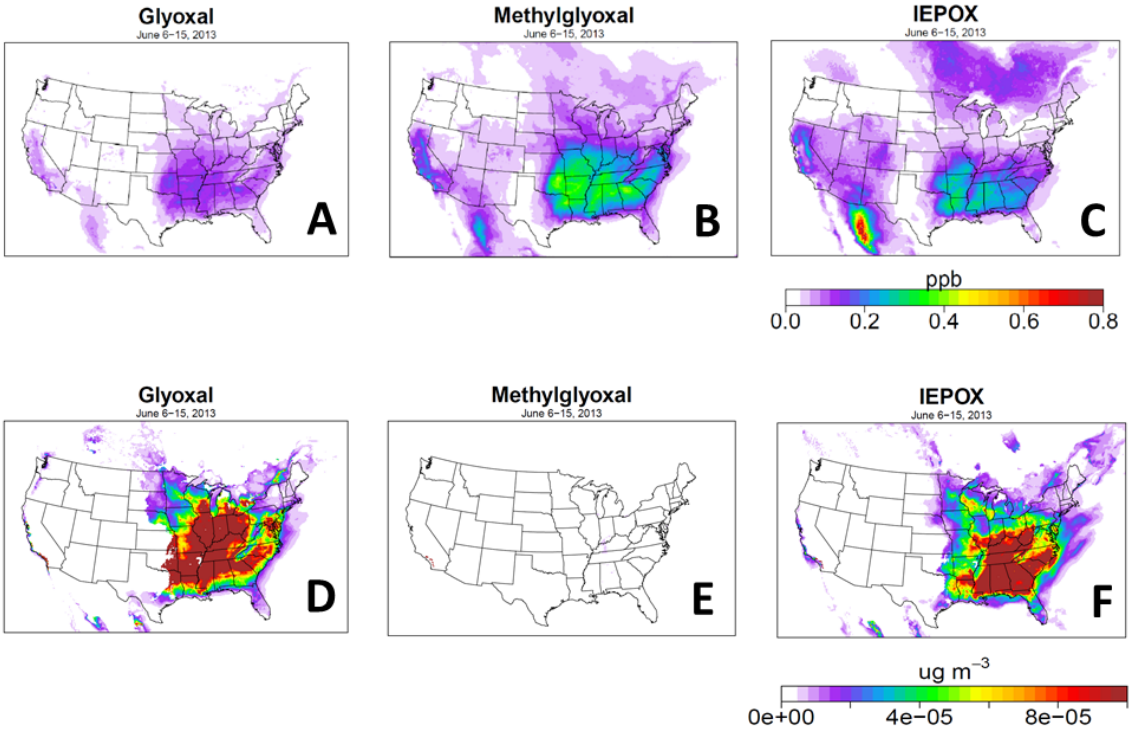

to Henry's law and IEPOX is predicted to have a slightly lower particle phase concentration than glyoxal. Salting significantly changes the relative importance of water-soluble aerosol precursor species. Based solely on gas-phase data, it would appear that methyl glyoxal is the most important species for aqueous SOA formation over the southeastern United States and that glyoxal is the least important. However, when salting is accounted for, glyoxal is far more important as an aqueous SOA precursor species than methyl glyoxal. Therefore, salting needs to be taken in to account when predicting SOA formation from water-soluble precursor species.

The aqueous phase aerosol concentrations for glyoxal are significantly lower than those predicted elsewhere, for example Figure 15 from Knote et al. (2014). In this figure, SOA formed from glyoxal is up to 1 $\mu g/m^3$, whereas in this work it is several orders of magnitude lower. This difference is because the work in Knote et al. (2014) includes aqueous-phase processing of glyoxal, such as the formation of oligomers and nitrogen-containing compounds, whereas this work only includes simple gas-particle partitioning of glyoxal. Salting influences that partitioning, which is the critical first step to creating SOA by aqueous-phase processing.

Time series data for these three species taken from the Centreville, AL site and downtown Los Angeles are shown in Figures 4.8 and 4.9. Glyoxal is shown in the top panel of each graph, methyl glyoxal in the middle, and IEPOX on the bottom. The time series are for Centreville, AL (red) and Los Angles (blue). There is significantly more variability in the gas-phase time series for Centreville. Here, methyl glyoxal (average concentration of 270 pptv) and IEPOX (average concentration of 250 pptv have significantly higher gas-phase concentrations than glyoxal (average concentration of 88 pptv). However, once the partitioning due to Henry's law and salting is accounted for, methyl glyoxal is least abundant in the particle phase with an average concentration of $2.3\times10^{-6}\mu g/m^3$. Glyoxal has an average concentration of $3.7\times10^{-5}\mu g/m^3$ and IEPOX has an average concentration of $1.7\times10^{-4}\mu g/m^3$. Thus in Centreville the inclusion of salting in for glyoxal and salting out for other molecules means that the relative importance of molecules in the aerosols (where IEPOX dominates) is very different than the relative importance of the molecules in the gas phase (where methyl glyoxal dominates).

Figure 4.8: Gas-phase concentrations of glyoxal (top), methyl glyoxal (middle), IEPOX (bottom) in Centreville, AL (red) and Los Angeles, CA (blue). Concentrations are significantly more variable in Centreville. Methyl glyoxal and IEPOX have significantly higher concentrations than glyoxal.

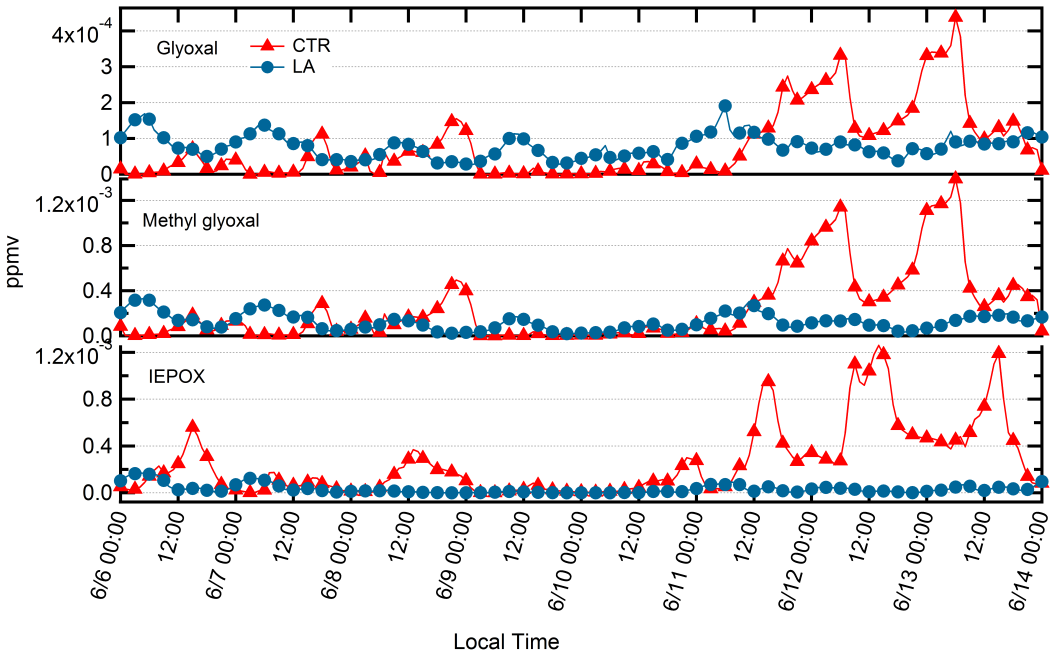

Figure 4.9: Particle-phase concentrations of glyoxal (top), methyl glyoxal (middle), IEPOX (bottom) for Centreville, AL (red) and Los Angeles (blue) IEPOX and glyoxal have significantly higher aqueous-phase concentrations than methyl glyoxal.

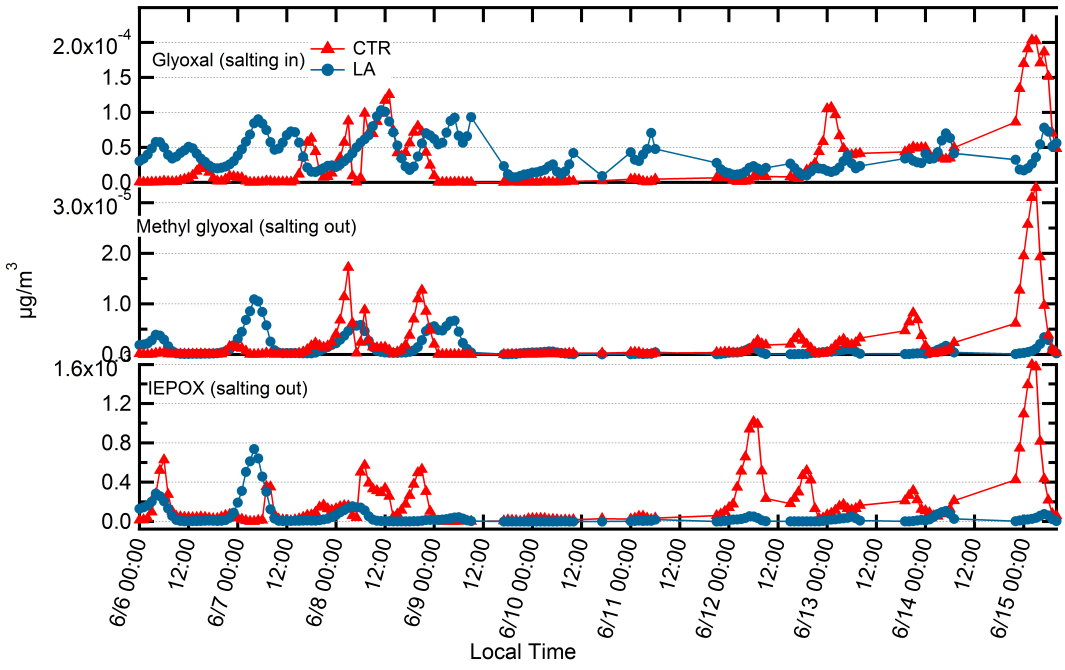

In Los Angeles, glyoxal, methyl glyoxal, and IEPOX are predicted to have gas-phase concentrations of 80 pptv, 130 pptv, and 34 pptv, respectively. Once partitioning and salting is accounted for, they are expected to have particle-phase concentrations of $3.9\times10^{-5}\mu g/m^3$, $1.5\times10^{-6}\mu g/m^3$, and $5.3\times10^{-5}\mu g/m^3$, respectively. This shows a similar trend to the Centreville data: despite having the highest gas-phase concentration, methyl glyoxal has the lowest particle-phase concentration.

4.4 Outlook

We have reported the first laboratory measurements of salting constants for glyoxal and methyl glyoxal in four atmospherically-relevant salts: ammonium sulfate, ammonium nitrate, sodium nitrate, and sodium chloride. Glyoxal salts in to all salts, which is consistent with results from Kampf et al. (2013). Surprisingly, methyl glyoxal salts out of all four of these salts, despite its structural similarity to glyoxal and its high Henry's law constant. Additionally, we provide initial evidence that salting constants are additive which is consistent with work from Gordon and Thorne (1967b).

We then apply these salting constants to the CMAQ model for a one-week period during the SOAS campaign. This model predicts that methyl glyoxal should be the most abundant species in the gas phase, followed by IEPOX and glyoxal. However, when just Henry's law is applied, IEPOX is the dominant species found in the particle phase due to its high Henry's law constant, followed by glyoxal and methyl glyoxal. This is consistent with Sareen et al. (2015) ES&T Letters (in prep). However, when the salting is accounted for, glyoxal and IEPOX are predicted to be found in the aqueous phase in similar concentrations, assuming that IEPOX salts out with the same K_S values as methyl glyoxal, especially in the case when additive salting from ammonium sulfate and ammonium nitrate is assumed.

This work has several implications for modeling: 1) salting has a significant impact on the partitioning of gas-phase species to the aerosol aqueous phase, and should be taken in to account in modeling studies. 2) Small changes in chemical structure can have significant impacts on the salting behavior of the molecule, and this behavior is different for each salt. Therefore, the K_S

values for water-soluble aerosol precursors should ideally be measured for the species of interest in the atmospherically-relevant salt(s). In the absence of measurements, proxy salting constant values should be chosen with care. 3) Salting constants appear to be additive, so all aerosol salts should be accounted for in terms of salting effects, not just the dominant anion.

Chapter 5

Theory of Setschenow Salting and Gibbs Energies: applications to organic matricies and isoprene epoxide

Salting constants describe how the partitioning of an organic molecule changes in the presence of a salt solution compared to a pure water solution. When the molecule shifts towards the gas phase rather than the aqueous phase, this is called salting out. When the reverse happens, this is called salting in. Salting can have profound impacts on the formation of secondary organic aerosol through multiphase processing, as it controls the amount of precursor molecule that is available in the aerosol water. Here, we present salting constant measurements for two such precursor molecules, glyoxal and methyl glyoxal, in a variety of salts. However, it is not always practical to measure salting constants, as the species of interest may not be readily available. We also compare the measurements against salting constants calculated from two literature theories used to predict salting for benzene and other single-ring aromatics, as well as quantum calculations that predict interactions of the molecules with the salt ions. We find that salting behavior is best represented by a combination of these theories, and use this to predict salting constants for IEPOX and the tetrol resulting from acid-catalyzed ring opening, which are both important aerosol precursor species but are difficult to obtain for measurements.

5.1 Introduction

Most atmospheric aerosols contain an inorganic fraction (Zhang et al., 2007; Philip et al., 2014). This fraction is typically made of up salts containing ammonium, sodium, nitrate, sulfate,

and chloride resulting from sea spray (NaCl particles) or gas-phase processing of anthropogenic precursor gases (nitrate, sulfate, and ammonium). The hygroscopicity of these inorganic ions is responsible for the majority of the water taken up by the aerosols and the formation of an aerosol aqueous phase (Nguyen et al., 2014; Wang et al., 2014b). Salt concentrations tend to be quite high in aerosols; between 3 M and 20 M (Kampf et al., 2013).

Organic aerosol formation by aqueous-phase processing is a topic of recent interest (De Haan et al., 2009b,a; Galloway et al., 2009; Shapiro et al., 2009; De Haan et al., 2010; Ervens and Volkamer, 2010; Sareen et al., 2010; Powelson et al., 2013; Waxman et al., 2013; Woo et al., 2013; Hawkins et al., 2014). Small, water-soluble species such as glyoxal, methyl glyoxal, acetaldehyde, glycolaldehyde, or IEPOX (isoprene epoxydiols) partition to the aerosol aqueous phase by Henrys law. They can then undergo further aqueous-phase reactions such as oligomerization, reactions with nitrogen-containing species, reactions with sulfate ions, and aqueous-phase oxidation reactions in the presence of OH radicals (Carlton et al., 2007; Ervens and Volkamer, 2010; Surratt et al., 2010; Ortiz-Montalvo et al., 2014).

The presence of salts in the aqueous phase can significantly impact the solubility and activity of organics in the aerosol as well as modify bulk (as opposed to surface) reaction rate constants. This process is called salting: when salts increase the solubility of the organic, this is called salting in with respect to the organic and when salts decrease the solubility of the organic, this is called salting out. This effect was first published in 1889 by Setschenow who described this effect in terms of an organics solubility in water (Setschenow, 1889):

$$log\left(\frac{S_0}{S}\right) = K_S C_{salt} \tag{5.1}$$

where S_0 and S are the solubility of the organic in pure water and the salt solution respectively, K_S is the salting constant or Setschenow constant, and C_{salt} is the concentration of the salt solution, typically in molarity. Kampf et al. modified this equation to describe salting in terms of Henrys law constants (Kampf et al., 2013):

$$log\left(\frac{K_{H,w}}{K_{H,salt}}\right) = K_S C_{salt} \tag{5.2}$$

where $K_{H,w}$ is the Henrys law constant of the organic in pure water and $K_{H,salt}$ is the Henrys law constant in the salt solution. Therefore, this effect changes the partitioning of these species between the gas and aqueous phase. If the molecule salts in, partitioning towards the aqueous phase is favored which increases the amount of precursor molecule available for further reactions and SOA formation. If the molecule salts out, the reverse is true.

Recent measurements show that glyoxal salts in to ammonium sulfate aerosols (Kampf et al., 2013). A series of quantum chemical calculations showed that this is because the hydrated forms of aqueous-phase glyoxal, especially the mono-hydrate, bind to sulfate more strongly than water in the sulfate hydration shell (Kurtén et al., 2015). This results in the loss of free glyoxal in the aqueous phase as it is tied up as part of the hydration shell. Therefore, additional glyoxal must partition in to the aqueous phase to maintain equilibrium thus increasing the effective Henrys law constant. It was also recently shown that the salting constants for glyoxal vary with salt, and that despite being structurally and chemically similar to glyoxal, methyl glyoxal salts out of solution (Waxman, Sareen et al. 2015 ES&T, in prep). Therefore, when modeling SOA formation from these species it is important to obtain salting constants for the organic species of interest and the salt in the aerosol or use significant care when choosing a proxy value as the structure of the organic and the chemical composition of the salt can greatly impact the salting effect.

However, in many cases these values are unknown and it can be difficult to obtain them. Synthesizing an SOA precursor molecule could be quite difficult as they are often multi-functional. In is also possible that hypothesized aqueous phase reaction products may have no known synthetic route, but knowing the salting constant value may still be desirable. Therefore, additional methods for determining a salting constant, such as through quantum calculations, are necessary. Endo et al. (2012) and Wang et al. (2014) used two models, AIOMFAC and COSMO*therm* to calculate salting constants for species as well as generating a poly-parameter linear free energy relationship (pp-LFER) from measured salting constants to predict those for unmeasured species. However, all of their calibration species for the pp-LFER were large molecules unlikely to be observed in the aerosol aqueous phase. Therefore, their pp-LFER equation is unlikely to be applicable to

small, water-soluble molecules. Additionally, their AIOMFAC and COSMOtherm calculations only predicted salting out for these species which all salted out in measurements. It is unknown if these models are capable of reproducing the salting in measurements observed for glyoxal.

Here we present additional experimental data for two aerosol precursor species, glyoxal and methyl glyoxal, as well as quantum calculations for interactions with salt ions. We additionally compare the measured salting constants and quantum calculations for these molecules against predictions of salting constants made from equations described in the literature that were created to explain the salting behavior of aromatics. We use this to hypothesize the driving factors between glyoxal salting in and methyl glyoxal salting out, and then use this to predict the salting behavior of IEPOX and the tetrol resulting from acid-catalyzed ring opening, SOA precursors of recent interest formed from isoprene but whose syntheses are difficult.

5.2 Experimental

5.2.1 Laboratory Studies

Laboratory-based salting measurements are additionally described elsewhere (Waxman, Sareen, et al 2015 ES&T, in prep). Briefly, we make relative measurements of Henrys law constants rather than absolute by adding known, constant concentrations of organic to the aqueous phase and measuring the relative change in the gas phase signal. Glyoxal or methyl glyoxal, 0.2 M or 0.1 M respectively, (both from 40% w/w solution, Sigma Aldrich) were added to salts solutions of a known concentration between 0.0 and 3.0 M (ammonium sulfate, ammonium nitrate, sodium chloride, sodium nitrate, sodium oxalate, tetramethyl ammonium bromide (methyl glyoxal ITMS only), and tetrabutyl ammonium bromide (methyl glyoxal ITMS only), all from Sigma Aldrich). These solutions were allowed to equilibrate at room temperature for 45 minutes. At longer time scales, glyoxal was observed to react with ammonium to form imidazoles and the aqueous phase concentration could no longer be considered consistent between the 0.0 M salt solution (where no reaction occurs due to absence of ammonium) and 3.0 M salt solution where the maximum concen-

tration of imidazoles are formed. The pH of the sodium oxalate solutions were modified to ensure that they remained in the free anion state (e.g. $C_2O_4^{2-}$).

A solid-phase micro extraction (SPME) fiber (65 μm poly(dimethylsiloxane)/divinylbenzene (PDMS/DVB), Supelco) was then exposed to the headspace of 17 mg/mL of a continuously-stirred *O*-(2,3,4,5,6-pentafluorophenyl)methylhydroxylamine hydrochloride (PFBHA, Sigma Aldrich) solution for two minutes and then to the headspace above the salting solution (1 minute for methyl glyoxal, 15 minutes for glyoxal due to the difference in Henrys law constant) and were then measured by GC-FID. This procedure derivatized the carbonyl groups to oximes, both lowering the vapor pressure of the product and increasing the sensitivity of the GC to the products. The GC program was as follows: 40°C for 2 minutes, 10°C/min to 110°C, 5°C/min to 155°C, 10°C/min to 280°C, 280°C for 5 minutes. The inlet was held at 250°C. PFBHA was always measured in significant excess to the oxime products, indicating that the amount of oxime formed was limited by the amount of gas-phase glyoxal or methyl glyoxal, rather than the amount of PFBHA. Tests showed that after one run, all PFBHA and oxime products had been volatilized off of the SPME fiber, eliminating the need to run blanks between measurements.

GC-FID instruments are most sensitive to reduced carbon (e.g. carbon atoms in alkyl moieties) (Scanlon and Willis, 1985). PFBHA derivatization turns an aldehyde group into an oxime and simultaneously adds seven reduced carbon atoms per carbonyl group. Prior to derivatization, glyoxal molecules contain zero reduced carbon atoms and methyl glyoxal only has one so derivatization makes GC-FID much more sensitive to these species. Derivatization by PFBHA is a common technique for quantifying small aldehydes like glyoxal, methyl glyoxal, formaldehyde, and acetaldehyde by GC-FID (Koziel et al., 2001; Reisen et al., 2003; Apel et al., 2008; Gómez-Alvarez and Valcárcel, 2009; Gómez-Alvarez et al., 2012; Hamilton et al., 2013).

To verify this method for measuring salting constants, values for methyl glyoxal were also measured using electron impact (EI) mass spectrometry with a quadruople ion trap instrument (Thermo Finnigan). A novel inlet for this instrument was designed specifically for salting constant measurements and is described elsewhere (Waxman, Sareen, et al. 2015, ES&T, in prep). Excellent

agreement is observed between the salting constant values for methyl glyoxal between the two methods for ammonium sulfate, sodium nitrate, and sodium chloride, validating both the GC-FID and EI-MS methodology. A slight difference is observed between the two methods for ammonium nitrate; the source of this difference is presently unclear.

5.2.2 Computational Methodology

Electrostatic interactions between the organics and salt ions were calculated using quantum chemical calculations. All geometry optimizations and frequency calculations were performed with Gaussian09 (Frisch et al., 2009) using the M06-2X functionality (Zhao and Truhlar, 2008). The M06-2X functionality was chosen on basis of recent benchmarks showing its adequate performance in describing sulfur containing compounds and yielding reliable thermodynamics for sulfuric acid-water clusters (Elm et al., 2012, 2013a; Leverentz et al., 2013). For the initial conformational sampling solvent effects are taken into account using a Polarizable Continuum Model with the integral equation formalism variant (IEFPCM) (Miertuš et al., 1981; Tomasi et al., 2005).

Methyl glyoxal can exist in three different forms in aqueous solution: unhydrated, mono-hydrated and di-hydrated. Recently, we showed that glyoxal has an unfavorable interaction with sulfate, but that partitioning into sulfate aerosol could occur through the hydrates leading to a salting-in effect (Kurtén et al., 2015). Therefore only the methyl glyoxal hydrates are further considered in this study. Methyl glyoxal monohydrate exists in two different forms since water can be added either to the aldehyde or ketone moiety, which will be denoted monohydrate-a and monohydrate-k, respectively. The lowest Gibbs free energy conformations of the methyl glyoxal hydrates were identified using a systematic rotor approach to construct a rotamer library which rotates the internal dihedral angles making all possible rotations in increments of 120 degrees. Utilizing this approach narrowed down the energetically relevant conformations (within 3 kcal/mol of the lowest identified) to five monohydrate-a, nine monohydrate-k and thirteen dihydrate conformations. In Figure 5.1 the lowest identified free energy conformations are shown optimized at the M06-2X/6-31+G(d) level of theory in water. The relative stability of the monohydrates indicates

Figure 5.1: The lowest energy isomers of methyl glyoxal hydrates: a) monohydrate-a, b) monohydrate-k and c) dihydrate, respectively. Calculated at the M06-2X/6-31+G(d) level of theory in water.

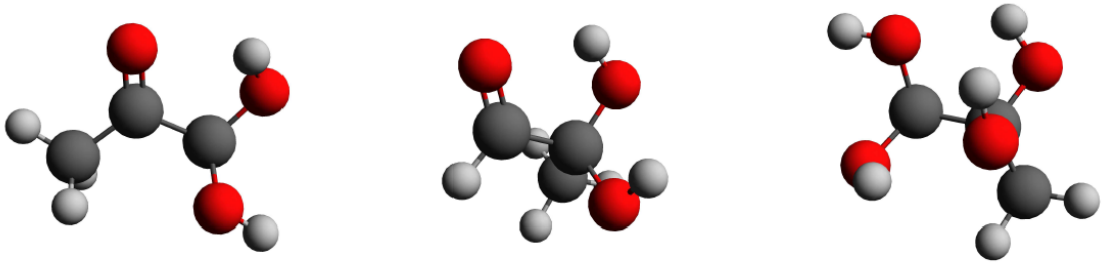

(a) Monohydrate-1 **(b) Monohydrate-2** **(c) Dihydrate-1**

that monohydrate-a is 4.28 kcal/mol more stable than monohydrate-k, and therefore the second monohydrate would only exist in insignificant concentrations. The formation of the dihydrate will occur from adding water to monohydrate-a through the following reaction:

$$\text{monohydrate-a} + H_2O \rightleftharpoons \text{dihydrate}$$

The formation free energy of the dihydrate is found to be +1.75 kcal/mol, and therefore the dihydrate will most likely be found in very low concentrations as well. This indicates that only the monohydrate-a conformation needs to be taken into account when exploring the salting-in/out effect of methyl glyoxal. From here on in, we refer to monohydrate-a as simply monohydrate.

To investigate potential salting-in/out effects of methylglyoxal with various ions, the following reactions between the methyl glyoxal monohydrate and the ions Cl^-, NO_3^-, SO_4^{2-}, oxalate ($C_2O_4^{2-}$), Na^+ and NH_4^+ are studied:

$$\text{monohydrate} + Cl^- \rightleftharpoons (Cl^-)(\text{monohydrate}) \quad (1)$$

$$\text{monohydrate} + NO_3^- \rightleftharpoons (NO_3^-)(\text{monohydrate}) \quad (2)$$

$$\text{monohydrate} + SO_4^{2-} \rightleftharpoons (SO_4^{2-})(\text{monohydrate}) \quad (3)$$

$$\text{monohydrate} + C_2O_4^{2-} \rightleftharpoons (C_2O_4^{2-})(\text{monohydrate}) \quad (4)$$

$$\text{monohydrate} + Na^+ \rightleftharpoons (Na^+)(\text{monohydrate}) \quad (5)$$

$$\text{monohydrate} + NH_4^+ \rightleftharpoons (NH_4^+)(\text{monohydrate}) \quad (6)$$

The dianions are known to be unstable in the gas-phase and prone to electron spill (Simons, 2008). It has been shown that at least three water molecules are required to stabilize sulfate and oxalates excess electrons (Wang et al., 2000; Liu et al., 2014). We recently reported on the reaction between glyoxal and its hydrates with the sulfate dianion, where we circumvented the electron detachment issue by investigating the water displacement reactions instead of the direct complex formation (Kurtén et al., 2015). By utilizing a similar approach for methylglyoxal, the cluster reactions can be modeled using the following displacement reactions:

$$\text{monohydrate} + (Cl^-)(H_2O)_3 \rightleftharpoons (Cl^-)(\text{monohydrate})(H_2O)_2 + H_2O \quad (7)$$

$$\text{monohydrate} + (NO_3^-)(H_2O)_3 \rightleftharpoons (NO_3^-)(\text{monohydrate})(H_2O)_2 + H_2O \quad (8)$$

$$\text{monohydrate} + (SO_4^{2-})(H_2O)_6 \rightleftharpoons (SO_4^{2-})(\text{monohydrate})(H_2O)_5 + H_2O \quad (9)$$

$$\text{monohydrate} + (C_2O_4^{2-})(H_2O)_6 \rightleftharpoons (C_2O_4^{2-})(\text{monohydrate})(H_2O)_5 + H_2O \quad (10)$$

$$\text{monohydrate} + (Na^+)(H_2O)_3 \rightleftharpoons (Na^+)(\text{monohydrate})(H_2O)_2 + H_2O \quad (11)$$

$$\text{monohydrate} + (NH_4^+)(H_2O)_3 \rightleftharpoons (NH_4^+)(\text{monohydrate})(H_2O)_2 + H_2O \quad (12)$$

Aside from the electron detachment issue, any potential errors in the entropy contribution are simultaneously reduced by keeping the number of molecules fixed in the displacement reactions. We have chosen to hydrate the singly charged ions by three water molecules and the doubly charged ions with six water molecules to be certain that there are no errors due to electron detachment. The structure of the ion-water clusters have in several cases previously been identified and were extracted from the following publications: $(Cl^-)(H_2O)_n$ from Nadykto et al. (2009), $(NO_3^-)(H_2O)_n$ and $(C_2O_4^{2-})(H_2O)_n$ from Liu et al. (2014), $(NH_4^+)(H_2O)_n$ from Pickard IV et al. (2005) and $(SO_4^{2-})(H_2O)_n$ from Lambrecht et al. (2011). In case of the $(Na^+)(H_2O)_3$ cluster, we were unable to find any literature structure and it was thereby manually constructed.

To identify the most stable complexes between the methyl glyoxal monohydrate and the ions of reaction reactions (1)-(6), we utilized a semi-empirically guided technique, which relies on several thousands of randomly generated guess conformations. This sampling technique has previously been utilized to study clusters involving sulfuric acid, water and ammonia together with methanol

(Elm et al., 2013b), glycine (Elm et al., 2013c), pinic acid (Elm et al., 2014), and methane sulfonic acid (Bork et al., 2014). We refer the reader to these investigations for further details about the sampling. Once these complexes were identified, all conformations within 3 kcal/mol of the lowest energy structure were then hydrated by two/five water molecules in the same pattern as indicated by the isolated ion-hydrates from the above ion-water cluster publications.

The final identified cluster structures are further refined using the 6-311++G(3df,3pd) basis set. In a solvent the utilization of the large basis set leads to several spurious low lying imaginary frequencies and the structures were therefore optimized in vacuum. From the vacuum structure the thermal correction to the Gibbs free energy can then be examined and added to a single point energy calculation in a water solvent. Using this procedure allows for a thorough exploration of the potential energy surface of the clusters and should yield a good estimate for the binding free energy of methylglyoxal hydrates to the different ions in aqueous solution. To estimate the difference in binding free energy between methylglyoxal and glyoxal, the obtained methyl glyoxal clusters were re-optimized with the methyl group substituted with a hydrogen atom. While this approach does not include further sampling, it should give a reasonable estimate for the corresponding glyoxal clusters.

Similar calculations were done for trans-β-IEPOX, which was determined to be the most relevant isomer of IEPOX (Bates et al., 2014). From hereon in, "IEPOX" is meant to refer to this isomer.

5.3 Results and Discussion

5.3.1 Experimental and Quantum Calculation Results

The salting constant measurements for glyoxal and methyl glyoxal in ammonium sulfate, ammonium nitrate, sodium nitrate, sodium chloride, tetramethyl ammonium bromide, and tetrabutyl ammonium bromide (and sodium oxalate and sodium phosphate?) are given in Table 5.1. Where measurements from multiple methods are available, the value reported is the average. In

all cases, glyoxal salts in and methyl glyoxal salts out. For both molecules, ammonium sulfate has the strongest effect, followed by sodium chloride. The nitrate salts have the weakest effect on salting, but a non-zero effect. Additionally, the two nitrate salts have slightly different effects: ammonium nitrate has a slightly stronger effect than sodium nitrate. This trend is consistent with the literature. Endo et al. (2012) measured salting constants for a number of molecules in NaCl and Wang et al. (2014a) measured salting constants for the same species in ammonium sulfate. In all cases, the molecules salted out of ammonium sulfate more strongly than sodium chloride. Gordon and Thorne (1967a) measured salting constants of naphthalene in sodium sulfate as well as a number of chloride salts and found that sulfate caused naphthalene to salt out more strongly than any of the chloride salts. Görgényi et al. (2006) measured salting constants for chloroform, benzene, chlorobenzene, and anisole in a wide variety of nitrate, chloride, and sulfate salts. For chloroform, chlorobenzene, and anisole, sulfate salting constants were significantly higher than the chloride salting constants which were higher than the nitrate salting constants. For benzene, they found that sulfate had the strongest effect but nitrate and chloride salts had similar effects.

Results of quantum calculations are given in Table 5.2. Equilibrium constants were calculated using:

$$K = exp^{\frac{-\Delta G}{RT}} \tag{5.3}$$

This lists the ΔG values for the displacement of one water molecule with either a glyoxal monohydrate molecule or a methyl glyoxal monohydrate molecule. These values are all negative for anions and positive for cations. This means that these monohydrates are expected to replace water in the hydration shell, and in the case of glyoxal, replace the water molecules in the hydration shell surrounding NO_3^-, SO_4^{2-}, and $C_2O_4^{2-}$ quite significantly as these ΔG values result in equilibrium constants between 88 (Cl^-) and 16000 ($C_2O_4^{2-}$) for glyoxal and between 4 (Cl^-) and 230 ($C_2O_4^{2-}$) for methyl glyoxal. However, they are not expected to significantly displace water molecules in the hydration shells of the cations, as the equilibrium constants for these replacements are around 0.5,

Table 5.1: Salting constant values for glyoxal and methyl glyoxal in a number of salts with measurements and calculations for Debye theory and McDevit and Long theory. Calculations are given for the monohydrate forms of glyoxal and methyl glyoxal as they are expected to be the most important for salting.

Salt	**Measurement (M^{-1})**	**Debye (M^{-1})**	**McDevit & Long (M^{-1})**
		Glyoxal	
$(NH_4)_2SO_4$	-0.20±0.05	0.21	0.77
NH_4NO_3	-0.07±0.03	0.072	-0.22
$NaNO_3$	-0.072±0.008	0.079	-0.010
NaCl	-0.10±0.02	0.085	0.23
$Na_2C_2O_4$	-6.3	0.20	2.90
Na_3PO_4	–	0.47	1.45
$(CH_3)_4NBr$	–	0.058	-0.58
$(Butyl)_4NBr$	–	0.046	-2.28
		Methyl glyoxal	
$(NH_4)_2SO_4$	0.18±0.03	0.25	0.89
NH_4NO_3	0.085±0.04	0.084	-0.26
$NaNO_3$	0.02±0.03	0.091	-0.012
NaCl	0.06±0.03	0.098	0.27
$Na_2C_2O_4$	–	0.24	3.35
Na_3PO_4	–	0.54	1.67
$(CH_3)_4NBr$	0.01±0.03	0.068	-0.67
$(Butyl)_4NBr$	0.28±0.06	0.053	-2.63
		IEPOX	
$(NH_4)_2SO_4$	–	0.37	1.33
		IEPOX tetrol	
$(NH_4)_2SO_4$	–	0.38	1.35

which means that all water molecules in the hydration shell is slightly favored. The fact that the quantum calculations predict salting in for both glyoxal and methyl glyoxal with hydration shell replacement indicates that this model may not be sole interaction between the organics and salt. However, we note that the uncertainty on the quantum calculations is ±2 kcal/mol. In the case of glyoxal, this results in an equilibrium constant greater than 1 within the entire range of the ΔG calculations. In the case of methyl glyoxal, the equilibrium constant can be slightly less than 1 for both Cl^- and SO_4^{2-} at the far end of the ΔG range. Thus weak salting in is within the error bars of the salting constant predictions for interactions between methyl glyoxal and these two anions.

However, the trends predicted by the quantum calculations differ from those observed experimentally. Glyoxal is expected to salt in to sulfate and nitrate nearly equally, and to chloride significantly less, which is in contrast with the observations of sulfate having the strongest effect, followed by chloride, and then nitrate. The interaction between methyl glyoxal and nitrate is expected to be the strongest, so methyl glyoxal should salt in most strongly (or salt out least strongly) to nitrate, which is consistent observations. However, methyl glyoxal is expected to interact more strongly with sulfate than chloride, so it should salt in least (or salt out most strongly) to chloride, where as it salts out of sulfate most strongly. This is clearly inconsistent with observations and provides further indications that the substitution of a water molecule with a glyoxal monohydrate or methyl glyoxal monohydrate in the hydration shell of an anion is not the only effect driving salting.

The most unusual salting constant measurement is that for glyoxal in sodium oxalate. This shows the incredibly strong salting in constant of -6.3 M^{-1}, as observed in Table 5.1. However, it is predicted by the quantum calculations to behave quite similarly to sulfate, as observed in Table 5.2. To determine if the measured salting constant is within the uncertainty of the calculations, we can do an analysis similar to the one in Kurtén et al. (2015). Briefly, they derive an equation for $K_{H,salt}$:

$$K_{H,salt} = K_H \left(1 + K_{hyd1} + K_{hyd2}K_{hyd1} + \frac{[C_2O_4^{2-}]}{[H_2O]} \left(K_{hydr1}K_{R2} + K_{hyd2}K_{hyd1}K_{R3}\right)\right) \quad (5.4)$$

Table 5.2: Calculated ΔG, ΔG range assuming ±2 kcal/mol, K, K range assuming ±2 kcal/mol for glyoxal and methyl glyoxal

Ion	ΔG (kcal/mol)	ΔG range (kcal/mol)	K	K range
		Glyoxal		
Cl^-	-2.61	-0.61 to -4.61	88	2.8 to 2700
NO_3^-	-5.26	-3.26 to -7.26	8400	270 to 260000
SO_4^{2-}	-5.48	-3.48 to -7.48	12000	390 to 380000
$C_2O_4^{2-}$	-5.62	-3.62 to -7.62	16000	500 to 480000
Na^+	0.50	2.50 to -1.50	0.42	.014 to 13
NH_4^+	0.28	2.28 to -1.72	0.62	0.020 to 19
		Methyl glyoxal		
Cl^-	-0.75	1.25 to -2.75	3.6	0.12 to 110
NO_3^-	-2.45	-0.45 to -4.45	67	2.2 to 2100
SO_4^{2-}	-1.89	0.11 to -3.89	26	0.83 to 800
$C_2O_4^{2-}$	-3.16	-1.16 to -5.16	230	7.3 to 7100
Na^+	1.46	3.46 to -0.54	6100	0.0026 to 2.5
NH_4^+	0.38	2.38 to -1.62	1600	0.017 to 16
		IEPOX		
SO_4^{2-}	-1.65	0.35 to -3.65	17	0.55 to 528
		IEPOX tetrol		
SO_4^{2-}	-1.88	0.12 to -3.88	25	0.81 to 784

where K_{hyd1} is the equilibrium constant for the first hydration of glyoxal with a value of 203 (Ervens and Volkamer, 2010), K_{hyd2} is the equilibrium constant for the second hydration of glyoxal with a value of 350 (Ervens and Volkamer, 2010), K_{R2} is the equilibrium constant for the displacement of a water in the hydration shell of oxalate by glyoxal monohydrate, and K_{R3} is the equilibrium constant for the replacement of a water molecule in the hydration shell of oxalate by glyoxal dihydrate.

The values in Table 5.2 were calculated for the displacement of a water molecule by glyoxal monohydrate, since in Kurtén et al. (2015) they found that the monohydrate bound more strongly than the dihydrate by 1.76 kcal/mol. Assuming that this will hold true for oxalate as well, the ΔG values for glyoxal monohydrate is -5.62 kcal/mol and the value for glyoxal dihydrate is -3.86 kcal/mol. These correspond to K_{R2} and K_{R3} values of 15600 and 757, respectively, at 293 K. Substituting these values in, we obtain:

$$K_{H,salt} = K_H \left(72658 + \frac{[C_2O_2^{2-}]}{[H_2O]} (43500000) \right) \tag{5.5}$$

Further following the work of Kurtén et al. (2015), we normalize to water and convert to concentration of oxalate (assuming a the molar density of water is 55.5 mols/kg) and we obtain the following equation:

$$\log \frac{K_{H,w}}{K_{H,salt}} = -\log(1 + 14.4 c_{oxalate}) \tag{5.6}$$

where $c_{oxalate}$ is the molality of the oxalate solution. This is not linear with the concentration of oxalate, K_S value is expected to vary depending on the oxalate concentration chosen. Using the value of the two concentrations measured in the lab (0.075 M and 0.15 M), the average K_S value is calculated to be -3.78. This underestimates the measure K_S value, which is not surprising given that the calculated ΔG values are so similar, but the actual salting behavior is so different.

However, the ΔG values have a 2 kcal/mol uncertainty. If they are changed by 1 kcal/mol so that ΔG for glyoxal monohydrate is -6.62 kcal/mol and the ΔG for glyoxal dihydrate is -4.86 kcal/mol, we obtain the following equation:

$$\log \frac{K_{H,w}}{K_{H,salt}} = -\log(1 + 80.25 c_{oxalate}) \tag{5.7}$$

Table 5.3: Molar volume and estimated dielectric constant values for glyoxal, methyl glyoxal, IEPOX, and the IEPOX tetrol. Molar volumes were calculated in-house. Dielectric constant was taken to be that for glycerol and the value was taken from the CRC Handbook for Chemistry and Physics.

Molecule	Molar Volume (cm^3/mol)	Dielectric Constant
Glyoxal	42.23	45.53
Glyoxal monohydrate	52.49	45.53
Glyoxal dihydrate	56.88	45.53
Methyl glyoxal	59.49	45.53
Methyl glyoxal monohydrate	60.61	45.53
IEPOX	91.03	45.53
IEPOX tetrol	92.54	45.53

If we plug in the $c_{oxalate}$ values used to measure the salting constant and take the average, we obtain a K_S of -9.36. This now over-estimates the measured salting constant, but indicates that matching the measured salting constant is possible within the uncertainty of the ΔG calculations. In fact, if the calculated ΔG value is increased by only 0.5 kcal/mol so that the value for glyoxal monohydrate is -6.12 kcal/mol and the value for glyoxal dihydrate is -4.36 kcal/mol, we obtain an averaged salting constant of -6.29, which matches the measurement quite closely. Thus it is possible that the very strong salting behavior of glyoxal in oxalate solutions could be due to a strong interaction of glyoxal with oxalate.

5.3.2 Literature Models of Salting

Several theories have been proposed in the literature to explain salting out (typically of small aromatics such as benzene, toluene, and xylenes) and predict salting constants. Values used for the calculations are given in Table 5.3 and 5.4 for organic solute parameters and inorganic ion parameters, respectively.

5.3.2.1 Debye Theory

Debye and McAulay (1925) proposed a theory for predicting salting constants based primarily on ionic charge, ion size, and change in dielectric constant of the organic solute in water compared

Table 5.4: Properties of inorganic ions used for salting constant calculations. [a]Kaulgud and Pokale (1995). [b]Vetter et al. (1991). [c]Marcus (2013). [d]Calculated as described in Mukerjee (1961). [e]Millero (1971). [f]Value for HPO_4^{2-} from Millero (1971).

Ion	Radius ($\mathring{A}$)	V_S (cm^3/mol)	$\overline{V_S^0}$ (cm^3/mol)
Na+	1.845[a]	4.3[c]	-1.2[e]
NH_4^+	2.179[a]	13.0[c]	17.9[e]
Me_4N^+	3.366[a]	55.4[c]	89.6[e]
Bu_4N^+	4.843[a]	158.6[c]	275.7[e]
Cl^-	1.803[a]	23.8[c]	17.8[e]
Br^-	1.966[a]	30.3[c]	24.7[e]
NO_3^-	2.126[a]	20.2[c]	26.2[e]
SO_4^{2-}	2.20[a]	61.5[c]	14.0[e]
$C_2O_4^{2-}$	3.2[b]	147.1[d]	16.0[e]
PO_4^{3-}	2.40[b]	62.07[d]	7.7[f]

with a pure organic solution. They quantify salting through the equation:

$$logf = \alpha\nu n' \frac{\sum \nu_i z_i^2}{\nu} \frac{\epsilon^2}{2D_0 akT} \tag{5.8}$$

where nu is the total number of ions, n is the concentration of salt, ν_i is the number of ions of species i, z_i is the charge of ions of species i, ϵ is the charge of the electron (4.77×10^{-10} stat couloumbs), D_0 is the dielectric constant of water (80.4), a is the average radius of the salt (cm), k is the Boltzmann constant (1.37×10^{-16} erg/K), T is the temperature (K), and α is the dielectric decrement. Therefore, this can be rewritten as:

$$logf = K_S n' \tag{5.9}$$

where

$$K_S = \alpha \frac{\sum \nu_i z_i^2}{a} \frac{\epsilon^2}{2D_0 kT} \tag{5.10}$$

According to Saylor et al. (1952) α can be calculated as:

$$\alpha = \frac{(D_0 - D_B)\,\partial V_B}{D_0} \tag{5.11}$$

where D_0 is the dielectric constant of water, D_B is the dielectric constant of the organic solute, and ∂V_B is the volume of an organic solute molecule, calculated from the molar volume of the organic solute. We were unable to find published dielectric constants for either glyoxal or methyl glyoxal. A survey of the CRC Handbook for Chemistry and Physics listed glycerol ($C_3H_8O_3$) as the species with the largest dielectric constant of small organics (C_2 or C_3) containing only C, H, and O. The dielectric constant for glycerol, 46.53, was thus used as D_B for both glyoxal and methyl glyoxal. Molar volumes for the species were calculated in-house, and effective ionic radii were taken from Kaulgud and Pokale (1995) when available and from Vetter et al. (1991) otherwise (oxalate, phosphate).

Results of these calculations are shown in Figure 5.2 (glyoxal), Figure 5.3 (methyl glyoxal), and the calculations for the monohydrates are given in Table 5.1. All values calculated are positive, that is, this theory predicts that both glyoxal and methyl glyoxal should salt out of all solutions.

The dielectric constant for the organic solute is what determines whether the Debye theory will predict salting in or salting out. If the dielectric constant of the solute is less than water, the theory will predict salting out; if it is larger than the value for water the solute will salt in. Unfortunately, measured values of the dielectric constant for glyoxal and methyl glyoxal are unavailable. The largest value listed in the CRC Handbook of Chemistry and Physics for molecules with 2 or 3 carbon atoms and containing only carbon, hydrogen, and oxygen was used as a proxy, and this value is still approximately half that of water. Therefore, this is likely an upper limit on the actual dielectric constants for these molecules and thus a lower limit on the calculated salting constants as a decrease in the dielectric constant will result in an increase in the salting constant. Therefore, we believe that while the selection of the dielectric constant will influence the absolute magnitude of the predicted salting constants, it is unlikely to affect the sign and even if the correct dielectric constants were to be obtained, the molecules would still be predicted to salt out.

As observed in Figures 5.2 and 5.3, the salting constants are grouped together with similar values for ammonium nitrate, sodium nitrate, sodium chloride, tetramethylammonium bromide, and tetrabutyl ammonium bromide (all of the -1 anions), ammonium sulfate and sodium oxalate (-2 anions) and sodium phosphate (-3 anion). Therefore, the charge of the species is the main driving force for the magnitude of the salting constant in this method. The mean diameter of the salt drives the trends within an ion charge cluster, with an inverse correlation between the size of the salt and the predicted salting constant.

As observed in Table 5.1, this theory does not entirely capture the relative order of the salting constants. It correctly predicts that for methyl glyoxal, ammonium sulfate should have a stronger salting out effect than ammonium nitrate, sodium nitrate, and sodium chloride but it does not get the order of these three salts correct. Additionally, it does not predict that tetrabutylammonium bromide should have the greatest effect on salting out for methyl glyoxal. It does, however, predict salting values that fairly closely match the measurements. Because the value of the dielectric constant used for these calculations is likely an upper limit, these are lower limits for salting constant values.

Figure 5.2: Salting constants for unhydrated glyoxal (solid lines), glyoxal monohydrate (dotted lines), and glyoxal dihydrate (dashed lines) calculated using Debye theory.

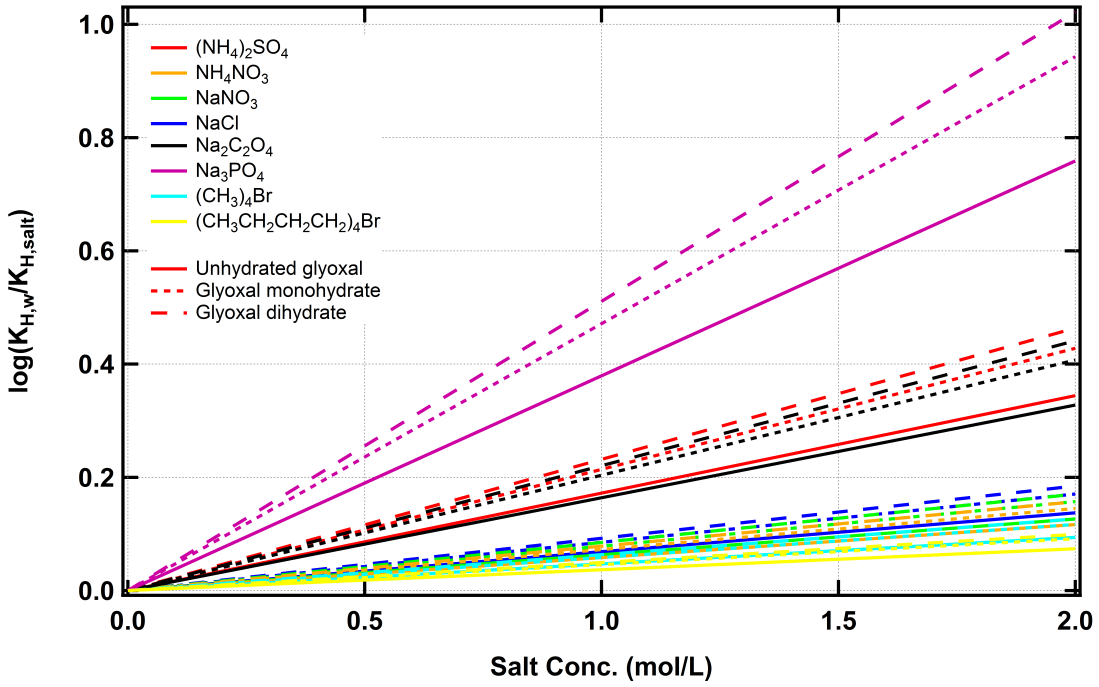

Figure 5.3: Salting constants for methyl glyoxal measurements (solid lines), and calculations for unhydrated methyl glyoxal (dotted lines) and methyl glyoxal monohydrate (dashed lines) using Debye theory.

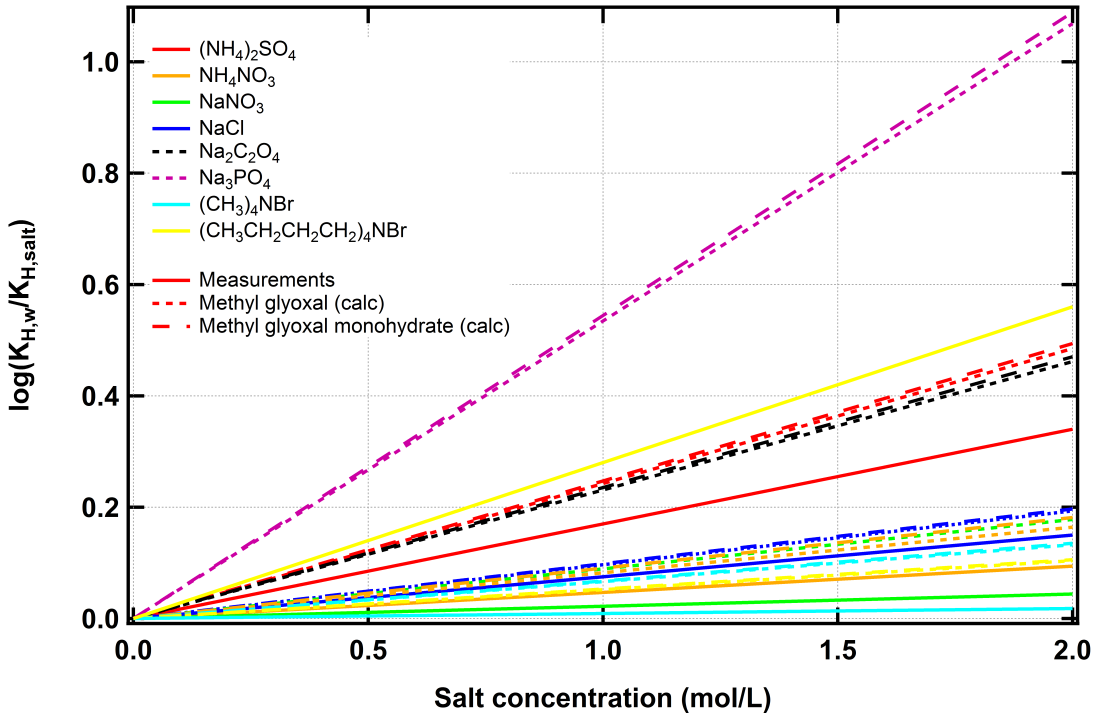

5.3.2.2 McDevit and Long Theory

McDevit and Long (1952) proposed a theory based on internal pressure to predict the salting constants for benzene in a number of salts. They describe salting through the equation:

$$K_S = \frac{\overline{V_i^0}}{RT}\frac{dP_e}{dC_S} = \frac{\overline{V_i^0}\left(V_S - \overline{V_S^0}\right)}{RT\beta_0} \tag{5.12}$$

where $\overline{V_i^0}$ is the partial molar volume of the organic species at infinite dilution, R is the gas constant, T is the temperature, $\frac{dP_e}{dC_S}$ is the change in effective pressure with salt concentration which can be calculated from the compressibility of salt solutions, V_S is the molar volume of salt as a molten liquid, $\overline{V_S^0}$ is the partial molar volume of salt at infinite dilution, and β_0 is the compressibility of water. This equation quantifies their description of salting the total volume of solution contracts upon adding salt to water, resulting in a compression of the solution (described by $V_S - \overline{V_S^0}$). This makes it more difficult to insert a non-electrolyte of volume in the solution because the organic creates a cavity in the aqueous solution. The added difficulty of inserting an organic species results in salting out. They also describe this solution contraction as forming an internal pressure, which forces the organic species out of solution. They compare their calculated values against measurements for benzene and find that this theory over-predicts salting constants by a factor of two to three. They explain that this is because the volume of the organic molecule is treated as continuous, rather than as discrete molecules and that adding a correction factor for the fraction of the volume taken up by the ion improves quantitative agreement (McDevit and Long, 1952).

Salting constant calculations using this theory are given in Figure 5.4 (glyoxal, glyoxal monohydrate, and glyoxal dihydrate) and Figure 5.5 (methyl glyoxal and methyl glyoxal monohydrate). McDevit and Long recommend the use of $\frac{dP_e}{dC_S}$ whenever possible; however these values are not available for many salt solutions whereas V_S and $\overline{V_S^0}$ are. $\overline{V_i^0}$ was calculated in-house. When available, V_S and $\overline{V_S^0}$ values were taken from work by (Marcus, 2013), who obtained them from (Millero, 1971). When V_S values were unavailable (for $C_2O_4^{2-}$ and PO_4^{3-}), they were calculated as described by Mukerjee (1961). No values were available for PO_4^{3-}; the value for HPO_4^{2-} was used instead as its size is expected to be similar to PO_4^{3-}. Tables 5.3 and 5.4 contain the values used in this work

Figure 5.4: Salting constants for unhydrated glyoxal (solid lines), glyoxal monohydrate (dotted lines) and glyoxal dihydrate (dashed lines) for a variety of salts calculated using McDevit and Long theory.

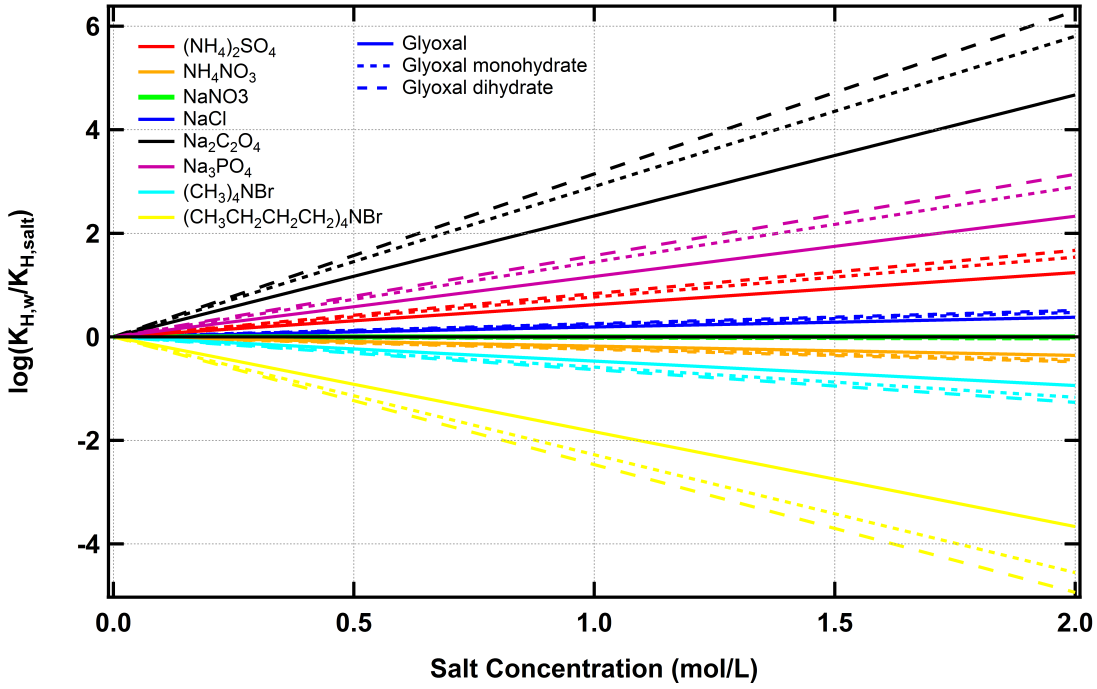

Figure 5.5: Salting constants for methyl glyoxal measurements (solid lines), methyl glyoxal (dotted lines) and methyl glyoxal monohydrate (dashed lines) for a variety of salts calculated using McDevit and Long theory.

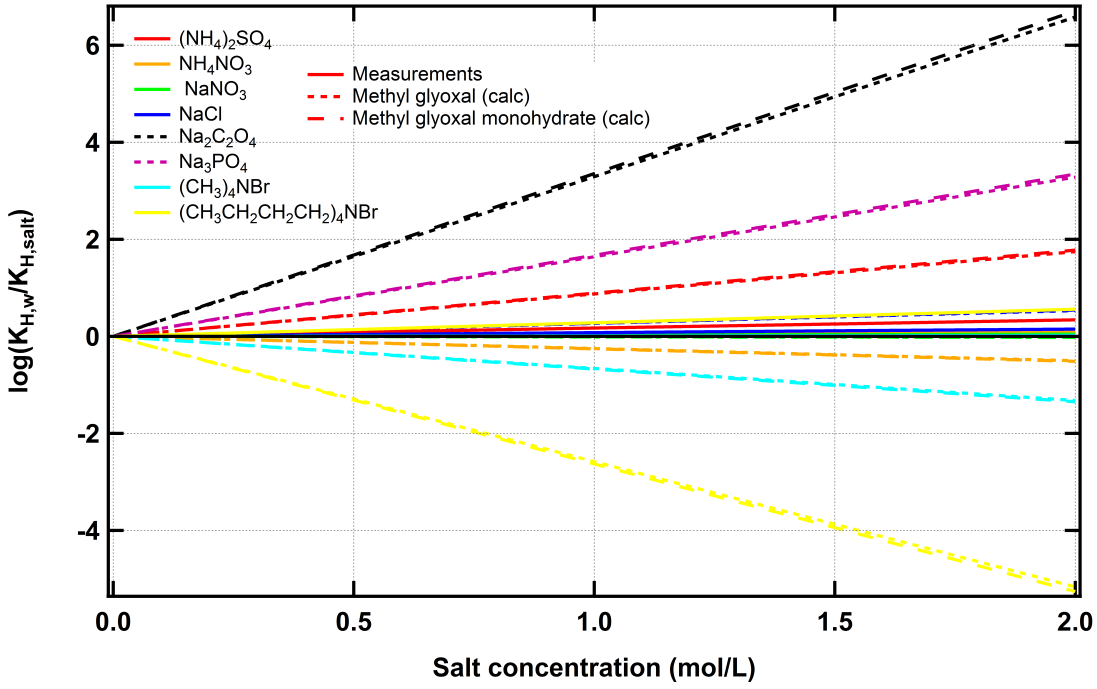

for calculations. The partial molar volumes for methyl glyoxal and methyl glyoxal monohydrate are very similar, so these lines are typically very close together. The partial molar volumes for glyoxal monohydrate and glyoxal dihydrate are larger than the value for glyoxal, so these lines are somewhat more spread out than for methyl glyoxal. As seen in Figure 5.5 and in Table 5.1, the calculations significantly over-estimate the measured salting constants by a factor of about 5. This is somewhat greater the factor of 2-3 that McDevit and Long quote for benzene. Because some of the ions (e.g. tetrabutylammonium) are so much larger than glyoxal or methyl glyoxal, it is unlikely that organic volume correction factor will make a significant difference for some of the systems as the ion volume will dominate over the organic solute volume and the correction factor will thus be small. Additionally, the volume correction will be unable to change the sign of the salting factor.

Unlike the Debye theory, this theory produces constants for salting in. This presumably results from the expansion of solution upon the addition of salts (when is negative or when the volume of the salt at infinite dilution is larger than the volume of the salt in the molten state) but aside from noting that this theory can predict salting in, it is not discussed in their work. The implied volume expansion was not observed in the lab.

Like the Debye work, this focuses on effects due to the properties of the salt solutions rather than interactions between the organics and salt. Salting in is calculated for both glyoxal and methyl glyoxal for ammonium nitrate, tetramethyl ammonium bromide, and tetrabutyl ammonium bromide. Because the salting depends only on the properties of the salt, this is predicted for the same salts for both molecules. This is clearly not the case, as glyoxal salts in regardless of the salt and glyoxal salts out, regardless of the salt. For the species where this theory predicts salting out for methyl glyoxal, it gets the order correct: ammonium sulfate is calculated to have more of an effect than sodium chloride. McDevit and Long also report that their theory predicts that chloride has more of an effect than nitrate when they apply it to salting constant calculations for benzene, which is further consistent with our results for methyl glyoxal.

5.3.3 Multifactor K_S Calculation

Clearly, none of the above prediction methods fully captures the complexities of salting. Because glyoxal salts in and methyl glyoxal salts out, salting in versus out must partially be determined by the properties of the organic molecule, which is a factor that McDevit and Long theory does not capture as it predicts the sign of salting based entirely on salt properties. The Debye theory and the quantum calculations both determine the sign of salting based on molecular properties (the dielectric constant for Debye, electrostatic interactions between the organic solute and the anion for the quantum calculations), but neither of these is fully correct either. Debye theory predicts that both glyoxal and methyl glyoxal should salt out because their dielectric constant is very likely lower than that of water. The quantum calculations predict that both glyoxal and methyl glyoxal should salt in due to the favorable interactions of the hydrated forms with the anions.

However, each of these likely plays a part in the very complicated interactions that result in salting behavior. It is likely the strength of the interaction of the organic molecule with the anion along with other factors that determine whether a molecule salts in or out. To quantify this, a fit was made to the equation:

$$K_{S,meas} = C_1 \times \Delta G_{anion} + C_2 \times K_{S,Debye} + C_3 \times K_{S,McDevit} \tag{5.13}$$

where $K_{S,meas}$ is the measured salting constant for glyoxal or methyl glyoxal in ammonium sulfate, ammonium nitrate, sodium nitrate, or sodium chloride, ΔG_{anion} is the strength of interaction between the monohydrate and the anion, $K_{S,Debye}$ is the salting constant calculated for the monohydrate in the aforementioned salts using Debye theory, and $K_{S,McDevit}$ is the salting constant calculated for the monohydrates in the aforementioned salts using McDevit and Long theory.

Once the fit coefficients were determined, K_S was calculated for each of the molecule-salt concentrations. The correlation between the calculated KS and the measured K_S is given in Figure 5.6. The calculated versus measured K_S values are plotted as solid red dots. The equation is clearly able to reproduce salting in for glyoxal (these values are clustered in the lower left hand corner of the plot) and simultaneously calculate salting out for methyl glyoxal (these values cluster in the

upper right corner of the plot). If the calculation perfectly reproduced the measurements, all of the data points would be expected to fall on the 1:1 line (solid black line). This is not the case, and the dashed red line gives the fit between the two. It has a slope 0.835 which is somewhat less than one and slightly under-estimates the methyl glyoxal values, but the R^2 value is 0.833, indicating a high degree of correlation between the two.

IEPOX is a diol and in the aqueous phase, the epoxide ring is opened by acid catalysis, resulting in a tetrol. Because both IEPOX and the tetrol product are poly-ols, they are expected to interact with the anions in a similar manner as the glyoxal and methyl glyoxal hydrates. Therefore, this empirical fit is expected to reasonably estimate the salting constants for these molecules. The interaction between IEPOX and sulfate is shown in Figure 5.7.

The values for the literature calculations for IEPOX and the IEPOX tetrol in ammonium sulfate are given in Table 5.1. Because they have similar molar volumes, these theories predict that they will have very similar salting constants. Their molar volumes are significantly larger than those for glyoxal and methyl glyoxal so they are calculated to salt out more for a given salt. When these values and the ΔG of interaction are plugged in to the poly-parameter fit, we calculate that IEPOX is expected to salt out with a salting constant of 0.24 M^{-1} and the tetrol is expected to salt out with a salting constant of 0.23 M^{-1}. Therefore, IEPOX and the tetrol are expected to behave similarly to methyl glyoxal in that they salts out of ammonium sulfate moderately weakly.

This is in contrast with Xu et al. (2015) who found that in the southeastern United States, IEPOX SOA correlates strongly with sulfate, to the extent that the authors state that "isoprene-derived SOA is directly mediated by the abundance of sulfate" (Xu et al., 2015). This apparent discrepancy could be explained by additional products formed as part of IEPOX SOA. In the particle phase, IEPOX can react with sulfate to form organosulfates. Additionally, sulfate can act as a nucleophile to catalyze the ring opening of the ring to form the tetrol. Thus while this discrepancy is not yet resolved and the formation of IEPOX SOA is an active area of investigation, this likely salting out is not necessarily inconsistent with the correlation of IEPOX SOA with sulfate.

Figure 5.6: Correlation between measured K_S values and K_S values calculated from the fit (red circles: glyoxal; blue circles: methyl glyoxal). The 1:1 line is a solid black line; if the equation perfectly reproduced the K_S measurements all points would be expected to lie on this line. The fit of the calculated K_S values to the measured K_S values is given by the green dashed line. This has an R^2 value of 0.833 showing a high degree of correlation.

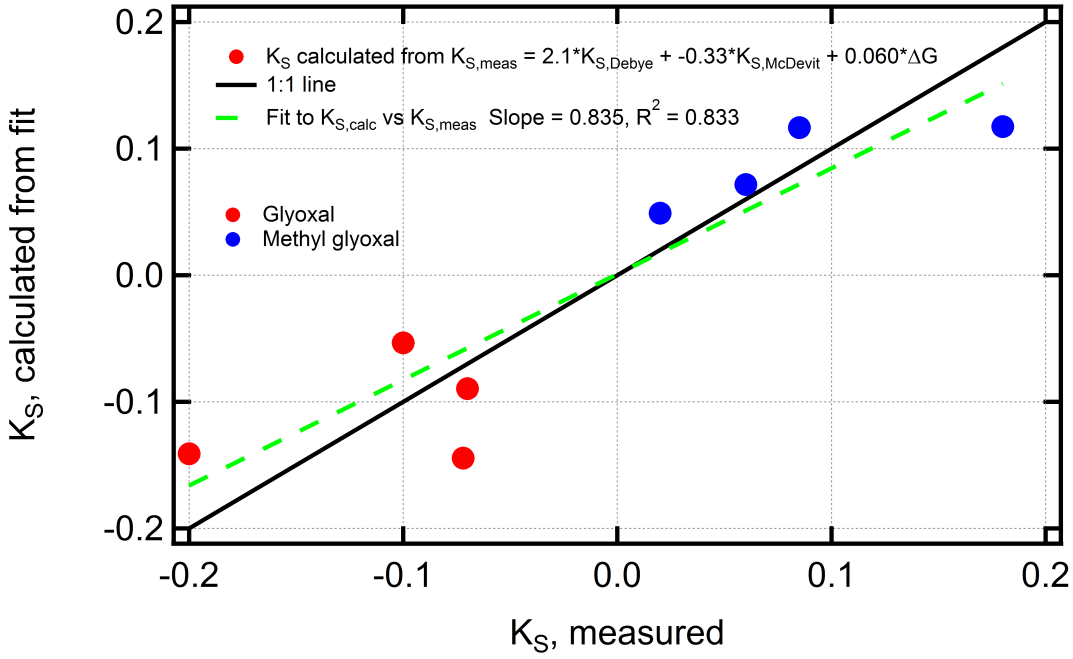

Figure 5.7: Modeled interaction between IEPOX and sulfate. The OH groups on the IEPOX molecule replace a water molecule in the sulfate hydration shell.

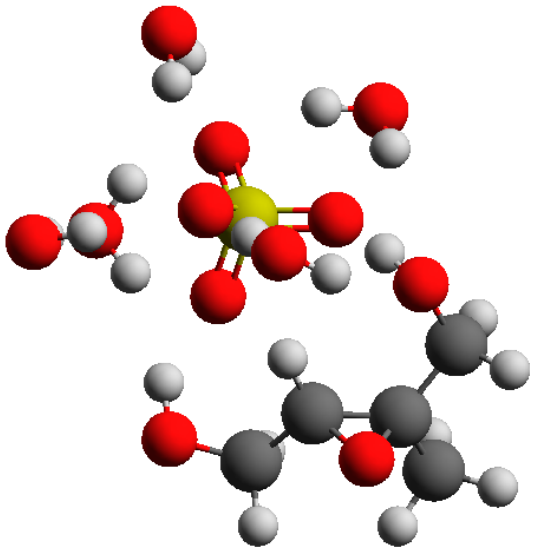

5.4 Conclusions

In this work, we report the first quantum calculations for the interaction of glyoxal, methyl glyoxal, and trans-β-IEPOX with aerosol-relevant salts. The quantum calculations all predict electrostatically-favorable interactions between the organic solute molecules and the anions. Based on these results, all three molecules would be expected to salt in to all aerosol salt solutions. This is in contrast with laboratory measurements which show that while glyoxal does indeed salt in to solutions of aerosol-relevant salts, methyl glyoxal salts out.

We therefore turn to literature explanations, and find that these are also unable to fully explain the salting behavior of glyoxal and methyl glyoxal. These theories were designed to explain the salting behavior of small aromatics such as benzene and toluene and thus are are not expected to capture the favorable interactions of the small water-soluble molecules with salt anions. These rely more on properties of the salt, such as its size or compressibility, rather than on properties of the organic to predict salting constants. Nevertheless, they do include important repulsive forces that likely contribute to methyl glyoxal salting out rather than salting in.

We fit a poly-parameter relationship to the predicted salting constants of two such salting theories as well as the ΔG values from the quantum calculations and obtain a high degree of correlation. We use this to predict the salting constant for tran-β-IEPOX and find that it likely salts out to a similar extent as methyl glyoxal. Thus the recently observed enhancement of isoprene-SOA in the presence of sulfate (Xu et al., 2015) is not likely due to IEPOX salting in. Rather, it could be due to IEPOX products, especially tetrols, salting in or the enhancement in organosulfate formation.

Chapter 6

Imidazole Formation from Glyoxal in Model Ammonium Sulfate Aerosol and Enhancement from NH_3

This chapter to be submitted to Atmos. Chem. Phys. Discus. as: Waxman, E. M., Slowik, J. G., Jakob, R., Bianchi, F., Hoffman, T., Holzinger, R., Huang, X.H.H., Kampf, C., Klein, F., Koenig, T., Krapf, M., Kumar, N.K., Laskin, A., Laskin, J., Oyama, B.S., Maxut, A., Noziére, B., Piazzalunga, A., Wang, S., Yu, J.Z., Baltensperger, U., Dommen, J., Prévôt, A.S.H., and Volkamer, R., Imidazole Formation from Glyoxal in Model Ammonium Sulfate Aerosol

Imidazoles are nitrogen-containing ring species that contribute to brown carbon in atmospheric aerosols. They can be formed from reactions of glyoxal with ammonium sulfate. Here, we tie the aerosol-phase formation of these imidazoles directly to glyoxal through the use of isotopically-labeled glyoxal. In the literature there are several proposed mechanisms for imidazole formation, all based on reactions in bulk solutions. We combine imidazole measurements from four different instruments and use time-resolved data to elucidate a mechanism for imidazole formation in the aerosols that differs slightly from the published bulk mechanisms. Additionally, we varied experimental conditions including relative humidity and particle pH to determine under which conditions imidazoles are most readily formed. We find a significant enhancement in total aerosol formation, imidazole formation, and total aerosol N/C with the addition of gas-phase NH_3 and at moderate relative humidity (75%). Additionally, we use size-resolved data to determine the impact of aerosol surface to volume ratios on imidazole formation and see if the reactions are surface-enhanced.

6.1 Introduction

Aerosol particles are the dominating factor in the uncertainty in the magnitude of the change in anthropogenic radiative forcing (Stocker et al., 2013). They contribute to changes in radiative forcing by both scattering and absorbing light. Predominantly inorganic aerosols, such as ammonium sulfate or sodium chloride, scatter light and decrease the amount of incident radiation (Toon et al., 1976). Predominantly black aerosols, such as soot particles, absorb light and reemit it as heat, increasing radiative forcing (Bond and Bergstrom, 2006; Bond et al., 2013). However, many aerosols fall between these extremes and contain both inorganic species as well as some organic carbon. These particles can both absorb and scatter light, especially if they contain brown carbon, which is organic carbon that absorbs at visible wavelengths.

Brown carbon can be formed from a number of different pathways, but one that is of recent interest is the formation of brown carbon through aqueous-phase processing, especially the reaction of small aldehyde with nitrogen-containing species such as ammonia or amines (De Haan et al., 2009b,a; Noziere et al., 2009; Shapiro et al., 2009; De Haan et al., 2010; Kampf et al., 2012b; Powelson et al., 2013). The reactions between glyoxal and ammonium can form imidazoles, which are conjugated nitrogen-containing rings. There are a number of proposed mechanisms for imidazole formation in the literature, and important structures, full names, and abbreviations are shown in Figure 6.1.

Yu et al. (2011) combined glyoxal (1-1.5 M) and ammonium sulfate (1-1.6 M) and studied the resulting product formation via NMR and UV-Vis spectroscopy. They identified imidazole (IM), imidazole-2-carboxaldehyde (IC), hydrated imidazole-2-carboxaldehyde (HIC), and glyoxal-substituted hydrated imidazole-2-carboxaldehyde (HGI), and based on their kinetic studies, proposed that IM and HIC are formed as first generation products, in equilibrium with HGI and IC, respectively. Kampf et al. (2012b) built upon this work. They mixed glyoxal (0.01 1.5 M) with ammonium sulfate (3.0 M) and identified a number of imidazole species, including some containing two rings using HPLC-ESI-MS. He proposes that IM, IC and HIC are all formed as first generation

Figure 6.1: Literature mechanisms for the formation of imidazole (IM), imdazole carboxaldehyde (IC), and bisimidazole (BI). Top panel: Mechanism from Yu et al. (2011) for the formation of IM and IC. Lower panel: Mechanism from Kampf et al. (2012b) for the formation of IM, IC, and BI.

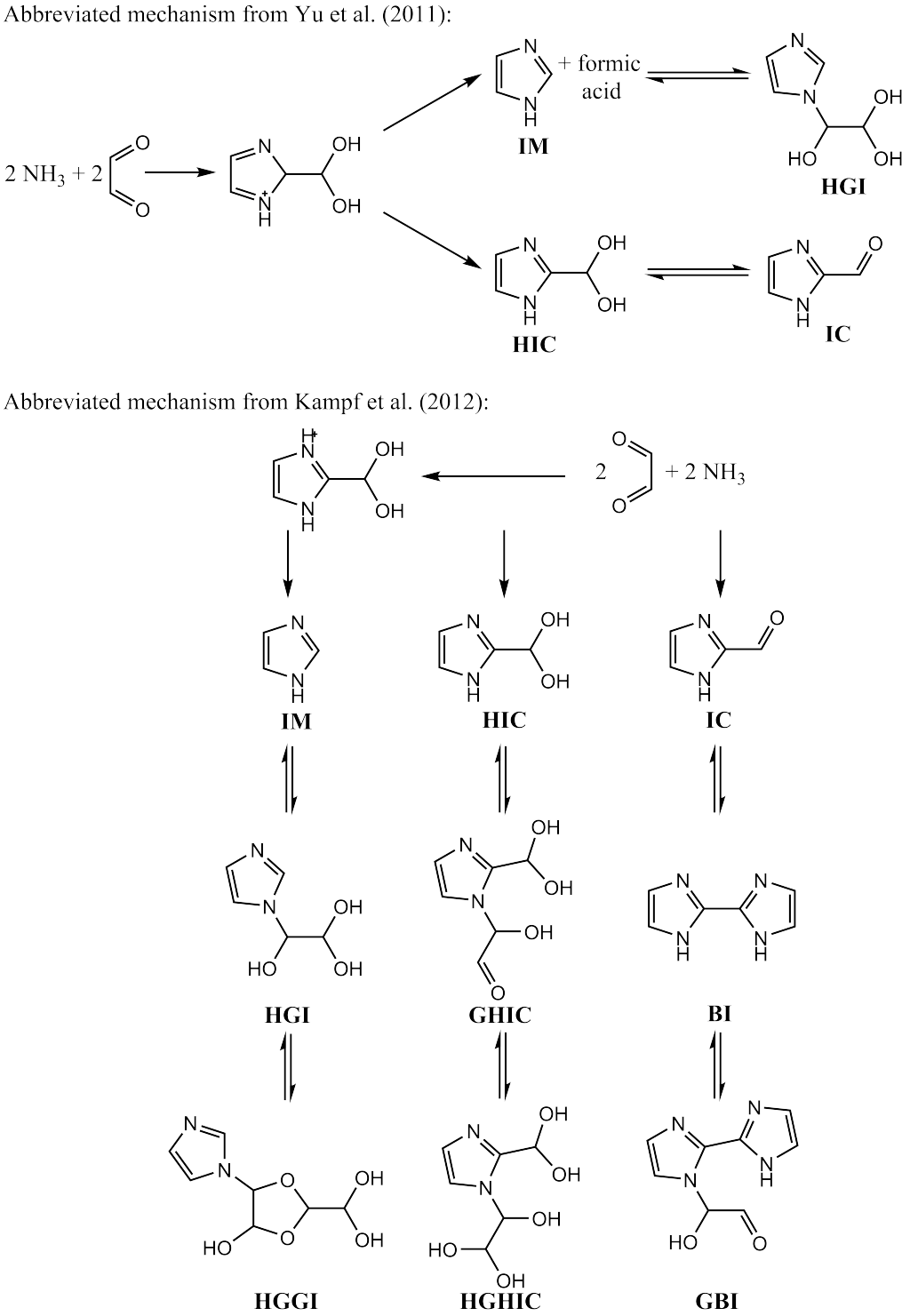

reaction products, and then IC can go on to form 2,2'-biimidazole (BI) as a second generation product based on kinetic studies on BI formation Kampf et al. (2012b). Abbreviated mechanisms from these works are shown in Figure 1, with species labeled. However, this work (and indeed much work on brown carbon formation from small aldehydes and ammonium or amines) was done in the bulk phase at lower-than-aerosol salt concentrations. Here, we present a study of imidazole formation by a suite of particle-phase instrumentation on model aerosols that have been formed in an atmospheric simulation chamber.

6.2 Experimental

6.2.1 PSI Chamber Experiments

Experiments were performed at the Paul Scherrer Institut in Villigen, Switzerland (Paulsen et al., 2005). This is a 27 m^3 Teflon chamber surrounded by wooden housing to control the chamber temperature. The chamber contains four banks of UV lights (Philips, Cleo performance 100W/ R) used for photolysis. The wooden housing is lined with aluminum panels to maximize reflection and illuminate the chamber homogeneously. Experiment 0 also used four 4 kW Xe-arc lamps with 410-nm long-pass filters to illuminate the aerosol with visible light over the course of the experiment as a comparison to the experiments done two years prior and published in Kampf et al. (2013).

Experiments were performed in the following manner: the chamber was first humidified to the desired relative humidity (62-85% RH) by flowing air over 18 MΩ water (Millipore, Bedford MA) heated in a Pyrex bulb and into the chamber. The chamber was then seeded with ammonium sulfate aerosol by passing a solution (nominally 1.6 g ammonium sulfate/L, Sigma Aldrich) through an atomizer built in-house until the inorganic seed concentration reached about 30 $\mu g/m^3$ sulfate. Particles were injected directly in to the chamber without drying to ensure that they remained deliquesced or metastable (depending on the experimental RH). NO (100 ppb) was then added to the chamber to titrate any O_3 to NO_2 and ensure the only oxidant in the chamber was OH. HONO was prepared by mixing $NaNO_2$ (0.003 M) and H_2SO_4 (0.01 M) which were continuously

mixed using a peristaltic pump (Taira and Kanda, 1990). The resulting HONO was added to the chamber at to a concentration of 10 ppbv. The chamber was allowed to mix for half an hour, and then if NH_3 was used it was added to the chamber at a concentration of nominally 20 ppb after conditioning the injection lines for twenty minutes.

UV lights were then turned on for 3 minutes, off for 3 minutes, and on for an additional 3 minutes. This first lights on period was a chamber cleanliness test any organics that partition off of the chamber walls would be oxidized by the OH radicals and would be expected to partition to the seed aerosols, resulting in an increase in the organics signal from the AMS. Acetylene (1 ppm) was injected in to the chamber. If using NH_3, another 20 ppb was injected after additional conditioning of the lines. The chamber was allowed to mix for 30 minutes, and then lights were turned on again (nominally 3 minutes on, 5 minutes off, 3 minutes on, but was monitored in real time to produce approximately 20 ppb) glyoxal was produced via the following reactions (Hatakeyama et al., 1986):

$$\text{R1: HONO} + h\nu \rightarrow \text{OH} + \text{NO}$$

$$\text{R2: } C_2H_2 + \text{OH} \rightarrow C_2H_2O_2 + \text{OH } (\sim 65\% \text{ yield})$$

$$\text{R3: } C_2H_2 + \text{OH} \rightarrow \text{formic acid} + \text{CO } (\sim 35\% \text{ yield})$$

The chamber was then allowed to sit for four hours, followed by another glyoxal production. This was repeated once more, and then the chamber was allowed to sit for approximately eight hours. Air was removed from the chamber due to the large number of filter samples that were taken over the course of the experiment. A small continuous dilution flow at the same relative humidity as the experiment was continuously added to the chamber to make up for the volume lost due to filter sampling.

All experiments were performed at 20°C. Two experiments, Experiment 16 and Experiment 17, were performed with 13C-labeled glyoxal ($^{13}CHO^{13}CHO$) for mechanistic studies. A variety of salts were used as seed aerosol including $(NH_4)_2SO_4$, NH_4NO_3, K_2SO_4, $NaNO_3$, and NaCl. However, this work will focuses on $(NH_4)_2SO_4$ (AS) experiments. A list of experimental conditions

Table 6.1: List of experiments and parameters varied during the campaign. AS: ammonium sulfate. Vis: 410-nm long-pass filtered light from Xe-arc lamps on during the entire experiment. Dark: The experiment was kept in the dark except for short UV pulses to produce glyoxal.

Exp.	Date	Seed	RH (%)	NH_3	Light	Max SO_4 ($\mu g/m^3$)	Max Org ($\mu g/m^3$)	Max Org/SO_4
0	16–17 May 2013	AS	75	N	Vis	36	17	0.85
1	20–21 May 2013	AS	75	Y	Dark	38	22	2.6
2	23–24 May 2013	AS	75	Y	Dark	45	23	1.2
5	29–30 May 2013	AS	75	N	Dark	37	4	0.45
11	14–15 June 2013	AS	62	Y	Dark	72	3	0.25
14	22–23 June 2013	AS	85	Y	Dark	95	25	0.50
15	25–26 June 2013	AS	85	Y	Dark	–	–	–
16	29–30 June 2013	AS	85	Y	Dark	–	–	–
17	2–3 July 2013	AS	85	Y	Dark	–	–	–

for ammonium sulfate experiments is given in Table 6.1.

6.2.2 Gas-phase measurements

Gas-phase glyoxal was measured using the CU-LED-CE-DOAS (Thalman and Volkamer, 2010). Briefly, light from a blue LED is focused in to an 87 cm long optical cavity consisting of two highly reflective mirrors (R = 0.999956). The light exiting the cavity is coupled to a QE-65000 spectrometer (380-490 nm) using a fiber optic cable. The sample flow from the chamber (∼0.15 L/min) was diluted with clean air (∼0.45 L/min) to reduce the relative humidity in the sampling lines and minimize glyoxal losses to the tubing. Immediately prior to this dilution a 2 μm Teflon filter was positioned to prevent aerosols from entering the cavity and thus reducing the light intensity due to Mie scattering. The instrument measured gas-phase glyoxal, ^{13}C glyoxal, NO_2, and O_4 from the chamber with a time resolution of 1 minute. It had a glyoxal detection limit of 30 pptv. Spectral fitting was done using WinDOAS software and is calibrated from absorption cross-section reference spectra for glyoxal, ^{13}C glyoxal, NO_2, and O_4. An isotopic gas-phase glyoxal cross section for ^{13}CHO^{13}CHO was recorded previously (Goss et al., 2015), which was used to quantify gas-phase glyoxal in the ^{13}C experiments.

NO, NO_2, and NO_x were measured by a 42C NO-NO_2-NO_x monitor (Thermo Environmenal

Instruments) and a Monitor Laboratories 9841A NO_x chemiluminescene monitor. O_3 was measured by both a Monitor Laboratories Ozone Analyzer 8810 and an Environics Series 300 Ozone Analyzer.

6.2.3 Particle-phase measurements

Three filter techniques were used to measure particle-phase measurements. Particle-phase molecules were identified using nanospray desorption electrospray ionization mass spec (nano-DESI) (Roach et al., 2010). Particles were collected on aluminum foil filters in a rotating MOUDI impactor. Due to the large mass necessary ($\sim$10 μg organic mass), the sampling time varied from approximately 1 hour to 2.5 hours. After collection, filters were put in filter holders, wrapped in Parafilm, and frozen until analysis. An acetonitrile-water mixture (70%/30%, v/v) was used as the electrospray solvent. Data analysis for the nano-DESI instrument has been described previously (Roach et al., 2010). Briefly, peaks with a signal-to-noise ratio of greater than 5 were selected for analysis. Those that appeared in both the blank (aluminum foil but no sample) as well as the sample (aluminum foil with sample) were discarded. The remaining peaks were identified using the Molecular Formula Calculator (v1.1).

After imidazole (IM), imidazole carboxaldehyde (IC) and bis imidazole (BI) were identified in the aerosols, ratios were determined by adding known quantities of IM, IC, and BI to the electrospray solvent. Adenine-d1 was used as an internal standard to account for any changes in ionization efficiency due to the matrix effect of the aerosol sample. The change in signal due to the presence of IM, IC, and BI on the sample was corrected for ionization efficiency and then used to calculate the concentration of the species in the droplet. Relative ionization efficiencies of IM, IC, and BI were determined by running a series of standards with known concentrations across a blank aluminum foil filter. They were determined to be insert values here after calculations.

Particles size distributions were measured using a scanning mobility particle sizer (SMPS) built in-house using a TSI CPC 3022. This SMPS uses a recirculating filtered air system so that the relative humidity inside the SMPS is the same as that in the chamber. Therefore, deliquesced or metastable particle size distributions were measured, rather than dry particle size distributions.

Particle-phase chemical composition was measured on-line using a High Resolution Time-of-Flight Aerosol Mass Spectrometer (HR-ToF-AMS) (DeCarlo et al., 2006). Due to the high resolution of the mass spectrometer, the chemical composition of individual ions was identified up to 110 amu. Collection efficiency was accounted for by comparing AMS measurements and particle water calculations from E-AIM IV (Friese and Ebel, 2010) with SMPS measurements.

Two additional sets of filter samples were collected and analyzed by HPLC-ESI-MS. These were collected by the Mainz group (LC-ESI Mainz) and the Lyon group (LC-ESI Lyon). The LC-ESI Mainz data was collected in a time-resolved fashion. Typically one or two blanks were collected prior to the first glyoxal production. Filters were then collected approximately 30 minutes, 60 minutes, 1.5 hours, and 2 hours after each glyoxal production. Particles were collected on to quartz filters for 30 minutes and stored in glass jars with Teflon-lined caps. Filters remained frozen until analysis. One half of each filter was analyzed for particle-phase glyoxal and oligomers, and the other half was analyze for imidazoles using an Orbitrap mass spectrometer. IM, IC, and BI were quantified using calibration curves from standards (Kampf et al., 2012b). Data is available for Experiments 0-11.

LC-ESI Lyon filters were collected at the end of each experiment. Aerosols were sampled on to quartz filters for nominally 3 hours (exact time varied by experiment). Blanks were collected for a minimum of two hours and typically overnight during chamber cleaning cycles. Filters were analyzed by HPLC-ESI-MS using an Orbitrap mass spectrometer. Quantification was done with calibration curves made from commercial IM and IC standards and a BI standard synthesized in-house.

6.3 Results and Discussion

6.3.1 Proof of formation from glyoxal

The final two experiments, Experiments 16 and 17, used isotopically labeled $^{13}CHO^{13}CHO$. From these experiments, we are able to tie imidazole formation directly to glyoxal. All of the

Table 6.2: Nitrogen-containing species identified in aerosols as products of glyoxal-ammonium reactions based on their ^{13}C signature. Chemical formula of protonated species, exact mass of the protonated species, and mass defect are given for both the ^{12}C and ^{13}C analogues.

Formula	Exact mass	Mass defect	Formula	Exact mass	Mass defect
$^{12}C_3H_5N_2^+$	69.04456	-2.4	$^{13}C_3H_5N_2^+$	72.05466	-1.8
$^{12}C_4H_5N_2O^+$	97.03942	-2.3	$^{13}C_4H_5N_2O^+$	101.05281	-2.5
$^{12}C_4H_5N_2O_2^+$	113.03443	-1.1	$^{13}C_4H_5N_2O_2^+$	117.04779	-1.5
$^{12}C_6H_7N_4^+$	135.06636	-1.2	$^{13}C_6H_7N_4^+$	141.08662	-0.2
$^{12}C_6H_9N_2O_4^+$	173.05568	0.0	$^{13}C_6H_9N_2O_4^+$	179.07587	0.3
$^{12}C_8H_9N_4O_2^+$	193.07191	-0.5	$^{13}C_8H_9N_4O_2^+$	201.09864	-1.0
$^{12}C_8H_{10}N_4O_4^+$	227.07730	-0.8	$^{13}C_8H_{10}N_4O_4^+$	235.10370	-2.6

glyoxal in these experiments is isotopically labeled, so any products resulting from glyoxal have a ^{13}C signature. The chamber background has isotopic abundances, so it is dominated by ^{12}C compounds. Therefore, any products resulting from background contamination will have a ^{12}C signature. Exact masses of imidazole species identified in both ^{12}C and ^{13} experiments are given in Table 6.2 and proposed structures are given in Figure 6.2.

The masses listed in Table 6.2 and Figure 6.2 correspond to the protonated species detected by the nano-DESI, as do the chemical formulas listed in Table 6.2. The structures and chemical formulas given in Figure 6.2 correspond to the neutral species. When applicable, species that have been identified previously are named by their acronym from Kampf et al. (2012b). The fact that the ^{13}C analogues are detected means that all of these molecules are produced from glyoxal.

Notably, the ^{13}C data from Experiment 16 shows analogues of these structures that contain mixed ^{12}C and ^{13}C masses due to a small amount of residual ^{12}C glyoxal that was likely partitioned to the chamber walls. As the masses increase from 100% ^{12}C to 100% ^{13}C, the decrease in number of ^{12}C carbons is always even and the increase in the number of ^{13}C carbons is always even. For example, $^{12}C_6H_6N_4$ BI was detected, as were $^{12}C_4{}^{13}C_2H_6N_4$, $^{12}C_2{}^{13}C_4H_6N_4$, and $^{13}C_6H_6N_4$. However, no species containing an odd number of ^{12}C and ^{13}C carbons were identified (e.g. $^{12}C_5{}^{13}C_1H_6N_4$ was not detected). This is further proof that these species are formed from glyoxal; since it is a two-carbon precursor the species with both isotopes are expected to contain even numbers of each

Figure 6.2: Proposed structures of species detected in both ^{12}C and ^{13}C data. m/z corresponds to the protonated masses detected by the nano-DESI; structures and chemical formulas are given for the neutral structure.

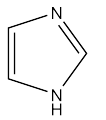

m/z 69.04456
$C_3H_4N_2$
IM

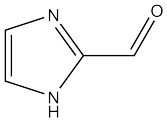

m/z 97.03924
$C_4H_4N_2O$
IC

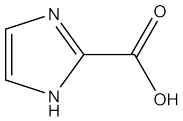

m/z 113.03443
$C_4H_4N_2O_2$

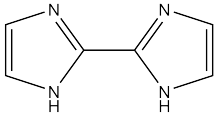

m/z 135.06636
$C_6H_6N_4$
BI

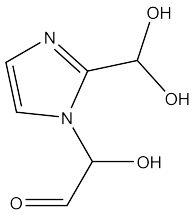

m/z 173.05568
$C_6H_8N_2O_4$
GHIC

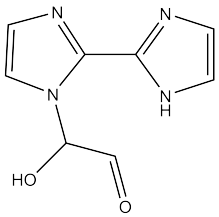

m/z 193.07191
$C_8H_8N_4O_2$
GBI

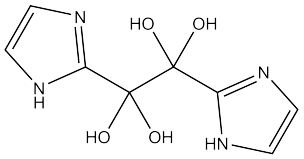

m/z 227.07730
$C_8H_{10}N_4O_4$

Table 6.3: Comparison of IM, IC, and BI detection between instruments. –: no samples were taken for this instrument during this experiment or data was not analyzed for this species. Y: species was detected. N: species was not detected above the instruments detection limit. value: maximum concentration measurement in $\mu g/m^3$. For the Mainz ESI system, sum of IC species is reported.

	IM				IC				BI			
Expt.	nano-DESI	AMS	Mainz ESI	Lyon ESI	nano-DESI	AMS	Mainz ESI	Lyon ESI	nano-DESI	AMS	Mainz ESI	Lyon ESI
0	–	0.1	0.032	0.099	–	0.017	0.008	0.032	–	0.0012	N	N
1	Y	0.85	0.580	0.856	Y	0.015	0.037	0.096	Y	0.021	0.031	1.151
2	Y	1.51	0.635	1.205	Y	0.018	0.012	0.078	Y	0.010	0.008	0.417
5	Y	0.067	0.024	0.128	Y	N	8E-4	N	Y	N	N	N
11	–	0.16	0.109	0.087	–	0.005	0.001	0.024	Y	0.001	0.003	N
14	–	1.08	–	0.10	–	0.037	–	0.04	N	0.003	–	0.042
15	Y	0.040	–	0.14	N	0.007	–	0.13	N	N	–	0.010

type of carbon.

6.3.2 IM, IC, and BI Detection

All instruments (Lyon ESI-MS, Mainz ESI-MS, nano-DES, and AMS) detected the imidazoles IM, IC, and BI in at least a subset of experiments. Detection and maximum detected concentration (if applicable) are given in Table 6.3 and shown in Figure 6.3. These species were selected for focused analysis because they are stable products with commercial or easily synthesized standards available for quantification.

The nano-DESI was used to qualitatively detect species as well as for a subset of analyses determine relative ratios of IM, IC, and BI by including internal standards for these speices. $[IM-H]^+$ was detected in Experiments 1, 2, 5, and 15 at exact mass of 69.04456 with a mass defect of -2.4 ppm on an Orbitrap mass spectrometer. The nano-DESI sampling system was not set up for Experiment 0, and filters were not analyzed for species identification of masses below 100 amu for Exp 11 or 14, so IM would not have been detected in these experiments. The nano-DESI detected $[IC-H]^+$ in experiments 1, 2, and 5 at exact mass 97.03942 with a mass defect of -2.3 ppm. This species also has a mass less than 100 amu, so it would not have been detected in Exp 11 and 14. $[BI-H]^+$ was detected in Exp 1, 2, 5, and 11, but not Exp 14 or 15 at exact mass 135.06636 with a

Figure 6.3: Comparison of IM detection for ammonium sulfate experiments. High resolution nano-DESI spectra are shown in panel A; a comparison of the maximum IM concentration measured by the AMS (red), LC-ESI Mainz (blue), and LC-ESI Lyon (green) shown in panel B.

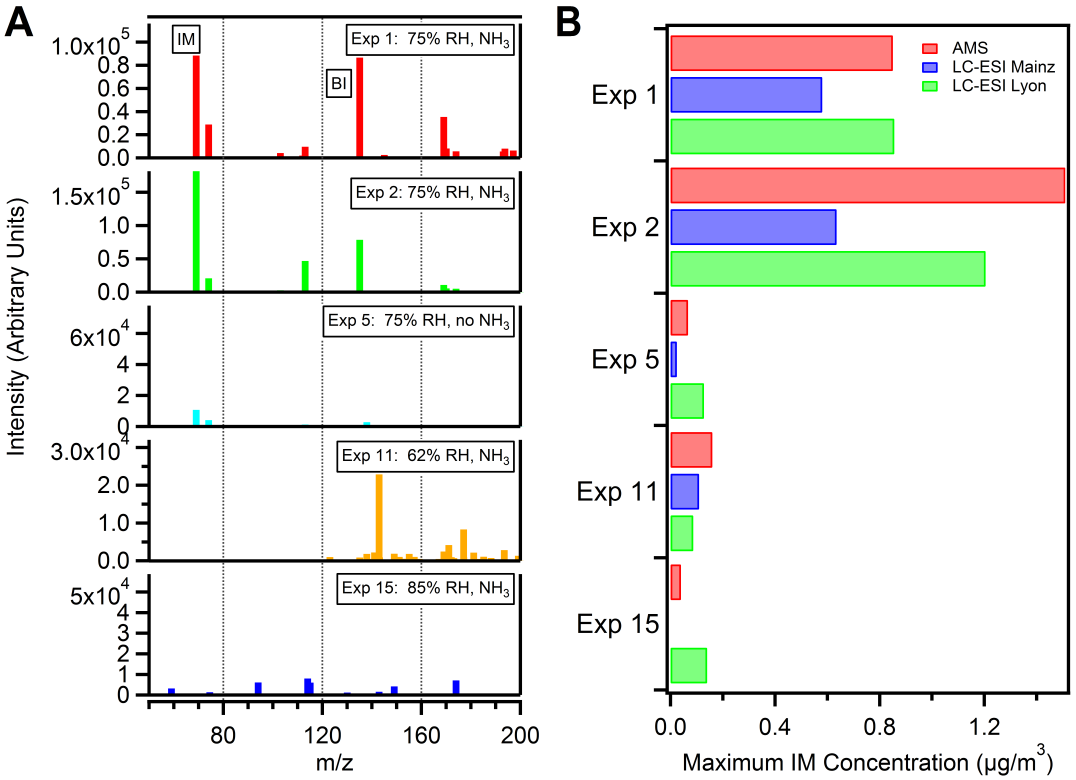

mass defect of -1.2 ppm.

Mass spectra from the nano-DESI are shown in Figure 6.3 in panel A. Experiment 1 is shown in red, Experiment 2 in green, Experiment 5 in turquoise, Experiment 11 in orange, and Experiment 15 in blue. IM and BI are extremely prominent peaks in Experiments 1 and 2. These are barely visible in Experiment 5, and not at all in the spectra from Experiment 11 or 15. The total signal is also significantly higher in Experiments 1 and 2 than in 5, 11, or 14. While this is qualitative species identification data, it suggests that significantly more imidazoles were formed in Experiments 1 and 2 than in 5, 11, or 15.

The AMS detected IM in all ^{12}C experiments at m/z 68.0375. The maximum measured concentrations of IM in $\mu g/m^3$ for Experiments 1, 2, 5, 11, and 15 are shown in Figure 6.3 in panel B in red. The AMS detects significantly higher concentrations of IM in Experiments 1 and 2 than 5, 11, or 15, which is consistent with the nano-DESI. IC was detected in Exp 0, 1, 2, 11, 14, and 15 at maximum concentrations of 0.017, 0.015, 0.018, 0.005, 0.037 ,and 0.007 $\mu g/m^3$ respectively. BI was detected in Exp 0, 1, 2, 11, and 14 at maximum concentrations of 0.0012, 0.021, 0.010, 0.001, and 0.003 $\mu g/m^3$ respectively. This is generally consistent with IM data, in which (with the exception of Exp. 14) the highest concentrations are observed in Experiments 1 and 2 with 75% RH and gas-phase NH_3.

The Mainz ESI-MS method detected IM using an Orbitrap in Exp 0, 1, 2, 5, and 11 at an exact mass of 69. 04544 ($C_3H_5N_2^+$) with a mass defect of 10.359. No data was collected for Exp 14 and 15. IC was also detected in all of those experiments at exact mass 97.04011 ($C_4H_5N_2O^+$) with a mass defect of 4.85, though for some filters the measurements are below the limit of quantification. In their system they found that IC quickly reacted to form HIC (115.05048 for $C_4H_7N_2O_2^+$, mass defect of 2.399) and $C_4H_4N_2O_2$ species (113.03471 for $C_4H_5N_2O_2^+$, mass defect of 1.381) so they also report a "sum of IC species" which is the sum of IC, HIC, and $C_4H_4N_2O_2$. They also detected BI in Exp 1, 2, and 11 at 135.06679 for $C_6H_7N_4^+$ with a mass defect of 1.978. Again, the highest concentrations of all three of these species were detected in Experiments 1 and 2.

The Lyon ESI-MS filters were taken at the end of each experiment, so this data is represen-

tative of final concentrations of imidazoles in the aerosols. They detect IM in all AS experiments at concentrations ranging from 0.081 $\mu g/m^3$ (Exp 11) to 1.205 $\mu g/m^3$ (Exp 2), with the highest concentrations in Experiments 1 and 2. They detect IC in Exp 0, 1, 2, 11, 14, and 15 at concentrations ranging from 0.024 $\mu g/m^3$ (Exp 11) to 0.13 $\mu g/m^3$ (Exp 15). They detect BI in Exp 1, 2, 14, and 15 at concentrations ranging from 0.010 $\mu g/m^3$ (Exp 15) to 1.151 $\mu g/m^3$ (Exp 1).

The data from the four instruments overall shows similar trends: typically the highest concentrations were observed in Exp 1 and 2 (AS, 75% RH, addition of gas-phase NH_3). Under other conditions (75% RH, no NH_3, Exp 5) the concentrations of the species decrease significantly to the point where several of the instruments are no longer able to detect IC and BI. This is further evidence that imidazole formation is pH-dependent (Noziere et al., 2009), as this is the only AS experiment formed under acidic conditions. This decrease is also likely due to the decrease in availability of ammonium as a reactant since excess is not available from the partitioning of gas-phase NH_3 to aqueous-phase NH_4^+. Additionally, if the RH is decreased but NH_3 is added (Exp 11), significantly lower imidazole concentrations are detected. This is hypothesized to be due to the kinetic limitation to glyoxal uptake that occurs above 12 M AS (Kampf et al., 2013). The decrease in imidazole concentration is also observed in the opposite direction when the RH is increased but NH_3 is added, again very low concentrations of imidazoles are detected and in some cases this is below instruments' detection limits. This is potentially due to the precursor concentration decrease: above 85% RH, AS aerosols are deliquesced and contain significantly more water than at lower RH. At the higher water concentrations, the AS will be more dilute resulting in both lower NH_4^+ concentrations as well as a decreased salting in effect for glyoxal (Kampf et al., 2013). This means that both precursor species necessary for imidazole formation will be available in lower concentrations, thus limiting the rate at which imidazoles are formed and limiting the ultimate concentration of imidazoles formed, due to the decrease in glyoxal uptake.

6.3.3 Proposed Imidazole Formation Mechanism

Time-resolved data was obtained from the AMS, nano-DESI, and Mainz HPLC-ESI, allowing insights in to imidazole formation mechanisms in aerosol to be probed. To eliminate the complexities of aerosol (and thus imidazole) wall loss, we investigate the mechanism by looking at ratios of species, specifically IM, IC, and BI, rather than focus absolute concentrations of the imidazoles. This accounts for the change in total aerosol loading as a result of wall losses, assuming that the imidazoles are well mixed within the aerosol and thus wall loss affects all species equally. This is a reasonable assumption because imidazole formation takes place in the aqueous phase rather than the gas phase (Yu et al., 2011; Kampf et al., 2012b) and thus losses should be due entirely to aerosol wall loss rather than gas-phase species wall loss.

The time series for the ratios of IC/IM, IC/BI, and IM/BI for Experiment 1 from nano-DESI data is shown in Figure 6.4. This is the only experiment where sufficient nano-DESI filters were collected for for time-resolved data and all three species were able to be quantified in order to calculate the ratios. The IC/IM ratio decreases as a function of time, as does the IC/BI ratio. However, the IM/BI ratio remains relatively flat at approximately 10.

The time series ratios from the LC-ESI Mainz data for Experiments 1 and 11 are shown in Figures 6.5 and 6.6. The LC-ESI Mainz analysis was done with the "sum of IC species" data as this was considered to be more representative of the true IC concentration than just IC. Ratios from Experiment 1 are broadly consistent with the nano-DESI data in that the IC/IM and IC/BI ratios decrease with time while the IM/BI ratio does not show a trend. However, the time constants from the LC-ESI Mainz data are significantly slower than the ones calculated from the nano-DESI data. Because there are more data points in the LC-ESI Mainz analysis, these time constants are likely more accurate than the ones calculated from the nano-DESI data. A similar trend is observed in the LC-ESI Mainz data from Exp 11 as well: the IC/IM and IC/BI ratios decrease as a function of time (through the first two glyoxal productions; an increase in both is observed after the third lights on).

Figure 6.4: Imidazole ratios for Experiment 1 calculated from nano-DESI data. A decrease in the IC/IM (red) and IC/BI (blue) ratios is observed, but the IM/BI (green) ratio remains relatively constant.

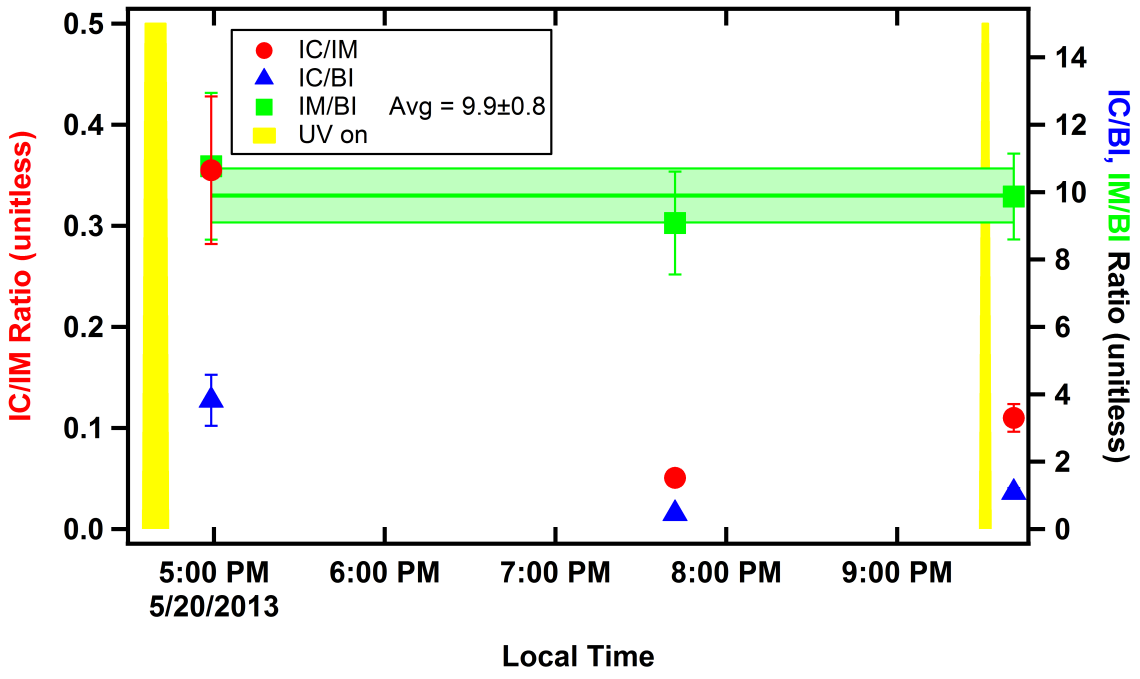

Figure 6.5: Imidazole ratios for Experiment 1 calculated from LC-ESI Mainz data. A decrease in the IC/IM (red) and IC/BI (blue) is also observed, but with significantly longer time constants than for the nano-DESI data. The IM/BI ratio (green) is somewhat noisier than the nano-DESI data, but is also approximately constant though at a much higher value.

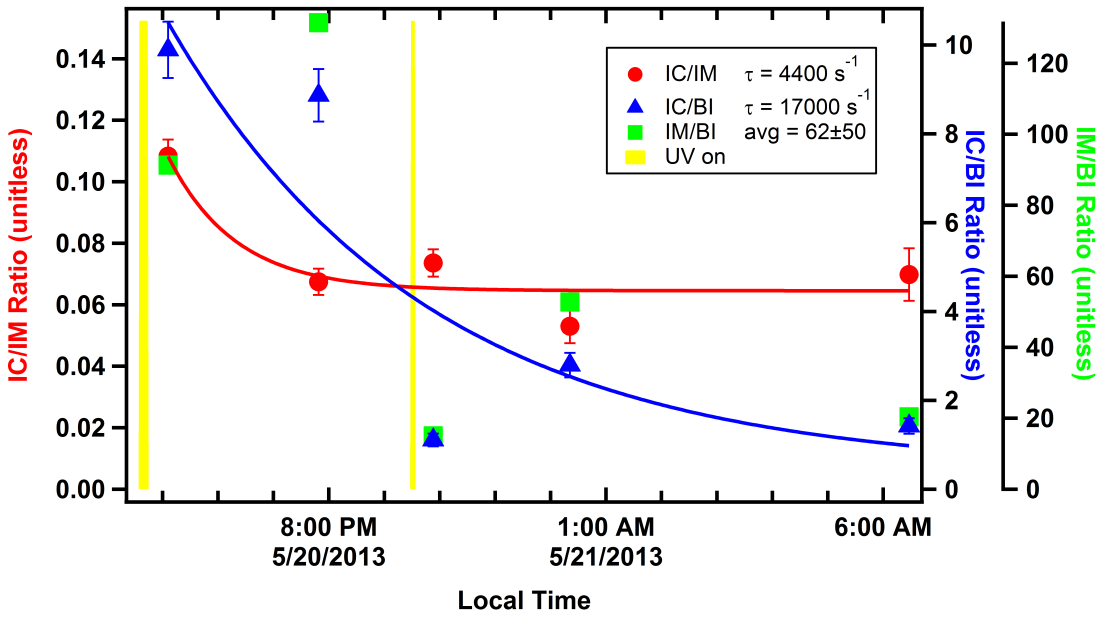

Figure 6.6: Imidazole ratios from LC-ESI Mainz data for Experiment 11. IC/IM (red) and IC/BI (blue) decrease, while IM/BI (green) is approximately constant.

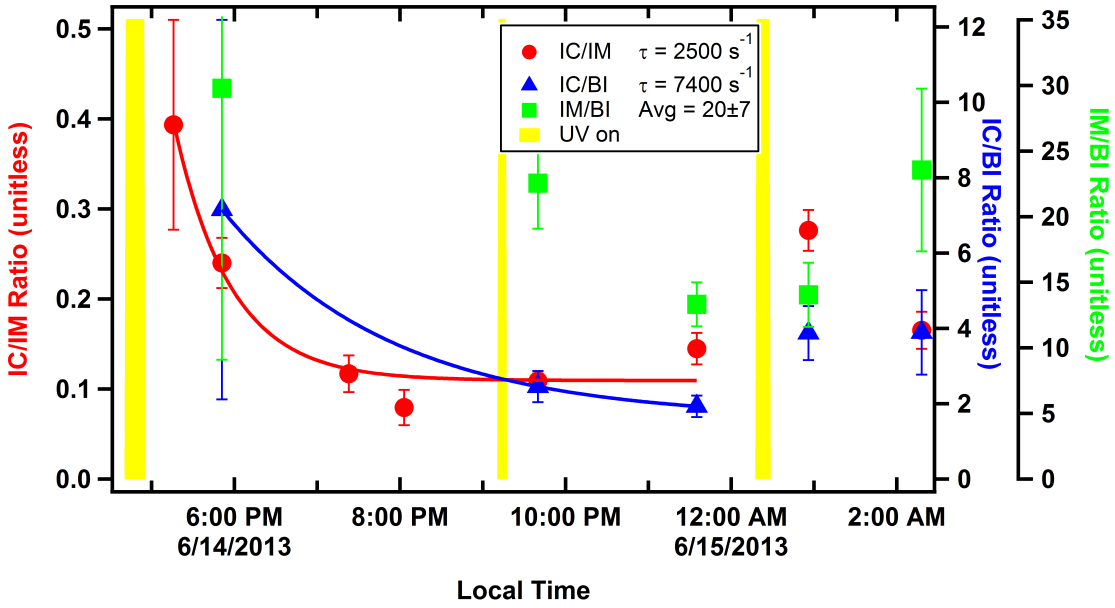

We note that the AMS, unlike the LC-ESI Mainz and the nano-DESI (which is a modified form of ESI), uses a hard ionization technique and IC, IM, and BI are thus expected to fragment during the ionization process. Additional fragments containing C and N that are not attributable to a specific species were detected, including CN^+ at m/z 26.0031, CHN^+ at m/z 27.0109, C_2N^+ at m/z 38.0031, C_2HN^+ at m/z 39.0109, $C_2H_2N^+$ at m/z 40.0187, and $C_2H_3N^+$ at m/z 41.0266. These ions could arise from the fragmentation of some or all of IM, IC, and BI. Indeed, the NIST EI spectra of IM and IC (BI is unavailable) show that C_2HN^+, $C_2H_2N^+$, $C_2H_3N^+$, and $C_3H_4N_2^+$ are fragments of both IM and IC. Thus in order to obtain true ratios from the AMS data, ions that are fragments of one or more imidazole species (which includes the ion for IM itself) must be assigned to the appropriate imidazole specie(s). Because this fragmentation issue affects the IM ion (which is the result of IM being ionized, as well as IC and very likely BI fragmenting), we consider the LC-ESI Mainz time series to be more accurate as there are no fragmentation interferences to account for and thus do not report the AMS time series. This fragmentation and contribution to m/z 68 could potentially be accounted for by nebulizing pure IM, IC, and BI in to the AMS; however such data is not presently available.

The mechanisms from Yu et al. (2011) and Kampf et al. (2012b) propose that IM and IC are formed in parallel and BI is formed from further reactions of IC. With this mechanism, the IC/IM ratio would be remain approximately constant at the ratio of the rate constants for IM and IC formation. The ratio of the formic acid/(IC+GI) to IC rate constants from Yu et al. (2011) is 0.163. The IC/(IM + GI) ratio is plotted in Figure 6.7. Error bars were calculated assuming a 0.1 mM error for IM and a 0.05 mM error for IC. With the exception of the first data point, this ratio is rather flat. The first data point has the largest error bars because the measured concentrations of IM and IC are so low. When the error bars are considered, this point is consistent with the other data points. The average of these ratios comes out to 0.163, which is the same as the ratio of the rate constants. Thus the decrease in IM/IC, as observed by the nano-DESI, LC-ESI Mainz, and AMS is inconsistent with the mechanism from Yu et al. (2011).

According to the Kampf et al. (2012b) mechanism, IC is converted to BI through the addition

Figure 6.7: IC/IM ratio from data in Yu et al. (2011). Error bars were calculated assuming a 0.1 mM error in the IM concentration and a 0.05 mM error in the IC concentration.

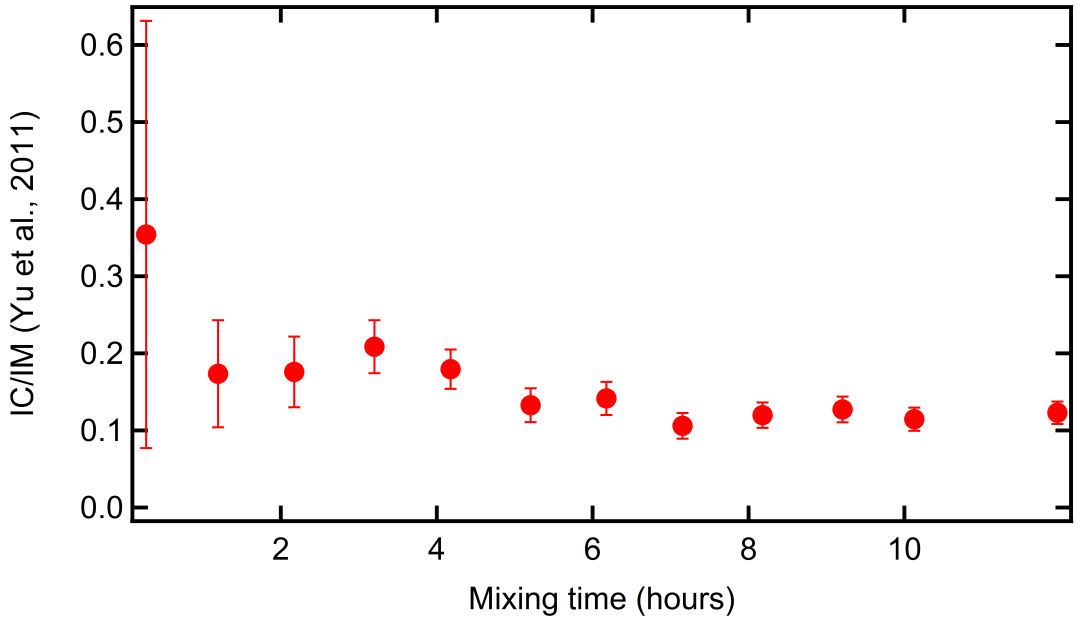

of a glyoxal molecule and two ammonium ions. The IC/BI ratio should initially be high prior to significant BI formation and then decrease as IC is converted to BI. This is consistent with all of the observed IC/IM and IC/BI ratios: they all decrease with time. Therefore, our data is consistent with a mechanism that proposes conversion of IC to BI.

The very clear decrease with IC/IM with time suggests that IC is converted in to IM, in the same way that the decrease in IC/BI with time suggests that IC is converted to BI. The LC-ESI Mainz data shows much larger time constants for the IC/BI ratio than the IC/IM ratio. This suggests that IC is converted to BI much more slowly than IM is formed. This difference in the time constants makes sense in terms of the mechanisms proposed by Yu et al. (2011) and Kampf et al. (2012b) because the formation of IM requires a unimolecular decomposition of the intermediate, while the formation of BI from IC requires the addition of a second glyoxal molecule and two additional ammonium ions to IC.

The approximately constant IM/BI ratio observed in the nano-DESI and LC-ESI Mainz data indicates that these are formed in parallel from a common precursor. The ratio between the two is the ratio of the rate constants for formation. The fact that the IM/BI ratio is rather high means that the rate constant for IM formation is significantly faster than the rate constant for BI formation. This is consistent with the unimolecular decomposition to form IM versus the addition of glyoxal plus two ammonium ions to form BI. Therefore, we propose that in our experiments, IC is formed first followed by conversion to IM and BI. The decrease in IC/IM and IC/BI ratios is consistent with conversion of IC in to IM and BI, and the approximately constant ratio of IM/BI is consistent with their formation from the same precursor, where the ratio is equal to the ratio of the rate constants. This proposed mechanism is shown in Figure 6.8.

6.3.4 Bulk versus surface evidence

Aerosols were observed to grow slightly upon exposure to glyoxal, as shown in Figure 6.9. The number of particles of a given mobility diameter (from SMPS data) is plotted as a function of time, where red represents the fewest number of particles and purple is the largest number of

Figure 6.8: Proposed imidazole formation mechanism in ammonium sulfate aerosols based on our data. IC is formed first and then converted in to IM and BI through decompostion or further reactions with glyoxal and NH_3, respectively.

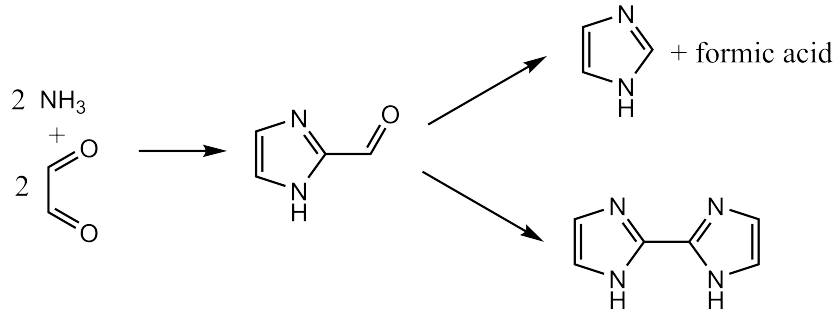

aerosols. The maximum number of particles in this experiment is observed at 12:30 pm on May 20, when seeding stops. The particle number concentration immediately begins to decrease as particles are lost to the walls. However, the size distribution due to wall loss prior to glyoxal production (4:50 pm on May 20) does not change significantly. There is a symmetric decrease in particle number on both sides of the mode diameter of 150 nm. However, a significant increase in the mode diameter is observed at 4:50 pm and a smaller one is observed at 9:30 pm. These correspond to gas-phase glyoxal production, and is thus evidence that glyoxal uptake and SOA formation occurs promptly after exposure to glyoxal.

The mode diameter AMS imidazole tracer at m/z 68 ($C_3H_4N_2^+$) is shown in Figure 6.10. The top panel shows the size distribution versus vacuum aerodynamic diameter (nm, from AMS data) for Exp. 1 and the bottom panel shows the size distribution for Exp. 11. The times selected correspond to the times during which the nano-DESI filters were sampled. AMS data is shown in dots; log-normal fits to the data are shown with solid lines. The normalized intensity was calculated by dividing the intensity in every size bin for a particular species by the maximum intensity of that particular species. This was done in order to plot all species on the same y-scale; otherwise the intensity of Org would far outweigh the intensity of m/z 43 or m/z 44, for example. On average, the mode diameters for Exp. 1 are about 130 nm larger than those for Exp. 11. This is due to the difference in relative humidity between the experiments. Exp. 1 was run at 75% RH while Exp.

Figure 6.9: SMPS aerosol growth in Experiment 1. Significant growth is seen at 4:30 pm when glyoxal was first produced.

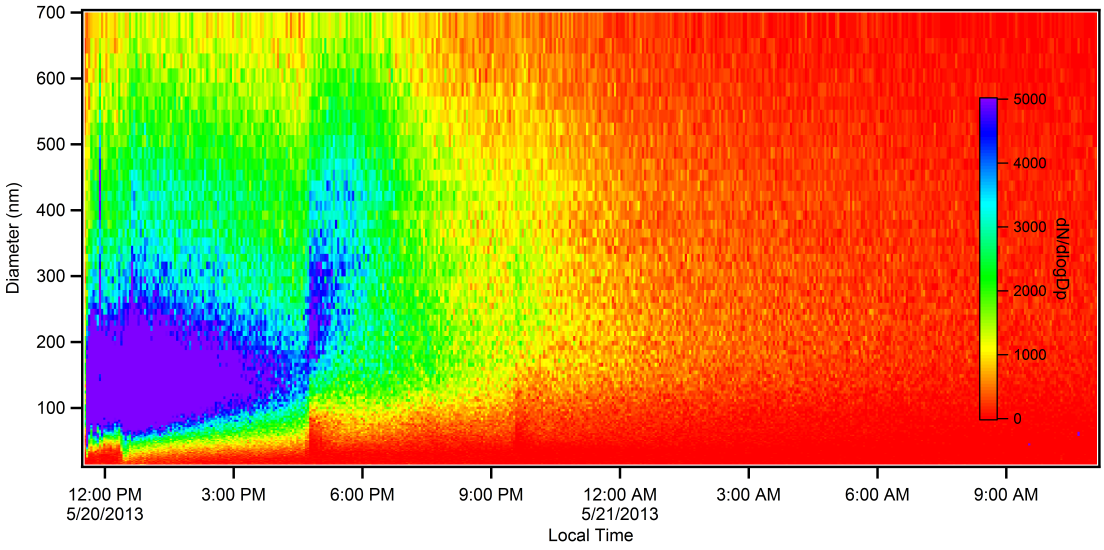

2 was run at 62% RH. Aerosols in both experiments would have been metastable, but the ones in Exp. 1 would have contained more water due to the higher RH and would thus be larger. There is a slight increase in the mode diameter is observed between the first two measurements from Exp. 1. This is likely due to continued glyoxal uptake and further SOA formation over the two hours of processing. The decrease in mode diameter between the second and third measurements is not statistically significant. The difference between the mode diameters in the measurements from Exp. 11 are not statistically different.

In order to determine if imidazoles are formed in aerosols through surface or bulk reactions, we utilize size-resolved data. Size-resolved data corresponding to approximately 30 minutes after the first glyoxal production during Experiment 1 is shown in Figure 6.11. The size distribution of the seed aerosol is represented by the sulfate data, shown in the top panel in red. It has a mode diameter of 912 nm. Total organics are shown in bright green, with m/z 43 ($C_2H_3O^+$, less oxidized organic species) and m/z 44 (CO_2^+, more oxidized organic species) in light green and dark green respectively. These have rather varied mode diameters, but all are smaller than the seed aerosol diameter. Glyoxal tracers CHO^+ (light blue) and $C_2H_2O_2^+$ (dark blue) have similar mode diameters to the total organic mode diameters. N-containing ions are shown in orange. These also all have mode diameters similar to that of the total organic signal.

A similar figure for Experiment 2 is shown in 6.12. This is similar to what was observed in Experiment 1: the mode of the sulfate size distribution is slightly higher than that for the total organics, and the glyoxal tracers and the majority of the imidazole tracers, especially IM, have similar mode diameters to the total organics.

Smaller aerosols have larger surface area to volume ratios, so if a species is formed from a surface process it is expected to be found preferentially in smaller aerosols. Therefore, since the organics, glyoxal tracers, and imidazole tracers all have mode diameters smaller than that of the bulk seed aerosol, it is possible that the formation of all of these has a surface component, or a surface-limiting component. However, the glyoxal tracers and imidazole tracers, especially the IM ion, have mode diameters that are consistent with the total organic signal mode diameter.

Figure 6.10: Comparison of IM ($C_3H_4N_2^+$) mode diameters for Exp 1 and Exp 11. Difference in mode diameters between experiments due to difference in RH: Exp 1 was run at 75% RH; Exp 11 was run at 62% RH.

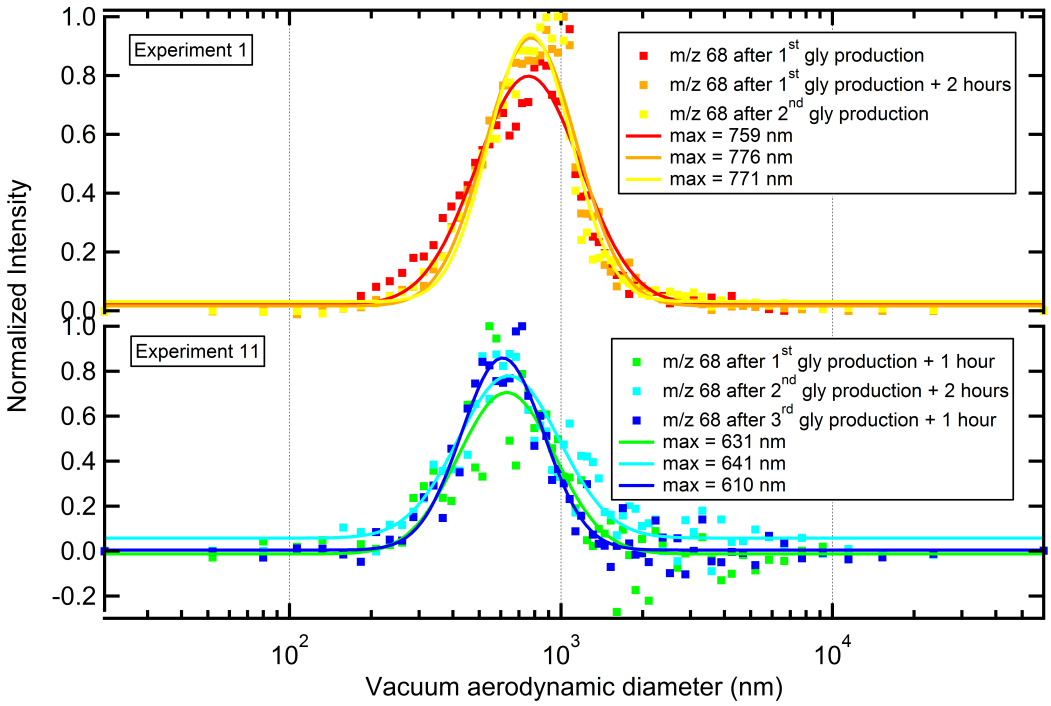

Figure 6.11: Size distributions from 30 minutes after first glyoxal production of Experiment 1 for sulfate (seed aerosol, red), total organics and bulk organic tracers (green), glyoxal tracers (blue), and imidazole tracers (orange).

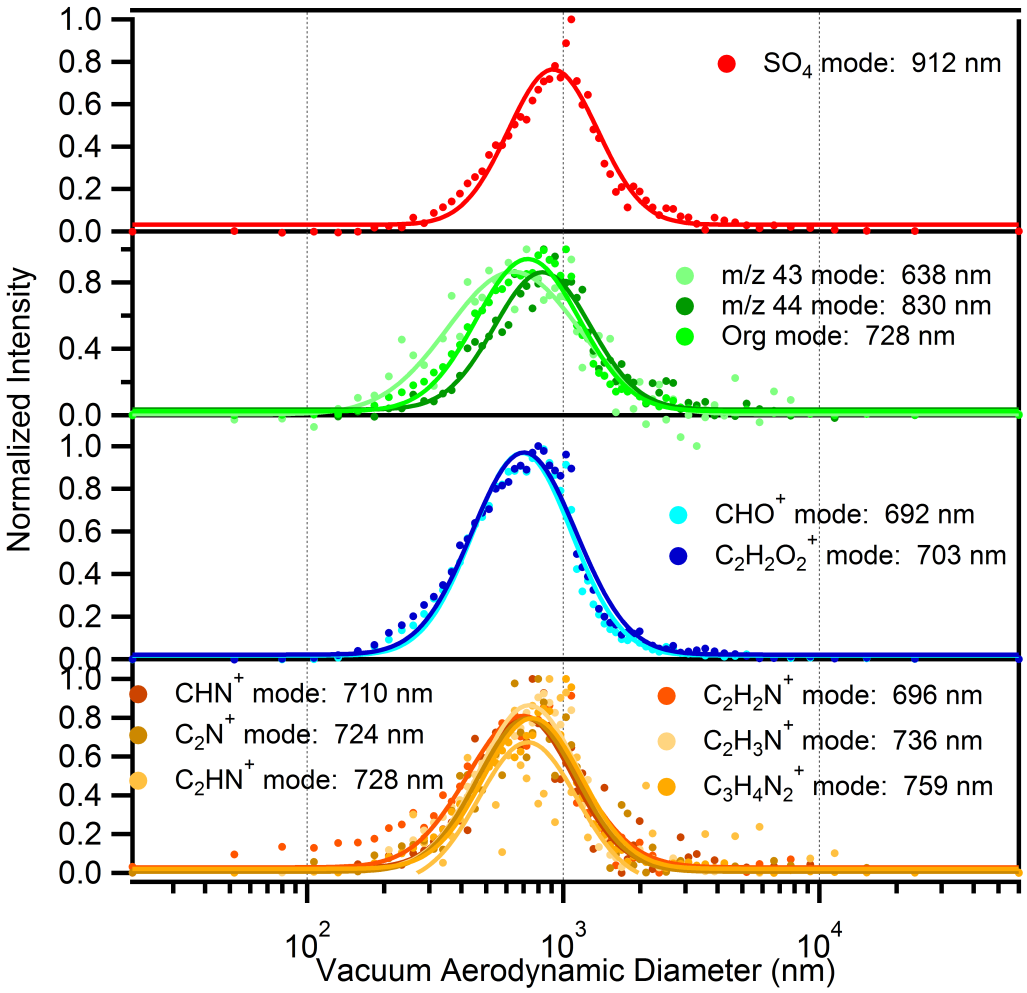

Figure 6.12: Size distributions from 30 minutes after first glyoxal production of Experiment 2 for sulfate (seed aerosol, red), total organics and bulk organic tracers (green), glyoxal tracers (blue), and imidazole tracers (orange).

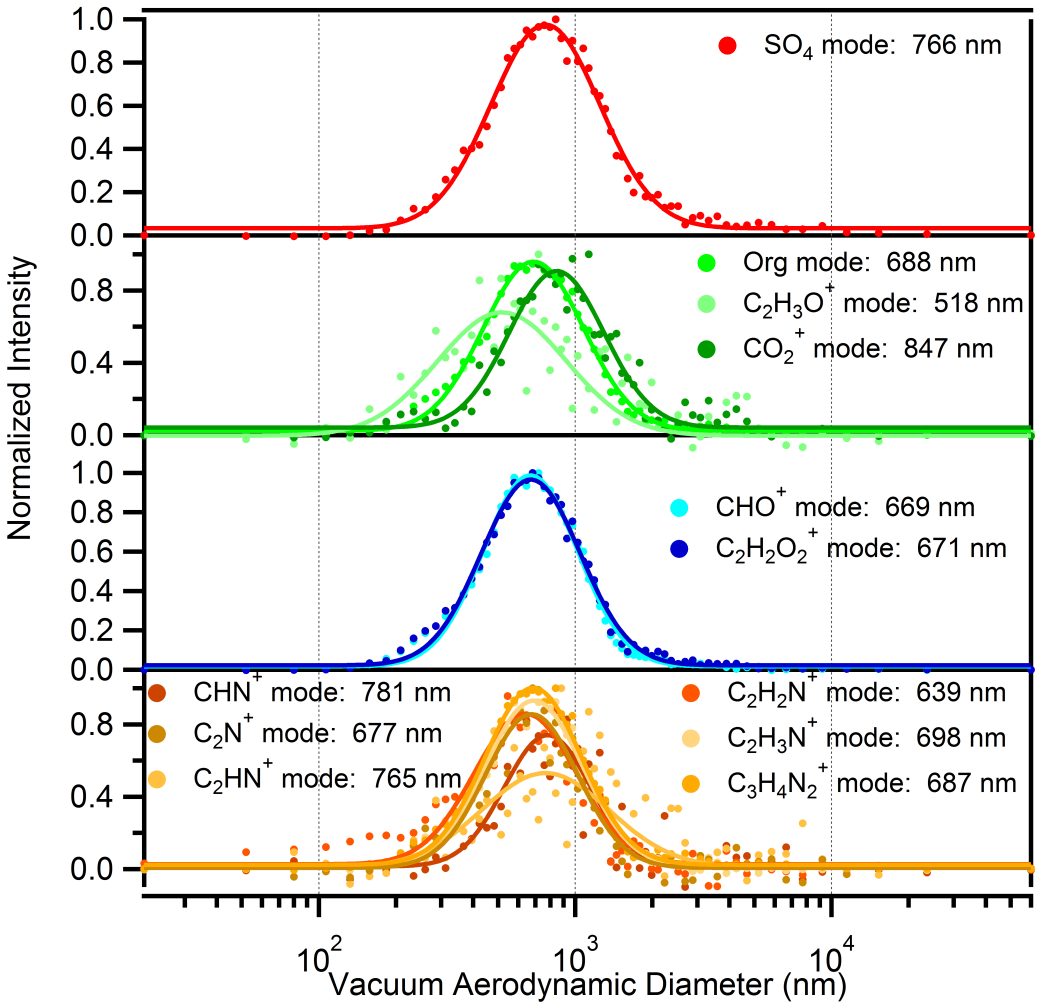

Therefore, in these experiments it is unlikely that imidazole formation is surface-enhanced any more than is the case for the bulk organic. The sum of glyoxal fragments plus imidazole fragments accounts for approximately 50% of the organic mass in Experiments 1 and 2, as seen in Figures 6.13 and 6.14. Therefore it is not surprising that the the mode diameters of the glyoxal tracers and imidazole tracers are very similar to the bulk organic mode diameter.

By contrast, in Experiment 11 the sum of glyoxal tracers plus imidazole tracers accounts for approximately one third of the organic mass (less than in Experiments 1 and 2), and glyoxal tracers account for most of that mass; imidazoles make up a much smaller fraction than in Experiments 1 and 2. This can be seen in Figure 6.15. The mode diameters for this experiment are shown in Figure 6.16. In this experiment, the bulk organic mode diameter is again smaller than the seed sulfate diameter. The glyoxal tracers, which make up a larger fraction of the organic mass than the imidazoles in this experiment, match the organic mode diameter more closely. In this experiment, the imidazole mode diameter is very similar to the sulfate mode diameter, suggesting that imidazole formation does not have a significant surface component. This could be due to the limited uptake due to the low relative humidity as discussed above. Overall, there is some evidence that suggests that imidazole formation could be a surface-limited process. This surface limitation could be diffusion of glyoxal or ammonium in to the bulk of the aerosol.

The IC and BI concentrations shown in Figures 6.13, 6.14, and 6.15 are likely lower limits because they are represented solely by the appropriate high-resolution ions and do not account for fragmentation in to m/z 68 and other fragments. By contrast this is therefore an upper limit on IM as the signal at $C_3H_4N_2^+$ is due to fragmentation from IC and BI, not just ionization of IM.

These figures, in combination with the mass closure for Experiment 5 shown in Figure 6.17 also show the effect of NH_3 on SOA mass. Experiments 1, 2, and 11 all had gas-phase NH_3 added; Experiment 5 did not. The mass of the imidazole fragments is much more prominent in the experiments with NH_3 than Experiment 5. This is unsurprising because the addition of NH_3 raises the pH of the aerosols and because imidazole formation is pH dependent and increases as pH increases. Additionally, it provides additional ammonium ions as reactants for imidazole formation.

Figure 6.13: AMS mass closure for Experiment 1. Org/SO_4 is shown in green, imidazole tracers/SO_4 are shown in oranges, and glyoxal tracers to SO_4 are shown in blues. The sum of glyoxal tracers plus imidazole tracers accounts for approximately 50% of the total organic mass.

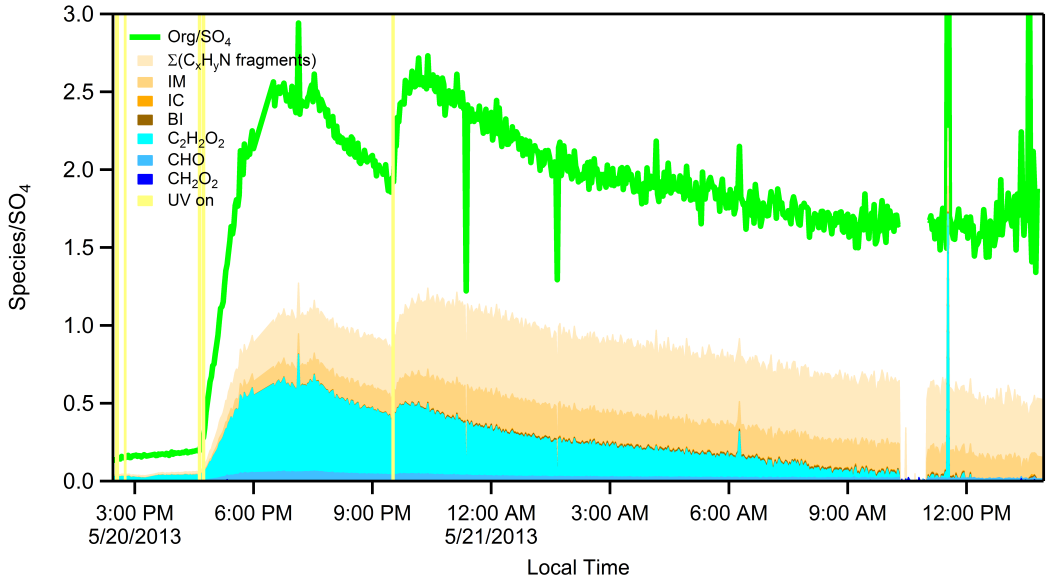

Figure 6.14: AMS mass closure for Experiment 2. Similar to Experiment 1 above, the sum of imidazole tracers plus glyoxal tracers accounts for approximately 50% of the organic mass.

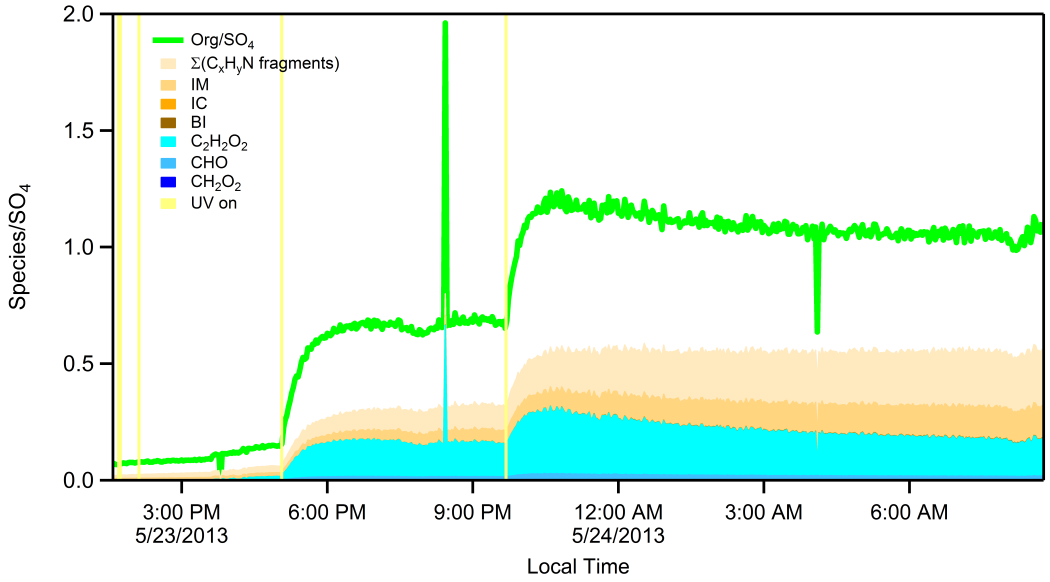

Figure 6.15: AMS mass closure for Experiment 11. The sum of glyoxal tracers plus imidazole tracers only accounts for approximately one third of the organic mass. Unlike in Experiments 1 and 2, the imidazole tracers do not dominate the mass that can be accounted for. Instead, the glyoxal tracers are much more prominent.

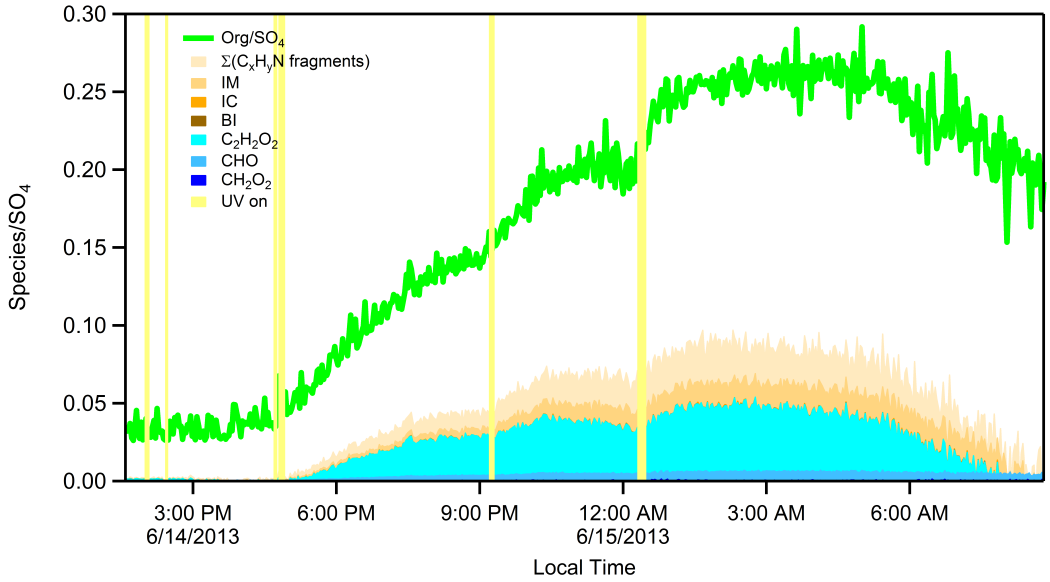

Figure 6.16: Size distributions from 30 minutes after first glyoxal production of Experiment 11 for sulfate (seed aerosol, red), total organics and bulk organic tracers (green), glyoxal tracers (blue), and imidazole tracers (orange).

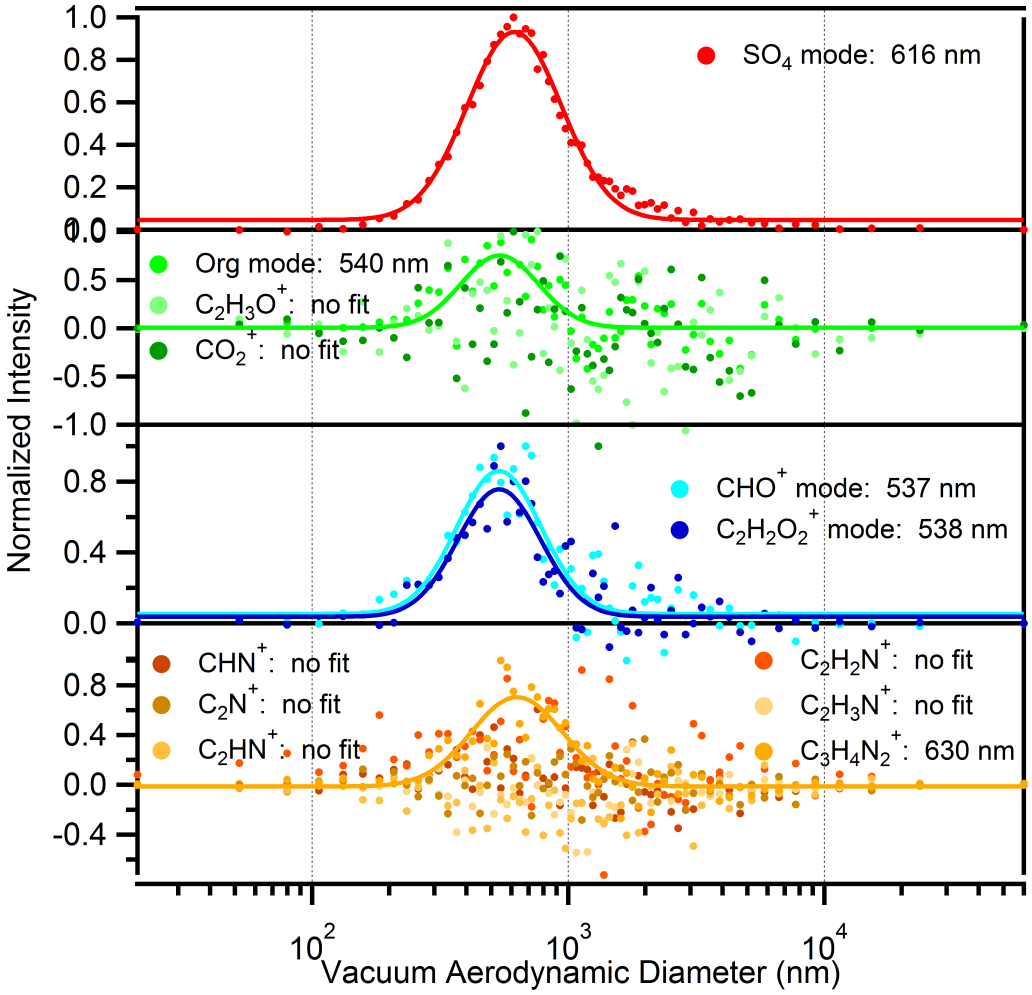

Figure 6.17: AMS mass closure for Experiment 5. The sum of glyoxal tracers plus imidazole tracers only accounts for approximately 20% of the organic mass.

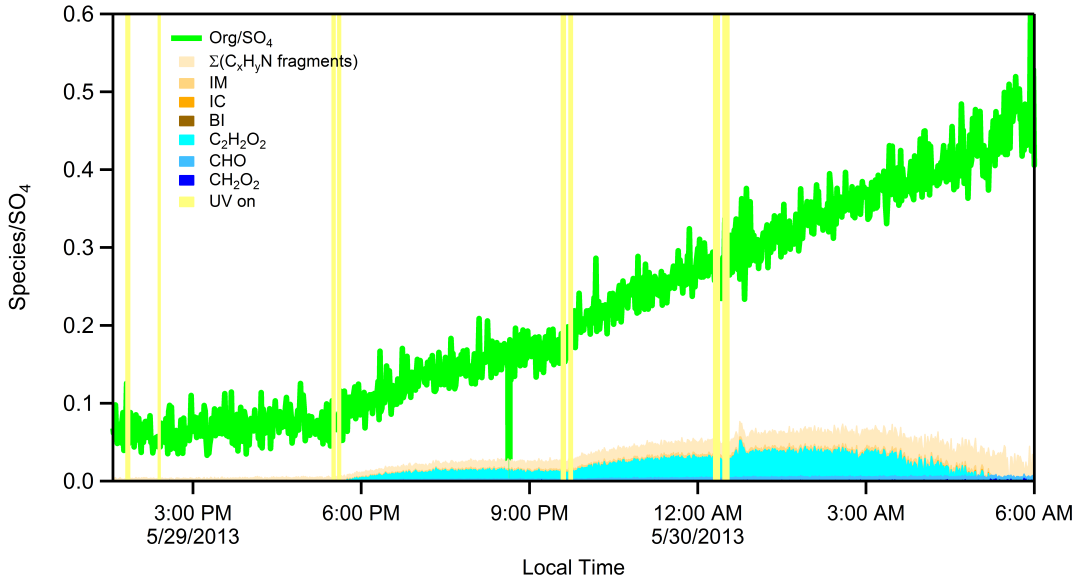

Table 6.4: Comparison of experimental results for experiments with (Exp. 1) and without (Exp. 5) added gas-phase NH_3. Maximum values given.

Experiment	Org. ($\mu g/m^3$)	Org/SO_4	Mass Closure	m/z 68 ($\mu g/m^3$)	N/C
1	22	2.6	50%	0.85	0.3
5	4	0.45	20%	0.07	0.05

The effect of NH_3 can also be seen in the atomic O/C and N/C plots, shown in Figures 6.18, 6.19, 6.20, and 6.21 for Experiments 1, 2, 5, and 11 respectively. Glyoxal has an O/C of 1, glyoxal monohydrate has an O/C of 1.5, and glyoxal dihydrate has an O/C of 2, so the extremely high O/C ratios for these experiments is reasonable given that the organic fraction of the aerosol is primarily made up of glyoxal and its reaction products. Typically the O/C ratio increases after glyoxal production as additional glyoxal is available to partition in to the aerosols.

In Experiments 1 and 2, the O/C ratio slowly decreases as the N/C ratio increases. This is consistent with glyoxal molecules being converted in to imidazole species: IM and BI have O/C ratios of 0 and N/C ratios of .66, and IC has an O/C of 0.25 and an N/C of 0.5. Thus as glyoxal gets converted in to nitrogen-containing species, the O/C will decrease and the N/C will increase. In Experiment 5, there is no added gas-phase NH_3 and the N/C remains quite low. In Experiment 11, gas-phase NH_3 is added and the N/C ratio is again observed to increase with time.

A summary of these properties is given in Table 6.4 comparing the addition of NH_3 (Experiment 1) with the absence of NH_3 (Experiment 5).

The difference in SOA formation and especially imidazole formation is also demonstrated in Figure 6.22. This figure shows the Org/SO_4 ratio (top panel) and m/z 68/SO_4 (bottom panel) for Experiments 1 and 5 (with and without gas-phase NH_3), normalized to gas-phase glyoxal concentration (yellow circles shown on the bottom panel).

The top panel shows the Org/SO_4 ratio for in the presence of added NH_3 (red) and in the absence of added NH_3 (blue). When the blue trace is multiplied by 6, it results in the blue dashed trace which almost matches the red trace. Thus the amount of organic aerosol formed in with the addition of NH_3 (when normalized to the aerosol seed concentration) is six or seven times

Figure 6.18: Atomic ratios for O/C (blue) and N/C (red) calculated from the AMS data for Experiment 1.

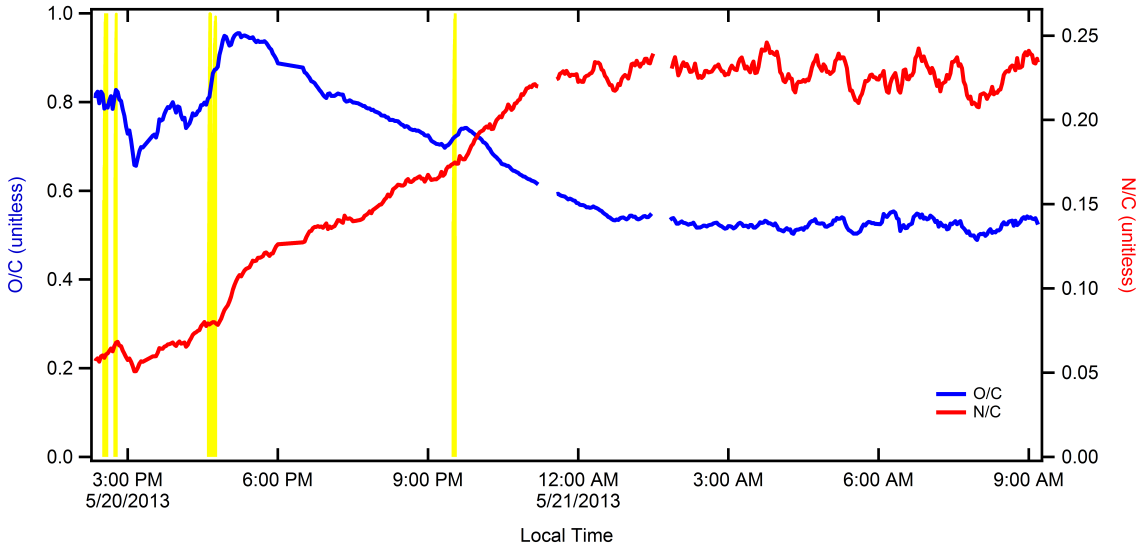

Figure 6.19: Atomic ratios for O/C (blue) and N/C (red) calculated from the AMS data for Experiment 2.

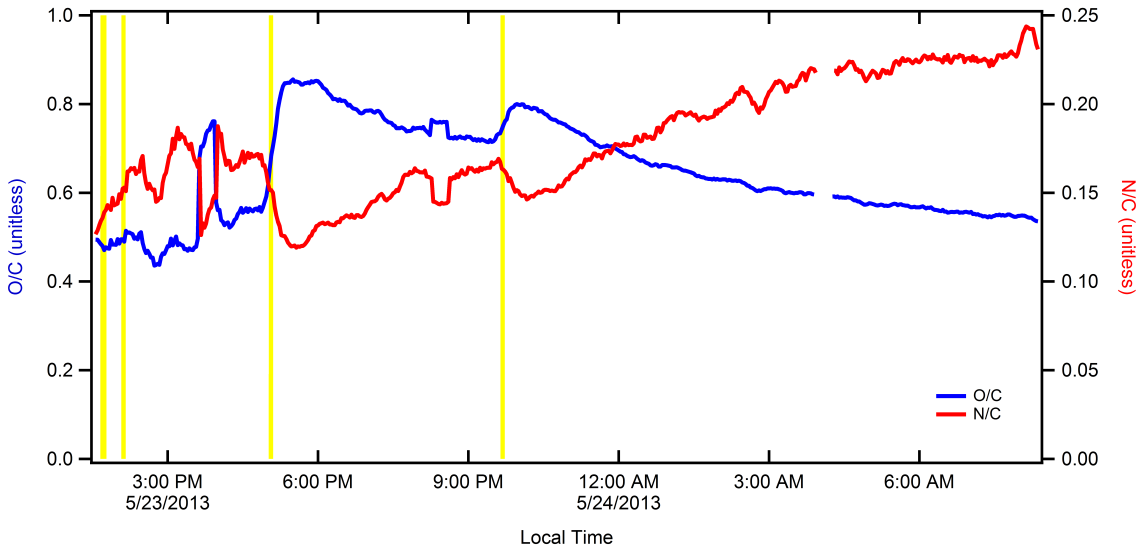

Figure 6.20: Atomic ratios for O/C (blue) and N/C (red) calculated from the AMS data for Experiment 5.

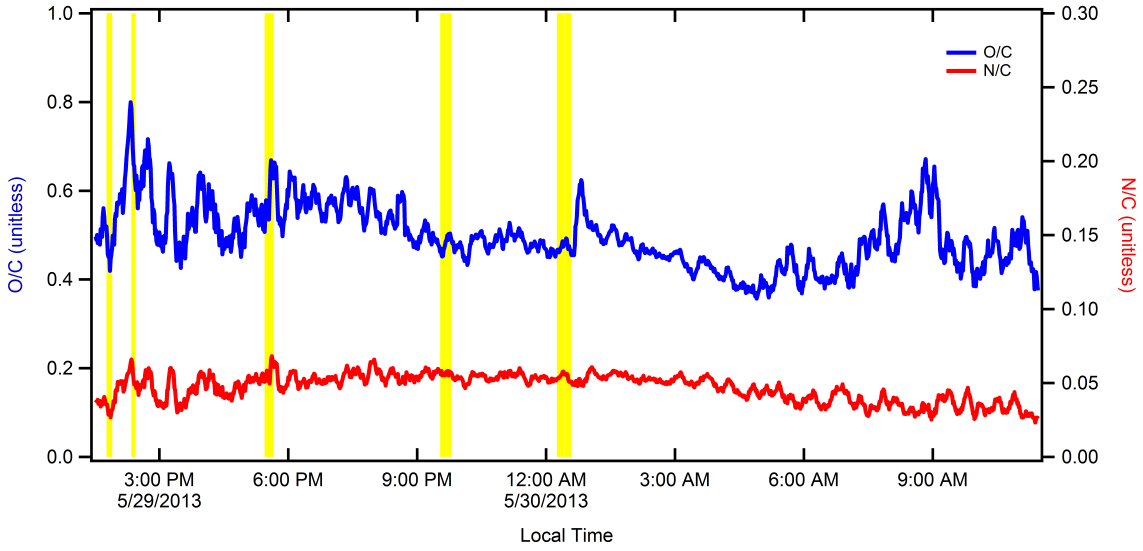

Figure 6.21: Atomic ratios for O/C (blue) and N/C (red) calculated from the AMS data for Experiment 11.

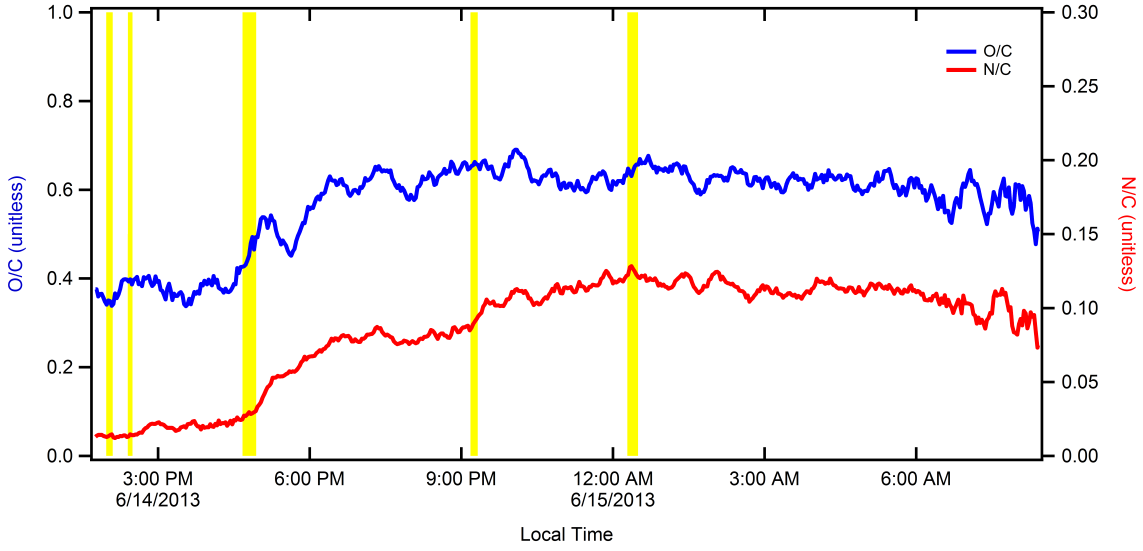

Figure 6.22: Comparison of experiments with and without gas-phase NH_3, normalized to gas-phase glyoxal concentration. Top panel: Org/SO_4 ratio. Red: with added NH_3. Blue: without added NH_3. Blue dashed lines: Blue line multiplied by 6. Bottom panel: m/z $68/SO_4$ (imidazole tracer). Color scheme is the same. Figure courtesy of S. Wang.

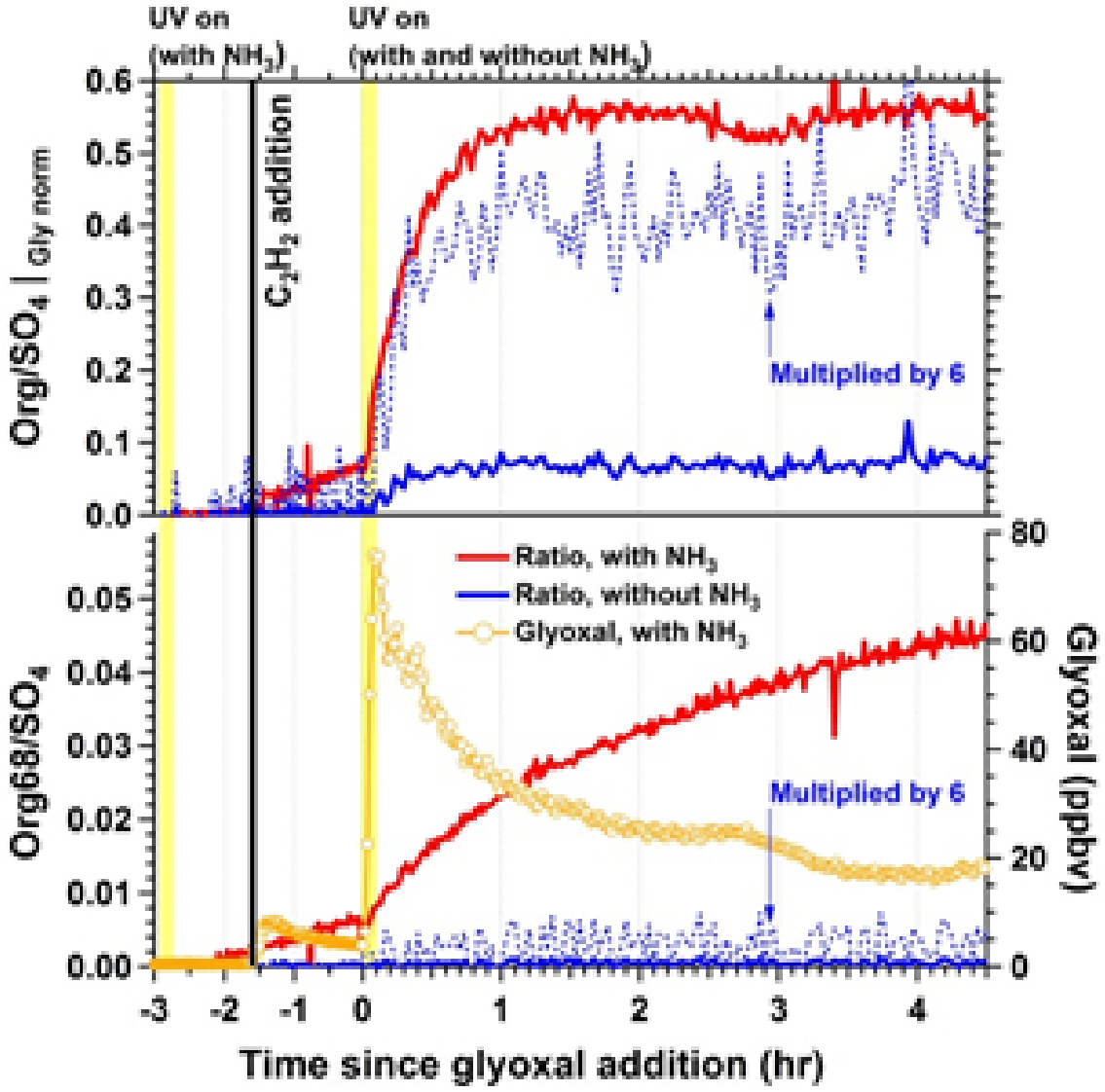

the amount formed without NH_3. The bottom panel shows the m/z 68/SO_4 ratio which is the formation of the IM tracer normalized to aerosol seed. Again, the red shows the ratio in the presence of added NH_3 and the blue shows the ratio in the absence of NH_3. In this case, the m/z 68/SO_4 ratio multiplied by six does not almost match the red trace. The ratio in the absence of NH_3 is approximately a factor of 50 lower than the ratio with added NH_3. Thus while the additional ammonia increases overall organic aerosol formation, it has a significantly stronger impact on the imidazole formation.

Surprisingly, analysis of the nano-DESI data did not show evidence of glyoxal oligomers. Further sensitivity studies were performed to determine the sensitivity of the instrument to glyoxal and oligomers. These were able to be detected on their own and in the presence of IM, IC, and BI, and both as a direct infusion ESI solution and using nano-DESI by running droplets over a blank aluminum foil. While the lack of detection of oligomers is inconsistent with the very high O/C ratios from the AMS data, it is additional evidence of the prevalence of nitrogen-containing organic compounds in the glyoxal/ammonium sulfate system.

6.4 Conclusions

We have performed a number of chamber experiments under varied relative humidity and pH conditions to study the effect of these parameters on SOA formation from glyoxal. Four instruments were used to study the particle-phase products: two HPLC-ESI methods (LC-ESI Mainz and LC-ESI Lyon), a modified ESI method (nano-DESI), and an Aerosol Mass Spectrometer (AMS). A number of imidazoles have been been detected as products of the glyoxal plus ammonium sulfate system. Three of these, that have commercially-available standards or can easily be synthesized, were measured by all three instruments. These are imidazole ($C_3H_4N_2$, IM), imidazole-2-carboxaldehyde ($C_4H_4N_2$, IM), and 2,2'-biimidazole ($C_6H_6N_2$, BI). All four instruments detect these three compounds. They find the highest concentrations in Experiments 1 and 2, which have moderate relative humidity (RH = 75%) and aerosols neutralized due to the addition of gas-phase NH_3. Significantly lower concentrations are observed in Experiment 5, which has a similar RH, but no additional

gas-phase NH_3. Lower concentrations of the imidazoles are additionally observed in Experiment 11, which has added gas-phase NH_3 but a lower relative humidity (62%) and Experiments 14 and 15 which also have added gas-phase NH_3 but high relative humidity (85%).

The time-resolved information from the LC-ESI Mainz, nano-DESI, and AMS data provide information on the mechanism of formation of IM, IC, and BI. Published mechanisms propose that IM and IC are formed from a common precursor intermediate, and then IC reacts further to form BI. Our time-resolved data suggests that in our aerosols, IC is formed first and then either decomposes to form IM, or reacts with additional glyoxal plus ammonium to form BI. Additionally, we see inconclusive evidence for a surface-limiting process for imidazole formation. Finally, we report several imidazole species that have not yet been published in the literature.

Chapter 7

Summary

This thesis presents an advancement in our understanding of the secondary organic aerosol (SOA) formation from the small, water-soluble molecules glyoxal (CHOCHO) and methyl glyoxal (CH_3COCHO). We have investigated their importance to aerosol chemical properties, studied how these species partition to aerosols, and studied particle-phase reactions that occur once glyoxal is in the aerosol aqueous phase.

In Chapter 2, we modeled SOA formation in Mexico City during the MCMA-2003 campaign using an explicit aqueous-phase mechanism for glyoxal processing. We found that the glyoxal uptake to the aerosol was best represented by either a surface-based photochemical process, or by an increased partitioning due to Henry's law in the morning followed by a change in aerosol phase state and thus a significant decrease in glyoxal uptake. The SOA formed from glyoxal (gly-SOA) was added to SOA predicted to be formed from semi- and intermediate volatility organic compounds (S/I-SOA) by two volatility basis set parameterizations and to a near-explicit gas-phase oxidation aerosol mechanism to determine if the addition of gly-SOA can bring the predicted O/C of modeled aerosol in to better agreement with measured O/C. We find that the incorporation of gly-SOA with an O/C of 1.5 brings modeled aerosol chemical properties within measurement uncertainty.

In Chapter 3, we apply a recently-measured ^{13}C glyoxal cross section to gas-phase measurements from a series of chamber experiments. Some of these chamber experiments used regular gly-

oxal (predominantly ^{12}CHO^{12}CHO with natural abundances of ^{12}CHO^{13}CHO and ^{13}CHO^{13}CHO), but two used pure isotopically labeled ^{13}CHO^{13}CHO. We are able to make selective on-line measurements of both ^{12}C and ^{13}C glyoxal. In this work, we also develop a high-resolution orthogonal cross section which identifies regions where the ^{12}C and ^{13}C cross sections are most different. We also run a number of sensitivity studies to identify regions where the orthogonal cross section is most stable, study the effect of instrument resolution on the cross section, and apply it to a time series during the chamber studies.

Small water-soluble organic molecules form SOA by partitioning to the aerosol aqueous phase according to Henry's law. However, the partitioning behavior of the molecules can change with the salt concentration in the aerosol. If the molecules become more soluble, this is called "salting in" and the reverse is "salting out". In Chapter 4, we present the first measurements of salting constants of glyoxal and methyl glyoxal in a variety of aerosol-relevant salts (ammonium sulfate, ammonium nitrate, sodium chloride, and sodium nitrate). We describe a novel atmospheric pressure mass spectrometer inlet designed for measurements of salting constants in water. We also measure salting constants using a more traditional of GC-FID and the comparison between the mass spectrometry method and the GC-FID method serves to validate both. We find that glyoxal salts in while methyl glyoxal salts out, and that sulfate has more of an effect than chloride, which has more of an effect on salting than nitrate. We then apply the relevant salting constants to CMAQ, a regional-scale model that predicts aerosol formation over the continental United States. Because of the high Henry's law constant for glyoxal compared to methyl glyoxal as well as the salting-in for glyoxal and salting out for methyl glyoxal, the aerosol-phase picture is very different than the gas-phase picture. Methyl glyoxal is predicted to be the most important in the gas phase, while glyoxal is predicted to be in far higher concentrations in the aerosol phase. This indicates that glyoxal will be a much more important SOA precursor than methyl glyoxal. This work also reports the results of sensitivity studies of salting on IEPOX which is a major SOA precursor currently thought to be modulated by sulfate in the southeastern United States.

In Chapter 5, we use quantum calculations to determine the strength of the interaction between organic solutes and inorganic anions in an attempt to explain salting behavior. We find that the strength of the bond between the anion and the OH groups in hydrated glyoxal or methyl glyoxal alone is unable to explain salting, as it predicts that methyl glyoxal should salt in as well as glyoxal. Therefore, quantum calculations by themselves are unable to explain the salting behavior of molecules. We utilize two literature explanations of salting constants: Debye theory (which predicts interaction primarily based on the number and charge of ions) and McDevit theory (which predicts interactions based on the compressibility of the salt) and apply these theories to calculate K_S values for glyoxal and methyl glyoxal. They give more weight to the properties of the salt than the properties of the organic and especially for McDevit theory are unable to account for electrostatically-favorable interactions between the organic and salt. Therefore, these theories also get salting constants wrong. However, because each of these components (quantum calculations, Debye theory, and McDevit theory) represents a particular set of interactions that affect salting, we perform a polyparameter fit in an attempt to reproduce the measured salting constants from the three components. This polyparameter fit results in good linearity and can be used to estimate salting constants for molecules that are similar to glyoxal and methyl glyoxal, such as IEPOX. We apply this polyparameter fit to trans-β-IEPOX in sulfate and it predicts that this molecule should salt out with similar behavior to methyl glyoxal.

In Chapter 6, we present the results of chamber experiments that focus on the chemical composition of gly-SOA. We are able to identify a number of nitrogen-containing products resulting from the reaction of glyoxal + NH_4^+ including imidazole (IM), imidazole-2-carboxaldehyde (IC), and 2,2'-biimidazole (BI). These species are important because they contribute to brown carbon formation. By using $^{13}CHO^{13}CHO$, we are able to show that these imidazoles are unambiguously formed from glyoxal. By comparing measurements from four instruments over several experiments that varied chamber relative humidity and aerosol pH, we are able to determine the conditions for maximum imidazole formation. We also use time-resolved filter samples and AMS data to propose

a mechanism for their formation. The literature methods propose that IM and IC are formed in parallel from a common precursor intermediate, and that IC goes on to form BI. However, our measurements suggest that IC is formed as a first generation product and then goes on to decompose to form IM, or reacts further to form BI. We also identify three imidazole structures that have not been published previously in the literature and are able to link them to formation from glyoxal through a ^{13}C signature. Additionally, we see a significant enhancement in SOA formation and aerosol N/C ratios in the presence of additional gas-phase NH_3. Total SOA formation is enhanced by a factor of 6-7 in the presence of NH_3 and imidazole formation is enhanced by approximately a factor of 50. The N/C ratio remains constant at about 0.05 in the absence of NH_3 but grows over the course of the experiment to almost 0.30 in the presence of NH_3. Thus under these conditions, SOA formation from glyoxal is greatly enhanced.

Bibliography

.

Aiken, A., P. Decarlo, J. Kroll, D. Worsnop, J. Huffman, K. Docherty, I. Ulbrich, C. Mohr, J. Kimmel, D. Sueper, Y. Sun, Q. Zhang, A. Trimborn, M. Northway, P. Ziemann, M. Canagaratna, T. Onasch, M. Alfarra, A. Prevot, J. Dommen, J. Duplissy, A. Metzger, U. Baltensperger, and J. Jimenez
2008. O/C and OM/OC ratios of primary, secondary, and ambient organic aerosols with high-resolution time-of-flight aerosol mass spectrometry. Environ. Sci. Technol., 42(12):4478–4485.

Alfarra, M., N. Good, K. Wyche, J. Hamilton, P. Monks, A. Lewis, and G. McFiggans
2013. Water uptake is independent of the inferred composition of secondary aerosols derived from multiple biogenic vocs. Atmos. Chem. Phys., 13:11769–11789.

Apel, E., T. Brauers, R. Koppmann, B. Bandowe, J. Boßmeyer, C. Holzke, R. Tillmann, A. Wahner, R. Wegener, A. Brunner, M. Jocher, T. Ruuskanen, C. Spirig, D. Steigner, R. Steinbrecher, E. Gomez-Alvarez, K. M uller, J. Burrows, G. Schade, S. Solomon, A. Ladst atter-Weißenmayer, P. Simmonds, D. Young, J. Hopkins, A. Lewis, G. Legreid, S. Reimann, A. Hansel, A. Wisthaler, R. Blake, A. Ellis, P. Monks, and K. Wyche
2008. Intercomparison of oxygenated volatile organic compound measurements at the SAPHIR atmosphere simulation chamber. J. Geophys. Res. Atmos., 113(D20).

Aregahegn, K., B. Noziere, and C. George
2013. Organic aerosol formation photo-enhanced by the formation of secondary photosensitizers in aerosols. Faraday Discuss., 165:123–134.

Aumont, B., S. Szopa, and S. Madronich
2005. Modelling the evolution of organic carbon during its gas-phase tropospheric oxidation: development of an explicit model based on a self generating approach. Atmos. Chem. Phys., 5:2497–2517.

Aumont, B., R. Valorso, C. Mouchel-Vallon, M. Camredon, J. Lee-Taylor, and S. Madronich
2012. Modeling SOA formation from the oxidation of intermediate volatility n-alkanes. Atmos. Chem. Phys., 12(16):7577–7589.

Avzianova, E. and S. Brooks
2013. Raman spectroscopy of glyoxal oligomers in aqueous solutions. Spectrochim. Acta Part A: Molec. Biomolec. Spec., 101:40–48.

Bates, K., J. Crounse, J. St. Clair, N. Bennett, T. Nguyen, J. Seinfeld, B. Stoltz, and P. Wennberg
2014. Gas phase production and loss of isoprene epoxydiols. J. Phys. Chem. A, 118(7):1237–1246.

Bertram, A. K., S. T. Martin, S. J. Hanna, M. L. Smith, A. Bodsworth, Q. Chen, M. Kuwata, A. Liu, Y. You, and S. R. Zorn
2011. Predicting the relative humidities of liquid-liquid phase separation, efflorescence, and deliquescence of mixed particles of ammonium sulfate, organic material, and water using the organic-to-sulfate mass ratio of the particle and the oxygen-to-carbon elemental ratio of the organic component. Atmos. Chem. Phys., 11(21):10995–11006.

Bian, Q., X. Huang, and J. Yu
2014. One-year observations of size distribution characteristics of major aerosol constituents at a coastal receptor site in Hong Kong–Part 1: Inorganic ions and oxalate. Atmos. Chem. Phys., 14(17):9013–9027.

Bigler, M., D. Wagenbach, H. Fischer, J. Kipfstuhl, H. Miller, S. Sommer, and B. Stauffer
2002. Sulphate record from a northeast greenland ice core over the last 1200 years based on continuous flow analysis. Annals of Glaciology, 35:250–256.

Bloss, C., V. Wagner, M. Jenkin, R. Volkamer, W. Bloss, J. Lee, D. Heard, K. Wirtz, M. Martin-Reviejo, G. Rea, J. Wenger, and M. Pilling
2005. Development of a detailed chemical mechanism (MCMv3.1) for the atmospheric oxidation of aromatic hydrocarbons. Atmos. Chem. Phys., 5:641–664.

Bogumil, K., J. Orphal, T. Homann, S. Voigt, P. Spietz, O. Fleischmann, A. Vogel, M. Hartmann, H. Kromminga, H. Bovensmann, J. Frerick, and J. Burrows
2003. Measurements of molecular absorption spectra with the SCIAMACHY pre-flight model: instrument characterization and reference data for atmospheric remote-sensing in the 230-2380 nm region. J. Photochem. Photobiol. A-Chem., 157(2-3):167–184.

Bond, T. and R. Bergstrom
2006. Light absorption by carbonaceous particles: An investigative review. Aerosol Sci. Technol., 40(1):27–67.

Bond, T., S. Doherty, D. Fahey, P. Forster, T. Berntsen, B. DeAngelo, M. Flanner, S. Ghan, B. Kärcher, D. Koch, S. Kinne, Y. Kondo, P. Quinn, M. Sarofim, M. Schultz, M. Schulz, C. Venkataraman, H. Zhang, S. Zhang, N. Bellouin, S. Guttikunda, P. Hopke, M. Jacobson, J. Kaiser, Z. Klimont, U. Lohmann, J. Schwarz, D. Shindell, T. Storelvmo, S. Warren, and C. C. S. Zender
2013. Bounding the role of black carbon in the climate system: A scientific assessment. J. Geophys. Res. - Atmos., 118:5380–5552.

Bork, N., J. Elm, T. Olenius, and H. Vehkamäki
2014. Methane sulfonic acid-enhanced formation of molecular clusters of sulfuric acid and dimethyl amine. Atmos. Chem. and Phys., 14(22):12023–12030.

Camredon, M., B. Aumont, J. Lee-Taylor, and S. Madronich
2007. The SOA/VOC/NO_x system: an explicit model of secondary organic aerosol formation. Atmos. Chem. Phys., 7(21):5599–5610.

Cappa, C. D., D. L. Che, S. H. Kessler, J. H. Kroll, and K. R. Wilson
2011. Variations in organic aerosol optical and hygroscopic properties upon heterogeneous OH oxidation. Geophys. Res. Lett., 116:D15204.

Carlton, A. and B. Turpin
2013. Particle partitioning potential of organic compounds is highest in the Eastern US and driven by anthropogenic water. Atmos. Chem. Phys., 13:10203–10214.

Carlton, A. G., B. J. Turpin, K. E. Altieri, S. Seitzinger, A. Reff, H.-J. Lim, and B. Ervens
2007. Atmospheric oxalic acid and SOA production from glyoxal: Results of aqueous photooxidation experiments. Atmos. Environ., 41(35):7588–7602.

Cerully, K., A. Bougiatioti, J. Hite, H. Guo, L. Xu, N. Ng, R. Weber, and A. Nenes
2014. On the link between hygroscopicity, volatility, and oxidation state of ambient and water-soluble aerosol in the southeastern united states. Atmos. Chem. Phys. Discuss., 14:30835–30877.

Chang, R.-Y., J. G. Slowik, N. C. Schantz, A. Vlasenko, J. Liggio, S. J. Sjostedt, W. R. Leaitch, and J. P. D. Abbatt
2010. The hygroscopicity parameter (κ) of ambient organic aerosol at a field site subject to biogenic and anthropogenic influences: relationship to degree of aerosol oxidation. Atmos. Chem. Phys., 10:5047–5064.

Chhabra, P. S., R. C. Flagan, and J. H. Seinfeld
2010. Elemental analysis of chamber organic aerosol using an aerodyne high-resolution aerosol mass spectrometer. Atmos. Chem. Phys., 10(9):4111–4131.

Coburn, S., I. Ortega, R. Thalman, B. Blomquist, C. Fairall, and R. Volkamer
2014. Measurements of diurnal variations and Eddy Covariance (EC) fluxes of glyoxal in the tropical marine boundary layer: description of the Fast LED-CE-DOAS instrument. Atmos. Meas. Tech., 7(10):3579–3595.

de Foy, B., E. Caetano, V. Magana, A. Zitacuaro, B. Cardenas, A. Retama, R. Ramos, L. Molina, and M. Molina
2005. Mexico City basin wind circulation during the MCMA-2003 field campaign. Atmos. Chem. Phys., 5:2267–2288.

De Haan, D., A. Corrigan, K. Smith, D. Stroik, J. Turley, F. Lee, M. Tolbert, J. Jimenez, K. Cordova, and G. Ferrell
2009a. Secondary organic aerosol-forming reactions of glyoxal with amino acids. Environ. Sci. Technol., 43(8):2818–2824.

De Haan, D., A. Corrigan, M. Tolbert, J. Jimenez, S. Wood, and J. Turley
2009b. Secondary organic aerosol formation by self-reactions of methylglyoxal and glyoxal in evaporating droplets. Environ. Sci. Technol., 43(21):8184–8190.

De Haan, D., L. Hawkins, J. Kononenko, J. Turley, A. Corrigan, M. Tolbert, and J. Jimenez
2010. Formation of Nitrogen-Containing Oligomers by Methylglyoxal and Amines in Simulated Evaporating Cloud Droplets. Environ. Sci. Technol., 45(3):984–991.

Debye, P. and J. McAulay
1925. Das elektrische feld der ionen und die neutralsalzwirkung. Physikalische Zeitschrift, 26:22–29.

DeCarlo, P. F., E. J. Dunlea, J. R. Kimmel, A. C. Aiken, D. Sueper, J. Crounse, P. O. Wennberg, L. Emmons, Y. Shinozuka, A. Clarke, J. Zhou, J. Tomlinson, D. R. Collins, D. Knapp, A. J. Weinheimer, D. D. Montzka, T. Campos, and J. L. Jimenez
2008. Fast airborne aerosol size and chemistry measurements above Mexico City and Central Mexico during the MILAGRO campaign. Atmos. Chem. Phys., 8(14):4027–4048.

DeCarlo, P. F., J. R. Kimmel, A. Trimborn, M. J. Northway, J. T. Jayne, A. C. Aiken, M. Gonin, K. Fuhrer, T. Horvath, K. S. Docherty, D. R. Worsnop, and J. L. Jimenez
2006. Field-deployable, high-resolution, time-of-flight aerosol mass spectrometer. Analytical Chemistry, 78(24):8281–8289.

DeCarlo, P. F., I. M. Ulbrich, J. Crounse, B. de Foy, E. J. Dunlea, A. C. Aiken, D. Knapp, A. J. Weinheimer, T. Campos, P. O. Wennberg, and J. L. Jimenez
2010. Investigation of the sources and processing of organic aerosol over the Central Mexican Plateau from aircraft measurements during MILAGRO. Atmos. Chem. Phys., 10:5257–5280.

Dibble, T.
2004. Prompt chemistry of alkenoxy radical products of the double H-atom transfer of alkoxy radicals from isoprene. J. Phys. Chem. A, 108(12):2208–2215.

Dinar, E., A. Riziq, C. Spindler, C. Erlick, G. Kiss, and Y. Rudich
2008. The complex refractive index of atmospheric and model humic-like substances (HULIS) retrieved by a cavity ring down aerosol spectrometer (CRD-AS). Faraday Discuss., 137:279–295.

Dockery, D., C. Pope, X. Xu, J. Spengler, J. Ware, M. Fay, B. Ferris, and F. Speizer
1993. An Association between Air Pollution and Mortality in Six U.S. Cities. N. Engl. J. Med., 329:1753–1759.

Donahue, N., S. Epstein, S. Pandis, and A. Robinson
. A two-dimensional volatility basis set: 1. organic-aerosol mixing thermodynamics. Atmos. Chem. Phys., 11(7).

Donahue, N., A. Robinson, C. Stanier, and S. Pandis
2006. Coupled Partitioning, Dilution, and Chemical Aging of Semivolatile Organics. Environ. Sci. Technol., 40(8):2635–2643.

Dzepina, K., C. D. Cappa, R. M. Volkamer, S. Madronich, P. F. DeCarlo, R. A. Zaveri, and J. L. Jimenez
2011. Modeling the Multiday Evolution and Aging of Secondary Organic Aerosol During MILAGRO 2006. Environ. Sci. Technol., 45(8):3496–3503.

Dzepina, K., R. M. Volkamer, S. Madronich, P. Tulet, I. M. Ulbrich, Q. Zhang, C. D. Cappa, P. J. Ziemann, and J. L. Jimenez
2009. Evaluation of recently-proposed secondary organic aerosol models for a case study in Mexico City. Atmos. Chem. Phys., 9(15):5681–5709.

Elm, J., M. Bilde, and K. Mikkelsen
2012. Assessment of density functional theory in predicting structures and free energies of reaction of atmospheric prenucleation clusters. J. Chem. Theory and Computation, 8(6):2071–2077.

Elm, J., M. Bilde, and K. Mikkelsen
2013a. Assessment of binding energies of atmospherically relevant clusters. Phys. Chem. Chem. Phys., 15(39):16442–16445.

Elm, J., M. Bilde, and K. Mikkelsen
2013b. Influence of nucleation precursors on the reaction kinetics of methanol with the OH radical. J. Phys. Chem. A, 117(30):6695–6701.

Elm, J., M. Fard, M. Bilde, and K. Mikkelsen
2013c. Interaction of glycine with common atmospheric nucleation precursors. J. Phys. Chem. A, 117(48):12990–12997.

Elm, J., T. Kurtén, M. Bilde, and K. Mikkelsen
2014. Molecular interaction of pinic acid with sulfuric acid: Exploring the thermodynamic landscape of cluster growth. J. Phys. Chem. A, 118(36):7892–7900.

Endo, S., A. Pfennigsdorff, and K.-U. Goss
2012. Salting-out effect in aqueous NaCl solutions: Trends with size and polarity of solute molecules. Environ. Sci. Technol., 46(3):1496–1503.

Epstein, S., E. Tapavicza, R. Furche, and S. Nizkorodov
2013. Direct photolysis of carbonyl compounds dissolved in cloud and fog droplets. Atmos. Chem. Phys., 13:9461–9477.

Ervens, B., S. Gligorovski, and H. Herrmann
2003. Temperature-dependent rate constants for hydroxyl radical reactions with organic compounds in aqueous solutions. Phys. Chem. Chem. Phys., 5(9):1811–1824.

Ervens, B., B. J. Turpin, and R. J. Weber
2011. Secondary organic aerosol formation in cloud droplets and aqueous particles (aqSOA): a review of laboratory, field and model studies. Atmos. Chem. Phys., 11(21):11069–11102.

Ervens, B. and R. Volkamer
2010. Glyoxal processing by aerosol multiphase chemistry: towards a kinetic modeling framework of secondary organic aerosol formation in aqueous particles. Atmos. Chem. Phys., 10(17):8219–8244.

Fayt, C. and M. van Roozendael
2001. WinDOAS 2.1, Software User Manual. Belgian Institute for Space Aeronomy: Brussels, Belgium.

Finlayson-Pitts, B. and J. Pitts
1999. Chemistry of the Upper and Lower Atmosphere: Theory, Experiments, and Applications. Acacemic Press.

Foley, K., S. Roselle, K. Appel, P. Bhave, J. Pleim, T. Otte, R. Mathur, G. Sarwar, J. Young, R. Gilliam, C. Nolte, J. Kelly, A. Gilliland, and J. Bash
2010. Incremental testing of the Community Multiscale Air Quality (CMAQ) modeling system version 4.7. Geoscientific Model Development, 3(1):205–226.

Fountoukis, C. and A. Nenes
2007. ISORROPIA II: a computationally efficient thermodynamic equilibrium model for K^+-Ca^{2+}-Mg^{2+}-NH^{4+}-Na^+-SO_4^{2-}-NO_3^--Cl^--H_2O aerosols. Atmos. Chem. Phys., 7(17):4639–4659.

Friese, E. and A. Ebel
2010. Temperature Dependent Thermodynamic Model of the System H^+-NH_4^+-Na^+-SO_4^{2-}- NO_3^--Cl^--H_2O. J. Phys. Chem. A, 114(43):11595–11631.

Frisch, M., G. Trucks, H. Schlegel, G. Scuseria, M. Robb, J. Cheeseman, G. Scalmani, V. Barone, B. Mennucci, and G. e. a. Petersson
2009. Gaussian 09, revision a. 1. Gaussian Inc., Wallingford, CT.

Fu, T.-M., D. Jacob, F. Wittrock, J. Burrows, M. Vrekoussis, and D. Henze
2008. Global budgets of atmospheric glyoxal and methylglyoxal, and implications for formation of secondary organic aerosols. J. of Geophys. Res.-Atmos., 113(D15):D15303.

Galloway, M., M. Powelson, N. Sedehi, S. Wood, K. Millage, J. Kononenko, A. Rynaski, and D. De Haan
2014. Secondary Organic Aerosol Formation during Evaporation of Droplets Containing Atmospheric Aldehydes, Amines, and Ammonium Sulfate. Environ. Sci. Technol.

Galloway, M. M., P. S. Chhabra, A. W. H. Chan, J. D. Surratt, R. C. Flagan, J. H. Seinfeld, and F. N. Keutsch
2009. Glyoxal uptake on ammonium sulphate seed aerosol: reaction products and reversibility of uptake under dark and irradiated conditions. Atmos. Chem. Phys., 9(10):3331–3345.

Galloway, M. M., C. L. Loza, P. S. Chhabra, A. W. H. Chan, L. D. Yee, J. H. Seinfeld, and F. N. Keutsch
2011. Analysis of photochemical and dark glyoxal uptake: Implications for SOA formation. Geophys. Res. Lett., 38:L17811.

Garland, R., A. Ravishankara, E. Lovejoy, M. Tolbert, and T. Baynard
2007. Parameterization for the relative humidity dependence of light extinction: Organic-ammonium sulfate aerosol. J. Geophys. Res., 112:D19303.

Gómez-Alvarez, E., M. Moreno-Vázquez, S. Gligorovski, H. Wortham, and M. Cases-Valcárcell
2012. Characterisation and calibration of active sampling solid phase microextraction applied to sensitive determination of gaseous carbonyls. Talanta, 88:252–258.

Gómez-Alvarez, E. and M. Valcárcel
2009. Research into conditions of quantitivity in the determination of carboniles in complex air matrices by adsorptive solid phase microextraction. Talanta, 77(4):1444–1453.

Gordon, J. and R. Thorne
1967a. Salt effects on non-electrolyte activity coefficients in mixed aqueous electrolyte solutionsII. Artificial and natural sea waters. Geochimica et Cosmochimica acta, 31(12):2433–2443.

Gordon, J. and R. Thorne
1967b. Salt Effects on the Activity Coefficient of Naphthalene in Mixed Aqueous Electrolyte Solutions. I. Mixtures of Two Salts. J. Phys. Chem., 71(13):4390–4399.

Görgényi, M., J. Dewulf, H. Van Langenhove, and K. Héberger
2006. Aqueous salting-out effect of inorganic cations and anions on non-electrolytes. Chemosphere, 65(5):802–810.

Goss, N., E. Waxman, S. Coburn, T. Koenig, R. Thalman, J. Dommen, J. Hannigan, G. Tyndall, and R. Volkamer
2015. Measurements of the Absorption Cross Section of $^{13}CHO^{13}CHO$ at Visible Wavelengths and Application to DOAS Retrievals. J. Phys. Chem. A., Mario Molina Festschrift, 119(19):4651–4657.

Grieshop, A. P., J. M. Logue, N. M. Donahue, and A. L. Robinson
2009. Laboratory investigation of photochemical oxidation of organic aerosol from wood fires 1: measurement and simulation of organic aerosol evolution. Atmos. Chem. Phys., 9(4):1263–1277.

Hamilton, J. F., M. Teresa Baeza-Romero, E. Finessi, A. R. Rickard, R. M. Healy, S. Peppe, T. J. Adams, M. J. S. Daniels, S. M. Ball, I. C. A. Goodall, P. S. Monks, E. Borras, and A. Munoz
2013. Online and offline mass spectrometric study of the impact of oxidation and ageing on glyoxal chemistry and uptake onto ammonium sulfate aerosols. Faraday Discuss., 165:447–472.

Hastings, W., C. Koehler, E. Bailey, and D. De Haan
2005. Secondary organic aerosol formation by glyoxal hydration and oligomer formation: Humidity effects and equilibrium shifts during analysis. Environ. Sci. Technol., 39(22):8728–8735.

Hatakeyama, S., N. Washida, and H. Akimoto
1986. Rate Constants and Mechanisms for the Reaction of OH (OD) Radicals with Acetylene, Propyne, and 2-Butyne in Air at 297 ± 2K. J. Phys. Chem., 90(1):173–178.

Hatch, L., J. Creamean, A. Ault, J. Surratt, M. Chan, J. Seinfeld, E. Edgerton, Y. Su, and K. Prather
2011. Measurements of isoprene-derived organosulfates in ambient aerosols by aerosol time-of-flight mass spectrometry-Part 1: Single particle atmospheric observations in Atlanta. Environ. Sci. Technol., 45(12):5105–5111.

Hawkins, L., M. Baril, N. Sedehi, M. Galloway, D. De Haan, G. Schill, and M. Tolbert
2014. Formation of Semisolid, Oligomerized Aqueous SOA: Lab Simulations of Cloud Processing. Environ. Sci. Technol., 48:2273–2280.

He, C., J. Liu, A. Carlton, S. Fan, L. Horowitz, H. Levy, and S. S. Tao
2013. Evaluation of factors controlling global secondary organic aerosol production from cloud processes. Atmos. Chem. Phys., 13:1913–1926.

Hennigan, C. J., M. H. Bergin, A. G. Russell, A. Nenes, and R. J. Weber
2009. Gas/particle partitioning of water-soluble organic aerosol in atlanta. Atmos. Chem. Phys., 9(11):3613–3628.

Hodzic, A. and J. L. Jimenez
2011. Modeling anthropogenically controlled secondary organic aerosols in a megacity: a simplified framework for global and climate models. Geoscientific Model Development, 4(4):901–917.

Hodzic, A., J. L. Jimenez, S. Madronich, M. R. Canagaratna, P. F. DeCarlo, L. Kleinman, and J. Fast
2010. Modeling organic aerosols in a megacity: potential contribution of semi-volatile and intermediate volatility primary organic compounds to secondary organic aerosol formation. Atmos. Chem. Phys., 10(12):5491–5514.

Hoffer, A., A. Gelencsèr, P. Guyon, G. Kiss, O. Schmid, G. Frank, P. Artaxo, and M. Andreae
2006. Optical properties of humic-like substances (HULIS) in biomass-burning aerosols. Atmos. Chem. Phys., 6:3563–3570.

Hoyle, C., G. Myhre, T. Berntsen, and I. Isaksen
2009. Anthropogenic influence on SOA and the resulting radiative forcing. Atmos. Chem. and Phys., 9(8):2715–2728.

Ip, H. S. S., X. H. H. Huang, and J. Z. Yu
2009. Effective Henry's law constants of glyoxal, glyoxylic acid, and glycolic acid. Geophysical Research Letters, 36:L01802.

Jerrett, M., R. Burnett, R. Ma, C. Pope, D. Krewski, K. Newbold, G. Thurston, Y. Shi, N. Finkelstein, E. Calle, and M. Thun
2005. Spatial Analysis of Air Pollution and Mortality in Los Angeles. Epidemiol., 16:727–736.

Jimenez, J. L., M. R. Canagaratna, N. M. Donahue, A. S. H. Prevot, Q. Zhang, J. H. Kroll, P. F. DeCarlo, J. D. Allan, H. Coe, N. L. Ng, A. C. Aiken, K. S. Docherty, I. M. Ulbrich, A. P. Grieshop, A. L. Robinson, J. Duplissy, J. D. Smith, K. R. Wilson, V. A. Lanz, C. Hueglin, Y. L. Sun, J. Tian, A. Laaksonen, T. Raatikainen, J. Rautiainen, P. Vaattovaara, M. Ehn, M. Kulmala, J. M. Tomlinson, D. R. Collins, M. J. Cubison, E. J. Dunlea, J. A. Huffman, T. B. Onasch, M. R. Alfarra, P. I. Williams, K. Bower, Y. Kondo, J. Schneider, F. Drewnick, S. Borrmann, S. Weimer, K. Demerjian, D. Salcedo, L. Cottrell, R. Griffin, A. Takami, T. Miyoshi, S. Hatakeyama, A. Shimono, J. Y. Sun, Y. M. Zhang, K. Dzepina, J. R. Kimmel, D. Sueper, J. T. Jayne, S. C. Herndon, A. M. Trimborn, L. R. Williams, E. C. Wood, A. M. Middlebrook, C. E. Kolb, U. Baltensperger, and D. R. Worsnop
2009. Evolution of organic aerosols in the atmosphere. Science, 326(5959):1525–1529.

Johnson, K. S., B. de Foy, B. Zuberi, L. T. Molina, M. J. Molina, Y. Xie, A. Laskin, and V. Shutthanandan
2006. Aerosol composition and source apportionment in the Mexico City Metropolitan Area with PIXE/PESA/STIM and multivariate analysis. Atmos. Chem. Phys., 6:4591–4600.

Kampf, C., A. Corrigan, A. Johnson, W. Song, P. Keronen, R. Königstedt, J. Williams, L. Russell, T. Petäjä, H. Fischer, and T. Hoffmann
2012a. First measurements of reactive α-dicarbonyl concentrations on PM 2.5 aerosol over the Boreal forest in Finland during HUMPPA-COPEC 2010–source apportionment and links to aerosol aging. Atmos. Chem. Phys., 12(14):6145–6155.

Kampf, C. J., R. Jakob, and T. Hoffmann
2012b. Identification and characterization of aging products in the glyoxal/ammonium sulfate system - implications for light-absorbing material in atmospheric aerosols. Atmos. Chem. Phys., 12(14):6323–6333.

Kampf, C. J., E. M. Waxman, J. G. Slowik, J. Dommen, L. Pfaffenberger, A. P. Praplan, A. S. H. Prevot, U. Baltensperger, T. Hoffmann, and R. Volkamer
2013. Effective Henry's Law Partitioning and the Salting Constant of Glyoxal in Aerosols Containing Sulfate. Environ. Sci. Technol., 47(9):4236–4244.

Kaulgud, M. and W. Pokale
1995. Measurement of the temperature of maximum density of aqueous solutions of some salts and acids. J. Chem. Soc. Faraday Trans., 91(6):999–1004.

Kieber, R., X. Zhou, and K. Mopper
1990. Formation of carbonyl compounds from uv-induced photodegradation of humic substances in natural waters: Fate of riverine carbon in the sea. Limnol. and Oceanog., 35(7):1503–1515.

Knote, C., A. Hodzic, J. Jimenez, R. Volkamer, J. Orlando, S. Baidar, J. Brioude, J. Fast, D. Gentner, A. Goldstein, P. Hayes, W. Knighton, H. Oetjen, A. Setyan, H. Stark, R. Thalman, G. Tyndall, R. Washenfelder, E. Waxman, and Q. Zhang
2014. Simulation of semi-explicit mechanisms of SOA formation from glyoxal in aerosol in a 3-D model. Atmos. Chem. Phys., 14:6213–6239.

Koziel, J., J. Noah, and J. Pawliszyn
2001. Field sampling and determination of formaldehyde in indoor air with solid-phase microextraction and on-fiber derivatization. Environ. Sci. Technol., 35(7):1481–1486.

Kroll, J., N. Ng, S. Murphy, R. Flagan, and J. Seinfeld
2005. Secondary organic aerosol formation from isoprene photooxidation under high-NO_x conditions. Geophys. Res. Lett., 32(18):L18808.

Kua, J., H. Krizner, and D. De Haan
2011. Thermodynamics and Kinetics of Imidazole Formation from Glyoxal, Methylamine, and Formaldehyde: A Computational Study. J. Phys. Chem. A, 115(9):1667–1675.

Kulmala, M.
2003. How particles nucleate and grow. Science, 302:1000–1001.

Kulmala, M. and V.-M. Kerminen
2008. On the formation and growth of atmospheric nanoparticles. Atmos. Res., 90:132–150.

Kulmala, M., J. Kontkanen, H. Junninen, K. Lehtipalo, H. Manninen, T. Nieminen, T. Petäjä, M. Sipilä, S. Schobesberger, P. Rantala, A. Franchin, T. Jokinen, E. Järvinen, M. Äijälä, J. Kangasluoma, J. Hakala, P. Aalto, P. Paasonen, J. Mikkilä, J. Vanhanen, J. Aalto, H. Hakola, U. Makkonen, T. Ruuskanen, R. Mauldin, J. Duplissy, H. Vehkamäki, J. Bäck, A. Kortelainen, I. Riipinen, T. Kurtén, M. Johnston, J. Smith, M. Ehn, T. Mentel, K. Lehtinen, A. Laaksonen, V.-M. Kerminen, and D. Worsnop
2013. Direct observations of atmospheric aerosol nucleation. Science, 339:943–946.

Kurtén, T., J. Elm, N. Prisle, K. Mikkelsen, C. Kampf, E. Waxman, and R. Volkamer
2015. Computational Study of the Effect of Glyoxal-Sulfate Clustering on the Henrys Law Coefficient of Glyoxal. J. Phys. Chem. A, 119:4509–4514.

Laden, F., J. Schwartz, F. Speizer, and D. Dockery
2006. Reduction in Fine Particulate Air Pollution and Mortality: Extended Follow-Up of the Harvard Six Cities Study. Am. J. Respir. Crit. Care Med., 173:667–672.

Lambe, A. T., T. B. Onasch, P. Massoli, D. R. Croasdale, J. P. Wright, A. T. Ahern, L. R. Williams, D. R. Worsnop, W. H. Brune, and P. Davidovits
2011. Laboratory studies of the chemical composition and cloud condensation nuclei (CCN) activity of secondary organic aerosol (SOA) and oxidized primary organic aerosol (OPOA). Atmos. Chem. Phys., 11(17):8913–8928.

Lambrecht, D., G. Clark, T. Head-Gordon, and M. Head-Gordon
2011. Exploring the Rich Energy Landscape of Sulfate–Water Clusters $SO_4^{2-}(H_2O)_{n=3--7}$: An Electronic Structure Approach. J. P. Chem. A, 115(41):11438–11454.

Laskin, A., J. Laskin, and S. Nizkorodov
2015. Chemistry of atmospheric brown carbon. Chem. Rev.

Laskin, J., A. Laskin, S. Nizkorodov, P. Roach, P. Eckert, M. Gilles, B. Wang, H. Lee, and Q. Hu
2014. Molecular Selectivity of Brown Carbon Chromophores. Environ. Sci. Techno., 48(20):12047–12055.

Lee, A., K. Hayden, P. Herckes, W. Leaitch, J. Liggio, A. Macdonald, 2, and J. Abbatt
2012. Characterization of aerosol and cloud water at a mountain site during WACS 2010: secondary organic aerosol formation through oxidative cloud processing. Atmos. Chem. Phys., 12:7103–7116.

Lee, A., R. Zhao, S. S. Gao, and J. P. D. Abbatt
2011. Aqueous-Phase OH Oxidation of Glyoxal: Application of a Novel Analytical Approach Employing Aerosol Mass Spectrometry and Complementary Off-Line Techniques. J. Phys. Chem., 115(38):10517–10526.

Lee, A., R. Zhao, R. Li, J. Liggio, S.-M. Li, and J. Abbatt
2013. Formation of Light Absorbing Organo-Nitrogen Species from Evaporation of Droplets Containing Glyoxal and Ammonium Sulfate. Environ. Sci. Techno., 47:12819?12826.

Lee-Taylor, J., S. Madronich, B. Aumont, A. Baker, M. Camredon, A. Hodzic, G. S. Tyndall, E. Apel, and R. A. Zaveri
2011. Explicit modeling of organic chemistry and secondary organic aerosol partitioning for Mexico City and its outflow plume. Atmos. Chem. Phys., 11(24):13219–13241.

Leverentz, H., J. Siepmann, D. Truhlar, V. Loukonen, and H. Vehkamaki
2013. Energetics of atmospherically implicated clusters made of sulfuric acid, ammonia, and dimethyl amine. J. Phys. Chem. A, 117(18):3819–3825.

Liggio, J., S. Li, and R. McLaren
2005a. Heterogeneous reactions of glyoxal on particulate matter: Identification of acetals and sulfate esters. Environ. Sci. Technol., 39(6):1532–1541.

Liggio, J., S. Li, and R. McLaren
2005b. Reactive uptake of glyoxal by particulate matter. J. Geophys. Res.-Atmospheres, 110(D10):D10304.

Lim, Y., Y. Tan, and B. Turpin
13. Chemical insights, explicit chemistry, and yields of secondary organic aerosol from OH radical oxidation of methylglyoxal and glyoxal in the aqueous phase. Atmos. Chem. Phys., 13:8651–8667.

Lim, Y. B., Y. Tan, M. J. Perri, S. P. Seitzinger, and B. J. Turpin
2010. Aqueous chemistry and its role in secondary organic aerosol (SOA) formation. Atmos. Chem. Phys., 10(21):10521–10539.

Lin, Y.-H., S. Budisulistiorini, K. Chu, R. Siejack, H. Zhang, M. Riva, Z. Zhang, A. Gold, K. Kautzman, and J. Surratt
2014. Light-Absorbing Oligomer Formation in Secondary Organic Aerosol from Reactive Uptake of Isoprene Epoxydiols. Environ. Sci. Technol., 48(20):12012–12021.

Liu, Y., A. Monod, T. Tritscher, A. Praplan, P. DeCarlo, B. Temime-Roussel1, E. Quivet, N. Marchand, J. Dommen, and U. Baltensperger
2012. Aqueous phase processing of secondary organic aerosol from isoprene photooxidation. Atmos. Chem. Phys., 12:5879–5895.

Liu, Y.-R., H. Wen, T. Huang, X.-X. Lin, Y.-B. Gai, C.-J. Hu, W.-J. Zhang, and W. Huang
2014. Structural exploration of water, nitrate/water, and oxalate/water clusters with basin-hopping method using a compressed sampling technique. J. Phys. Chem. A, 118(2):508–516.

Loeffler, K., C. Koehler, N. Paul, and D. De Haan
2006. Oligomer Formation in Evaporating Aqueous Glyoxal and Methyl Glyoxal Solutions. Environ. Sci. Technol., 40(20):6318–6323.

Luo, G. and F. Yu
2010. A numerical evaluation of global oceanic emissions of α-pinene and isoprene. Atmos. Chem. Phys., 10(4):2007–2015.

Marcus, Y.
2013. Prediction of salting-out and salting-in constants. J. Molec. Liq., 177:7–10.

McCormick, M., L. Thomason, and C. Trepte
1995. Atmospheric effects of the mt pinatubo eruption. Nature, 373:399–404.

McDevit, W. and F. Long
1952. The activity coefficient of benzene in aqueous salt solutions. Jour. Am. Chem. Soc., 74(7):1773–1777.

Meylan, W. and P. Howard
1991. Bond contribution method for estimating Henry's law constants. Environ. Toxicol. Chem., 10(10):1283–1293.

Miertuš, S., E. Scrocco, and J. Tomasi
1981. Electrostatic interaction of a solute with a continuum. A direct utilizaion of AB initio molecular potentials for the prevision of solvent effects. Chem. Phys., 55(1):117–129.

Millero, F.
1971. The molal volumes of electrolytes. Chem. Rev., 71(2):147–176.

Moise, T., J. Flores, and Y. Rudich
2015. Optical properties of secondary organic aerosols and their changes by chemical processes. Chem. Rev.

Monge, M. E., T. Rosenorn, O. Favez, M. Mueller, G. Adler, A. A. Riziq, Y. Rudich, H. Herrmann, C. George, and B. D'Anna
2012. Alternative pathway for atmospheric particles growth. Proc. Nat. Acad. Sci., 109(18):6840–6844.

Mukerjee, P.
1961. On Ion-Solvent Interactions. Part I: Partial Molal Volumes of Ions in Aqueous Solution, journal=J. Phys. Chem, volume=65, number=May, pages=740-744.

Nadykto, A., F. Yu, and A. Al Natsheh
2009. Anomalously strong effect of the ion sign on the thermochemistry of hydrogen bonded aqueous clusters of identical chemical composition. Int. J. Molec. Sci., 10(2):507–517.

Nakao, S., Y. Liu, P. Tang, C. . Chen, J. Zhang, and D. Cocker
2012. Chamber studies of SOA formation from aromatic hydrocarbons: observation of limited glyoxal uptake. Atmos. Chem. Phys., 12(9):3927–3937.

Ng, N. L., J. H. Kroll, A. W. H. Chan, P. S. Chhabra, R. C. Flagan, and J. H. Seinfeld
2007. Secondary organic aerosol formation from m-xylene, toluene, and benzene. Atmos. Chem. Phys., 7(14):3909–3922.

Nguyen, T., M. Coggon, R. Flagan, and J. Seinfeld
2013. Reactive Uptake and Photo-Fenton Oxidation of Glycolaldehyde in Aerosol Liquid Water. Environ. Sci. Technol., 47(9):4307–4316.

Nguyen, T., M. Petters, S. Suda, H. Guo, R. Weber, and A. Carlton
2014. Trends in particle-phase liquid water during the Southern Oxidant and Aerosol Study. Atmos. Chem. and Phys., 14(20):10911–10930.

Noziere, B., P. Dziedzic, and A. Cordova
2009. Products and Kinetics of the Liquid-Phase Reaction of Glyoxal Catalyzed by Ammonium Ions (NH_4^+). J. Phys. Chem. A, 113(1):231–237.

Ortiz-Montalvo, D., HäkkinenS.A.K., A. Schwier, Y. Lim, V. McNeill, and B. Turpin
2014. Ammonium Addition (and Aerosol pH) Has a Dramatic Impact on the Volatility and Yield of Glyoxal Secondary Organic Aerosol. Environ. Sci. Technol., 48:255–262.

Ortiz-Montalvo, D., Y. Lim, M. Perri, S. Seitzinger, and B. Turpin
2012. Volatility and Yield of Glycolaldehyde SOA Formed through Aqueous Photochemistry and Droplet Evaporation. Aerosol Sci. Technol., 46(9):1002–1014.

Paulot, F., J. Crounse, H. Kjaergaard, J. Kroll, J. Seinfeld, and P. Wennberg
2009. Isoprene photooxidation: new insights into the production of acids and organic nitrates. Atmos. Chem. Phys., 9(4):1479–1501.

Paulsen, D., J. Dommen, M. Kalberer, A. Prevot, R. Richter, M. Sax, M. Steinbacher, E. Weingartner, and U. Baltensperger
2005. Secondary organic aerosol formation by irradiation of 1,3,5-trimethylbenzene-NO_x-H_2O in a new reaction chamber for atmospheric chemistry and physics. Environ. Sci. Technol., 39(8):2668–2678.

Petters, M. and S. Kreidenweis
2007. A single parameter representation of hygroscopic growth and cloud condensation nucleus activity. Atmos. Chem. Phys., 7(8):1961–1971.

Philip, S., R. Martin, A. van Donkelaar, J.-H. Lo, Y. Wang, D. Chen, L. Zhang, P. Kasibhatla, S. Wang, Q. Zhang, Z. Lu, D. Streets, S. Bittman, and D. MacDonald
2014. Global chemical composition of ambient fine particulate matter for exposure assessment. Environ. Sci. Technol., 48(22):13060–13068.

Pickard IV, F., M. Dunn, and G. Shields
2005. Comparison of model chemistry and density functional theory thermochemical predictions with experiment for formation of ionic clusters of the ammonium cation complexed with water and ammonia; atmospheric implications. J. Phys. Chem. A, 109(22):4905–4910.

Pope, C., R. Burnett, M. Thun, E. Calle, D. Krewski, K. Ito, and G. Thurston
2002. Lung cancer, cardiopulmonary mortality, and long-term exposure to fine particulate air pollution. J. Am. Med. Assoc., 287:1132–1141.

Pope, C., R. Burnett, G. Thurston, M. Thun, E. Calle, D. Krewski, and J. Godleski
2004. Cardiovascular mortality and long-term exposure to particulate air pollution: Epidemiological evidence of general pathophysiological pathways of disease. Circulation, 109:71–77.

Pope, C. and D. Dockery
2006. Health effects of fine particulate air pollution: Lines that connect. J. Air & Waste Manage. Assoc., 56:709–742.

Pope, C., M. Thun, M. Namboodiri, D. Dockery, J. Evans, F. Speizer, and J. Heath
1995. Particulate Air Pollution as a Predictor of Mortality in a Prospective Study of U.S. Adults. Am. J. Respir. Crit. Care. Med., 151:669–674.

Powelson, M., B. Espelien, L. Hawkins, M. Galloway, and D. De Haan
2013. Brown carbon formation by aqueous-phase carbonyl compound reactions with amines and ammonium sulfate. Environ. Sci. Technol., 48(2):985–993.

Pye, H., R. Pinder, I. Piletic, Y. Xie, S. Capps, Y.-H. Lin, J. Surratt, Z. Zhang, A. Gold, D. Luecken, W. Hutzell, M. Jaoui, J. Offenberg, T. Kleindienst, M. Lewandowski, and E. Edney
2013. Epoxide pathways improve model predictions of isoprene markers and reveal key role of acidity in aerosol formation. Environ. Sci. Technol., 47(19):11056–11064.

Reisen, F., S. Aschmann, R. Atkinson, and J. Arey
2003. Hydroxyaldehyde products from hydroxyl radical reactions of Z-3-hexen-1-ol and 2-methyl-3-buten-2-ol quantified by SPME and API-MS. Environ. Sci. Technol., 37(20):4664–4671.

Renard, P., F. Siekmann, A. Gandolfo1, J. Socorro, G. Salque, S. Ravier, E. Quivet, J.-L. Clément, M. Traikia, A.-M. Delort, D. Voisin, R. Thissen, and A. Monod
2013. Radical mechanisms of methyl vinyl ketone oligomerization through aqueous phase OH-oxidation: on the paradoxical role of dissolved molecular oxygen. Atmos. Chem. Phys., 13:6473–6491.

Renard, P., F. Siekmann, G. Salque, C. Demelas, B. Coulomb, L. Vassalo, S. Ravier, B. Temime-Roussel, D. Voisin, and A. Monod
2015. Aqueous-phase oligomerization of methyl vinyl ketone through photooxidation – Part 1: Aging processes of oligomers. Atmos. Chem. Phys., 15:21–35.

Roach, P. J., J. Laskin, and A. Laskin
2010. Molecular Characterization of Organic Aerosols Using Nanospray-Desorption/Electrospray Ionization-Mass Spectrometry. Anal. Chem., 82(19):7979–7986.

Robinson, A. L., N. M. Donahue, M. K. Shrivastava, E. A. Weitkamp, A. M. Sage, A. P. Grieshop, T. E. Lane, J. R. Pierce, and S. N. Pandis
2007. Rethinking organic aerosols: Semivolatile emissions and photochemical aging. Science, 315(5816):1259–1262.

Romonosky, D., A. Laskin, J. Laskin, and S. Nizkorodov
2014. High-Resolution Mass Spectrometry and Molecular Characterization of Aqueous Photochemistry Products of Common Types of Secondary Organic Aerosols. J. Phys. Chem. A.

Rossignol, S., K. Aregahegn, L. Tinel, L. Fine, B. Noziere, and C. George
2014. Glyoxal induced atmospheric photosensitized chemistry leading to organic aerosol growh. Environ. Sci. Technol., 48(6):3218–3227.

Salcedo, D., T. B. Onasch, K. Dzepina, M. Canagaratna, Q. Zhang, J. Huffman, P. DeCarlo, J. Jayne, P. Mortimer, D. Worsnop, C. Kolb, K. Johnson, B. Zuberi, L. Marr, R. Volkamer, L. Molina, M. Molina, B. Cardenas, R. Bernabe, C. Marquez, J. Gaffney, N. Marley, A. Laskin, V. Shutthanandan, Y. Xie, W. Brune, R. Lesher, T. Shirley, and J. Jimenez
2006. Characterization of ambient aerosols in Mexico City during the MCMA-2003 campaign with Aerosol Mass Spectrometry: results from the CENICA Supersite. Atmos. Chem. Phys., 6:925–946.

Sander, R.
2015. Compilation of Henry's law constants, version 3.99. Atmos. Chem. and Phys., 15(8):4399–4981.

Sareen, N., A. Schwier, E. Shapiro, D. Mitroo, and V. McNeill
2010. Secondary organic material formed by methylglyoxal in aqueous aerosol mimics. Atmos. Chem. Phys., 10(3):997–1016.

Saylor, J., A. Whitten, I. Claiborne, and P. Gross
1952. The solubilities of benzene, nitrobenzene and ethylene chloride in aqueous salt solutions. J. Am. Chem. Soc., 74(7):1778–1781.

Scanlon, J. and D. Willis
1985. Calculation of flame ionization detector relative response factors using the effective carbon number concept. J. Chrom. Sci., 23(8):333–340.

Schöne, L., S. J., E. Szeremeta, T. Schaefer, D. Hoffmann, K. Rudzinski, R. Szmigielski, and H. Herrmann
2014. Atmospheric aqueous phase radical chemistry of the isoprene oxidation products methacrolein, methyl vinyl ketone, methacrylic acid and acrylic acid – kinetics and product studies. Phys. Chem. Chem. Phys., 16:6257–6272.

Schwikowski, M., A. Döscher, H. Gäggler, and U. Schotterer
1999. Anthropogenic versus natural sources of atmospheric sulphate from an alpine ice core. Tellus, 51B(5):938–951.

Seinfeld, J. and J. Pankow
2003. Organic Atmospheric Particulate Material. Annu. Rev. Phys. Chem., 54:121–140.

Seinfeld, J. H. and S. N. Pandis
2006. Atmospheric Chemistry and Physics: From Air Pollution to Climate Change, second edition. Hoboken, New Jersey: John Wiley & Sons, Inc.

Setschenow, J.
1889. Über die Konstitution der Salzlösungen auf Grund ihres Verhaltens zu Kohlensäure. Z. Phys. Chem., Vierter Band(1):117–125.

Shapiro, E. L., J. Szprengiel, N. Sareen, C. N. Jen, M. R. Giordano, and V. F. McNeill
2009. Light-absorbing secondary organic material formed by glyoxal in aqueous aerosol mimics. Atmos. Chem. Phys., 9(7):2289–2300.

Sheehy, P. M., R. Volkamer, L. T. Molina, and M. J. Molina
2010. Oxidative capacity of the Mexico City atmosphere - Part 2: A RO_x radical cycling perspective. Atmos. Chem. Phys., 10(14):6993–7008.

Shiraiwa, M., M. Ammann, T. Koop, and U. Pöschl
2011. Gas uptake and chemical aging of semisolid organic aerosol particles. Proc. Nat. Acad. Sci., 108(27):11003–11008.

Shirley, T. R., W. H. Brune, X. Ren, J. Mao, R. Lesher, B. Cardenas, R. Volkamer, L. T. Molina, M. J. Molina, B. Lamb, E. Velasco, T. Jobson, and M. Alexander
2006. Atmospheric oxidation in the Mexico City Metropolitan Area (MCMA) during April 2003. Atmos. Chem. Phys., 6:2753–2765.

Simons, J.
2008. Molecular anions. J. Phys. Chem. A, 112(29):6401–6511.

Sinreich, R., S. Coburn, B. Dix, and R. Volkamer
2010. Ship-based detection of glyoxal over the remote tropical Pacific Ocean. Atmos. Chem. Phys., 10(23):11359–11371.

Stocker, T., D. Qin, G.-K. Plattner, M. Tignor, S. Allen, J. Boschung, A. Nauels, Y. Xia, V. Bex, and P. Midgley
2013. Anthropogenic and Natural Radiative Forcing. Climate Change 2013: The Physical Science Basis. Contribution of Working Group I to the Fifth Assessment Report of the Intergovernmental Panel on Climate Change. Cambridge, United Kingdom and New York, NY, USA: Cambridge University Press.

Surratt, J., A. Chan, N. Eddingsaas, M. Chan, C. Loza, A. Kwan, S. Hersey, R. Flagan, P. Wennberg, and J. Seinfeld
2010. Reactive intermediates revealed in secondary organic aerosol formation from isoprene. Proc. Nat. Acad. Sci., 107(15):6640–6645.

Taira, M. and Y. Kanda
1990. Continuous generation system for low-concentration gaseous nitrous-acid. Analytical Chemistry, 62(6):630–633.

Tan, Y., M. J. Perri, S. P. Seitzinger, and B. J. Turpin
2009. Effects of Precursor Concentration and Acidic Sulfate in Aqueous Glyoxal-OH Radical Oxidation and Implications for Secondary Organic Aerosol. Environ. Sci. Technol., 43(21):8105–8112.

Thalman, R. and R. Volkamer
2010. Inherent calibration of a blue LED-CE-DOAS instrument to measure iodine oxide, glyoxal, methyl glyoxal, nitrogen dioxide, water vapour and aerosol extinction in open cavity mode. Atmos. Meas. Tech., 3(6):1797–1814.

Thalman, R. and R. Volkamer
2013. Temperature dependent absorption cross-sections of O_2-O_2 collision pairs between 340 and 630 nm and at atmospherically relevant pressure. Phys. Chem. Chem. Phys., 15(37):15371–15381.

Tomasi, J., B. Mennucci, and R. Cammi
2005. Quantum mechanical continuum solvation models. Chem. Rev., 105(8):2999–3094.

Toon, O. B., J. B. Pollack, and B. N. Khare
1976. Optical-Constants of several Atmospheric Aerosol Species - Ammonium-Sulfate, Aluminum-Oxide, and Sodium-Chloride. J. Geophys. Res.-Oceans and Atmospheres, 81(33):5733–5748.

Trainic, M., A. Abo Riziq, F. J. Lavi, A., and Y. Rudich
2011. The optical, physical and chemical properties of the products of glyoxal uptake on ammonium sulfate seed aerosols. Atmos. Chem. Phys., 11:9697–9707.

Unger, N.
2014. On the role of plant volatiles in anthropogenic global climate change. Geophys. Res. Lett., 41:8563–8569.

Vandaele, A., C. Hermans, S. Fally, M. Carleer, R. Colin, M. Merienne, A. Jenouvrier, and B. Coquart
2002. High-resolution Fourier transform measurement of the NO_2 visible and near-infrared absorption cross sections: Temperature and pressure effects. J. Geophys. Res. – Atmos., 107(D18):4348.

Vetter, I., H. Hanssum, and H. Bäumert
1991. Studies on the anion binding selectivity of sarcoplasmic reticulum membranes by ^{35}Cl-NMR. Biochimica et Biophysica Acta, 1067:9–16.

Volkamer, R., I. Barnes, U. Platt, L. Molina, and M. Molina
2006a. Remote sensing of glyoxal by differential optical absorption spectroscopy (DOAS): Advancements in simulation chamber and field experiments. In Environmental Simulation Chambers: Application to Atmospheric Chemical Processes, Pp. 129–141. Springer.

Volkamer, R. M., J. L. Jimenez, F. San Martini, K. Dzepina, Q. Zhang, D. Salcedo, L. T. Molina, D. R. Worsnop, and M. J. Molina
2006b. Secondary organic aerosol formation from anthropogenic air pollution: Rapid and higher than expected. Geophys. Res. Lett., 33(17):L17811.

Volkamer, R. M., F. S. Martini, L. T. Molina, D. Salcedo, J. L. Jimenez, and M. J. Molina
2007. A missing sink for gas-phase glyoxal in Mexico City: Formation of secondary organic aerosol. Geophys. Res. Lett., 34(19):L19807.

Volkamer, R. M., L. T. Molina, M. J. Molina, T. Shirley, and W. H. Brune
2005a. DOAS measurement of glyoxal as an indicator for fast VOC chemistry in urban air. Geophys. Res. Lett., 32(8):L08806.

Volkamer, R. M., U. Platt, and K. Wirtz
2001. Primary and secondary glyoxal formation from aromatics: Experimental evidence for the bicycloalkyl-radical pathway from benzene, toluene, and p-xylene. J. Phys. Chem. A, 105(33):7865–7874.

Volkamer, R. M., P. Spietz, J. Burrows, and U. Platt
2005b. High-resolution absorption cross-section of glyoxal in the UV-vis and IR spectral ranges. J. Photochem. Photobiol. A – Chemistry, 172(1):35–46.

Volkamer, R. M., P. J. Ziemann, and M. J. Molina
2009. Secondary Organic Aerosol Formation from Acetylene (C_2H_2): seed effect on SOA yields due to organic photochemistry in the aerosol aqueous phase. Atmos. Chem. Phys., 9(6):1907–1928.

Wang, C., Y. Lei, S. Endo, and F. Wania
2014a. Measuring and modeling the salting-out effect in ammonium sulfate solutions. Environ. Sci. Technol., 48(22):13238–13245.

Wang, X., X. Ye, H. Chen, J. Chen, X. Yang, and D. Gross
2014b. Online hygroscopicity and chemical measurement of urban aerosol in Shanghai, China. Atmos. Environ., 95:318–326.

Wang, X.-B., J. Nicholas, and L.-S. Wanga
2000. Electronic instability of isolated SO_4^{2-} and its solvation stabilization. J. Chem. Phys., 113(24).

Waxman, E., K. Dzepina, B. Ervens, J. Lee-Taylor, B. Aumont, J. Jimenez, S. Madronich, and R. Volkamer
2013. Secondary organic aerosol formation from semi- and intermediate-volatility organic compounds and glyoxal: Relevance of O/C as a tracer for aqueous multiphase chemistry. Geophys. Res. Lett., 40(5):978–982.

Whipple, E.
1970. The Structure of Glyoxal in Water. J. Am. Chem. Soc., 92(24):7183–7186.

Wong, Y.
1935. An application of orthogonalization process to the theory of least squares. Annals of Mathematical Statistics, 6:53–75.

Woo, J., D. Kim, A. Schwier, R. Li, and V. McNeill
2013. Aqueous aerosol SOA formation: impact on aerosol physical properties. Faraday Discuss., 165:357–367.

Xie, W., W. Shiu, and D. Mackay
1997. A review of the effect of salts on the solubility of organic compounds in seawater. Marine Environ. Res., 44(4):429–444.

Xu, L., H. Guo, C. Boyd, M. Klein, A. Bougiatioti, K. Cerully, J. Hite, G. Isaacman-VanWertz, N. Kreisberg, C. Knote, K. Olsonh, A. Koss, A. Goldstein, S. Hering, J. de Gouw, K. Baumann, S.-H. Lee, A. Nenes, R. Weber, and N. Ng
2015. Effects of anthropogenic emissions on aerosol formation from isoprene and monoterpenes in the southeastern United States. Proc. Nat. Acad. Sci., 112(1):37–42.

Xu, W., S. Guo, M. Gomez-Hernandez, M. Levy, J. Secrest, W. Marrero-Ortiz, A. Zhang, D. Collins, and R. Zhang
2014. Cloud Forming Potential of Oligomers Relevant to Secondary Organic Aerosols. Geophys. Res. Lett., 41(18):6538–6545.

Yasmeen, F., N. Sauret, J.-F. Gal, P.-C. Maria, L. Massi, W. Maenhaut, and M. Claeys
2010. Characterization of oligomers from methylglyoxal under dark conditions: a pathway to produce secondary organic aerosol through cloud processing during nighttime, journal=Atmos. Chem. Phys. 10:3803–3812.

Yli-Juuti, T. Zardini, A., A. Eriksson, A. Hansen, J. Pagels, E. Swietlicki, B. Svenningsson, M. Glasius, D. Worsnop, I. Riipinen, and M. Bilde
2013. Volatility of Organic Aerosol: Evaporation of Ammonium Sulfate/Succinic Acid Aqueous Solution Droplets. Environ. Sci. Technol., 47(21):12123–12130.

Yu, G., A. R. Bayer, M. M. Galloway, K. J. Korshavn, C. G. Fry, and F. N. Keutsch
2011. Glyoxal in aqueous ammonium sulfate solutions: Products, kinetics and hydration effects. Environ. Sci. Technol., 45(15):6336–6342.

Yu, L., J. Smith, A. Laskin, C. Anastaio, J. Laskin, and Q. Zhang
2014. Chemical characterization of SOA formed from aqueous-phase reactions of phenols with the triplet excited state of carbonyl and hydroxyl radical. Atmos. Chem. Phys., 14:13801–13816.

Zarzana, K., D. De Haan, M. Freedman, C. Hasenkopf, and M. Tolbert
2012. Optical properties of the products of alpha-dicarbonyl and amine reactions in simulated cloud droplets. Environ. Sci. Technol., 46(9):4845–4851.

Zhang, Q., J. L. Jimenez, M. R. Canagaratna, J. D. Allan, H. Coe, I. Ulbrich, M. R. Alfarra, A. Takami, A. M. Middlebrook, Y. L. Sun, K. Dzepina, E. Dunlea, K. Docherty, P. F. DeCarlo, D. Salcedo, T. Onasch, J. T. Jayne, T. Miyoshi, A. Shimono, S. Hatakeyama, N. Takegawa, Y. Kondo, J. Schneider, F. Drewnick, S. Borrmann, S. Weimer, K. Demerjian, P. Williams, K. Bower, R. Bahreini, L. Cottrell, R. J. Griffin, J. Rautiainen, J. Y. Sun, Y. M. Zhang, and D. R. Worsnop
2007. Ubiquity and dominance of oxygenated species in organic aerosols in anthropogenically-influenced northern hemisphere midlatitudes. Geophys. Res. Lett., 34(13):L13801.

Zhao, Y., A. Hallar, and L. Mazzolein
2013. Atmospheric organic matter in clouds: exact masses and molecular formula identification using ultrahigh-resolution FT-ICR mass spectrometry. Atmos. Chem. Phys., 13:12343–12362.

Zhao, Y. and D. Truhlar
2008. The M06 suite of density functionals for main group thermochemistry, thermochemical kinetics, noncovalent interactions, excited states, and transition elements: two new functionals and systematic testing of four M06-class functionals and 12 other functionals. Theoretical Chemistry Accounts, 120(1-3):215–241.

Zhou, S., L. Gonzalez, A. Leithead, Z. Finewax, R. Thalman, A. Vlasenko, S. Vagle, L. Miller, S.-M. Li, S. Bureekul, H. Furutani, M. Uematsu, R. Volkamer, and J. Abbatt
2014. Formation of gas-phase carbonyls from heterogeneous oxidation of polyunsaturated fatty acids at the air–water interface and of the sea surface microlayer. Atmos. Chem. Phys., 14(3):1371–1384.

Zhou, X. and K. Mopper
1990. Apparent partition coefficients of 15 carbonyl compounds between air and seawater and between air and freshwater; implications for air-sea exchange. Environ. Sci. Technol., 24(12):1864–1869.